REDUCED ORDER MODELLING IN NUCLEAR REACTOR THERMAL HYDRAULICS

A DISSERTATION
SUBMITTED TO THE DEPARTMENT OF MECHANICAL ENGINEERING
AND THE COMMITTEE ON GRADUATE STUDIES
OF IMPERIAL COLLEGE LONDON
FOR THE DEGREE OF
DOCTOR OF PHILOSOPHY

Sokratia Georgaka

October 2020

Abstract

The context of the present thesis is to assess the potential of Reduced Order Models (ROMs) for nuclear reactor thermal hydraulics applications. ROMs constitute advanced modelling techniques aiming at fast high fidelity simulations.

For the purposes of this research, two approaches have been selected and are investigated in depth: the Proper Orthogonal Decomposition (POD) with Galerkin projection (POD-Galerkin) and the hybrid method of Proper Orthogonal Decomposition with Interpolation using Radial Basis Functions, PODI - Galerkin, in the context of parametric model order reduction. Additionally, in terms of the POD method, two sampling techniques are presented and compared: the standard and the nested POD.

The aforementioned methods are applied to a parametric case of non-isothermal mixing in a T-junction pipe for laminar and turbulent flow regimes. The flow is governed by the 3D, unsteady Navier - Stokes equations coupled with the energy equation. Furthermore, a ROM for modelling buoyancy driven flows with the Boussinesq approximation is discussed. Two cases are considered: a closed flow, where the method is applied to a benchmark case of a differentially heated square cavity, and an open flow, where a case of a “cold-trap” formation in a U-bend pipe is investigated.

The suitability of the above techniques is assessed based on a comparison between the reduced order results and those obtained using high fidelity OpenFOAM solvers.

Declaration of Originality

I hereby declare that the work in the present thesis is entirely my own, unless explicitly referenced and acknowledged. This work has not previously submitted in any form for a degree in any other university or institution.

Copyright Declaration

Sokratia Georgaka
October 2020

To Haris & Ioannis,

Acknowledgments

First and foremost, I would like to express my sincere gratidute to my supervisor, Dr Mike Bluck, for providing me with the opportunity to conduct this research and for his continuous support, guidance and encouragement throughout these PhD years. I would also like to thank my industrial supervisor, Dr Sam Treasure, for his suggestions and inputs.

I am greatful to all people in the mathLab group in SISSA and especially to Prof Gianluigi Rozza, a pioneer in the field of model order reduction, and to Dr Giovanni Stabile, with whom I had the pleasure to work with during the time I spent in SISSA and beyond. Giovanni developed the ITHACA-FV library, on which the reduced order model implementation of this work has been developed on. His expertise and fruitful discussions we had, have been proven of outmost importance. I am also thankful to Kelbij Star for her insights and expertize on the implementation of buoyancy in the reduced order model and to all other ITHACA-FV developers for our useful fortnightly discussions on various aspects of the code.

I would like to thank my colleagues with whom I shared the office for the past three years and especially to Dr Giovanni Guistini for his useful suggestions and insights on computational fluid dynamics aspects. I am also grateful for the coffee breaks I had with my colleague and friend Aliki, which were a joyful escape from the office routine. I am also thankful to the people in the ICO Nuclear Energy Futures CDT and in particular to my friends Yadu and Sushi (Dhan-Sham Rana) for the great time we had in the USA.

The list would be incomplete without saying a big thanks to my friend Kyriakos for the extensive conversations we had each time I needed. Also, I would like to thank Dr Mourad Kara for the life-saving advices he gave me when I started this research.

My warmest thanks go to my partner, Ioannis, for riding this emotional doctorate rollercoaster together and for his endless patience and unconditional support during all the ups and downs, and to my family who supported me and raised me to never give up.

Last, but not least, Haris, thank you for making me stronger and more fulfilled than I had ever imagined.

I would like to acknowledge the financial support of Engineering and Physical Sciences Research Council (EPSRC) and Rolls-Royce.

Contents

List of Tables

List of Figures

Nomenclature

Abbreviations

BPOD	Balanced Proper Othogonal Decomposition
BT	Balanced Truncation
BWR	Boiling Water Reactor
CFD	Computational Fluid Dynamics
CPU	Central Processing Unit
DEIM	Discrete Empirical Interpolation
DMD	Dynamical Mode Decomposition
DNS	Direct Numerical Simulation
FOM	Full Order Model
HFM	High Fidelity Model
LES	Large Eddy Simulation
LFS	Lead Fast Reactor
LTI	Linear Time Invariant
PDE	Partial Differential Equation
PODI	Proper Orthogonal Decomposition with Interpolation
POD	Proper Orthogonal Decomposition
PPE	Pressure Poisson Equation
PWR	Pressurized Water Reactor
RANS	Reynolds-Averaged Navier-Stokes
RBF	Radial Basis Functions
RB	Reduced Basis
ROM	Reduced Order Model
SC	System Codes
SGS	Subgrid-Scale Model
SST	Shear-Stress Transport
SUP	Supremizer Enrichment Pressure
SVD	Singular Value Decomposition

URANS	Unsteady Reynolds-Averaged Navier-Stokes
VHTR	Very High Temperature Reactor

Bold Roman Symbols

$\bar{\boldsymbol{u}}$	Time-averaged velocity component
$\overline{\boldsymbol{D}}^R$	Reynolds-averaged strain rate tensor
$\boldsymbol{A}_r$	Reduced matrix of the LTI system
$\boldsymbol{b}$	Reduced vector of unknowns for pressure
$\boldsymbol{b}_r$	Reduced matrix of the LTI system
$\boldsymbol{c}$	Reduced vector of unknowns for temperature
$\boldsymbol{C}_r$	Reduced matrix of the LTI system
$\boldsymbol{f}$	Dirichlet boundary condition for velocity
$\boldsymbol{G}$	ROM convection matrix for the heat equation
$\boldsymbol{g}_r$	Mapping function
$\boldsymbol{h}$	Initial condition for velocity
$\boldsymbol{H}_M$	Hankel Matrix
$\boldsymbol{I}$	Identity matrix
$\boldsymbol{K}$	ROM mass matrix for the heat equation
$\boldsymbol{l}$	Reduced vector of unknowns for eddy viscosity
$\boldsymbol{M}$	ROM mass matrix
$\boldsymbol{N}$	ROM diffusion matrix for the heat equation
$\boldsymbol{n}$	Outward normal vector
$\boldsymbol{P}$	ROM pressure gradient matrix
$\boldsymbol{Q}$	ROM convection tensor
$\boldsymbol{Q}_{T1}$	ROM turbulent tensor
$\boldsymbol{Q}_{T2}$	ROM turbulent tensor
$\boldsymbol{S}_\phi$	Surface vector
$\boldsymbol{u}$	Velocity field
$\boldsymbol{u}'$	Fluctuating velocity component
$\boldsymbol{u}'$	Fluctuating velocity field
$\boldsymbol{U}_s$	Velocity snapshot matrix
$\boldsymbol{u}_s$	Velocity snapshots
$\boldsymbol{U}^{i}{}_{\text{nested}}$	I-th nested snapshot matrix
$\boldsymbol{U}_{sn}$	Global snapshot matrix resulted from nested POD
$\boldsymbol{V}$	Spatial basis function
$\boldsymbol{W}$	Eigenvector matrix
$\boldsymbol{w}$	Vector of weights

$\boldsymbol{W}_c$	Controllability Gramian
$\boldsymbol{W}_o$	Observability Gramian
$\boldsymbol{x}(t)$	State vector
$\boldsymbol{x}_o(t)$	Initial condition
$\boldsymbol{y}(t)$	Output

Greek Symbols

$\bar{\theta}$	Time-averaged temperature component
β^*	Proportionality constant
ϵ	Dissipation rate
ϵ_{L^2}	Relative error
η_i	I-th POD basis function for mass flux
γ	Spread of a kernel
Γ_ϕ	Diffusion Coefficient
λ	Langrange multiplier/ eigenvalues
μ	Dynamic viscosity
ω	Specific dissipation rate
ϕ	Transported quantity
ϕ_E	Flux over the East neighbouring control volume
ϕ_E	Flux over the West neighbouring control volume
ϕ_f	Flux over the control volume
ρ	Density
ρ_k	Kinematic density
τ	Viscous tensor
τ^R	Reynolds stress tensor
θ	Partial derivative
θ'	Fluctuating temperature component
ζ	Control functions
α_{dif_t}	Turbulent thermal diffusivity
α_{dif}	Thermal diffusivity
χ_i	I-th POD basis function for temperature
ϵ_{L^2}	L^2 norm error
Γ	Boundary of Ω
ν_t	Eddy viscosity
ν	Dimensionless kinematic viscosity
Ω	Bounded domain
ψ_i	I-th POD basis function for pressure

θ	Temperature field
ξ_i	I-th POD basis function for eddy viscosity

Bold Greek Symbols

$\boldsymbol{\alpha}$	Reduced vector of unknowns for velocity
$\boldsymbol{\Sigma}$	Diagonal matrix
$\boldsymbol{\Theta}$	Radial Basis Function kernels
$\boldsymbol{\Upsilon}$	Non-linear term
$\boldsymbol{\varphi_i}$	I-th POD basis function for velocity

Roman Symbols

$\bar{p}$	Time-averaged pressure component
$\dot{\mathbf{z}}(t)$	Adjoint system state
$\dot{m}$	Mass flux
$\hat{H}_s$	Reduced transfer function
$\hat{M}_n$	Moment matching
$\mathscr{k}$	Thermal conductivity
$\mathscr{G}$	Dynamical system - FOM
$\mathscr{G}_r$	Lower order dynamical system
$\mathscr{K}$	Training set space
$\mathscr{k}$	Thermal Conductivity
$\mathscr{P}$	Parameter space
$\mathscr{Q}$	Space-time domain
$\mathfrak{C}$	Correlation matrix
S	Subspace
c_p	Specific capacity
dt	Time-step
e	Initial condition for temperature
f	Face of the control volume
g	Dirichlet boundary condition for temperature
Gr	Grashof number
H^R	Heat flux term
H_s	Transfer function
k	Turbulent kinetic energy
N_t	Number of time instances
p'	Fluctuating pressure component
Pr	Prandtl number
Re	Reynolds number

S_ϕ	Source term
T	Final time of the simulation
u_D	Scaling coefficients
V_p	Control Volume
N_p^s	Number of unknowns for pressure at reduced order level before the truncation
N_u^h	Number of degrees of freedom for velocity at full-order level
N_u^r	Number of unknowns for velocity at reduced order level after the truncation
N_u^s	Number of uknowns for velocity at reduced level before the truncation
N_μ	Number of parameters in the training set $\mathscr{K}$
N_θ^s	Number of unknowns for temperature at reduced order level before the truncation
Pr_t	Turbulent Prandtl number
p	Pressure field

Mathematical Symbols

$\mathbb{R}^+$	Positive real numbers
$\mathbb{R}^d$	d-dimensional space
$\boldsymbol{\nabla}$	Gradient operator
$\boldsymbol{\nabla}\cdot$	Divergence operator
$\boldsymbol{\nabla}\times$	Curl operator
$\boldsymbol{\nabla}^s$	Symmetric gradient operator
$\boldsymbol{u}$	All vectors are denoted by bold italic symbols
χ	All scalars are denoted by italic symbols
Δ	Laplacian operator
$\dot{\boldsymbol{x}}$	Dotted symobls denote derivative with respect to time
$\langle\cdot,\cdot\rangle$	Inner product in $L^2(\Omega)$
$\lVert\cdot\rVert$	Norm in $L^2(\Omega)$
$\otimes$	Tensor product

Chapter 1

Introduction

The content of this chapter has been partially published in:

GEORGAKA, S., STABILE, G., ROZZA, G., and BLUCK, M.J. 2020. Parametric POD-Galerkin Model Order Reduction for Unsteady-State Heat Transfer Problems. Communications in Computational Physics, Vol 27, No. 1, pp. 1-32.

This chapter begins with the context of the present thesis, followed by an overview of Model Order Reduction applications in nuclear engineering. The scope of the present thesis is also discussed.

1.1 Context

Partial differential equations (PDEs) describe a variety of physical systems occurring in nature and in engineering. PDEs are complex and generally non-linear and their numerical solution requires considerable computational effort. For example, fluid flow, a phenomenon very common in many engineering fields, is governed by the Navier-Stokes equations and accurate numerical solutions provide vital insight into complex physical processes. Analytical solutions of these equations are impossible in most circumstances. For this reason, computational fluid dynamics (CFD) has seen progressive development since the 1970s and is now capable of solving many practical problems in fluid flow and heat transfer. With the continued development of improved algorithms and increasing computational power, CFD is now used in various engineering fields such as aerospace, nuclear, civil, mechanical as well as non-engineering fields such us neuroscience, meteorology etc.

Despite its popularity and applicability, the computational burden for simulating realistic large scale and many-query systems is still very high, even with the use of supercomputers. A good example of the challenges involved can be found in nuclear applications, where turbulence, multiphase flow and heat transfer phenomena occur in complex geometries; a fairly accurate CFD simulation of a single instance of an accident case scenario could take months or more to be performed. To address these challenges, System Codes (SC), such as RELAP, CATHARE, etc and sub-channel codes (COBRA, etc), constitute phenomenological reduced order methods based on considerable limiting physical assumptions. These codes, that were developed in the 1950s, rely on major physical and geometrical simplifications, such as averaging over the flow cross section leading to essentially 1D simulations.

These simplifications can save great amounts of computational time. However, the compromise is that they rely exclusively on experimental and phenomenological correlations to take account of heat transfer and turbulence and the like. In particular, these assumptions are particularly inadequate for 3D flows. In the recent years although these codes have been improved allowing some limited 3D capability, the accuracy is still inadequate and their application is very limited. The same applies in the field of neutronics for the study of reactor dynamics. Geometrical and physical simplifications are made to the governing equations in order to obtain a computationally affordable model. These simplifications include 1D geometries, homogenous core dynamics, uniform axial fluxes, etc. The challenge then, is to bridge the considerable gap between high fidelity full order models (FOMs) (e.g. CFD and its variants) and these over-simplistic surrogate models (system and sub-channel codes).

Surrogate models are derived from high fidelity models (HFM) usually using *Data-fit* (DF), *Hierarchical* or *Reduced Order Model* (ROM) methods. *Data-fit* models treat the Full Order Model (FOM) as a "black-box" method to obtain the data, the interpolation or regression of which evaluates the reduced order input-output mapping function. This non-intrusive procedure is advantageous, because it entirely bypasses system matrices and state vector calculations, hence it does not require access to legacy codes. However, it is a non physics-based method and, therefore, the surrogate model does not inherit the underlying physics of the problem. Moreover, DF models can not model conditions other than those that were used during the derivation of the DF surrogate model. On the contrary, *Hierarchical* surrogates, are physics-based models usually obtained by making various simplifications or considering coarser grids. However, *Hierarchical* models are low fidelity models. ROMs are usually formed by projection of the original system of equations onto a subspace. They are considered the most advantageous, because they preserve the structure of the problem, are physics-based and, most importantly, they retain the fidelity of the FOM.

Modern ROMs have been proposed as an alternative way of approximating systems like those mentioned above in a more sophisticated and reliable way. Unlike *Hierarchical* methods, such as SC, ROMs retain the fidelity of the FOM, while considerably reducing the computational burden. Compared to DF models, parametric ROMs can model well problems with different initial conditions to those used during their construction. Reduced order modelling is a highly promising area, which is currently flourishing in the science and engineering community. However, the biggest challenge is the construction of stable ROMs that are able to accurately predict the behaviour of the examined system. This requires careful consideration of strong nonlinearities, long term transient flows, turbulence and other multi-physics phenomena, which should be taken into account during the projection process.

1.2 Reduced Order Modelling in Nuclear Engineering

Complex transient phenomena, such as heat transfer, neutron fluxes, power instabilities and two phase flows are present in nuclear power plants. The high complexity and the non-linear behaviour of the nuclear power reactor systems make high fidelity modelling challenging. To accelerate the modelling process, various geometrical and physical simplifications have been proposed, but the loss in accuracy is considerable. Simplified models, which usually model only the most dominant phenomena have been developed. For example, instead of the Navier-Stokes equations, Euler equations are applied in 1D geometries. In addition, in neutronics, the system is described by the so-called point kinetics equations, where the reactor is taken as a point and the spatial flux profile is neglected.

These models can be partially seen as surrogate models, but the actual aim of the modern model order reduction is to develop a low-cost and high fidelity model. High fidelity nuclear reactor modelling usually requires large parametric spaces for the solution of the coupled PDEs. SC like RAMONA can model well parts of the system, but a complete analysis is prohibitive in terms of computational time and resources. A 'compact' model with fewer degrees of freedom is, therefore, necessary.

There has been a lot of simplified modelling research, mainly in the field of Boiling Water Reactor (BWR) stability analysis, which, triggered by some instability events, occurred in the 1980s. Under stable operating conditions, BWRs show linear behaviour. Two-phase flow, which is found in BWR heated channels, can trigger power in-phase or out-of-phase instabilities, mainly caused by density-wave oscillations. Density waves are formed, for example, by propagation of travelling voids, which are created at the bottom part of a BWR due to inlet flow reduction under stable power conditions. Understanding these instabilities is crucial, because they can lead to non-linear behaviour and serious mechanical and material damages.

In real environments, stability experiments are difficult due to the application of low flow and high power conditions. Instead, a high fidelity simulation would be much more favourable where complete solution manifolds could be investigated. Towards simplified models, Hopf bifurcation theory has attracted many researchers. Clausse and Lahey were the first to attempt modelling this behaviour 1991. The authors considered a 1D homogeneous equilibrium simplified model where the enthalpy is linearly dependent and in single phase and two phase regions, discretisation is performed by Galerkin nodal method (Clausse and Lahey 1991). In (Munoz-Cobo and Verdú 1991), a simplified model is derived for describing the limit cycles in BWRs using Hopf bifurcation. The authors applied the center manifold method to reduce the system's dimension from five to just two, showing that the reduced system preserves the key dynamics and thus bifurcation can be applied. Both models, when describing dense wave oscillations, take into account only two nodal regions, a single phase and a two phase, where there is thermodynamic equilibrium. However, there is a third region, the sub-cooled, which has to be taken into account, because it can affect the void feedback reactivity. The sub-cooled region, was taken into account in (Munoz-Cobo, Chiva, and Sekhri 2004), where a ROM was developed, considering a model with three nodes per channel. In (Dokhane 2004) and (Dokhane, Hennig, Rizwan-uddin, and Chawla 2007), Dokhane proposed a novel ROM for application in density wave oscillations and in-phase/out-of-phase instabilities, as well as in bifurcation analysis, in a complete two channel coupled system.

In neutronics, an equivalent to POD modes, known as lambda modes, was used for reduction of the two-group diffusion equations. As in the flow analysis a state vector can be written as a linear combination of POD modes, this theory suggests that the neutron flux can be approximated as a linear combination of basis functions, the lambda modes. Therefore, lambda modes can help us understand the formation of in-phase and out-of-phase instabilities. The theory of lambda modes was proposed by Miro in an attempt to integrate the transient neutron diffusion equation, using only a few dominant modes (lambda modes) (Miró, Ginestar, Verdú, and Hennig 2002). In (Ginestar, Miro, Verdu, and Hennig 2002), the authors performed a modal instability analysis of a BWR reactor using lambda modes. The analysis showed that the in-phase instabilities oscillate in the fundamental mode, whereas the out-of-phase instabilities are linked to the first and second sub-critical modes. The results were compared to those of RAMONA code and they match each other.

In the field of Pressurized Water Reactors (PWRs), ROMs have been developed in the context of control applications design, using Balanced Truncation (BT). The control systems of PWRs, need rectifications throughout their operation lifetime, due to the variation of reactivity and power. Optimal single controller linear designs are being considered for meeting these changes. In (Bendotti, Codrons, Falinower, and Gevers 1998), the authors derived and tested three different ROMs for simplifying the PWR controller design. In the case of open loop, the system contains unstable nodes and, therefore, the BT method cannot be directly applied. For this reason, a factorization of the transfer function has to be performed prior to BT. This process is called “output frequency weighted balanced truncation”. A second ROM for closed loop has been derived via direct BT and a third method via loop identification technique. Amongst the three techniques, the closed loop exhibits the best performance. In controller design, Bendotti used balanced realisation and BT, considering a model, where, in a PWR, slowly transient uncertain parameters exist due to changes in reactivity and power (Bendotti and Beck 1999).

Coolant flow plays a crucial role in the design and safe operation of nuclear reactors. Accurate modelling can be performed via CFD codes, such as Direct Numerical Solution (DNS) or Large Eddy Simulation (LES). These methods are time consuming, because refined meshes are required for modelling phenomena like turbulence near the wall region in rod bundles, or other instabilities. POD-ROMs are ideal candidates for modelling such phenomena, giving fairly accurate and rapid results. Even though large research has been carried out in other industries, the application of POD-ROMs in the field of nuclear engineering flow modelling is limited. For example, snapshot POD has been widely used for studying the coherent structures of turbulent flows in case of pipes, cavities, airfoils, cylinders etc. In more complex geometries, such as those found in nuclear reactors, due to the presence of a large number of rods, the counter rotating vortices in the narrow gaps can interact, giving rise to 3D vortex structures. In (Merzari and Ninokata 2011), Merzari and Ninokata applied snapshot POD for studying turbulent flow in the interior of a tightly packed rod bundle (pitch to diameter = 1.05) using LES snapshots. In comparison with single channel flow, the results showed a more complicated flow structure in rod bundles, mainly due to the presence of modes with multiple wavelengths and wavenumbers inherited by periodic boundary conditions.

The POD method is also present in reactor physics. In (Buchan, Pain, Fang, and Navon 2013a) an alternative snapshot technique for constructing POD based ROMs has been proposed for the calculation of the criticality factor. The classical eigenvalue problem is time independent but the snapshots should present time evolution, thus the authors proposed and developed a time-dependent eigenvalue problem. The resulting ROM is able to give reliable and fast results even when a different geometry is being applied. In (Banyay, Ahmadpoor, and Brigham 2014), the authors obtained a ROM for use in Very High Temperature Reactor (VHTR) lower plenum, using the POD-Galerkin method.

Reduced Basis (RB) methods have been applied to model the neutronic behaviour in nuclear reactors, offering reliable and rapid calculations. In (Sartori, Baroli, Cammi, Luzzi, and Rozza 2014), the authors applied the RB greedy algorithm to derive a ROM, considering the parametrised 2D multi-group diffusion equation, for studying the movement of the control rods. The ROM can be accurately predict the neutron flux profile, accounting also spatial effects due to the rod movements. Most importantly, the computational savings are considerable. The same authors, in (Sartori, Cammi, Luzzi, and Rozza 2016b), suggested a different hybrid sampling method for the generation of the RB. This hybrid method uses Centroidal Voronoi Tesselation (CVT) and POD for further reducing the dimension of the basis. Unlike the greedy algorithm, which relies on *a posteriori* error estimates, CVT leads to an even faster offline phase.

More recently, a ROM which couples neutronics and heat transfer effects was introduced in (Sartori, Cammi, Luzzi, and Rozza 2016a). The authors proposed a methodology for obtaining a RB multi-physics model using POD snapshots from Lead Fast Reactor (LFS) single channel. The ROM was able to accurately predict the neutron flux and temperature distribution while achieving considerable speed-ups when compared to the FOM Finite Element (FE) method.

1.3 Scope and contributions of the present thesis

The aim of the present thesis focuses on proposing ROMs that could be potentially used in the modelling of nuclear reactor thermal hydraulics. These systems usually contain a network of T-junction, straight or bend pipes, which allow the flow of liquid or gas coolant around the plant. The role of the coolant is to carry away the heat generated inside the nuclear reactor core and transport it to the turbines for electrical power generation. It also serves as a mean of keeping the temperature inside the core within safe limits, prohibiting the overheating of materials and fuel elements. It therefore plays a crucial role in the safety of nuclear power reactors.

This thesis is influenced by some challenging flow regimes and configurations that arise in nuclear reactor thermal hydraulic systems:

- Laminar and turbulent thermal mixing of two different temperature streams in T-junction pipes. This phenomenon leads to high transient temperature fluctuations in the pipe wall regions, which could potentially lead to thermal fatigue and subsequent failure of the piping material (cracks formation, breakage etc). Turbulent thermal mixing has been studied both experimentaly and computationally in (Ayhan and Sokmen 2012; Frank, Lifante, Prasser, and Menter 2010; Kuczaj, Komen, and Loginov 2010; Naik-Nimbalkar, Patwardhan, Banerjee, Padmakumar, and Vaidyanathan 2010; Tunstall, Laurence, Prosser, and Skillen 2016b; Walker, Simiano, Zboray, and Prasser 2009). In the computational case, various turbulent modelling techniques have been studied, inluding the Large Eddy Simulation (LES) and the Unsteady Reynolds Averaged Navier Stokes (URANS) or the combination of the two methods. These methods, given the high Reynolds numbers and the nature of the problem, require fine 3D meshes, leading to high computational costs. The laminar case is also considered in this work, since, from model reduction point of view, it entails challenges related to the coupling between the Navier-Stokes and the energy equations.

- Modern nuclear power plants benefit from the mechanism of natural convection to drive the coolant in case of accident (natural circulation). These so-called passive systems are found, for instance, in PWR reactors, where a natural circulation loop is formed due to the difference in temperature between the core (heat source) and the steam generator (sink). The flowrate is maintainted due to gravity, by placing the core at a lower elevation than the steam generator. This, therefore guarantees the removal of the decay heat without the need of backup diesel generators, which could fail as happened in the Fukushima Daiici accident (Hollnagel and Fujita 2013).

Considering the above, for the purposes of this thesis, the following flow configurations and ROMs have been selected and assessed:

- Parametric POD - Galerkin for laminar flow problems with heat transfer, applied in T-junction pipes.

- Parametric Hybrid Proper Orthogonal Decomposition with Interpolation (PODI) - Galerkin for turbulent flow problems with heat transfer. The proposed ROM is validated on thermal mixing in a T-junction pipe.
- Parametric POD - Galerkin for laminar buoyancy driven flows in enclosed geometries, tested in a differentially heated square cavity.
- POD - Galerkin for laminar buoyancy driven flows in open geometries, tested in a U-bend pipe.

The contributions of this thesis, which, to the best of the author's knowledge, are presented for the first time in the field of model order reduction and modelling of nuclear thermal hydraulics are the following:

- Proposing a ROM derived from laminar problems that involve thermal mixing and heat transfer phenomena, such as those occurring in T-junction pipes. The proposed parametric POD-Galerkin method takes into account the parametrised, unsteady, 3D Navier-Stokes equations one-way coupled with the parametrised unsteady energy equation.
- A ROM for applications in turbulent heat transfer/thermal mixing problems. A hybrid parametric Proper Orthogonal Decomposition with Interpolation (PODI)-Galerkin is proposed, where the PODI method is used for the treatment of the eddy viscosity term. Two different types of POD are studied, the standard POD and the nested POD methods.
- Development of a parametric POD-Galerkin method for enclosed buoyancy driven flows in a differentially heated square cavity.
- Development of a POD-Galerkin ROM for modelling open buoyancy driven flows. The ability of the proposed ROM to predict complex phenomena such as the "cold-trap" formation in a U-bend pipe is studied. A Pressure-Poisson Equation (PPE) method, adjusted to accomodate the buoyancy term, is proposed for the treatment of the pressure term.

1.4 Outline

The rest of the thesis is organized as follows:

- **Chapter 2** gives a general overview and literature review of the most popular projection based model order reduction methods, indicating their suitability for applications in fluid dynamics. A short mathematical description of each method is provided along with some applications.

- **Chapter 3** presents the mathematical background for the Full Order Model. This includes the Navier-Stokes equations of fluids, the energy equation as well as turbulence modelling. The turbulence modelling techniques that are discussed are the Large Eddy Simulation (LES) and Unsteady Reynolds Averaged Navier-Stokes (URANS). In the last section, the Finite Volume method is discussed in detail.

- **Chapter 4** provides the mathematical framework for the Reduced Order Model. The method presented in this chapter is the Proper Orthogonal Decomposition-Galerkin for parametric problems, which is the main method that is followed in this thesis. For the stabilization of the equations, the supremizer enrichment method and a Pressure Poisson Equation methods are also presented.

- **Chapter 5** deals with model order reduction for laminar heat transfer problems, using the parametric POD-Galerkin method. A mathematical formulation for both the FOM and the ROM is provided as well as a method for treating parametric boundary conditions. This chapter contains a numerical application of the suggested method applied in a T-junction pipe. Two cases are considered, one where the parameters of interest are the time and the two temperature inlet boundary conditions, and one where the parameteric dependence is on the time and the kinematic viscosity.

- **Chapter 6** introduces a hybrid model order reduction method for modelling turbulent heat transfer problems. The hybrid method suggested in this chapter treats the reduction of the eddy viscosity term in a non-intrusive way, using the Proper Orthogonal Decomposition with Interpolation (PODI). The interpolation is performed with Radial Basis Functions (RBF). In this way, the turbulence treatment in the Reduced Order Model is transparent to the turbulence modelling method that used in the Full Order Model. This makes the ROM faster and independent of the turbulence treatment of the FOM. The reduction of the velocity, temperature and pressure are performed using the intrusive

POD-Galerkin method. For the assembly of the POD snapshot matrix, a Nested POD method is introduced and compared against the standard POD method. The former method tends to be faster where problems with a large number of parameter values are considered. The hybrid model order reduction method is validated on a T-junction thermal mixing problem with parametric velocity inlet boundary conditions. The robustness of the ROM is tested on several sets of inlet velocity boundary values which belong in the range of the training space but they are not overalapped by the training points. Nested and standard POD methods are also compared for this test case.

- **Chapter 7** suggests a model order reduction method for buoyancy driven flows where the FOM equations are formulated using the Boussinesq approximation. Therefore, a strong coupling between the velocity and temperature is implied. The ROM is derived with the POD-Galerkin method. Two cases are studied: an enclosed flow in a parametric differentially heated square cavity, where the pressure term is neglected, and an open flow in a U-bend pipe with a "cold-trap" formation, where the pressure is reconstructed by exploiting the Pressure Poisson Equation.

- **Chapter 8** draws conclusions of the present work and suggests ideas for further development.

1.5 Summary of the Chapter

The present chapter introduced the context and the scope of the present thesis as well as discussed the status of model order reduction methods that have been applied in nuclear engineering.

Chapter 2

Projection Based Model Order Reduction Methods

The scope of this chapter is to discuss the aspects of the most popular projection based model order reduction methods and assess their suitability for applications in nuclear thermal hydraulics. For the computation of the reduced basis, methods including BT, POD, Balanced Proper Orthogonal Decomposition (BPOD) and parametric methods are discussed. Model order reduction methods have originally been developed for Linear Time-Invariant (LTI) systems, which are discussed in this chapter. Although CFD mostly deals with non-linear equations (Navier-Stokes), the following methods can be extended to non-linear cases. To demonstrate the idea of model order reduction, the mathematical framework in this chapter is presented for LTI systems, but also non-linear examples are given in the literature review.

2.1 General Overview

Considering a dynamical system, $\mathscr{G}$, of the order of m, which is usually very large ($m > \mathscr{O}(10^5)$), the general idea of model order reduction is to approximate $\mathscr{G}$ with a lower order model, $\mathscr{G}_r$, of the order of r, where $r << m$. For example, let's consider the following LTI system in the form of $\dot{\boldsymbol{x}}(t) = \boldsymbol{f}(\boldsymbol{x}(t), \boldsymbol{u}(t))$ with output $\boldsymbol{y}(t) = \boldsymbol{l}(\boldsymbol{x}(t), t)$, inputs $\boldsymbol{u}$, and initial condition $\boldsymbol{x}(0) = \boldsymbol{x}_0$. The $\boldsymbol{f}()$ and $\boldsymbol{l}()$ represent vector functions. The vector $\boldsymbol{x} \in \mathbb{R}^m$ represents the state variables, the order of which, m, indicates the order or the degrees of freedom of the FOM. The output has only been considered as a function of $\boldsymbol{x}(t)$ since, for many physical applications, the matrix that weights the system's inputs is null.

Assuming that the evolution of the state vector, $\boldsymbol{x}$, is given by the following LTI system:

$$\begin{aligned} \dot{\boldsymbol{x}}(t) &= \boldsymbol{A}\boldsymbol{x}(t) + \boldsymbol{B}\boldsymbol{u}(t), \\ \boldsymbol{y}(t) &= \boldsymbol{C}\boldsymbol{x}(t), \end{aligned} \tag{2.1.1}$$

where $\boldsymbol{x} \in \mathbb{R}^m$, $\boldsymbol{A} \in \mathbb{R}^{mxm}$, $\boldsymbol{B} \in \mathbb{R}^{mxk}$, $\boldsymbol{C} \in \mathbb{R}^{qxm}$ are given matrices, $\boldsymbol{u} \in \mathbb{R}^k$ and $\boldsymbol{y} \in \mathbb{R}^q$. Assume also the initial condition $\boldsymbol{x}(0) = \boldsymbol{x}_0 \in \mathbb{R}^m$. The general approach of model order reduction is:

- Sampling and approximation of the state vector $\boldsymbol{x}$ in a reduced basis of dimension $n < m$
- Truncation of the reduced basis, obtaining a new dimension $r << n$
- Reduction of the order of the FOM equations by projection onto the reduced basis

The state variable is usually approximated as the following linear combination:

$$\boldsymbol{x}(t) \approx \boldsymbol{V} x_r, \tag{2.1.2}$$

where $\boldsymbol{V}$ is a matrix of spatial basis vectors with columns spanning an $n << m$ dimensional subspace $\mathscr{S}$ and x_r the reduced state vector. The dimension of the basis and, hence of the system, is usually further reduced to $r << n$ by applying a basis truncation. A projection is then employed in order to force equations (2.1.1) in the reduced space $\mathscr{S}$. The reduced order system can be written as:

$$\begin{aligned} \dot{\boldsymbol{x}}_r(t) &= \boldsymbol{A}_r\boldsymbol{x}_r(t) + \boldsymbol{B}_r\boldsymbol{u}(t), \\ \boldsymbol{y}_r(t) &= \boldsymbol{C}_r\boldsymbol{x}_r(t), \end{aligned} \tag{2.1.3}$$

where $\boldsymbol{A}_r \in \mathbb{R}^{rxr}$, $\boldsymbol{B}_r \in \mathbb{R}^{rxk}$, $\boldsymbol{C}_r \in \mathbb{R}^{qxr}$ are the reduced matrices, figure (2.1).

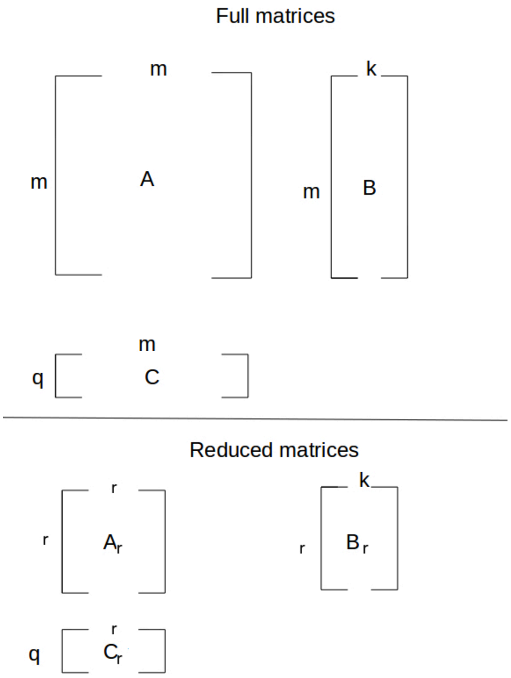

Figure 2.1: System matrices in FOM and ROM

In case of non-linear systems, the LTI system (2.1.1) is modified in order to accomodate the non-linear term, $\boldsymbol{\Upsilon}(\boldsymbol{x})$, as follows:

$$\begin{aligned} \dot{\boldsymbol{x}}(t) &= \boldsymbol{\Upsilon}(\boldsymbol{x}) + \boldsymbol{B}\boldsymbol{u}(t), \\ \boldsymbol{y}(t) &= \boldsymbol{C}\boldsymbol{x}(t). \end{aligned} \tag{2.1.4}$$

The previous system, (2.1.4), is reduced to

$$\begin{aligned} \dot{\boldsymbol{x}}_r(t) &= \boldsymbol{\Upsilon}_r(\boldsymbol{x}_r) + \boldsymbol{B}_r\boldsymbol{u}(t), \\ \boldsymbol{y}_r(t) &= \boldsymbol{C}_r\boldsymbol{x}_r(t), \end{aligned} \tag{2.1.5}$$

where $\boldsymbol{\Upsilon}_r$ is the reduced non-linear term and $r << n$. For simplicity, the discusion is continued for LTI systems, but the same principles can be applied to non-linear systems as well. Non-linear model order reduction will be discussed in depth later, with the introduction of the Navier-Stokes equations.

During the projection, the residual of the approximation, $\boldsymbol{r} = \boldsymbol{V}\boldsymbol{A}\boldsymbol{x}_r + \boldsymbol{B}\boldsymbol{u} - \boldsymbol{V}\dot{\boldsymbol{x}}_r$, is forced to be orthogonal (Petrov-Galerkin condition) to the reduced basis $\boldsymbol{V}$, so that

$\boldsymbol{V}^T\boldsymbol{r} = 0$. Thus, the projected reduced matrices (figure (2.1)) can be written as:

$$\begin{aligned} \boldsymbol{A}_r &= \boldsymbol{V}^T\boldsymbol{A}\boldsymbol{V}, \\ \boldsymbol{B}_r &= \boldsymbol{V}^T\boldsymbol{B}, \\ \boldsymbol{C}_r &= \boldsymbol{C}\boldsymbol{V}. \end{aligned} \tag{2.1.6}$$

This method is known as Galerkin projection. A figure, showing a projection based model order reduction method is presented in (2.2). The temporal coefficients, $\alpha_i(t)$ (this is the same as x_r but in the following chapters will be reffered as $\alpha_i(t)$), can be calculated by the projection of the basis functions onto the snapshots or using the ROM via the Galerkin projection as we will discuss in chapter 4. Calculating the temporal coefficients directly using the basis projection onto the snapshots generally restricts the applicability of the 'ROM' to temporal or physical parametrization. For such cases, the dynamic ROM can be used to simulate other non-observed parameter values within the training range or to evolve in time. On figure (2.2), the bottom temporal coefficients represent the reduced ODEs derived using Galerkin projection.

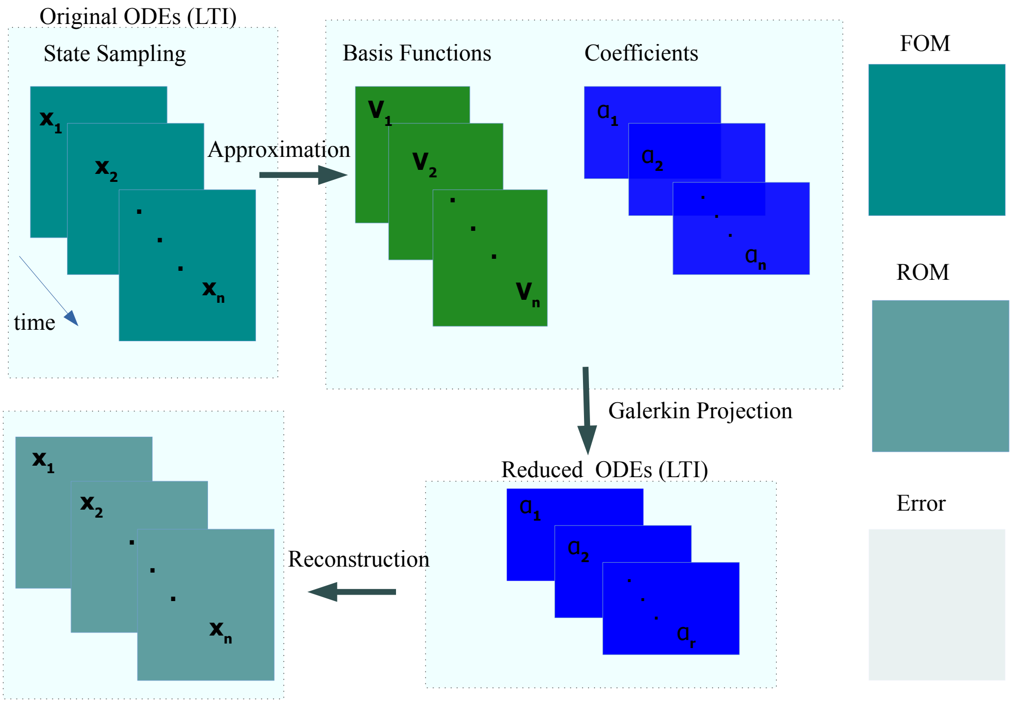

Figure 2.2: Projection Based Model Order Reduction Procedure.

2.2 Balanced Truncation

Balanced Truncation (BT) was originally developed in control theory for input-output LTI systems and is based on the singular value decomposition (SVD) of the Hankel matrix for the calculation of the Hankel singular values. Considering the LTI system given by the equations (2.1.1), the positive-definite [1] controllability ($\boldsymbol{W}_c$) and observability ($\boldsymbol{W}_o$) Gramians are computed using the Lyapunov equations,

$$\begin{aligned} \boldsymbol{A}\boldsymbol{W}_c + \boldsymbol{W}_c\boldsymbol{A}^* + \boldsymbol{B}\boldsymbol{B}^* = 0, \\ \boldsymbol{A}^*\boldsymbol{W}_o + \boldsymbol{W}_o\boldsymbol{A} + \boldsymbol{C}^*\boldsymbol{C} = 0, \end{aligned} \tag{2.2.1}$$

where the * denotes conjugate transpose and the Gramians ($m \times m$ matrices) $\boldsymbol{W}_c$ and $\boldsymbol{W}_o$ are defined as:

$$\begin{aligned} \boldsymbol{W}_c = \textstyle\int_0^\infty e^{\boldsymbol{A}t}\boldsymbol{B}\boldsymbol{B}^* e^{\boldsymbol{A}^*t}dt, \\ \boldsymbol{W}_o = \textstyle\int_0^\infty e^{\boldsymbol{A}^*t}\boldsymbol{C}\boldsymbol{C}^* e^{\boldsymbol{A}t}dt. \end{aligned} \tag{2.2.2}$$

Moore (Moore 1981) introduced the Balanced Realization approach, where, using a coordinate state transformation $\boldsymbol{x} = \boldsymbol{T}\boldsymbol{x}_r$, "balanced" the Gramians by making them equal. The matrix $\boldsymbol{T}$ is non-singular of the order of m. The transformed system matrices are obtained by projection, as follows:

$$\begin{aligned} \boldsymbol{A}' &= \boldsymbol{T}^{-1}\boldsymbol{A}\boldsymbol{T}, \\ \boldsymbol{B}' &= \boldsymbol{T}^{-1}\boldsymbol{B}, \\ \boldsymbol{C}' &= \boldsymbol{C}\boldsymbol{T}, \\ \boldsymbol{W}_c' &= \boldsymbol{T}^{-1}\boldsymbol{W}_c\boldsymbol{T}^{-1*}, \\ \boldsymbol{W}_o' &= \boldsymbol{T}^*\boldsymbol{W}_o\boldsymbol{T}. \end{aligned} \tag{2.2.3}$$

The balancing matrices $\boldsymbol{T}$ and $\boldsymbol{T}^{-1}$ can be computed using Cholesky factorization and eigenvalue decomposition. This results to the diagonal Hankel matrix, $\boldsymbol{H}_M$, which is defined as:

$$\boldsymbol{H}_M = \boldsymbol{T}^{-1}\boldsymbol{W}_c\boldsymbol{T}^{-1*} = \boldsymbol{T}^*\boldsymbol{W}_o\boldsymbol{T} = diag(\sigma_1, \sigma_2, ...\sigma_m) = \boldsymbol{\Sigma}. \tag{2.2.4}$$

Further to this, Moore introduced the BT method, where the idea is to keep only

---

[1] A symmetric matrix $\boldsymbol{M} = [m_{ij}]$ is positive-definite if $\boldsymbol{\phi}^T\boldsymbol{M}\boldsymbol{\phi} > 0\,\forall$ column vectors $\boldsymbol{p}$

the most energetic Hankel singular values. The Hankel singular values are ordered in descenting order as $\sigma_1 \geq \sigma_2 \geq \cdots \geq \sigma_n \geq 0$ and contain the contribution of each mode to the input-output system. The diagonal matrix, $\boldsymbol{\Sigma}$, can be partitioned as:

$$\boldsymbol{\Sigma} = \begin{bmatrix} \boldsymbol{\Sigma}_1 & \mathbf{0} \\ \mathbf{0} & \boldsymbol{\Sigma}_2, \end{bmatrix}$$

where the largest Hankel singular values are contained in $\boldsymbol{\Sigma_1}$, while the smallest in $\boldsymbol{\Sigma_2}$. The system matrices $\boldsymbol{A}'$, $\boldsymbol{B}'$ and $\boldsymbol{C}'$ can also be partitioned in a similar way as

$$\boldsymbol{A}' = \begin{bmatrix} \boldsymbol{A}_{11} & \boldsymbol{A}_{12} \\ \boldsymbol{A}_{21} & \boldsymbol{A}_{22}, \end{bmatrix}$$

$$\boldsymbol{B}' = \begin{bmatrix} \boldsymbol{B}_1 \\ \boldsymbol{B}_2 \end{bmatrix}$$

and

$$\boldsymbol{C}' = [\boldsymbol{C}_1 \boldsymbol{C}_2]. \tag{2.2.5}$$

$\boldsymbol{A}_{11}$, $\boldsymbol{B}_1$ and $\boldsymbol{C}_1$ can be seen as the reduced system matrices ($\boldsymbol{A}_r$, $\boldsymbol{B}_r$ and $\boldsymbol{C}_r$) of the reduced system (2.1.3) and thus the ROM can be written as:

$$\begin{aligned} \dot{\boldsymbol{x}}_r(t) &= \boldsymbol{A}_{11}\boldsymbol{x}_r(t) + \boldsymbol{B}_1\boldsymbol{u}(t), \\ \boldsymbol{y}_r(t) &= \boldsymbol{C}_1\boldsymbol{x}_r(t). \end{aligned} \tag{2.2.6}$$

The reduced bases $\boldsymbol{V}$ and $\boldsymbol{W}$ are equivalent to the first rows of $\boldsymbol{T}^{-1}$.

Pernebo and Silverman in (Pernebo and Silverman 1982) further investigated the BT method in both time continuous and discrete problems, showing asymptotic stability. Therefore, in terms of stability, this method yields a well behaved ROM. As Glover suggested in (Glover 1984),for LTI continuous systems, BT possesses *a priori* error bounds which, for LTI systems, are the lowest possible. Beyond first order linear systems, Reis and Styker (Reis and Stykel 2008) introduced BT for second order systems, where, unlike first-order systems, the ROM does not possess a guaranteed stability.

BT has been widely applied in the study of control systems with approximately $\mathscr{O}(10^4)$ dimensions. However, for large-scale systems, in the order of $\mathscr{O}(10^5)$ and above, such as fluid dynamics problems, BT becomes computationally intractable due to the dense Gramian matrices. In addition, the classical BT is only appliacable to LTI systems. In (Dones, Skogestad, and Preisig 2011), the authors extended the BT to non-linear systems, where a linearisation process, referred to as empirical Gramians, is performed in advance. Empirical balanced truncation for non-linear systems has also been employed in (Condon and Ivanov 2004) and in (Lall, Marsden, and Glavaški 2002), where, in the latter, a Galerkin projection is performed.

2.3 Proper Orthogonal Decomposition

An essential tool in the development of ROMs is the POD or Karhunen - Loève decomposition. POD was originally conceived as a data analysis method for finding an optimal lower-dimensional orthonormal basis in a least-squares sense. It works for multidimensional dynamical systems, using data from high fidelity simulations (such as CFD) or from experiments. POD can be seen as a modal decomposition technique, which provides modes ranked according to their energy.

For the calculation of the POD basis, consider the state vector $\boldsymbol{x} \in \mathbb{R}^m$, given by equations (2.1.1) and its approximation (2.1.3). Using the theory of snapshots, introduced by Sirovich in (Sirovich 1987b), the discretized state variable, which is sampled as $\boldsymbol{X} = \{\boldsymbol{x}_1(t), \boldsymbol{x}_2(t), ...\boldsymbol{x}_l(t)\}$, $\boldsymbol{X} \in \mathbb{R}^{m \times l}$, is given by the trajectories $\boldsymbol{x}_i(t)_{i=1}^{l}$, which are taken in the discrete time instances $t \in [0, t_l]$. The aim of the POD is to find a subspace $\mathbb{R}^r \subset \mathbb{R}^m$, $r << m$, which optimally approximates $\boldsymbol{X}$ in a least-squares sense. If $\boldsymbol{X}_r \in \mathbb{R}^r$ is the state in the reduced basis space, then the POD seeks for a subspace which minimises the projection error:

$$\min ||\boldsymbol{X} - \boldsymbol{\Pi}_r \boldsymbol{X}||^2 := \int_0^{t_l} ||\boldsymbol{x}_i(t) - \boldsymbol{\Pi}_r \boldsymbol{x}_i(t)||^2 dt, \tag{2.3.1}$$

where $\boldsymbol{\Pi}_r$ is an orthogonal projection operator.

In fluid dynamics, POD has been successfully applied in two main areas: the search for an optimal basis in a lower dimensional space and the identification of hidden patterns (in terms of size, shape, location) in complex datasets. Amongst other related methods, POD is usually considered the most efficient method for capturing the dominant structures of large scale systems. Lumley (Lumley 1967) was the first to apply POD in the study of turbulent flow, using spatial velocity correlations.

Classical statistical methods, which rely on averaging quantities, consider turbulence as a complex chaotic phenomenon with little or no underlying structure. On the contrary, coherent structures exist and turbulent flow is composed of organised motions. It is the superposition of these that presents the apparent complexity. To identify large eddy structures, Bakewell and Lumley (Bakewell 1967) applied POD to experimental data taken from the boundary layer of homogeneous turbulent pipe flow. The authors came to an important conclusion regarding the formation of shear turbulent flow: it is created and sustained not only in the wall region, but also in the viscous sub-layer. They also showed that in the wall region, the creation and evolution of counter-rotating eddy pairs is governed by the non-linear mechanism of vortex stretching. Payne and Lumley (Payne and Lumley 1967) studied cylinder wake flows using POD. A counter-rotating eddy pair serves as the dominant mode. However, they mentioned that for more accurate results, more data and grid points are needed. A detailed review on identification of coherent structures in turbulent flows can be found in (Berkooz, Holmes, and Lumley 1993).

The theory of Lumley has been proven very successful for relatively small datasets. However, it is limited for processing large datasets of experimental and numerical data. To overcome this, Sirovich (Sirovich 1987a) introduced the snapshot POD (as opposed to the direct POD) method as an efficient way of identifying the dominant modes of large scale systems, when the spatial dimension is larger than the temporal dimension. Snapshots are instantaneous solutions obtained by a high-fidelity solver (e.g., CFD) or by experimental data on which POD is performed. The snapshot POD can be seen as the discrete version of the continuous POD method and therefore it is an approximation of the 'full' POD. This fact limits the accuracy of the ROM to the quality (information contained) and the number of snapshots selected. Therefore, the choise of the snapshots is very important and the snapshots should contain the important physical properties of the FOM, such us flow periodicity, reversal, bifurcation etc.

Rempfer and Fasel in (Rempfer and Fasel 1994) performed simulations on a flat plate boundary layer to prove that, in the case of flow fields, which present symmetry along a coordinate, POD can describe spatially evolving structures. In (Baltzer, Adrian, and Wu 2010) the snapshot POD was used for identification of coherent structures in a turbulent boundary layer, where the evolution of large-scale motions appears. Bernero and Fiedler (Bernero and Fiedler 2000) applied snapshot POD to Particle Image Velocimetry (PIV) data obtained from a jet in a counterflow, to show that, even in such chaotic structures, a combination of PIV and snapshot POD could reveal a few dominant patterns. Another related application of POD methods is in data reconstruction. In (Bui-Thanh, Damodaran, and Willcox 2004) the authors showed that POD is an efficient method for reconstructing flow fields in aerodynamics when data is missing.

The use of POD in the construction of ROMs is a more recent development. In (Hall, Thomas, and Dowell 2000) snapshot POD was applied to transonic and subsonic unsteady aerodynamic flows. The authors obtained accurate ROMs with meaningful results, suggesting also that ROMs could be suitable for active control applications.

So-called POD-Galerkin ROMs have been widely used in optimal control problems, design optimisation, data reconstruction and many-query systems. Ravindran (Ravindran 2000) developed a POD-Galerkin ROM for optimal control of channel flow. The results showed accurate short-time ROM behaviour and high computational savings. These two characteristics are essential for real-time control applications. Bourguet and Braza (Bourguet, Braza, and Dervieux 2007)used a POD-Gelerkin ROM in the study of 2D transonic, compressible, unsteady flows around a NACA0012 airfoil, where two dominant flow structures were identified: the von Karman instability and buffeting. The resulting ROM is in an excellent agreement with the dynamics of the high fidelity model. An observation from this work is that the non-linear terms arising in the calculation of the ROM are relatively expensive. Examples of ROMs based on finite volume FOMs of the Navier-Stokes equations are demonstrated in the work of (Haasdonk and Ohlberger 2008; Lorenzi, Cammi, Luzzi, and Rozza 2016; Stabile and Rozza 2018).

In regard to non-isothermal problems, a first attempt to develop a POD-Galerkin ROM for modelling the temperature field in a rapid thermal processing chamber is described in (Aling, Banerjee, Bangia, Cole, Ebert, Emami-Naeini, Jensen, Kevrekidis, and Shvartsman 1997), where the authors considered a 2D steady-state problem. In (Alonso, Velazquez, and Vega 2009) a ROM for studying heat transfer in a backwards facing step flow, using a combination of POD and a genetic algorithm was presented. A heat transfer POD-Galerkin ROM is presented in (Raghupathy, Ghia, Ghia, and Maltz 2009), where the 1D conduction heat equation is considered. A POD study for the heat conduction equation is also presented in (Wang, Yu, Cao, Zou, and Yu 2012) and in (Han, Yu, and Zhang 2014). The problem of natural circulation is studied in (Li, Su, Chu, and Xu 2013) where a FOM of the coupled Navier-Stokes and energy equations is used to develop a ROM. However, the resulting POD-Galerkin ROM only considers perturbations of the (two-dimensional) temperature field, and assumes that the flow field remains fixed. These assumptions restrict the study to small perturbation temperature control applications.

A POD-Galerkin methodology for groundwater flow problems driven by spatially distributed stochastic forcing terms is presented in (Pasetto, Guadagnini, and Putti 2011), where the authors considered collecting the POD snapshots in the probability space. Their proposed method results in a Reduced Order Monte Carlo framework (ROMC). Another reduced order modelling technique, other than the POD-Galerkin, can be found in the study of uncertainty propagation in porous media (Müller, Jenny, and Meyer 2011), where the authors applied the Karhunen - Loève (KL) decomposition (or POD) and polynomial chaos with sparse Smolyak quadrature for the flow problem. In (Li, Luo, and Chen 2011), the POD method was applied to 2D solute transport problems. In (Busto, Stabile, Rozza, and Vazquez-Cendon 2019), the authors proposed a POD-Galerkin ROM for the Navier-Stokes one-way coupled heat transport equations based on a hybrid finite element - finite volume method.

2.4 Balanced Proper Orthogonal Decomposition

A hybrid of the BT and POD methods, the Balanced POD (BPOD), is considered an effective method for capturing the dynamical features of a field, due to its dependence on the BT Hankel matrix. While POD spans an orthogonal basis, BPOD spans a bi-orthogonal set which is ranked based on the Hankel singular values, containing both spatial and temporal features. Hence, BPOD can capture the low energetic but highly observable modes. Unlike BT, BPOD is applicable to large systems as the observability and controllability Gramians are empirically computed, using the POD method of snapshots.

To form the snapshot matrices $\mathbf{X}$ and $\mathbf{Y}$, impulse state response snapshots are taken from the system (2.1.1) and its conjugate $\dot{\mathbf{z}}(t) = \mathbf{A}^*\mathbf{z}(t) + \mathbf{B}^*\upsilon$, respectively. Thus, the controllability and observability empirical Gramians can be factored as:

$$\begin{aligned} \mathbf{W}_c &\approx \mathbf{X}\mathbf{X}^*, \\ \mathbf{W}_o &\approx \mathbf{Y}\mathbf{Y}^*. \end{aligned} \tag{2.4.1}$$

This can be seen as the equivalence to Cholesky factorization, which is applied to BT. For finding the balancing transformation matrices, the same procedure as in the case of BT is followed, where the eigenvalue decomposition is applied to the matrix $\mathbf{Y}^*\mathbf{X}$.

The study of BPOD based ROMs has attracted many researchers, mainly for its applications in flow response and control problems. In (Ilak and Rowley 2008), the authors applied the BPOD method to data obtained by DNS simulation of a linearised transitional channel flow, showing that, unlike POD, BPOD captures the transient growth very well. The authors used a different projection approach, the non-orthogonal Petrov-Galerkin projection with adjoint modes. A non-intrusive, projection-free BPOD approach has been suggested by Flinois and Morgans (Flinois, Morgans, and Schmid 2015) for applications to unstable systems. The authors proved that the expensive projection step is superfluous and the BPOD can be directly performed onto the unstable system. However, this method is only valid for LTI systems. In (Dergham, Sipp, Robinet, and Barbagallo 2011), the authors constructed a BPOD ROM using snapshots computed in the frequency domain. The authors considered two cases: a stable flow over a backward step and a transient flow over a square cavity. In both cases, they obtained accurate and well-behaved ROMs.

As long as snapshots from adjoint system response are needed, BPOD is usually inapplicable on experimental data. In addition, the classical BPOD method applies to linearised systems, although, extensions to non-linear systems are possible.

2.5 Parametric Model Order Reduction

Many problems in engineering, such as control applications, optimisation, design, real-time applications, require the knowledge of some output quantities of interest, such as pressure drop, flow rates, strains, etc. These quantities are often linear, low dimensional outputs of high dimensional state vectors, such as velocity, pressure or temperature. Unlike non-parametric model order reduction, parametric ROMs are parameter dependent. For this kind of problems, the LTI system of (2.1.1) is modified as follows:

$$\begin{aligned}\dot{\boldsymbol{x}}(\boldsymbol{\mu},t) &= \boldsymbol{A}(\boldsymbol{\mu})\boldsymbol{x}(t) + \boldsymbol{B}(\boldsymbol{\mu})\boldsymbol{u}(t),\\ \boldsymbol{y}(\boldsymbol{\mu},t) &= \boldsymbol{C}(\boldsymbol{\mu})\boldsymbol{x}(\boldsymbol{\mu},t),\end{aligned} \tag{2.5.1}$$

where $\boldsymbol{x} \in \mathbb{R}^m$ and $\boldsymbol{\mu} \in \mathbb{R}^{N_p}$ denote parameter dependent system matrices. As in the case of non-parametric systems, the ROM is usually obtained by projecting the equations (2.5.1) onto the reduced basis, using Galerkin (or Petrov-Galerkin) projection. In this method, the state $\boldsymbol{x}(t)$, is approximated as linear combination of basis vectors:

$$\boldsymbol{x}(\boldsymbol{\mu},t) \approx \boldsymbol{V}\boldsymbol{x}_{\boldsymbol{r}}(\boldsymbol{\mu},t), \tag{2.5.2}$$

where $n << m$ and $\boldsymbol{V} \in \mathbb{R}^{mxn}$ represents the basis, which spans the parametric subspace $\mathcal{S}_V$. Combining equations (2.5.2) and (2.5.1), leads to

$$\begin{aligned}\boldsymbol{r} &= \boldsymbol{V}\dot{\boldsymbol{x}}_r(\boldsymbol{\mu},t) - \boldsymbol{A}(\boldsymbol{\mu})\boldsymbol{V}\boldsymbol{x}_r(\boldsymbol{\mu},t) - \boldsymbol{B}(\boldsymbol{\mu})\boldsymbol{u}(t),\\ y_r(\boldsymbol{\mu},t) &= \boldsymbol{C}(\boldsymbol{\mu})\boldsymbol{V}\boldsymbol{x}_r(\boldsymbol{\mu},t),\end{aligned} \tag{2.5.3}$$

where $\boldsymbol{r}$ is the residual of the approximation. The system (2.5.3) is over-determined since it has n unknowns but m equations. For this reason, a well-determined system is obtained by multiplying the state with the reduced basis and inserting into (2.5.3). The basis $\boldsymbol{V}$ is orthogonal to the residual, i.e. $\boldsymbol{V}^T\boldsymbol{r}(\boldsymbol{\mu}, t) = 0$. The parametric ROM is obtained by substituting the new state onto (2.5.3), which can be written as follows:

$$\begin{aligned} \dot{\boldsymbol{x}}_r(\boldsymbol{\mu}, t) &= \boldsymbol{A}_r(\boldsymbol{\mu})\boldsymbol{x}_r(\boldsymbol{\mu}, t) + \boldsymbol{B}_r(\boldsymbol{\mu})\boldsymbol{u}(\boldsymbol{\mu}, t), \\ \boldsymbol{y}_r(\boldsymbol{\mu}, t) &= \boldsymbol{C}_r(\boldsymbol{\mu})\boldsymbol{x}_r(\boldsymbol{\mu}, t), \end{aligned} \tag{2.5.4}$$

where

$$\begin{aligned} \boldsymbol{A}_r(\boldsymbol{\mu}) &= \boldsymbol{V}^T\boldsymbol{A}(\boldsymbol{\mu})\boldsymbol{V}, \\ \boldsymbol{B}_r(\boldsymbol{\mu}) &= \boldsymbol{V}^T\boldsymbol{B}(\boldsymbol{\mu}), \\ \boldsymbol{C}_r(\boldsymbol{\mu}) &= \boldsymbol{C}(\boldsymbol{\mu})\boldsymbol{V}. \end{aligned} \tag{2.5.5}$$

The reduced basis $\boldsymbol{V}$ is computed using one of the methods mentiond in the previous sections (POD, BT, BPOD etc) using either global or local bases strategies.

In (Ballarin and Rozza 2016) the authors proposed a monolithic model order reduction approach based on POD-Galerkin for parametrised fluid-structure interaction problems. Also in (Ballarin, Manzoni, Quarteroni, and Rozza 2014), stable POD-Galerkin for the parametrised, incompressible, steady Navier-Stokes equations was presented. POD-Galerkin model order reduction for parametric PDEs also applied for haemodynamics studies in (Ballarin, Faggiano, Ippolito, Manzoni, Quarteroni, Rozza, and Scrofani 2016).

An interpolation method of the local POD bases was proposed by Lieu and Lesoinne in (Lieu and Lesoinne 2004), where, to evaluate POD bases for different Mach numbers in transonic flows, two different interpolation techniques were applied and compared. Lagrange interpolation and subspace angle interpolation were utilised, where the former was found to be inaccurate, as the interpolation of local orthogonal bases does not always result to orthogonal bases. On the contrary, subspace angle interpolation had been proven more accurate. The reason is that the interpolation is applied to subspace angles and not to the basis vectors. Subspace angle interpolation has also been studied in (Lieu, Farhat, and Lesoinne 2005). The authors interpolated POD bases from two different Mach numbers to construct ROMs able to predict for Mach numbers which lie in the range between the two original Mach numbers. However, this method is limited to interpolation of only two reduced bases. An alternative method based on interpolation on spaces tangent to Grassmann manifolds was proposed in (Amsallem and Farhat 2008). This method preserves orthonormality of the new basis and, therefore, is applicable to the interpolation of more than two orthonormal bases. In (Degroote, Vierendeels, and Willcox 2010) the authors were proposed a novel interpolation method among precomputed projection-based ROMs to evaluate new ROMs for different parameter values. The authors proposed a heuristic algorithm for selecting the space in which the interpolation can be performed.

The computational cost of solutions that cover the whole domain is prohibitive for high dimensional parameter spaces. Greedy POD algorithm is an approach for optimally sampling high dimensional parametric spaces. The combination of advanced algorithms and rigorous error bounds assure, in a way, that the reduced basis will be represented by the best snapshots. The greedy algorithm, which is based on Noor's and Peters's algorithm (Noor and Peters 1980), was proposed in (Veroy, Prud'Homme, Rovas, and Patera 2003) and provided globally optimal reduced basis with *a posteriori* error estimators. These qualities promise high computational savings for applications to affine parametric problems. In (Veroy and Patera 2005), the authors applied the greedy algorithm in real-time applications governed by the incompressible Navier-Stokes equations, where they derived a rapidly converged reduced basis. In thermo-fluid dynamics, Deparis and Rozza (Deparis and Rozza 2009) applied the greedy algorithm for studying convection in a cavity, governed by the multi-parametric, steady Navier-Stokes equations. Their study includes both physical, Grashof and Prandtl, and geometrical aspect ratio, dependence. The authors showed that the online stage remains unaffected in terms of computational time while the offline stage is still computationally efficient. A detailed description of reduced basis methods with various applications to elliptic problems can be found in (Nguyen, Rozza, Huynh, and Patera 2010).

2.6 Summary of the Chapter

This chapter gave an overview of projection based model order reduction techniques, as well as discussed some popular methods for the calculation of the reduced basis space. Parametric model order reduction, a method this thesis is mostly dealing with, was also discussed.

Chapter 3

Mathematical Framework - Full Order Model

In this chapter the mathematical framework for the FOM is presented. This includes the governing equations of fluids, a review of the Unsteady Reynolds-Averaged Navier-Stokes (URANS) turbulence modelling method as well as a description of the finite volume method.

3.1 Governing Equations of Fluids

The first step towards modelling a system is to derive a set of governing equations, defining the physics of the problem. In fluid dynamics, these are the Navier - Stokes equations and are derived using three fundamental conservation laws of mass, momentum and energy. The transient Navier - Stokes equations are formulated, in conservative form, as:

$$\begin{aligned} \frac{\partial(\rho \boldsymbol{u})}{\partial t} + \nabla \cdot (\rho \boldsymbol{u}) &= 0, && (3.1.1) \\ \frac{\partial(\rho \boldsymbol{u})}{\partial t} + \nabla \cdot (\rho \boldsymbol{u} \otimes \boldsymbol{u}) &= -\nabla p + \nabla \cdot \boldsymbol{\tau}, && (3.1.2) \end{aligned}$$

where p is the pressure and the viscous tensor, $\boldsymbol{\tau}$, is:

$$\boldsymbol{\tau} = \begin{bmatrix} \tau_{xx} & \tau_{xy} & \tau_{xz} \\ \tau_{yx} & \tau_{yy} & \tau_{yz} \\ \tau_{zx} & \tau_{zy} & \tau_{zz} \end{bmatrix}$$

For an incompressible, Newtonian fluid and in the absence of any external forces, the stress tensor is proportional to the rate of deformation. This can be writen as:

$$\tau_{ij} = \mu(\frac{\partial u_i}{\partial x_j} + \frac{\partial u_j}{\partial x_i}), \tag{3.1.3}$$

where the proportionality constant, μ, is called dynamic viscosity.

It can be shown that the stress divergence is:

$$\nabla \cdot \boldsymbol{\tau} = \mu \Delta \boldsymbol{u}. \tag{3.1.4}$$

Hence, substituting equation (3.1.4) into the momentum equation (3.1.1) and deviding by the density, ρ, one obtains the following set of equations for a Newtonian, incompressible fluid:

$$\begin{aligned} \nabla \cdot \boldsymbol{u} &= 0, & (3.1.5) \\ \frac{\partial \boldsymbol{u}}{\partial t} + \nabla \cdot (\boldsymbol{u} \otimes \boldsymbol{u}) - \nu \Delta \boldsymbol{u} &= -\nabla p, & (3.1.6) \end{aligned}$$

where ν denotes the kinematic viscosity, which is μ/ρ and now p is the normalized pressure, p/ρ. The energy equation is also considered in this research, in the form of a convection-diffusion equation. This can be expressed as :

$$\frac{\partial \theta}{\partial t} + \nabla \cdot (\boldsymbol{u}\theta) - \alpha_{diff} \Delta \theta = 0, \tag{3.1.7}$$

where α_{diff} is the thermal diffusivity and θ is the fluid temperature. The thermal diffusivity is defined as $\alpha_{diff} = \hbar/\rho c_p$, where $\hbar$ is the thermal conductivity and c_p is the specific heat capacity.

3.2 Turbulence Modelling

Turbulence is described by chaotic and random motion in which the transported quantities (pressure, velocity etc) exhibit spatial and temporal fluctuations. Unlike laminar flows, which can be numerically solved by any standard discretisation technique (e.g. finite volume), turbulent flows need some additional approximations. For ducts, a flow is considered turbulent if the non-dimensional Reynolds number ($\mathrm{Re} = UL/\nu$) is greater than 4000, laminar if Re<2300 and transient when 2300< Re <4000. The Reynolds number indicates the significance of the inertia forces to viscous forces. Turbulent motion is diffusive, leading to enhanced mixing and, therefore, to greater heat and momentum transfer.

In the modelling of turbulent flows, the instantaneous velocity component $\boldsymbol{u}(\boldsymbol{x}, t)$ is decomposed into a time-averaged component, $\overline{\boldsymbol{u}}(\boldsymbol{x}, t)$, superimposed by a fluctuating component, $\boldsymbol{u'}(\boldsymbol{x}, t)$. This can be expressed as follows:

$$\boldsymbol{u}(\boldsymbol{x}, t) = \overline{\boldsymbol{u}}(\boldsymbol{x}) + \boldsymbol{u}'(\boldsymbol{x}, t). \tag{3.2.1}$$

The fluctuating component, $\boldsymbol{u'}(\boldsymbol{x}, t)$, is known as turbulent fluctuation and is always three dimensional (in space), even for flows with mean values changing only in two dimensions. This decomposition is known as Reynolds decomposition. Turbulent flows contain rotational flow structures, called turbulent eddies, which vary in size. Larger eddies acquire energy from the mean flow by a process called vortex stretching. The smaller in size eddies derive energy from the larger eddies through an energy cascade process. Viscous dissipation converts turbulent energy from the smallest eddies into thermal internal energy leading to energy losses.

Regarding turbulence predictions, there are various computational approaches available which involve modelling or simulation. The former include the Reynolds-Averaged Navier-Stokes equations (RANS or URANS for the Unsteady) method and the Large Eddy Simulation (LES) while the latter, the CPU expensive Direct Numerical Simulation (DNS). In RANS/URANS, which nowadays, is widely applied in industry, due to its lower computational cost, compared to the other methods, the Navier-Stokes equations are solved in an averaged manner (enseble or time). On the other hand, in

LES approach, the Navier-Stokes equations are spatially averaged. In this approach, the larger eddies are directly resolved whereas the smaller eddies (smaller than the mesh size) are modelled. LES comes a with much greater computational cost than RANS and, sometimes, is almost impractical for industrial applications. DNS numerically solves the Navier-Stokes equations and resolves the whole spectrum of eddies but this results in a vast computational cost.

Amongst the various methods available (Spalart-Almaras, $k-\epsilon$, $k-\omega$, Reynolds Stresses etc) in RANS/URANS, in this research, the $k-\omega$ has been chosen due to its accuracy in the near wall region. There are two variations of the $k-\omega$ model, the standard $k-\omega$ and the Shear Stress Transport (SST) $k-\omega$. The former is desrcribed by a two-transport-equation model for k and ω and the specific dissipation rate (ϵ/k) is based on Wilcox (Wilcox 1998) method. The latter is a combination of the standard $k-\omega$ model in proximity of the walls and the standard $k-\epsilon$ model in the bulk of the flow. To ensure smooth transition between the two different models, a blending function is used.

To derive the full-order equations, which also include turbulence modelling, we start with the incompressible, transien Navier-Stokes equations which are one-way coupled with the transient energy equation. According to equations (3.1.5, 3.1.6 and 3.1.7) and considering a Eulerian framework and domain $Q = \Omega \times [0, T_s] \subset \mathbb{R}^d \times \mathbb{R}^+$ with $d = 2, 3$, the equations are formulated as follows:

$$\begin{cases} \frac{\partial \boldsymbol{u}}{\partial t} + \boldsymbol{\nabla} \cdot (\boldsymbol{u} \otimes \boldsymbol{u}) - \nabla \cdot \nu \nabla \boldsymbol{u} = -\nabla p & \text{in } Q, \\ \boldsymbol{\nabla} \cdot \boldsymbol{u} = \boldsymbol{0} & \text{in } Q, \\ \frac{\partial \theta}{\partial t} + \nabla \cdot (\boldsymbol{u}\theta) - \alpha_{dif} \Delta \theta = 0 & \text{in } Q. \end{cases} \tag{3.2.2}$$

3.3 URANS

Similar to equation (3.2.1), the instantaneous velocity, pressure and temperature are decomposed into an averaged and a fluctuating component as follows:

$$\boldsymbol{u}(\boldsymbol{x},t) = \overline{\boldsymbol{u}}(\boldsymbol{x}) + \boldsymbol{u}'(\boldsymbol{x},t) \tag{3.3.1}$$

$$p(\boldsymbol{x},t) = \overline{p}(\boldsymbol{x}) + p'(\boldsymbol{x},t), \tag{3.3.2}$$

$$\theta(\boldsymbol{x},t) = \overline{\theta}(\boldsymbol{x}) + \theta'(\boldsymbol{x},t). \tag{3.3.3}$$

In RANS modelling, the mean components are zero. Taking this into account and substituting equations (3.3.1) into equations (3.2.2), the URANS and energy equations are:

$$\begin{cases} \nabla \cdot \overline{\boldsymbol{u}} = 0, \\ \frac{\partial \overline{\boldsymbol{u}}}{\partial t} + \nabla \cdot (\overline{\boldsymbol{u}} \otimes \overline{\boldsymbol{u}}) - \nu \Delta \overline{\boldsymbol{u}} = -\nabla \overline{p} - \nabla \cdot \boldsymbol{\tau}^R, \\ \frac{\partial \overline{\theta}}{\partial t} + \nabla \cdot (\overline{\boldsymbol{u}}\overline{\theta}) - (\alpha_{dif} \Delta \overline{\theta}) - \boldsymbol{H}^R = 0, \end{cases} \tag{3.3.4}$$

where the extra terms $\boldsymbol{\tau}^R = -(\overline{\boldsymbol{u}'\boldsymbol{u}'})$ and $\boldsymbol{H}^R = (\overline{\theta'\boldsymbol{u}'})$ are the Reynolds stress tensor and the heat flux term, respectively. Therefore, these two new terms must be modelled in order to close the system of the equations. One possible solution, which is followed in this work, is the eddy viscosity models with the Boussinesq hypothesis. The Reynolds stress is modelled using the eddy viscosity ν_t and the heat flux using a gradient diffusion hypothesis, as follows:

$$\boldsymbol{\tau}^R = -(\overline{\boldsymbol{u}'\boldsymbol{u}'}) = 2\nu_t \overline{\boldsymbol{D}}^R - 2/3k\boldsymbol{I} = \nu_t[\nabla \overline{\boldsymbol{u}} + (\nabla \overline{\boldsymbol{u}})^T] - 2/3k\boldsymbol{I}, \tag{3.3.5}$$

$$\boldsymbol{H} = -\alpha_{dif_t} \nabla \overline{\theta}, \tag{3.3.6}$$

where α_{dif_t} is the turbulent thermal diffusivity, modelled as ν_t/Pr_t, and Pr_t the turbulent Prandtl. $\overline{\boldsymbol{D}}^R$ is the mean strain-rate tensor and $\boldsymbol{I}$ is the identity matrix. Combining all the above and denoting from now on $\overline{\boldsymbol{u}}$, $\overline{p}$ and $\overline{\theta}$ as $\boldsymbol{u}$, p and θ, respectively, equations (3.2.2) including also the turbulence modelling, are as follows

:

$$\begin{cases} \frac{\partial \boldsymbol{u}}{\partial t} + \boldsymbol{\nabla} \cdot (\boldsymbol{u} \otimes \boldsymbol{u}) = \boldsymbol{\nabla} \cdot \big[- p\boldsymbol{I} + (\nu + \nu_t)\big(\nabla \boldsymbol{u} + (\nabla \boldsymbol{u})^T\big) & \\ -\frac{2}{3}k\boldsymbol{I}\big] & \text{in } Q, \\ \boldsymbol{\nabla} \cdot \boldsymbol{u} = \boldsymbol{0} & \text{in } Q, \\ \frac{\partial \theta}{\partial t} + \nabla \cdot (\boldsymbol{u}\theta) - (\alpha_{dif} + \alpha_{dif_t})\Delta\theta = 0 & \text{in } Q, \\ \nu_t = j(k, \omega), & \end{cases} \tag{3.3.7}$$

where k is the turbulent kinetic energy, $k = \frac{1}{2}\overline{\boldsymbol{u'} \cdot \boldsymbol{u'}}$ and $\omega = \frac{\epsilon}{k\beta^*}$ the specific dissipation rate with β^* being a constant of proportionality and $\epsilon \propto \frac{\partial k}{\partial t}$ the specific dissipation rate. A variation of the standard $k - \omega$, the $k - \omega - SST$ ($k - \omega$ Shear Stress Transport) (Menter 1994) is selected for the scope of this research. The formulation that OpenFOAM uses can be found in (*OpenFOAM user guide* 2016-2017). The $k-\omega-SST$ model is a hybrid of the standard Wilcox $k-\omega$ and the $k-\epsilon$, where a blending function activates the former in the near-wall region while the latter, is switched in the free-stream. Therefore, it combines the benefits of the two models.

3.4 Poisson Equation for Pressure

For the numerical solution of the Navier - Stokes equations (3.2.2), described in the previous section, several difficulties arise and special treatment is required. These include the non-linearity of the convective term and the coupling between velocity and pressure fields in the momentum equation, as well as the lack of an explicit equation for the pressure field.

The difficulty associated with the non-linearity is usually dealt with the use of iterative solvers. For compressible flows, the continuity equation, (3.1.3), serves as a transport equation for density and, in conjunction with the energy equation (3.1.7), the pressure can be obtained by exploiting the equation of state, $p = p(\rho, \theta)$. However, for incompressible flows, since the density is constant, such approach is not possible. One possible way of handling both problems associated with the Navier-Stokes equations is the implementation of the Semi-Implicit Method for Pressure Linked Equations (SIMPLE) (Patankar and Spalding 1972) solver. The SIMPLE algorithm, which is based on a guess-and-correct method, is summarized in the following algorithm (3.1):

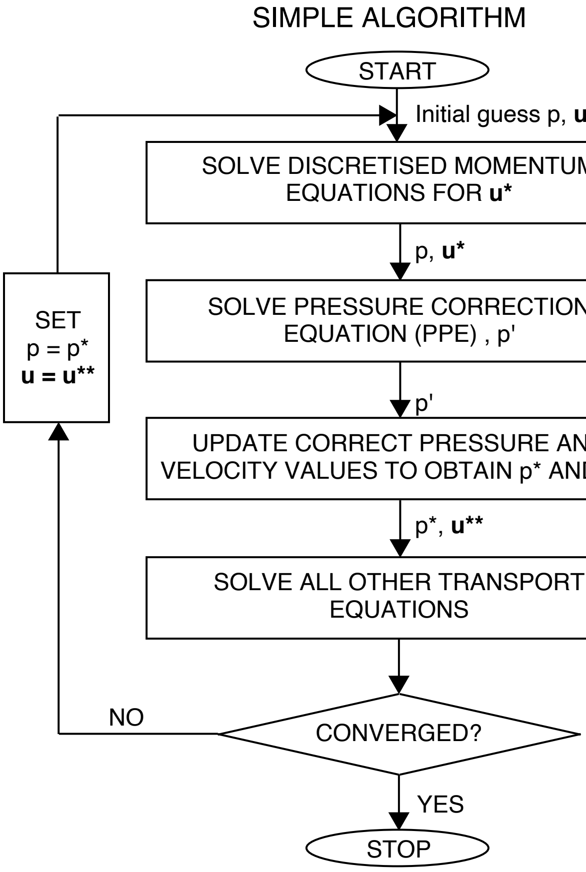

Figure 3.1: SIMPLE Algorithm.

The above SIMPLE algorithm had originally been developed for steady-state problems but it can be extended to transient problems by starting with a guessed solution at time t to obtain converged values for velocity and pressure fields, as shown in algorithm (3.1). Then, the converged values are used as initial guess at time $t + \Delta t$. The same procedure is repeated until the maximum time of the simulation is reached. Other methods for dealing with the velocity/pressure coupling include the Pressure Implicit with Splitting of Operators (PISO) algorithm (Issa 1986) (3.2) or the PIMPLE algorithm (Barton 1998) which is a hybrid of SIMPLE and PISO. SIMPLE, PISO and PIMPLE are segregated solvers. This means that they are more memory-efficient than coupled solvers but, as the equations are solved one at a time, leads to a slower convergence.

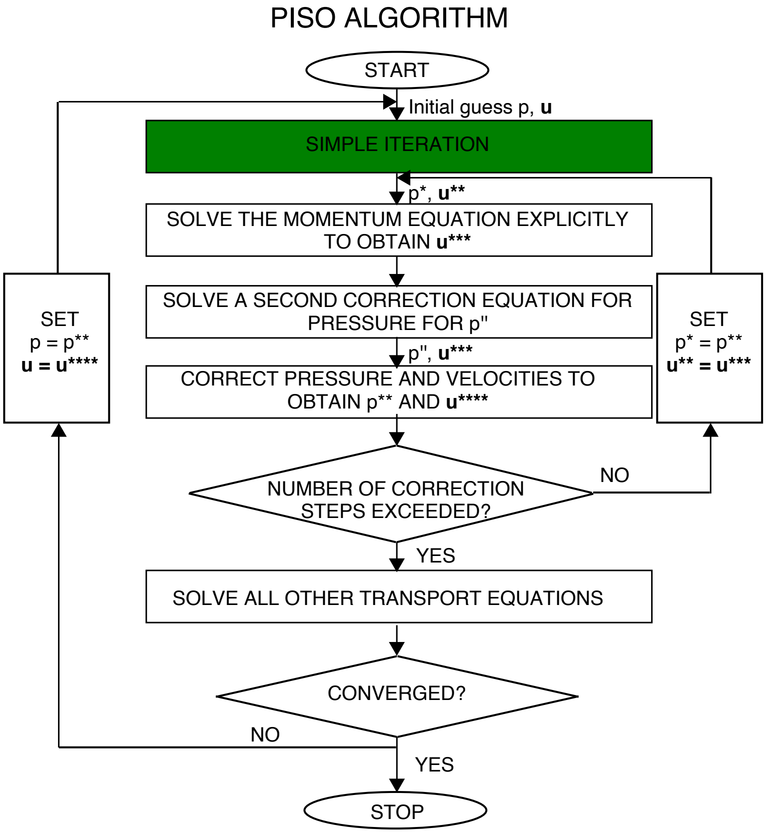

Figure 3.2: PISO Algorithm.

The correction equation for pressure is derived by taking the divergence of the momentum equation (3.1.6) (or the equivalent one when turbulence modelling is considered) and enforcing the incompressibility condition, leading to the following Poisson equation for pressure:

$$\Delta p = -\nabla \cdot (\boldsymbol{u} \cdot \nabla \boldsymbol{u}). \tag{3.4.1}$$

3.5 The Finite Volume Approximation

The full order system, which is represented by the partial differential equations (3.2.2), is transformed into a system of discrete algrebraic equations. It can then be solved with any iterative or direct numerical method. The system is discretized in a finite volume method using the open source C++ library OpenFOAM (*OpenFOAM website* 2011-2012). The equations (3.2.2) include temporal derivatives, as well as conventive and diffusive terms, and each of these terms is treated in a different way. The first step towards discretisation of the spatial terms is the division of the computational domain into arbitrarily small control volumes (cells) such the one depicted in figure (3.3). The transient term is discretized in time by splitting the total time interval of the simulation into a number of discrete time steps. In the finite volume method, the integral form of the equations is discretized over a control volume and, therefore, the quantities of interest are conserved (mass, momentum etc).

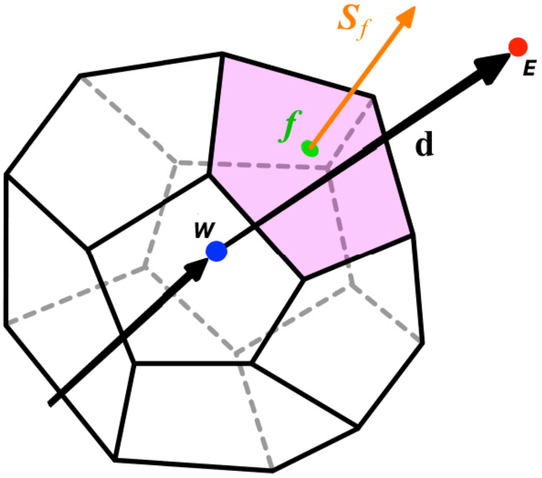

Figure 3.3: Example of a polyhedral control volume around a centroid W (Guerrero 2015).

Considering a general transported quantity ϕ, the transport equation can be written as:

$$\int_{V_P} \frac{\partial \phi}{\partial t} dV + \int_{V_P} \nabla \cdot (\boldsymbol{u}\phi) dV - \int_{V_P} \nabla \cdot (\Gamma_\phi \nabla \phi) dV = 0, \tag{3.5.1}$$

where the source term has been set to zero. Therefore external sources are not considered. The first term in equation (3.5.1) represents the temporal derivative, the second the convective and the third the diffusive term. Using Gauss theorem, the volume integrals in equation (3.5.1) are transformed into surface integrals:

$$\frac{\partial}{\partial t} \int_{V_p} \phi dV + \oiint_{\partial V_P} d\boldsymbol{S} \cdot (\boldsymbol{u}\phi) - \oiint_{\partial V_P} d\boldsymbol{S} \cdot (\Gamma_\phi \nabla \phi) = 0, \tag{3.5.2}$$

where ∂V_P represents a closed surface, which bounds the control volume V_P and $\boldsymbol{n} d\boldsymbol{S} = d\boldsymbol{S}$.

Taking each term in equation (3.5.2) separately and starting with the approximation of the convective term which is as follows:

$$\oiint_{\partial V_P} d\boldsymbol{S} \cdot (\boldsymbol{u}\phi) = \sum_f \int_f d\boldsymbol{S} \cdot (\boldsymbol{u}\phi) \approx \sum_f \boldsymbol{S}_f \cdot (\boldsymbol{u}\phi)_f, \tag{3.5.3}$$

where the integral has been replaced with a summation of fluxes over the faces of the control volumes. The suffix, f, represents the integration point at the face' centroid and $\boldsymbol{S}_f$ is the face area vector normal to the interface, as shown in figure (3.3).

It is obvious from equation (3.5.3), that the value of the transported quantity over the faces of the control volume, ϕ_f, is necessary. This value is computed using values from neighbouring control volumes usually with central differencing or upwind schemes. The central differencing scheme, according to figure (3.4), is in fact the following linear interpolation:

$$\phi_f = \phi_E + \frac{|x_f - x_E|}{|\boldsymbol{d}|}(\phi_W - \phi_E), \tag{3.5.4}$$

where the suffixes W and E refer to quantities in the West and East neighbouring cells. This scheme is second order accurate, because it is derived from the Taylor's expansion, where the second and higher order derivatives are neglected. In case of uniform grids, where f is midway (as in figure (3.4)), equation (3.5.4) is reduced to $\phi_f = (\phi_E + \phi_W)/2$.

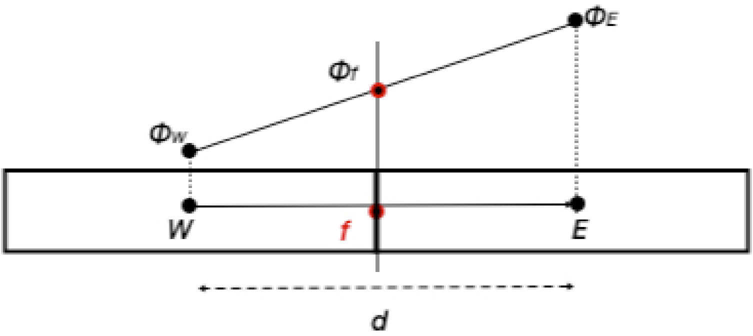

Figure 3.4: Central differencing discretisation scheme.

For problems where the effect of the convective term is important (high Pèclet number - $Pe = advection/diffusion$), this scheme is inadequate, as it can cause an unbounded numerical solution, which defers from the analytical one. For such problems, the upwind scheme is preferable, offering boundness of the solution (Moukalled, Mangani, and Darwish 2015). According to figure (3.5), the face flux ϕ_f depends on the flow direction as follows :

$$\phi_f = \begin{cases} \phi_W, & \text{for } \dot{m} \geq 0 \\ \phi_E, & \text{for } \dot{m} \leq 0, \end{cases}$$

where $\dot{m} = S_f \cdot (\rho \boldsymbol{u})$ is the mass flux through the face f.

Despite the good stability of the upwind scheme, even for high Pèclet numbers, its first order accuracy makes it less accurate than the central differencing scheme. To tackle with this behaviour, variations of the two schemes, including bounded central differencing and second order accurate upwind schemes have been developed (Moukalled, Mangani, and Darwish 2015).

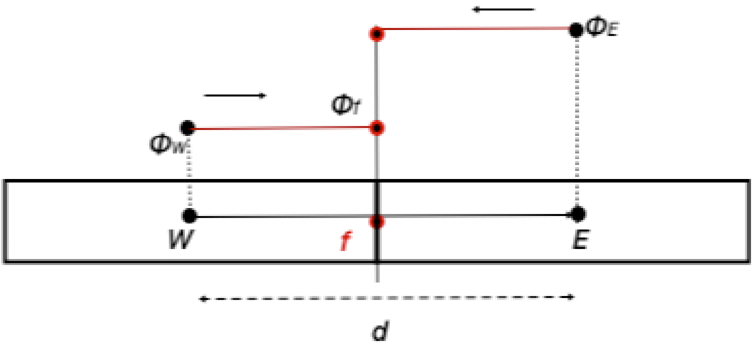

Figure 3.5: Upwind discretisation scheme.

The diffusive term is discretized as:

$$\oiint_{\partial V_P} d\boldsymbol{S} \cdot (\Gamma_\phi \nabla \phi) = \sum_f \int_f d\boldsymbol{S} \cdot (\Gamma_\phi \nabla \phi) \approx \sum_f \boldsymbol{S}_f \cdot (\Gamma_\phi \nabla \phi)_f, \tag{3.5.5}$$

where Γ_ϕ is the diffusion coefficient and is calculated by the harmonic mean between the neighbouring control volumes, E and W as:

$$(\Gamma_\phi)_f = \frac{(\Gamma_\phi)_E (\Gamma_\phi)_W}{(\Gamma_\phi)_E + \frac{|x_f - x_E|}{|\boldsymbol{d}|}((\Gamma_\phi)_W - (\Gamma_\phi)_E)}. \tag{3.5.6}$$

The calculation of the face gradient is not very straightforward as it depends on the mesh. For orthogonal meshes, where the surface vector $\boldsymbol{S}_f$ is parallel to the distance

d, the flux gradient is:

$$\boldsymbol{S}_f \cdot \nabla(\phi_f) = |\boldsymbol{S}_f| \frac{\phi_W - \phi_E}{|\boldsymbol{d}|}, \tag{3.5.7}$$

where the face gradient can be calculated from the values of the neighbouring control volumes. For non-orthogonal meshes, the value of the gradient, $\nabla(\phi_f)$, is calculated by weighted interpolation of the gradient values at the cell centres W and E, as follows:

$$\nabla(\phi_f) = f_x \nabla(\phi_f)_W + (1 - f_x)\nabla(\phi_f)_E, \tag{3.5.8}$$

where f_x is the interpolation factor and the value of $\nabla(\phi_f)_W$ and $\nabla(\phi_f)_E$ at the cell centres, W and E is obtained as:

$$\nabla(\phi_{W,E}) = \frac{\sum_f \boldsymbol{S}_f \phi_f}{V_{W,E}}. \tag{3.5.9}$$

In the case of non-orthogonal meshes (vectors $\boldsymbol{S}_f$ and $|\boldsymbol{d}|$ are not parallel), such as the one shown in figure (3.6), a non-orthogonal correction is introduced. In this approach, the surface vector is written as the sum of an orthogonal vector and a non-orthogonal vector $\boldsymbol{O}_f$ and $\boldsymbol{N}_f$ respectively:

$$\boldsymbol{S}_f = \boldsymbol{O}_f + \boldsymbol{N}_f. \tag{3.5.10}$$

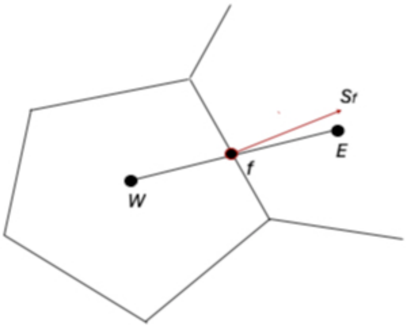

Figure 3.6: Control volume in a non-orthogonal mesh.

Therefore, the flux gradient is written as:

$$\boldsymbol{S}_f \cdot (\nabla\phi_f) = \boldsymbol{O}_f \cdot (\nabla\phi_f) + \boldsymbol{N}_f \cdot (\nabla\phi_f) = |\boldsymbol{O}_f| \frac{\phi_W - \phi_E}{|\boldsymbol{d}|} + \boldsymbol{N}_f \cdot (\nabla\phi_f), \tag{3.5.11}$$

where the orthogonal contribution is calculated in the same way as in the orthogonal mesh, case (3.5.7), while the non-orthogonal contribution is calculated implicitly and special treatment is necessary (Moukalled, Mangani, and Darwish 2015).

Replacing the terms in equation (3.5.2) with the approximated ones, (3.5.3) and (3.5.5), we obtain the following equation:

$$\int_t^{t+\Delta t} [(\frac{\partial \rho\phi}{\partial t})_{V_P} V_P + \sum_f \boldsymbol{S}_f \cdot (\rho \boldsymbol{u}\phi)_f - \sum_f \boldsymbol{S}_f \cdot (\rho \Gamma_\phi \nabla \phi)_f] dt = 0. \tag{3.5.12}$$

The temporal discretisation can be performed using any temporal discretisation scheme such as Crank-Nicolson, backward differencing, Euler etc. For more information the reader is referred to (Jasak 1996; Moukalled, Mangani, and Darwish 2015).

3.6 Summary of the Chapter

The scope of the present chapter was to provide the mathematical background for the full order model. This includes the governing equations of fluids, treatment of the turbulence as well as ways of tackling with the coupled Navier-Stokes equations in the computational level. The finite volume discretisation method, by which the FOM is discretized in the present thesis, was also presented.

Chapter 4

Mathematical Framework - Reduced Order Model

This chapter provides the mathematical background for the ROM. It starts with the mathematical formulation of the Proper Orthogonal Decomposition method for parametric problems followed by a modified POD approach, the Nested-POD. A description of two methods, the supremizer enrichment and the Pressure Poisson Equations, for stabilising the governing equations and including the pressure term is also discussed. Finally, the mathematical formulation of the Galerkin projection is provided.

4.1 Proper Orthogonal Decomposition for Parametric Model Reduction

The POD method for non-parametric model order reduction has been discussed in section (2.3). This section aims to provide a more detailed overview of the POD for parametric problems. Let us consider for example a set of velocity snapshots (observations) $\boldsymbol{u}_s$ which belong to the L^2 Hilbert space. The space is equipped with an L^2 inner product, which, for arbitrary functions $f(x)$ and $g(x)$, is defined as $\langle f, g\rangle_{L_2(\Omega)} = \int_\Omega f(x)g^*(x)dx$, and with an L^2 norm, $||f(x)|| = \sqrt{\langle f, f\rangle_{L_2(\Omega)}}$. The star denotes complex conjugate. The L^2 space is a natural choise when incompressible fluid mechanics problems are considered since, based on the definition of the norm, the kinetic energy is described as $k = 1/2\rho||\boldsymbol{u}||$ (Berkooz, Holmes, and Lumley 1993). The idea is to write the state vector as a linear combination of temporal coefficients

$\alpha(\boldsymbol{\mu}, t)$ and basis functions $\boldsymbol{\phi}(\boldsymbol{x})$: $\boldsymbol{u}(\boldsymbol{x}, \boldsymbol{\mu}, t) \approx \boldsymbol{u}_s = \sum_{i=1}^{N_u^s} \alpha_i(\boldsymbol{\mu}, t)\boldsymbol{\phi}_i(\boldsymbol{x})$.

The first step is the training phase, where snapshots are collected using a high fidelity solver or experimental results. For the purposes of this work, only numerical simulations using the high fidelity OpenFOAM (Jasak 1996) solver have been considered. The snapshots, which belong to a finite Hilbert space $\mathscr{H} = \mathbb{R}^{N_u^h}$, are placed into an $N_u^h \times N_u^s$ snapshot matrix, $\boldsymbol{U}_s$,

$$\boldsymbol{U}_s = \begin{bmatrix} u_1^1(\mu^1) & \dots & u_1^{N_u^s}(\mu^1) & \dots & u_1^{N_u^s}(\mu^{N_p}) \\ \vdots & \dots & \vdots & \dots & \vdots \\ u_{N_u^h}^1(\mu^1) & \dots & u_{N_u^h}^{N_u^s}(\mu^1) & \dots & u_{N_u^h}^{N_u^s}(\mu^{N_p}), \end{bmatrix}$$

where N_u^h is the number of degrees of freedom (grid points × number of components) and N_u^s is the number of snapshots. Since we are dealing with parametric model order reduction, the total number of snapshots is not equal to the number of time instances only. The size of the parameter space should also be taken into account. The FOM is solved for each $\boldsymbol{\mu}^k \in \mathscr{K} = \{\mu^1, \dots, \mu^{N_p}\} \subset \mathscr{P}$, where $\mathscr{K}$ is a finite dimensional training set of samples chosen inside the parameter space $\mathscr{P}$ and for each time instance $t^k \in \{t^1, \dots, t^{N_t}\} \subset [0, T]$. Therefore, the total number of snapshots, $N_{u tot}^s$, is equal to $N_p \cdot N_u^s$ but for simplicity it will be referred to as N_u^s.

Let us define an enseble $\mathscr{V}$, which consists of the total number snapshots $\{\boldsymbol{u}_i(\boldsymbol{x}, \boldsymbol{\mu}, t)\}_{i=1}^{N_u^s}$ and let $\{\boldsymbol{\phi}_j\}_{j=1}^{N_u^s}$ be an orthonormal basis of $\mathscr{V}$ with $N_u^s = dim\{\mathscr{V}\}$. We can write each element of $\mathscr{V}$ as the following linear combination:

$$\boldsymbol{u}(\boldsymbol{x}, \boldsymbol{\mu}, t) = \sum_{j=1}^{N_u^s} \langle \boldsymbol{u}_j(\boldsymbol{x}, \boldsymbol{\mu}), \boldsymbol{\phi}_j(\boldsymbol{x}) \rangle_{L_2(\Omega)} \boldsymbol{\phi}_j(\boldsymbol{x}). \tag{4.1.1}$$

One of the attributes of the POD method is the minimisation of the error between the velocity snapshots and their projection onto the POD basis. The POD seeks an orthonormal basis $\boldsymbol{\phi}$, such that $\forall\ \omega \in \{1, .., N_u^s\}$:

$$\min \frac{1}{N_u^s} \sum_{i=1}^{N_u^s} ||\boldsymbol{u}_i(\boldsymbol{x}, \boldsymbol{\mu}) - \sum_{j=1}^{\omega} \frac{\langle \boldsymbol{u}_i(\boldsymbol{x}, \boldsymbol{\mu}), \boldsymbol{\phi}_j(\boldsymbol{x}) \rangle_{L_2(\Omega)}}{||\boldsymbol{\phi}(\boldsymbol{x})||^2} \boldsymbol{\phi}_j(\boldsymbol{x})||_{L^2}^2, \tag{4.1.2}$$

subject to $\langle \boldsymbol{\phi}_i(\boldsymbol{x}), \boldsymbol{\phi}_j(\boldsymbol{x})\rangle_{L_2(\Omega)} = \delta_{ij}$.

The above minimisation problem is equivalent to maximising the following averaged quantity:

$$\max \frac{|\langle \boldsymbol{u}(\boldsymbol{x},\boldsymbol{\mu}), \boldsymbol{\phi}(\boldsymbol{x})\rangle_{L_2(\Omega)}|^2}{||\boldsymbol{\phi}(\boldsymbol{x})||^2}, \tag{4.1.3}$$

where $|\cdot|$ denotes the absolute value.

Since multiple local maximum values can result from the maximization problem (4.1.3), we maximize the quantity $|\langle \boldsymbol{u}(\boldsymbol{x},\boldsymbol{\mu}), \boldsymbol{\phi}(\boldsymbol{x})\rangle_{L_2(\Omega)}|^2$ subject to the constrain $||\boldsymbol{\phi}(\boldsymbol{x})||^2 = 1$ (Berkooz, Holmes, and Lumley 1993). To achieve this, for the first basis function, we create a function according to Lagrange method for constrained problem optimization:

$$L(\boldsymbol{\phi}(\boldsymbol{x})) = |\langle \boldsymbol{u}(\boldsymbol{x},\boldsymbol{\mu}), \boldsymbol{\phi}(\boldsymbol{x})\rangle_{L_2(\Omega)}|^2 - \lambda^u(||\boldsymbol{\phi}(\boldsymbol{x})||^2 - 1), \tag{4.1.4}$$

where λ^u is a Lagrange multiplier for velocity. We required that the derivative of the Lagrange function, L, to be zero for all variations $\boldsymbol{\phi}(\boldsymbol{x}) + \delta\boldsymbol{\xi}(\boldsymbol{x})$:

$$\begin{gathered}
\frac{d}{d\delta} L(\boldsymbol{\phi}(\boldsymbol{x}) + \delta\boldsymbol{\xi}(\boldsymbol{x}))|_{\delta=0} = \frac{d}{d\delta}[|\langle \boldsymbol{u}(\boldsymbol{x},\boldsymbol{\mu}), \boldsymbol{\phi}(\boldsymbol{x}) + \delta\boldsymbol{\xi}(\boldsymbol{x})\rangle_{L_2(\Omega)}| - \\
-\lambda^u(\langle \boldsymbol{\phi}(\boldsymbol{x}) + \delta\boldsymbol{\xi}(\boldsymbol{x}), \boldsymbol{\phi}(\boldsymbol{x}) + \delta\boldsymbol{\xi}(\boldsymbol{x})\rangle_{L_2(\Omega)})]|_{\delta=0} = \\
= 2[|\langle \boldsymbol{u}(\boldsymbol{x},\boldsymbol{\mu}), \boldsymbol{\xi}(\boldsymbol{x})\rangle_{L_2(\Omega)} \langle \boldsymbol{\phi}(\boldsymbol{x}), \boldsymbol{u}(\boldsymbol{x},\boldsymbol{\mu})\rangle_{L_2(\Omega)}| - \\
-\lambda^u \langle \boldsymbol{\phi}(\boldsymbol{x}), \boldsymbol{\xi}(\boldsymbol{x})\rangle_{L_2(\Omega)}] = 0
\end{gathered}$$

where it has been implied that the vectors $\boldsymbol{u}$, $\boldsymbol{\phi}$ and $\boldsymbol{\xi}$ are real. Using the conjugate symmetry property of the inner product, we can write:

$$\begin{gathered}
|\langle \boldsymbol{u}(\boldsymbol{x},\boldsymbol{\mu}), \boldsymbol{\xi}(\boldsymbol{x})\rangle_{L_2(\Omega)} \langle \boldsymbol{\phi}(\boldsymbol{x}), \boldsymbol{u}(\boldsymbol{x},\boldsymbol{\mu})\rangle_{L_2(\Omega)}| - \lambda^u \langle \boldsymbol{\phi}(\boldsymbol{x}), \boldsymbol{\xi}(\boldsymbol{x})\rangle_{L_2(\Omega)}] = \\
= |\langle \boldsymbol{u}(\boldsymbol{x},\boldsymbol{\mu}) \langle \boldsymbol{u}(\boldsymbol{x},\boldsymbol{\mu}), \boldsymbol{\phi}(\boldsymbol{x})\rangle_{L_2(\Omega)}, \boldsymbol{\xi}(\boldsymbol{x})\rangle_{L_2(\Omega)}| - \lambda \langle \boldsymbol{\phi}(\boldsymbol{x}), \boldsymbol{\xi}(\boldsymbol{x})\rangle_{L_2(\Omega)} \\
= \langle \mathfrak{C}\boldsymbol{\phi}(\boldsymbol{x}) - \lambda^u \boldsymbol{\phi}(\boldsymbol{x}), \boldsymbol{\xi}(\boldsymbol{x})\rangle_{L_2(\Omega)} = 0,
\end{gathered}$$

where $\mathfrak{C}$ is the correlation matrix defined as $\mathfrak{C} = \langle \boldsymbol{u}(\boldsymbol{x},\boldsymbol{\mu}), \boldsymbol{u}(\boldsymbol{x},\boldsymbol{\mu})\rangle_{L_2(\Omega)}$.

The previous equation can be reduced to the eigenvalue problem:

$$\mathfrak{C}\boldsymbol{\phi}(\boldsymbol{x}) = \lambda^u \boldsymbol{\phi}(\boldsymbol{x}), \tag{4.1.5}$$

as $\boldsymbol{\xi}(\boldsymbol{x})$ has been arbitrarily chosen. Therefore, the eigenfunctions of equation (4.1.5) compose the optimal POD basis, $\boldsymbol{\phi}(\boldsymbol{x})$, with the real, summetric correlation matrix, $\mathfrak{C}$, being its kernel (Berkooz, Holmes, and Lumley 1993):

$$\mathfrak{C}_{ij} = \langle \boldsymbol{u}_i, \boldsymbol{u}_j \rangle_{L_2(\Omega)} \qquad \text{for } i, j = 1, \ldots, N_u^s. \tag{4.1.6}$$

Written in matrix form,

$$\mathfrak{C}\boldsymbol{\Phi} = \boldsymbol{\lambda^u}\boldsymbol{\Phi}, \tag{4.1.7}$$

where the dimensions of the matrices, $\mathfrak{C} \in \mathbb{R}^{N_u^s \times N_u^s}$, $\boldsymbol{\Phi} \in \mathbb{R}^{N_u^s \times N_u^s}$ (the matrix with the eigenvectors) and $\boldsymbol{\lambda^u} \in \mathbb{R}^{N_u^s \times N_u^s}$ (the diagonal matrix containing the eigenvalues for the velocity field). Since the correlation matrix is positive and semi-definite [1] , it has non-negative, real eigenvalues. The POD basis functions, $\boldsymbol{\phi}(\boldsymbol{x})$, are calculated and normalized as:

$$\begin{aligned} \boldsymbol{\phi}_i(\boldsymbol{x}) &= \frac{1}{\sqrt{\lambda_i^u N_u^s}} \sum_{j=1}^{N_u^s} \boldsymbol{u}_j(\boldsymbol{x}) \boldsymbol{\Phi}_{i,j}, && (4.1.8) \\ \langle \boldsymbol{\phi}_i, \boldsymbol{\phi}_j \rangle_{L_2(\Omega)} &= \delta_{ij} \quad \forall\, i, j = 1, \ldots, N_u^s, && (4.1.9) \end{aligned}$$

where $\boldsymbol{\Phi}_{i,j}$ is the i^{th} element of eigenvector $\boldsymbol{\Phi}$ corresponding to the eigenvalue λ_j^u.

The same approximation is applied for the pressure and temperature fields. However, as pressure and temperature are scalar fields, the basis functions, denoted as $\psi(\boldsymbol{x}) \in \mathbb{R}^{N_p^h}$ and $\chi(\boldsymbol{x}) \in \mathbb{R}^{N_\theta^h}$ respectively, are now scalar functions. For each field, different temporal coefficients are considered, denoted as $b(t, \boldsymbol{\mu})$ and $c(t, \boldsymbol{\mu})$ respectively. Therefore, the POD decomposition of the velocity, pressure and temperature

---

[1] A symmetric matrix $\boldsymbol{M} = [m_{ij}]$ is positive-semidefinite if $\boldsymbol{\phi}^T \boldsymbol{M} \boldsymbol{\phi} \geq 0 \,\forall$ column vectors $\boldsymbol{p}$

is:

$$\begin{aligned} \boldsymbol{u}(\boldsymbol{x},\boldsymbol{\mu},t) \approx \boldsymbol{u}_s &= \sum_{i=1}^{N_u^s} \alpha_i(\boldsymbol{\mu},t)\boldsymbol{\phi}_i(\boldsymbol{x}), && (4.1.10)\\ p(\boldsymbol{x},\boldsymbol{\mu},t) \approx p_s &= \sum_{i=1}^{N_p^s} b_i(\boldsymbol{\mu},t)\psi_i(\boldsymbol{x}), && (4.1.11)\\ \theta(\boldsymbol{x},\boldsymbol{\mu},t) \approx \theta_s &= \sum_{i=1}^{N_\theta^s} c_i(\boldsymbol{\mu},t)\chi_i(\boldsymbol{x}), && (4.1.12) \end{aligned}$$

where $\boldsymbol{u}_s$, p_s and θ_s are the decomposed original fields in the reduced space.

The associated basis functions for pressure and temperature are calculated and normalized according to equation (4.1.8) as follows:

$$\begin{aligned} \psi_i(\boldsymbol{x}) &= \frac{1}{\sqrt{\lambda_i^p N_p^s}} \sum_{j=1}^{N_p^s} p_j(\boldsymbol{x})\Psi_{i,j}, && (4.1.13)\\ \langle \psi_i, \psi_j \rangle_{L_2(\Omega)} &= \delta_{ij} \quad \forall\, i,j = 1,\dots,N_p^s, && (4.1.14) \end{aligned}$$

$$\begin{aligned} \chi_i(\boldsymbol{x}) &= \frac{1}{\sqrt{\lambda_i^\theta N_\theta^s}} \sum_{j=1}^{N_\theta^s} \theta_j(\boldsymbol{x})X_{i,j}, && (4.1.15)\\ \langle \chi_i, \chi_j \rangle_{L_2(\Omega)} &= \delta_{ij} \quad \forall\, i,j = 1,\dots,N_\theta^s, && (4.1.16) \end{aligned}$$

where λ_i^p and λ_i^θ are the *ith* eigenvalues for pressure and temperature field, respectively.

To take into advantage the L^2-norm optimality of the POD method, the 'most-energetic' modes should be retained. Therefore, the original spatial POD basis, $\mathscr{V}$ =span$[\boldsymbol{\phi}_1, \boldsymbol{\phi}_2, ...\boldsymbol{\phi}_{N_u^s}]$, is truncated using the following energy retain quantity:

$$E_{N_u^r} = \frac{\sum_{i=1}^{N_u^r} \lambda_i^u}{\sum_{j=1}^{N_u^s} \lambda_j^u}, \qquad (4.1.17)$$

where N_u^r is the number of the most energetic modes, which are retained. Therefore, the truncated POD space, $\hat{\mathscr{V}}$ =span$[\boldsymbol{\phi}_1, \boldsymbol{\phi}_2, ...\boldsymbol{\phi}_{N_u^r}] \subset \mathscr{V}$, has a new cardinality N_u^r, which is smaller than the original cardinality, N_s^r . A summary of the POD method is shown in algorithm (1).

The reduced fields are:

$$\begin{aligned}
\boldsymbol{u}(\boldsymbol{x}, \boldsymbol{\mu}, t) \approx \boldsymbol{u}_r &= \sum_{i=1}^{N_u^r} \alpha_i(\boldsymbol{\mu}, t)\boldsymbol{\phi}_i(\boldsymbol{x}), && (4.1.18)\\
p(\boldsymbol{x}, \boldsymbol{\mu}, t) \approx p_r &= \sum_{i=1}^{N_p^r} b_i(\boldsymbol{\mu}, t)\psi_i(\boldsymbol{x}), && (4.1.19)\\
\theta(\boldsymbol{x}, \boldsymbol{\mu}, t) \approx \theta_r &= \sum_{i=1}^{N_\theta^r} c_i(\boldsymbol{\mu}, t)\chi_i(\boldsymbol{x}), && (4.1.20)
\end{aligned}$$

where the coefficients α_i, b_i and c_i can be computed by projecting the snapshots onto the POD basis:

$$\begin{aligned}
\alpha_i(\boldsymbol{\mu}, t) &= \langle \boldsymbol{u}_i(\boldsymbol{x}, \boldsymbol{\mu}), \boldsymbol{\phi}_j(\boldsymbol{x})\rangle_{L_2(\Omega)}, && (4.1.21)\\
b_i(\boldsymbol{\mu}, t) &= \langle p_i(\boldsymbol{x}, \boldsymbol{\mu}), \psi_j(\boldsymbol{x})\rangle_{L_2(\Omega)}, && (4.1.22)\\
c_i(\boldsymbol{\mu}, t) &= \langle \theta_i(\boldsymbol{x}, \boldsymbol{\mu}), \chi_j(\boldsymbol{x})\rangle_{L_2(\Omega)}. && (4.1.23)
\end{aligned}$$

The snapshot POD projection error corresponds to the eigenvalues of the truncated modes (Quarteroni, Manzoni, and Negri 2016) and is given by the following expression:

$$\sum_{i=1}^{N_u^s} ||\boldsymbol{u}_i(\boldsymbol{x}, \boldsymbol{\mu}, t) - \sum_{j=1}^{\omega} \langle \boldsymbol{u}_i(\boldsymbol{x}, \boldsymbol{\mu}), \boldsymbol{\phi}_j(\boldsymbol{x})\rangle_{L_2(\Omega)} \boldsymbol{\phi}_j(\boldsymbol{x})||_{L^2}^2 = \sum_{i=\omega+1}^{N_u^s} \lambda_i. \qquad (4.1.24)$$

Algorithm 1 The algorithm for the generation of the POD basis functions

```
    Input: snapshots ${\boldsymbol{u}_i(\boldsymbol{x}, \boldsymbol{\mu})}_{i=1}^{N_u^s}$, correlation matrix $\mathfrak{C} \in \mathbb{R}^{N_u^s \times N_u^s}$
    Output: POD basis, $\boldsymbol{\phi}(\boldsymbol{x})$.
Set $\boldsymbol{U}_s = [u_1^1(\boldsymbol{\mu}^1), ..., u_1^{N_u^s}(\mu^{N_p})] \in N_u^h \times N_u^s$;
Calculate the correlation matrix $\mathfrak{C}_{ij} = \frac{1}{N_s^u}\boldsymbol{u}_i^T \boldsymbol{u}_j \in \mathbb{R}^{N_u^s \times N_u^s}$;
Solve the eigenvalue problem: $\mathfrak{C}\boldsymbol{\phi} = \boldsymbol{\lambda}\boldsymbol{\phi}$;
Define energy quantity: $E_{N_u^r} = \frac{\sum_{i=1}^{N_u^r} \lambda_i}{\sum_{j=1}^{N_u^s} \lambda_j}$;
Truncate the basis $\boldsymbol{\phi}(\boldsymbol{x})$ with cardinality $N_u^s$ to a basis $\boldsymbol{\phi}(\boldsymbol{x})$ with cardinality $N_u^r$;
Return POD basis $\boldsymbol{\phi}(\boldsymbol{x}) \in N_u^r$;
```

4.2 Nested POD

The global POD method becomes too expensive when it comes to training spaces with many training points, leading to dense matrix eigenproblems. Considering for example the velocity snapshots, the computational effort to the solution of the quadratic eigenvalue problem, (4.1.5), scales as $\mathscr{O}([N_u^s]^3)$. The nested POD method approximates the global POD space by solving one "small" eigenvalue problem for each local parameter space. The local POD bases are then weighted by the eigenvalues and a global snapshot matrix is created by appending the local weighted POD bases.

A standard POD is then performed to the snapshot matrix and the basis is calulating according to the method described in (6.2). The advantage of the nested POD over the global POD method is the numerical efficiency, since the computational effort for the former scales as $\mathscr{O}([\sum_{i=1}^{N_p} N_t^3 + [N_u^{nested}]^3)$, where N_u^{nested} is the the dimension of the snaphot matrix resulted from the nested POD.

The nested POD acts to the following N_p local matrices:

$$\boldsymbol{U}_{nested} = \begin{bmatrix} u_1^1(\mu^i) & u_1^2(\mu^i) & \dots & u_1^{N_u^s}(\mu^i) \\ \vdots & \vdots & \dots & \vdots \\ u_{N_u^h}^1(\mu^i) & u_{N_u^h}^2(\mu^i) & \dots & u_{N_u^h}^{N_u^s}(\mu^i) \end{bmatrix}$$

where i runs from 1 to N_p.

The global POD matrix is then formed by selecting the first N_u^{rn} modes, according to the energy quantity (4.1.17), weighted by their eigenvalues. The concatenation of the weighted modes results to the following global POD matrix:

$$\boldsymbol{U}_{s_n} = \Big[\begin{array}{ccccccc} \lambda_1^1 \phi_1^1(\mu^1) & \dots & \lambda_1^{N_u^{rn}} \phi_1^{N_u^{rn}}(\mu^1) & \lambda_1^1 \phi_1^1(\mu^2) & \dots & \lambda_1^1 \phi_1^{N_u^{rn}}(\mu^{N_p}) \\ \vdots & \dots & \vdots & \vdots & \dots & \vdots \\ \lambda_1^1 \phi_{N_u^h}^1(\mu^1) & \dots & \lambda_1^{N_u^{rn}} \phi_{N_u^h}^2(\mu^1) & \lambda_1^2 \phi_{N_u^h}^1(\mu^2) & \dots & \lambda_1^{N_u rn} \phi_{N_u^h}^{N_u^{rn}}(\mu^{N_p}) \end{array} \Big]$$

As soon as the snapshot matrix $\boldsymbol{U}_{s_n}$ is formed, the procedure is the same as the one described in section (6.2).

4.3 Galerkin Projection

In the previous section, a POD approach for the calculation of the reduced spaces has been discussed. The next step is the projection of the full order Navier - Stokes equations coupled with the energy equation (one-way coupling), shown below, onto the reduced space.

$$\begin{cases} \frac{\partial \boldsymbol{u}}{\partial t} + \boldsymbol{\nabla} \cdot (\boldsymbol{u} \otimes \boldsymbol{u}) - \nabla \cdot \nu \nabla \boldsymbol{u} = -\nabla p & \text{in } Q, \\ \boldsymbol{\nabla} \cdot \boldsymbol{u} = \boldsymbol{0} & \text{in } Q, \\ \frac{\partial \theta}{\partial t} + \nabla \cdot (\boldsymbol{u}\theta) - \alpha_{dif} \Delta \theta = 0 & \text{in } Q. \end{cases} \tag{4.3.1}$$

For the projection, the Galerkin approach is used, where the full order momentum equation is projected onto the velocity basis $\boldsymbol{\phi}(\boldsymbol{x})$, the continuity onto the pressure modes, $\psi(\boldsymbol{x})$, and the energy equation onto the temperature basis $\chi(\boldsymbol{x})$, according to the following equations:

$$\begin{cases} \langle (\frac{\partial \boldsymbol{u}}{\partial t} + \boldsymbol{\nabla} \cdot (\boldsymbol{u} \otimes \boldsymbol{u}) - \nabla \cdot \nu \nabla \boldsymbol{u} + \nabla p), \boldsymbol{\phi}) \rangle_{L_2(\Omega)} = 0, \\ \langle \boldsymbol{\nabla} \cdot \boldsymbol{u}, \psi \rangle_{L_2(\Omega)} = 0, \\ \langle (\frac{\partial \theta}{\partial t} + \nabla \cdot (\boldsymbol{u}\theta) - \alpha_{dif} \Delta \theta), \chi \rangle_{L_2(\Omega)} = 0. \end{cases} \tag{4.3.2}$$

There is yet the continuity equation, which, has not been exploited yet but a detailed discussion follows in the next section.

Expanding the inner products in the above set of equations and exploiting the orthogonality condition, the following set of ODEs is obtained:

$$\sum_{j=1}^{N_u^r} M_{ij} \frac{\partial \alpha_j}{\partial t} = \sum_{j=1}^{N_u^r} \sum_{k=1}^{N_u^r} Q_{ijk} \alpha_j \alpha_k + \nu \sum_{i=1}^{N_u^r} L_{ij} \alpha_i - \sum_{i=1}^{N_p^r} P_{ij} b_i, \tag{4.3.3}$$

$$\sum_{j=1}^{N_p^r} R_{ij} \alpha_j = 0, \tag{4.3.4}$$

$$\sum_{j=1}^{N_\theta^r} K_{ij} \frac{\partial c_j}{\partial t} = \sum_{j=1}^{N_u^r} \sum_{k=1}^{N_\theta^r} G_{ijk} \alpha_j c_k + \alpha_{dif} \sum_{j=1}^{N_\theta^r} N_{ij} c_j, \tag{4.3.5}$$

where the reduced quadratic and linear terms, Q_{ijk}, P_{ij}, R_{ij}, L_{ij}, G_{ijk}, K_{ij} and N_{ij}

are represented by the following matrices:

$$(\boldsymbol{M}_{ij}) = \langle \boldsymbol{\phi}_i, \boldsymbol{\phi}_j \rangle_{L_2(\Omega)}, \tag{4.3.6}$$

$$(\boldsymbol{Q}_{ijk}) = \langle \nabla \cdot (\boldsymbol{\phi}_i \otimes \boldsymbol{\phi}_j), \boldsymbol{\phi}_k \rangle_{L_2(\Omega)}, \tag{4.3.7}$$

$$(\boldsymbol{L}_{ij}) = \langle \nu \Delta \boldsymbol{\phi}_i, \boldsymbol{\phi}_j \rangle_{L_2(\Omega)}, \tag{4.3.8}$$

$$(\boldsymbol{P}_{ij}) = \langle \nabla \psi_i, \boldsymbol{\phi}_j \rangle_{L_2(\Omega)}, \tag{4.3.9}$$

$$(\boldsymbol{R}_{ij}) = \langle \nabla \cdot \boldsymbol{\phi}_i, \psi_j \rangle_{L_2(\Omega)}, \tag{4.3.10}$$

$$(\boldsymbol{K}_{ij}) = \langle \chi_i, \chi_j \rangle_{L_2(\Omega)}, \tag{4.3.11}$$

$$(\boldsymbol{G}_{ijk}) = \langle \nabla \cdot (\boldsymbol{\phi}_i \chi_j), \chi_k \rangle_{L_2(\Omega)}, \tag{4.3.12}$$

$$(\boldsymbol{N}_{ij}) = \langle \alpha_{dif} \Delta \chi_i, \chi_j \rangle_{L_2(\Omega)}. \tag{4.3.13}$$

For computational efficiency reasons, the non-linear convective term is stored as a third order tensor and at each Newton iteration the $i-th$ component is evaluated as $(\boldsymbol{Q}(\alpha)\alpha)_i = \boldsymbol{\alpha^T Q_{i\bullet\bullet}\alpha}$. The same approach is followed for G_{ijk}, which is evaluated as $(\boldsymbol{G}(\alpha)\boldsymbol{c})_i = \boldsymbol{\alpha}^T \boldsymbol{G}_{i\bullet\bullet}\boldsymbol{c}$.

The projected initial conditions read:

$$\alpha_i(0) = (\boldsymbol{u}(\boldsymbol{x}, \boldsymbol{\mu}, 0), \boldsymbol{\phi}_i), c_i(0) = (\theta(\boldsymbol{x}, \boldsymbol{\mu}, 0), \chi_i). \tag{4.3.14}$$

To summarize all the above, the ROM is governed by the following system of ODEs:

$$\begin{cases} \boldsymbol{M}\dot{\boldsymbol{\alpha}} = -\boldsymbol{\alpha}^T \boldsymbol{Q}\boldsymbol{\alpha} + \nu \boldsymbol{L}\boldsymbol{\alpha} - \boldsymbol{P}\boldsymbol{b}, \\ \boldsymbol{K}\dot{\boldsymbol{c}} = -\boldsymbol{\alpha}^T \boldsymbol{G}\boldsymbol{c} + \alpha_{dif}\boldsymbol{N}\boldsymbol{c}, \\ \boldsymbol{R}\boldsymbol{\alpha} = 0, \end{cases} \tag{4.3.15}$$

which are then solved by any temporal discretisation scheme. The ROM is implemented in ITHACA-FV, a C++ library based on OpenFOAM (Stabile and Rozza no date). This library contains reduced solvers for a variety of problems such as steady laminar and turbulent, unsteady laminar and unsteady turbulent via the non-intrusive RBF method as well as unsteady turbulent via Galerkin projection. My contribution was to develop the following solvers for the purpose of the current thesis:

- unsteady laminar with addition of the energy equation (reffered to as *Unstea-*

dyNST and *ReducedUnsteadyNST*)

- unsteady turbulent using RBF with addition of the energy equation (reffered to as *UnsteadyNSTTurb* and *ReducedUnsteadyNSTTurb*)
- unsteady buoyant Boussinesq which is reffered to as *UnsteadyBB* and *ReducedUnsteadyBB* (in collaboration with K.S Star (Star, Stabile, Georgaka, Belloni, Rozza, and Degroot 2019)).

The *UnsteadyNST*, *UnsteadyNSTTurb* and *UnsteadyBB* classes handle the 'Offline' phase (4.1) which contains the FOM solution via OpenFOAM solvers, the snapshot acquisition and the calculation of the basis functions via the POD. The calculation of the reduced matrices is also part of those classes as well as the computation of any lifting functions (more details on chapter 5) or supremizers.

The corresponding reduced classes (*ReducedUnsteadyNST*, *ReducedUnsteadyNSTTurb* and *ReducedUnsteadyBB*) manage the 'Online' phase which contains the solution of the projected equations (ROM - 4.3.15) using the Powell's hybrid method ("dogleg") via the *Eigen::HybridNonLinearSolver* module, which is part of the third party library Eigen (Guennebaud, Jacob, et al. 2010). The *Eigen::HybridNonLinearSolver* solver follows a modified Newton-Raphson procedure. The eigen library is also used for all the linear and non-linear algebra operations in ITHACA-FV. Since an iterative method is used for the solution of the non-linear ROM equations, the tolerance of the convergence of the residuals is set to 1×10^{-5}. In this work, the temporal discretization is performed by the backward Euler method. The reconstruction of the fields via the equations (4.1.19, 4.1.20 and 4.1.20) is also part of the reduced class.

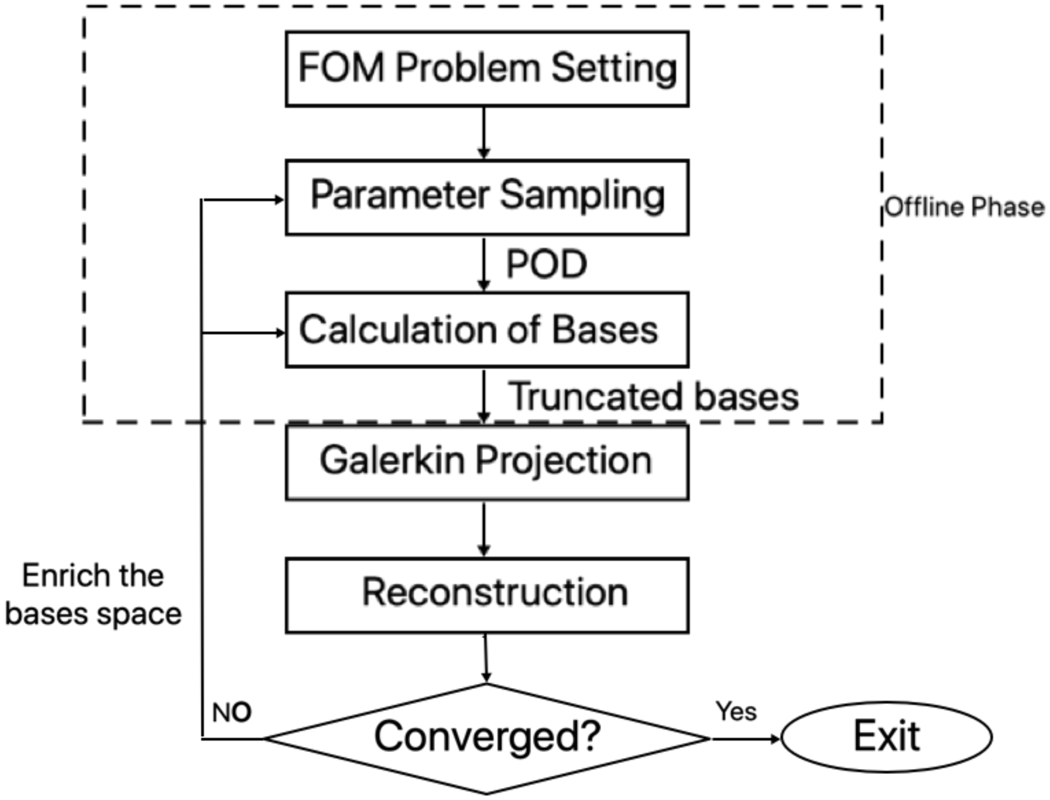

Figure 4.1: Flow diagram of the POD-Galerkin ROM procedure.

4.4 Pressure Term

The projection of the pressure gradient, (∇p), onto the POD basis can be derived using Green's theorem as follows:

$$\langle \boldsymbol{\phi}, \nabla p \rangle_{L_2(\Omega)} = \int_{\Omega} \boldsymbol{\phi} \cdot \nabla p d\Omega = -\int_{\Omega} \nabla \cdot \boldsymbol{\phi} p d\Omega + \int_{\partial\Omega} p \boldsymbol{\phi} \cdot \boldsymbol{n} dS = \int_{\partial\Omega} p \boldsymbol{\phi} \cdot \boldsymbol{n} dS. \quad (4.4.1)$$

Depending on the flow configuration, the contribution of the pressure field is either negligible or zero and therefore is not always taken into account. In some ROMs, the volume integral term is taken equal to zero since, for incompressible flows, the velocity basis functions are computed from linear combinations of divergence free snapshots. Therefore, the pressure term depends only on the boundary Γ. However, this requires that each individual POD mode is divergence free, which is true up to a numerical point (subject to machine precision error) (Lee and Dowell 2020). What is more, in the case where enclosed flows ($\boldsymbol{\phi} \cdot \boldsymbol{n} = 0$ on $\partial\Omega$) or flows with inlet-outlet conditions with the outlet being far away from the obstacle are modelled, the pressure term vanishes completely (Deane, Kevrekidis, Karniadakis, and Orszag 1991; Ma and Karniadakis 2002). However, as indicated in (Noack, Papas, and Monkewitz 2005a), the pressure term can not always be neglected, especially when unstable shear layers are studied or when pressure drop calculations are important, such as pressure drop in pipes.

If the pressure term is considered in the reduced level as having separate modes and temporal coefficients to those of velocity, the system of equations (4.3.15) has N_u equations but $N_u + N_p$ unknowns. Therefore, a saddle point problem is arising for the temporal coefficients a and b. To tackle with this issue, many different approaches have been proposed. A possible approach, is presented in (Stabile and Rozza 2018) in finite volume and in (Ballarin, Manzoni, Quarteroni, and Rozza 2014; Rozza and Veroy 2007) in finite element context, where a supremizer enrichment method is proposed, which also ensures that the inf-sup stability holds in the ROM level as well. In this way, a unique solution is achieved for the saddle-point problem.

A second approach relies on the pressure poisson equation, which circumvents the saddle-point problem. The continuity equation can not be directly exploited as the snapshots are in fact already divergence free and so the velocity modes are. However, instead of the incompressibility constraint, a continuity equation for pressure can be employed, which is the known Pressure Poisson equation. This method is proposed in (Akhtar, Nayfeh, and Ribbens 2009b) where the PPE is projected onto a pressure POD basis. In (Bergmann, Bruneau, and Iollo 2009) a global POD basis for both pressure and velocity fields was proposed, where the fields were decomposed using the same temporal coefficients. In such approach, in the ROM level, only the momentum equation is exploited.

4.5 Supremizer Enrichment

In this work, since the ROM is derived from a FOM which is descritized by the finite volume method, the resulting POD spaces do not automatically fulfill the inf-sup (Ladyzhenskaya-Brezzi-Babuska) condition (Boffi, Brezzi, and Fortin 2013; Brezzi and Bathe 1990). If a finite element method had been chosen, this condition would have been met by, for instance, selecting Taylor-Hood $\mathbb{P}^{\nvDash} - \mathbb{P}^{\nVdash}$ finite element spaces. The inf-sup or Ladyzhenskaya-Brezzi-Babuska (LBB) condition is formulated as follows:

$$\inf_{p \in \mathscr{Q}} \sup_{\boldsymbol{v} \in \mathscr{V}} \frac{\langle \nabla \cdot \boldsymbol{v}, p \rangle}{||\nabla \boldsymbol{v}|| \, ||p||} \geq \beta > 0. \tag{4.5.1}$$

where β is a constant and $p \in \mathscr{Q} = L^2(\Omega)$ and $\boldsymbol{v} \in \mathscr{V} = H_0^1(\Omega)$ are test functions of the velocity and pressure's function space which comes from the weak formulation of the Navier-Stokes equations and multiplies the continuity equation. The space $\mathscr{V} = H_0^1(\Omega)$ has norm $|\boldsymbol{v}|_1 = ||\nabla \boldsymbol{v}||$.

In the supremizer enrichment approach, the idea is that the velocity POD space is enriched with supremizer modes so that the LBB condition is fulfilled in the reduced order level. There are two ways of calculating the supremizer modes, the exact and the approximated (Ballarin, Manzoni, Quarteroni, and Rozza 2014; Stabile and Rozza 2018). In both ways, since the finite volume method is used for the solution, the supremizer problem is epxressed in the strong form. In the exact method, this problem is solved for each pressure mode, ψ_i, as follows:

$$\begin{cases} \Delta \boldsymbol{s_i} = -\boldsymbol{\nabla} \psi_i & \text{in } \Omega \\ \boldsymbol{s_i} = \boldsymbol{0} & \text{on } \partial\Omega, \end{cases} \tag{4.5.2}$$

where $\boldsymbol{s_i}$ denotes the supremizer solution. The velocity space is then enriched with the resulting supremizer modes, which form a supremizer space $S = \{S(\psi_i)\}_{i=1}^{N_p^r}$. The resulting dimension of the enriched velocity space is $N_u^r + N_{sup}^r$, where N_{sup}^r is the cardinality of the space of the supremizer modes. In this way, a supremizer mode is added for every pressure mode and the inf-sup condition is met (Ballarin, Manzoni, Quarteroni, and Rozza 2014).

In the approximated approach, the supremizer enrichment is given by solving the supremizer problem for each pressure snapshot as follows:

$$\begin{cases} \Delta \boldsymbol{s_i} = -\boldsymbol{\nabla} p_i & \text{in } \Omega \\ \boldsymbol{s_i} = \boldsymbol{0} & \text{on } \partial\Omega. \end{cases} \tag{4.5.3}$$

The supremizer snapshot matrix, $\boldsymbol{S} = [\boldsymbol{s}(p_1), ..., \boldsymbol{s}(p_{N_p^s})] \in \mathbb{R}^{N_{sup}^h \times N_{sup}^s}$, is formed and the POD approach similar to one described in the previous section, as well as an energy quantity (4.1.17) is applied to truncate the supremizer's reduced space, keeping only the most energetic, N_{sup}^r, modes. Therefore, the resulting enriched velocity space has a new cardinality of $N_u^r + N_{sup}^r$. A benefit of the approximated against the exact method is the reduced computational cost it entails.

It is worth mentioning that, the basis functions of the enriched velocity space are not all orthogonal. The addition of the extra, non-divergence free, supremizer modes into the velocity space provides a closure to the saddle problem, by allowing for the exploitation of the continuity equation in (4.3.15).

4.6 Pressure Poisson Equation in the Reduced Level

In the PPE approach, the momentum equation (3.1.6) is projected onto the pressure modes, ψ_i. The projection is written as follows:

$$\langle \Delta p, \psi \rangle_{L_2(\Omega)} = \langle -\nabla \cdot (\boldsymbol{u} \nabla \boldsymbol{u}), \psi \rangle_{L_2(\Omega)}. \tag{4.6.1}$$

Integrating by parts the LHS:

$$\langle \nabla p, \nabla \psi \rangle_{L_2(\Omega)} = \langle \nabla \cdot ((\boldsymbol{u} \cdot \nabla)\boldsymbol{u}), \psi \rangle_{L_2(\Omega)} \tag{4.6.2}$$

where the basis functions ψ are considered smooth and zero on the boundary ($\psi_\Gamma = 0$), therefore the boundary term generated by the integration by parts is zero.
The Galerkin projection of the Navier - Stokes and energy equations, 4.3.2, is now:

$$\begin{cases} \langle (\frac{\partial \boldsymbol{u}}{\partial t} + \boldsymbol{\nabla} \cdot (\boldsymbol{u} \otimes \boldsymbol{u}) - \nabla \cdot \nu \nabla \boldsymbol{u} + \nabla p), \boldsymbol{\phi}) \rangle_{L_2(\Omega)} = 0, \\ \langle \nabla p, \nabla \psi \rangle_{L_2(\Omega)} - \langle \nabla \cdot (\boldsymbol{u} \cdot \nabla \boldsymbol{u}), \psi \rangle_{L_2(\Omega)} = 0, \\ \langle (\frac{\partial \theta}{\partial t} + \nabla \cdot (\boldsymbol{u}\theta) - \alpha_{dif} \Delta \theta), \chi \rangle_{L_2(\Omega)} = 0. \end{cases} \tag{4.6.3}$$

The modified ROM equations are:

$$\begin{cases} \boldsymbol{M}\dot{\boldsymbol{\alpha}} = -\boldsymbol{\alpha}^T\boldsymbol{Q}\boldsymbol{\alpha} + \nu\boldsymbol{L}\boldsymbol{\alpha} - \boldsymbol{P}\boldsymbol{b}, \\ \boldsymbol{K}\dot{\boldsymbol{c}} = -\boldsymbol{\alpha}^T\boldsymbol{G}\boldsymbol{c} + \alpha_{dif}\boldsymbol{N}\boldsymbol{c}, \\ \boldsymbol{D}\boldsymbol{b} = \boldsymbol{\alpha}^T\boldsymbol{U}\boldsymbol{\alpha}, \end{cases} \tag{4.6.4}$$

where the new matrices are defined as:

$$(\boldsymbol{D}_{ij}) = \langle \nabla\psi_i, \nabla\psi_j \rangle_{L_2(\Omega)}, \tag{4.6.5}$$

$$(\boldsymbol{U}_{ijk}) = \langle \nabla \cdot (\nabla \cdot (\boldsymbol{\phi}_j \otimes \boldsymbol{\phi}_k)), \nabla\psi_k \rangle_{L_2(\Omega)}, \tag{4.6.6}$$

$$\tag{4.6.7}$$

where the matrix $\boldsymbol{U}_{ijk}$ is treated in the same way as the $\boldsymbol{Q}_{ijk}$ and $\boldsymbol{G}_{ijk}$ matrices. In the ROM, the coupled velocity-PPE equations are treated in a monolithic way.

4.7 Summary of the Chapter

In this chapter, the mathematical background for the ROM was provided. This included a detailed mathematical formulation of the POD-Galerkin method, as well as methods for the treatment of the pressure term in the reduced level. A variation of the classical POD method, the Nested POD was also dicussed.

Chapter 5

Model Order Reduction for Laminar Heat Transfer

In this chapter a POD-Galerkin method is derived for the parametric, 3D, unsteady Navier-Stokes equations one-way coupled with the energy equation. The method is tested on a T-junction, a set-up. Two parametric cases are considered: first the parametrisation on the two temperature inlet boundary conditions, and in the second case, on a physical parameter, the kinematic viscosity. The open-source finite volume solver OpenFOAM is used to generate the FOM solutions, which are then used as an input training space for the ROM.

The content of this chapter has been published in:

GEORGAKA, S., STABILE, G., ROZZA, G., and BLUCK, M.J. 2020. Parametric POD-Galerkin Model Order Reduction for Unsteady-State Heat Transfer Problems. Communications in Computational Physics, Vol 27, No. 1, pp. 1-32.

5.1 Mathematical Framework for the Full Order Model

The FOM is described by the incompressible, transient, parametrised Navier-Stokes equations, coupled with the energy equation (one-way coupling). In an Eulerian framework and domain $Q = \Omega \times [0, T_s] \subset \mathbb{R}^d \times \mathbb{R}^+$ with $d = 2, 3$, these equations can be expressed as follows:

$$\begin{cases} \frac{\partial \boldsymbol{u}(\boldsymbol{x},\boldsymbol{\mu},t)}{\partial t} + \boldsymbol{\nabla} \cdot (\boldsymbol{u}(\boldsymbol{x},\boldsymbol{\mu},t) \otimes \boldsymbol{u}(\boldsymbol{x},\boldsymbol{\mu},t)) - \boldsymbol{\nabla} \cdot \nu(\boldsymbol{\mu}) \boldsymbol{\nabla} \boldsymbol{u}(\boldsymbol{x},\boldsymbol{\mu},t) = -\boldsymbol{\nabla} p(\boldsymbol{x},\boldsymbol{\mu},t) & \text{in } Q, \\ \boldsymbol{\nabla} \cdot \boldsymbol{u}(\boldsymbol{x},\boldsymbol{\mu},t) = \boldsymbol{0} & \text{in } Q, \\ \frac{\partial \theta(\boldsymbol{x},\boldsymbol{\mu},t)}{\partial t} + \nabla \cdot (\boldsymbol{u}(\boldsymbol{x},\boldsymbol{\mu},t)\theta(\boldsymbol{x},\boldsymbol{\mu},t)) - \alpha_{dif} \Delta \theta(\boldsymbol{x},\boldsymbol{\mu},t) = 0 & \text{in } Q, \\ \boldsymbol{u}(\boldsymbol{x},\boldsymbol{\mu},t) = \boldsymbol{f}(\boldsymbol{x}) & \text{on } \Gamma_{In} \times [0, T_s], \\ \theta(\boldsymbol{x},\boldsymbol{\mu},t) = g(\boldsymbol{x},\boldsymbol{\mu}) & \text{on } \Gamma_{In} \times [0, T_s], \\ \boldsymbol{u}(\boldsymbol{x},\boldsymbol{\mu},t) = \boldsymbol{0} & \text{on } \Gamma_{w} \times [0, T_s], \\ (\nu(\boldsymbol{\mu}))\nabla \boldsymbol{u} - p\boldsymbol{I})\boldsymbol{n} = \boldsymbol{0} & \text{on } \Gamma_{o} \times [0, T_s], \end{cases} \tag{5.1.1}$$

where $\boldsymbol{u}$ is the fluid velocity, p the normalized pressure (devided by the fluid density), θ is the fluid temperature, α_{dif} is the thermal diffusivity, $\nu(\boldsymbol{\mu})$ is the kinematic viscosity and $\boldsymbol{\mu}$ is the vector of parameters. T_s represents the time of the simulation, $\Gamma = \Gamma_{In} \cup \Gamma_w \cup \Gamma_o$ is the boundary of Ω and it consists of three different parts Γ_{In}, Γ_o and Γ_w that indicate, respectively, inlet, outlet and physical wall boundaries. The functions $\boldsymbol{f}(\boldsymbol{x},\boldsymbol{\mu})$ and $g(\boldsymbol{x},\boldsymbol{\mu})$ represent the boundary conditions for the non-homogeneous Dirichlet boundaries. Time independence of the boundary conditions $\boldsymbol{f}$ and $\boldsymbol{g}$ is also assumed. Two cases are considered: one with parametric dependency on the temperature inlet boundary conditions and a second with parametric dependency on the kinematic viscosity.

5.2 Boundary Conditions and Snapshot Homogenization

One of the key aspects of the present work is the development of reduced order methods with parametrised boundary conditions. For this reason particular attention is paid to this aspect. To enforce Dirichlet boundary conditions in the reduced order model we employ a similar approach as the one in (Stabile and Rozza 2018). This method was firstly proposed in (Graham, Peraire, and Tang 1999) for boundary conditions that can be parametrised by a single multiplicative coefficient, as in the present case, and generalized for every type of function in (Gunzburger, Peterson, and Shadid 2007).

A lifting function is used to homogenize the snapshots so that they become independent of the boundary conditions. At the reduced order level, it is possible to specify the new boundary values and these values are then added back. The homogenized velocity value is written as:

$$\boldsymbol{u}'(\boldsymbol{x},\boldsymbol{\mu},t)=\boldsymbol{u}(\boldsymbol{x},\boldsymbol{\mu},t)-\sum_{j=1}^{N_{BC}}u_{D_j}(\boldsymbol{\mu})\boldsymbol{\phi}_{c_j}, \tag{5.2.1}$$

where $\boldsymbol{\phi}_{c_j}$ are divergence free control functions, which are equal to the number of the parametrised boundaries, and N_{BC} is the number of parametrised boundary conditions.

The coefficients u_{D_j} are determined is such a way to make the snapshots homogeneous after the subtraction of the chosen control function multiplied by the coefficient itself. Since we chose to have a number of control functions, which is equal to the number of parametrised boundaries and that each control function assumes a uniform and unitary value at the boundary to which it refers and uniform null values on the other parametrised boundaries, the coefficient u_{D_j} will assume the value that the snapshots have at the boundary. This process is described in algorithm (2).

The POD is applied to the homogeneous snapshots and the boundary value is added back so that:

$$\boldsymbol{u}(\boldsymbol{x},\boldsymbol{\mu},t)=\sum_{j=1}^{N_{BC}}u_{D_j}(\boldsymbol{\mu})\boldsymbol{\phi}_{c_j}+\sum_{i=1}^{N_u^s}\alpha_i(t,\boldsymbol{\mu})\boldsymbol{\phi}_i(\boldsymbol{x}). \tag{5.2.2}$$

The values of the lifting functions are obtained by deviding the Dirichlet boundary in different parts $\Gamma_D=\bigcup_{i=1}^{N_{BC}}\Gamma_{D_i}$, one for each parametrised boundary condition. Then a full order problem is solved for each boundary condition following algorithm 3. In the case of a problem with a non-linear dependency with respect to the boundary conditions, the full order problem should be solved with values of the boundaries as close as possible to those that one would like to test during the online stage. Also, in case of a non-zero forcing term, the forcing term should also be considered in the evaluation of the lifting functions.

For the energy equation a similar approach is followed. Unlike with the velocity case, where a 'no-slip' condition is specified on the walls, in heat transfer problems,

Algorithm 2 The algorithm for the generation of the velocity lifting functions

```
Input: $N_{BC}$, $\Gamma_D = \bigcup_{i=1}^{N_{BC}} \Gamma_{D_i}$, $N_u^s$=Total number of snapshots
Output: $\{\boldsymbol{\phi}_{c_i}\}_{i=1}^{N_{BC}}$
for $i = 1$ to $N_{BC}$ do
    for $j = 1$ to $N_{BC}$ do
        if $i = j$ then $\boldsymbol{u}|_{\Gamma_{D_j}} = 1$; else $\boldsymbol{u}|_{\Gamma_{D_j}} = 0$
    end for
    for $l = 1$ to $N_u^s$ do
        Solve the full order problem and store the solution $\rightarrow \boldsymbol{u}_{il}$
    end for
    $\boldsymbol{\phi}_{c_i} = \frac{1}{N_u^s} \sum_{l=1}^{N_u^s} \boldsymbol{u}_{il}$
end for
```

a homogeneous Neumann boundary condition is usually assigned (adiabatic walls). Usually, together with the boundary conditions, an initial condition for the internal field (IF) is also prescribed. A modification of the algorithm (2) is proposed here where also the initial value of the internal field is removed from the snapshots. In this way, one could parametrize the internal field initial condition as well. Therefore, apart from the lifting functions that are obtained for every Dirichlet boundary condition, the domain is now devided into $N_{BC}+1$ different parts $\Omega_R = \bigcup_{i=1}^{N_{BC}} \Gamma_{D_i} \bigcup \Theta_{IF}$ where the extra lifting function accounts for the initial internal field. The algorithm (3) is modified as follows:

Algorithm 3 The algorithm for the generation of the temperature lifting functions

```
Input: $N_{BC}+1$, $\Omega_R = \bigcup_{i=1}^{N_{BC}} \Gamma_{D_i} \bigcup \Theta_{IF}$, $N_\theta^s$= Total number of snapshots
Output: $\{\chi_{c_i}\}_{i=1}^{N_{BC+1}}$
for $i = 1$ to $N_{BC}+1$ do
    for $j = 1$ to $N_{BC}+1$ do
        if $i = j$ then $\theta|_{\Gamma_{R_j}} = 1$; else $\theta|_{\Gamma_{R_j}} = 0$
    end for
    for $l = 1$ to $N_\theta^s$ do
        Solve the full order problem and store the solution $\rightarrow \theta_{il}$
    end for
    $\chi_{c_i} = \frac{1}{N_\theta^s} \sum_{l=1}^{N_\theta^s} \theta_{il}$
end for
```

During the calculation of the lifting functions, the adiabatic walls and the outlet still have homogeneous Neumann conditions as in the FOM. The boundary condition independent temperature is written as:

$$\theta'(\boldsymbol{x},\boldsymbol{\mu},t) = \theta(\boldsymbol{x},\boldsymbol{\mu},t) - \sum_{j=1}^{N_{BC+1}} \theta_{R_j}(\boldsymbol{\mu})\chi_{c_j}(\boldsymbol{x}). \tag{5.2.3}$$

The POD is then applied to the homogenised temperature snapshots and, at the reduced order level, the boundary values, as well as the internal field initial value, are added back to the temperature equation:

$$\theta(\boldsymbol{x}, \boldsymbol{\mu}, t) = \sum_{j=1}^{N_{BC}+1} \theta_{R_j}(\boldsymbol{\mu}) \chi_{c_j}(\boldsymbol{x}) + \sum_{i=1}^{N_\theta^s} c_i(t, \boldsymbol{\mu}) \chi_i(\boldsymbol{x}). \tag{5.2.4}$$

5.3 Non-isothermal Mixing in T-junction - Parametrisation of the Temperature Inlet Boundary Conditions

The first test case consists of a 3D T-junction shaped pipe with main pipe hydraulic diameter $D_m = 140$mm, branch pipe hydraulic diameter $D_b = 80$mm and lengths of $L_m = 3$m and $L_b = 0.44$m respectively. The branch pipe is placed at the position of $0.33 * L_m$. Streams of cold and hot water enter the system from the main and the branch pipe and mix together in the T-junction region. The thermal diffusivity is taken as $0.160 \times 10^{-6}\text{m}^2\text{s}^{-1}$ under atmospheric pressure. A summary of the physical parameters is demonstrated in table (5.1). The computational domain consists of 34490 elements, is devided into three boundary parts plus one part for the initial condition of the internal field, $\Omega_R = \Gamma_m \bigcup \Gamma_b \bigcup \Gamma_o \bigcup \Theta_{IF}$, as shown in figure (5.1). The initial conditions are as shown in table(5.2).

Table 5.1: Summary of the physical parameters.

	Main Pipe	Branch Pipe
u (ms^{-1})	0.01	0.02
θ (K)	323.15	343.15
D (mm)	140	80
Re	140	240

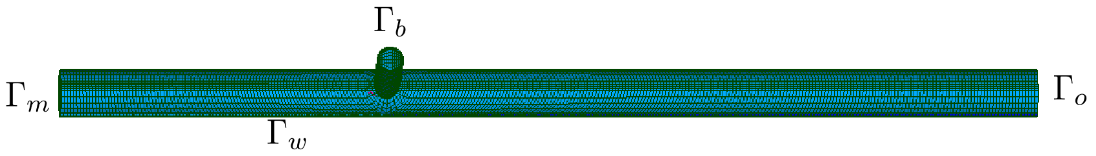

Figure 5.1: Sketch of the T-junction 3D mesh.

The FOM simulation is performed in OpenFOAM using a modified *icoFoam* solver, which accounts also for the temperature transport equation. *IcoFoam* (Jasak 1996) is a transient solver, which uses the PISO algorithm (3.2) to solve the incompressible Navier-Stokes equations. The spatial discretisation of the convective terms is achieved using a combination of a second order central-differencing and upwind schemes. The diffusive terms are discretized using second order central-differencing corrected schemes. For the temporal discretisation, a first order Euler backward implicit scheme is used. The ROM computations are performed in the ITHACA-FV.

The FOM simulation is performed for $T = 45s$ with time-step $dt = 5 \times 10^{-3}$s and snapshots are collected every 0.2s using an equispaced grid method in time. Therefore, the dimension of the correlation matrix is 225×225 and $N_u^s = N_\theta^s = N_p^s = 225$. A convergence test as the number of snapshots increases has been performed. The frequency with which the snapshots are collected has been doubled, thus the snapshots are now collected every 0.1s. This make the dimension of the correlation matrix to be 450×450 and $N_u^s = N_\theta^s = N_p^s = 450$. To assess the quality of the ROM, the relative ϵ_{L^2} error is calculated. This, for velocity and pressure is defined as follows:

$$\epsilon_{L^2}(t) = \frac{||X_{FOM}(t) - X_{ROM}(t)||_{L^2(\Omega)}}{||X_{FOM}(t)||_{L^2(\Omega)}}\%, \tag{5.3.1}$$

where X_{FOM} is the value of a particular field in the FOM model and X_{ROM} the one that is calculated using the ROM. For temperature, the error is normalized by the temperature change ($\Delta\theta$), according to the following equation:

$$\epsilon_{L^2}(t) = \frac{||\theta_{FOM}(t) - \theta_{ROM}(t)||_{L^2(\Omega)}}{||\Delta\theta(t)||_{L^2(\Omega)}}\%, \tag{5.3.2}$$

Figure (5.2) shows the comparison between the two different sampling frequencies, showing that the relative error between the FOM and the ROM slightly improves with the enrichment of the training space.

Table 5.2: Table with the boundary conditions where Γ_m refers to the main pipe inlet, Γ_b to the branch pipe and Γ_0 is the outlet.

	Γ_m	Γ_b	Γ_w	Γ_o	Θ_{IF}
$\boldsymbol{u}$	$(0.01, 0, 0)$	$(0, 0, -0.02)$	$(0, 0, 0)$	$\nabla \boldsymbol{u} \cdot \boldsymbol{n} = 0$	$(0, 0, 0)$
p	$\nabla p \cdot \boldsymbol{n} = 0$	$\nabla p \cdot \boldsymbol{n} = 0$	$\nabla p \cdot \boldsymbol{n} = 0$	0	0
θ	323.15	343.15	$\nabla \theta \cdot \boldsymbol{n} = 0$	$\nabla \theta \cdot \boldsymbol{n} = 0$	323.15

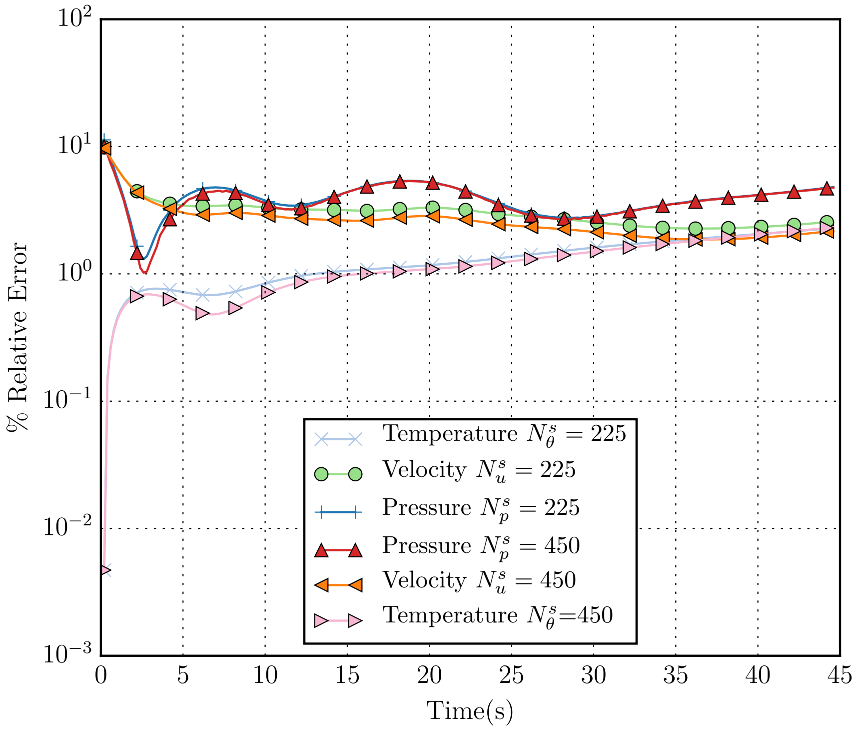

Figure 5.2: $\%\epsilon_{L^2}(t)$ error for two sampling frequencies for the snapshot collection, per 0.2s where $N_u^s = N_\theta^s = N_p^s = 225$ and per $0.1s$ where $N_u^s = N_\theta^s = N_p^s = 450$s. The ROM is tested on $\theta_m = 323.15K$ and $\theta_b = 343.15K$.

Table (5.3) demonstrates the minimum, maximum and average $\%\epsilon_{L^2}$ error for each sampling frequency. The statistics also show that the average reconstruction error slightly improves with snapshot addition. The biggest improvement throughout the simulation is seen for the velocity field. This could be attributed to the non-linear term in the momentum equation. However, since the difference in the convergence is small, for computational saving reasons, the first sampling frequency (per 0.2s) will be used for the generation of the results.

To determine the number of retained POD modes, the cumulative energy of the eigenvalues for velocity, temperature, pressure and supremizer fields is plotted in Figure (5.6). Table (5.4) depicts the cumulative energy of the first 5 and the 10^{th} POD mode for velocity, temperature, pressure and supremizer. It is clear that the first mode captures most of the system's energy (principal mode). In order to retain approximately 99.9% of the system's energy, 5 modes for velocity, 5 for temperature and 3 for the pressure and supremizer are selected. The truncation reduces the original POD space from $N_u^s = N_p^s = N_\theta^s = N_{sup}^s = 225$ to $N_u^r = 5$, $N_\theta^r = 5$, $N_p^r = 3$ and

$N^r_{sup} = 3$. Figures (5.3),(5.4) and (5.5) show the first 4 POD modes for velocity, temperature and pressure respectively.

Table 5.3: Statistics of the relative $\epsilon_{L^2}(t)$ error for velocity, temperature and pressure fields for two sampling frequencies, per 0.2s and per 0.1s.

	$\boldsymbol{u}$ per 0.2s	p per 0.2s	θ per 0.2s	$\boldsymbol{u}$ per 0.1s	p per 0.1s	θ per 0.1s
Minimum $\epsilon_{L^2}(t)\%$	2.268	1.307	0.005	1.862	1.021	0.005
Maximum $\epsilon_{L^2}(t)\%$	9.854	11.286	3.361	9.692	9.984	3.351
Average $\epsilon_{L^2}(t)\%$	3.089	3.969	2.294	2.672	3.850	2.267

Table 5.4: Cumulative Energy of the POD modes (1-5 and 10) for velocity, temperature, pressure and supremizer.

N Modes	$\boldsymbol{u}$	θ	p	$\boldsymbol{s}$
1	0.977065	0.909840	0.999999	0.997702
2	0.992858	0.976271	0.999999	0.999957
3	0.996520	0.991552	0.999999	0.999981
4	0.997990	0.996845	1.000000	0.999999
5	0.998780	0.998688	1.000000	0.999999
10	0.999864	0.999960	1.000000	0.999999

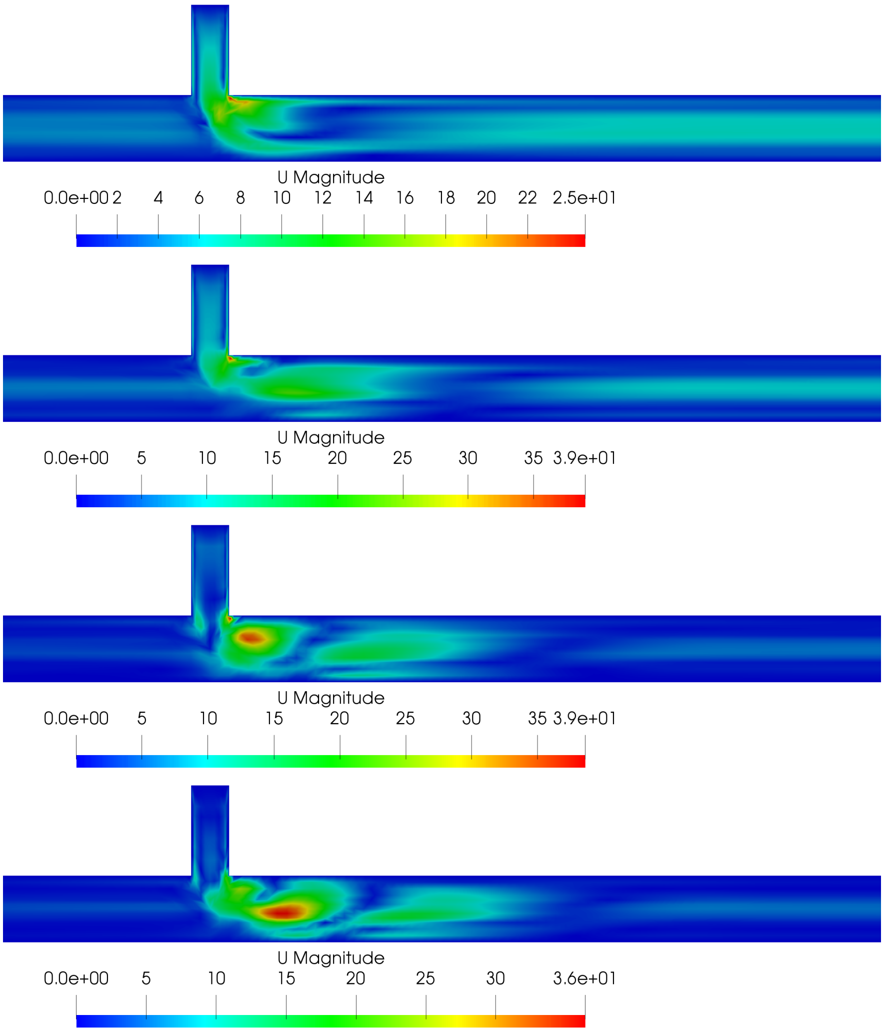

Figure 5.3: First four basis functions for velocity corresponding to testing points $\theta_m = 333.15K$and $\theta_b = 353.15K$. The figure is a vertical slice through the pipe's centreline.

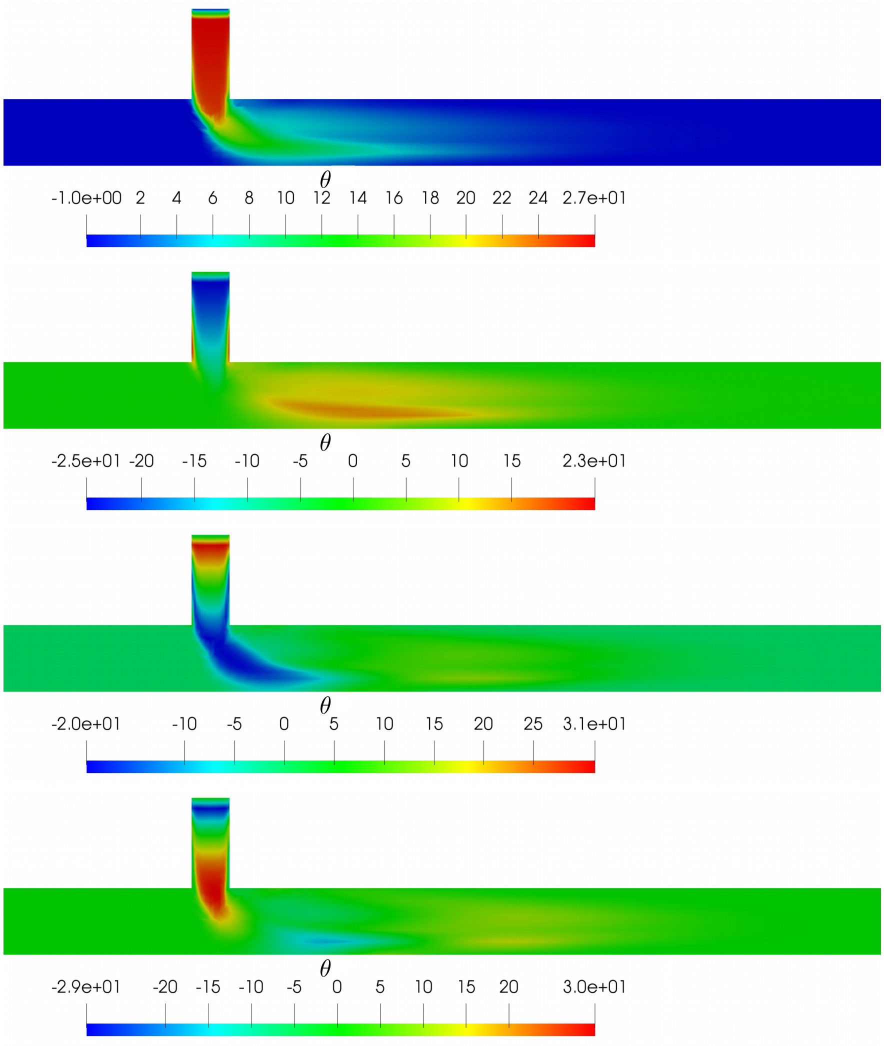

Figure 5.4: First four basis functions for temperature corresponding to testing points $\theta_m = 333.15K$ and $\theta_b = 353.15K$. The figure is a vertical slice through the pipe's centreline.

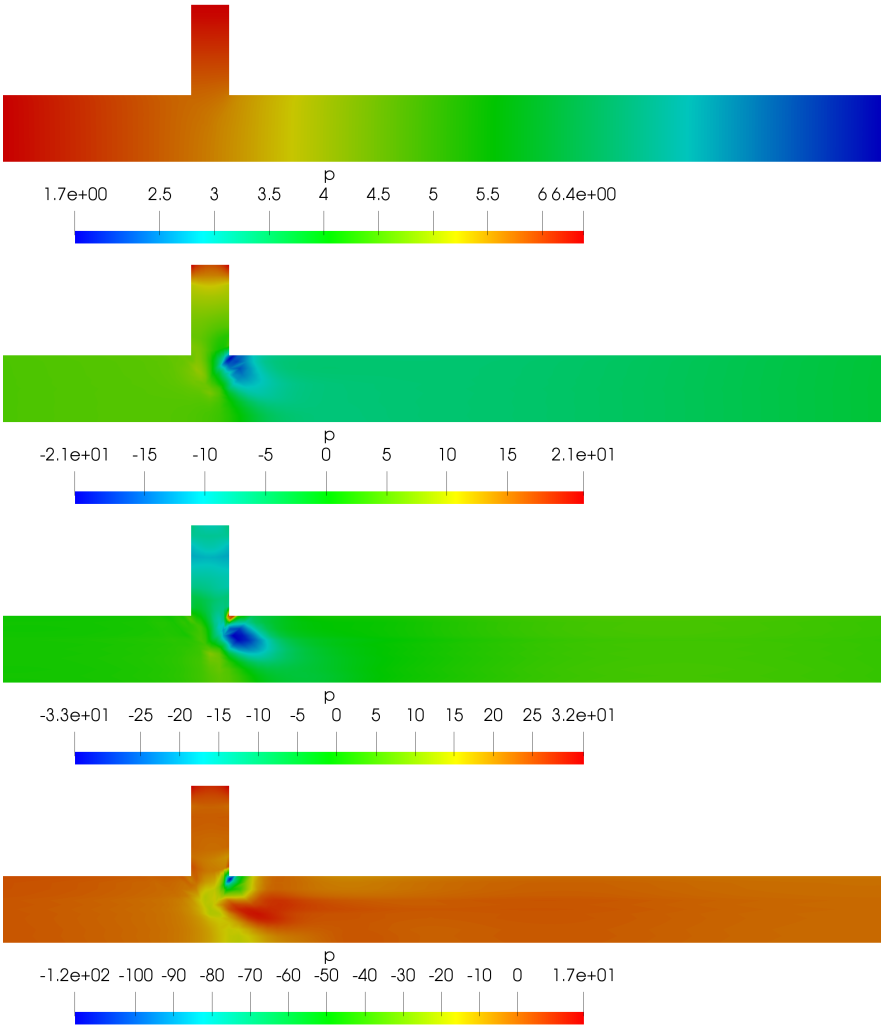

Figure 5.5: First four basis functions for pressure corresponding to testing points $\theta_m = 333.15K$ and $\theta_b = 353.15K$. The figure is a vertical slice through the pipe's centreline.

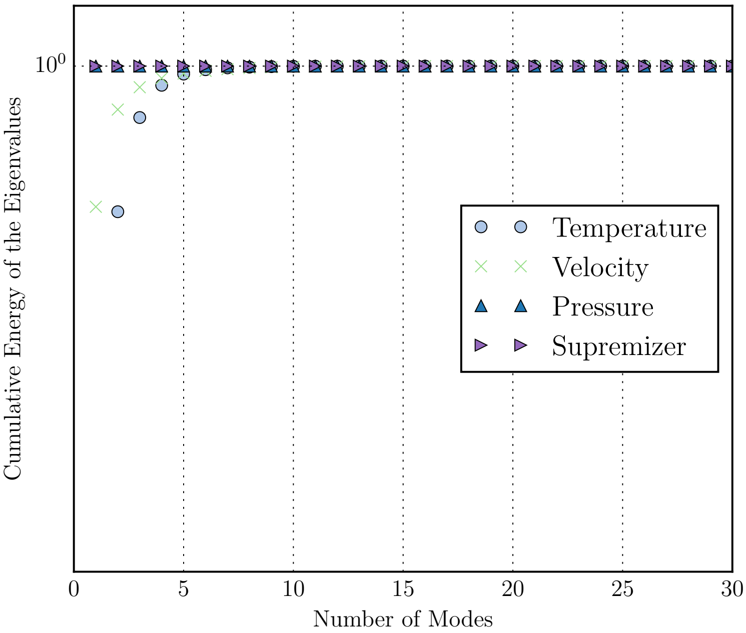

Figure 5.6: Cumulative energy of the eigenvalues for temperature, velocity, pressure and supremizer fields.

The resulting velocity, temperature and pressure fields are reconstructed with the $\%\epsilon_{L^2}$ error plotted in figure (5.7). The error seems to be larger for the velocity during the first time-steps. This could be happening because in the beggining of the simulation the flow exhibits a more transient behaviour than later, where it eventually reaches the steady-state. Sampling in a non equispaced manner and including more snapshots during the first time-steps, could reduce the error. Perhaps, to enhance the results, one could also consider using a weighted-POD method (Chen, Navon, and Fang 2011).

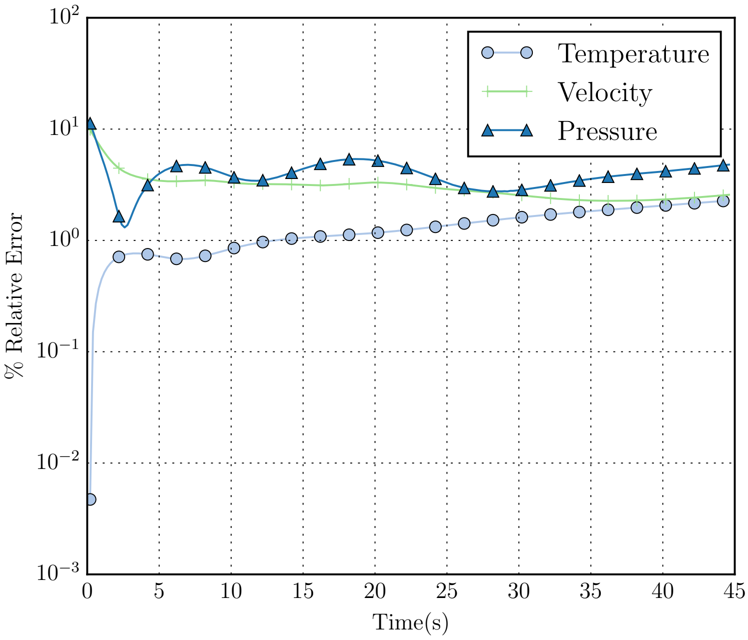

Figure 5.7: $\%\epsilon_{L^2}(t)$ error plots for temperature, velocity and pressure fields obtained on the test case for temperature inlet boundary conditions $\theta_m = 333.15K$ and $\theta_b = 353.15K$.

As in this case the temperature inlets are parametrised, the ROM, which is trained only on inlets $\theta_m = 323.15K$ and $\theta_b = 343.15$, has been tested on a set of different values of the temperature inlets. For each case, the ϵ_{L^2} error between the FOM and the ROM is plotted and shown in figure (5.8). The minimum, maximum and average relative errors are also summarized in table (5.5). The maximum ϵ_{L^2} for the reconstructed temperature field is less than 3.5% (5.5) for all cases.

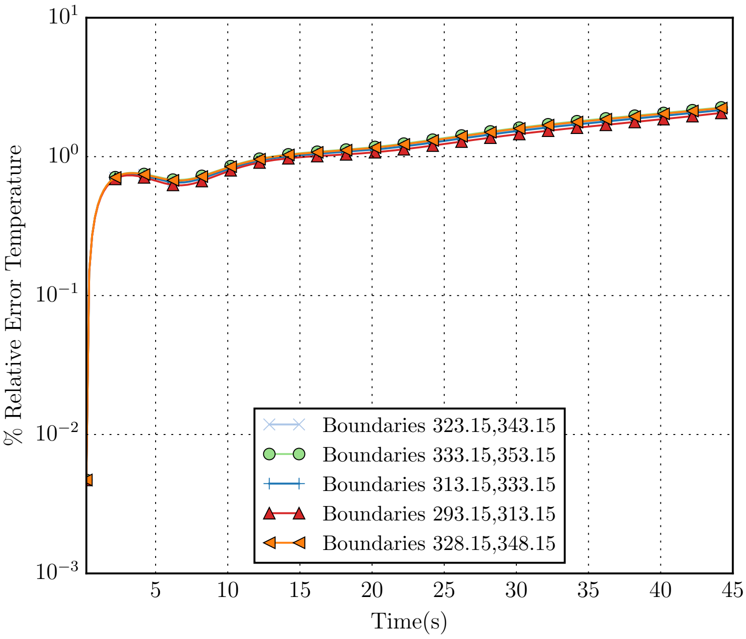

Figure 5.8: $\%\epsilon_{L^2}(t)$ error for different temperature inlet conditions.

Table 5.5: Statistics of the relative for the temperature field for five different sets of temperature inlet boundary conditions. The sets are $A : 323.15, 333.15K$, $B : 313.15, 333.15K$, $C : 333.15, 353.15K$, $D : 293.15, 313.15K$ and $E : 328.15, 348.15K$.

	A	B	C	D	E
Minimum $\epsilon_{L^2}(t)\%$	0.005	0.005	0.005	0.005	0.005
Maximum $\epsilon_{L^2}(t)\%$	3.361	3.274	3.451	3.097	3.401
Average $\epsilon_{L^2}(t)\%$	2.294	2.232	2.357	2.108	2.326

Due to the linearity of the energy equation, for different tested temperature inlet values than the trained values, the ROM can reproduce the fields with similar accuracy, as shown in figure (5.8), without having to sample and enrich the POD space with additional points. To compare the FOM and ROM results, a test for temperature inlet values of $\theta_m = 333.15K$ and $\theta_b = 353.15K$ has been performed and the results are shown in figures (5.9),(5.10) and (5.11), for velocity, temperature and pressure respectively. One could observe that the biggest error is found in the area of the branch pipe, figure (5.12). This error could be caused by the fact that the length of the branch pipe is not long enough, so the flow is not fully developed by the time it reaches the mixing region. Therefore, this region is characterized by large gradients.

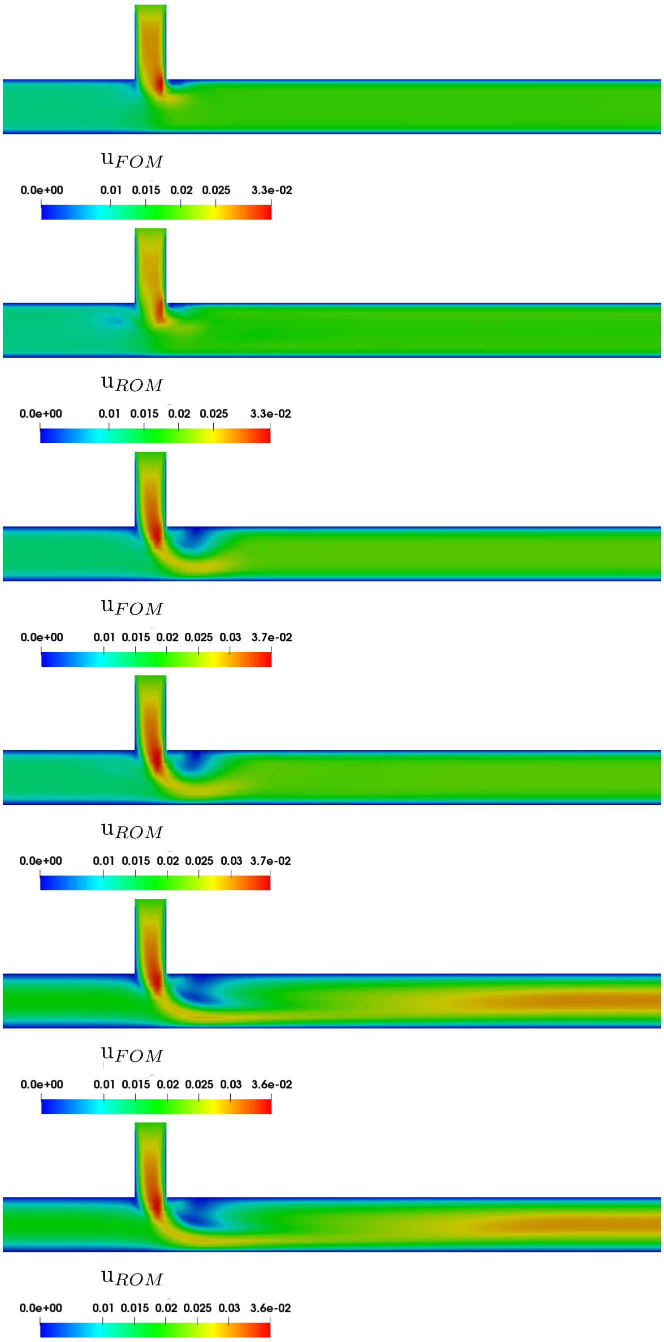

Figure 5.9: Comparison of the velocity field for the full order (odd rows) and reduced order model (even rows). The fields are depicted for time instances equal to $t = 3\text{s}, 10\text{s}$ and 45s respectively. The figure is a vertical slice through the pipe's centreline.

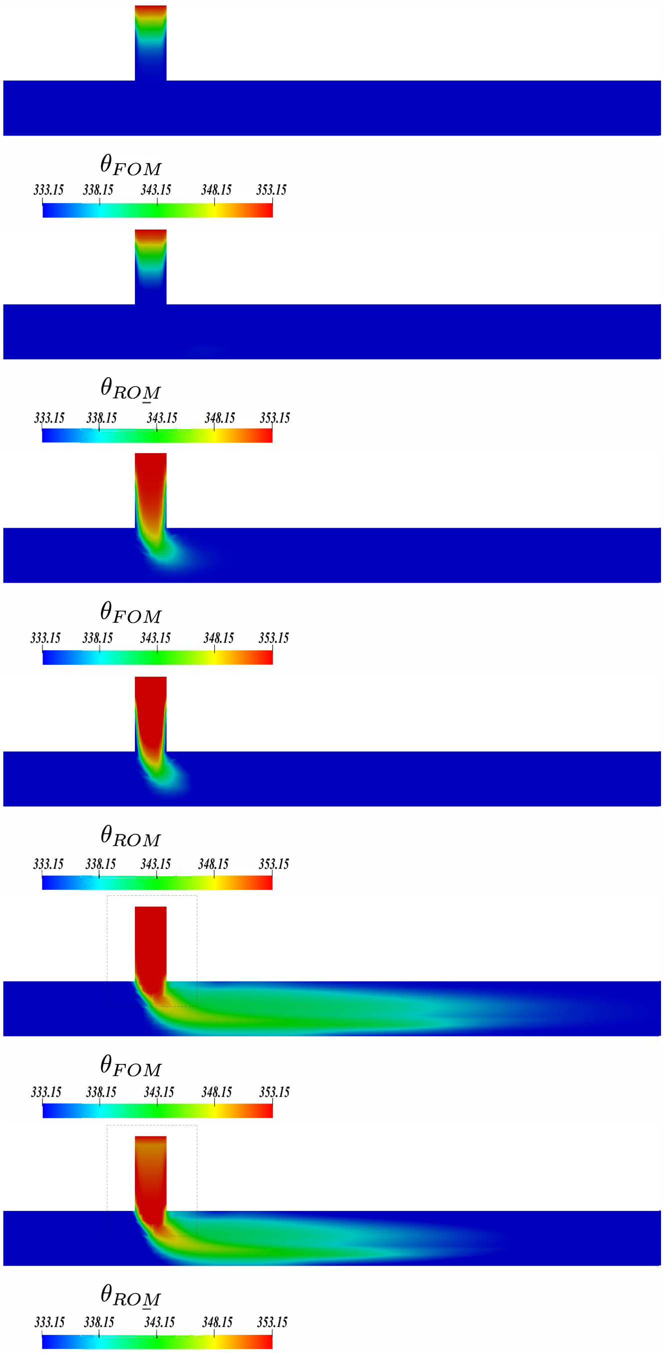

Figure 5.10: Comparison of the temperature field for the full order (odd rows) and reduced order model (even rows). The fields are depicted for time instances equal to $t = 3\text{s}, 10\text{s}$ and 45s respectively. The figure is a vertical slice through the pipe's centreline. The black square refers to the area zoomed in Figure 5.12

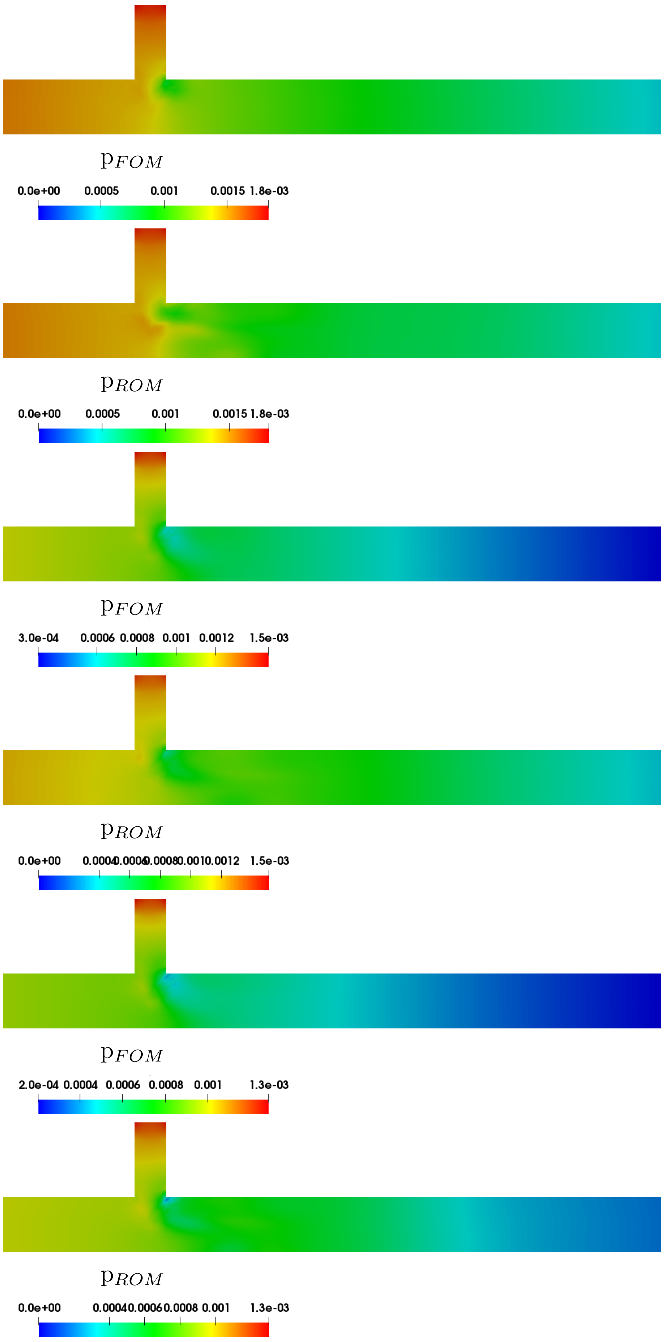

Figure 5.11: Comparison of the pressure field for the full order (odd rows) and reduced order model (even rows). The fields are depicted for time instances equal to $t = 3\text{s}, 10\text{s}$ and 45s respectively. The figure is a vertical slice through the pipe's centreline.

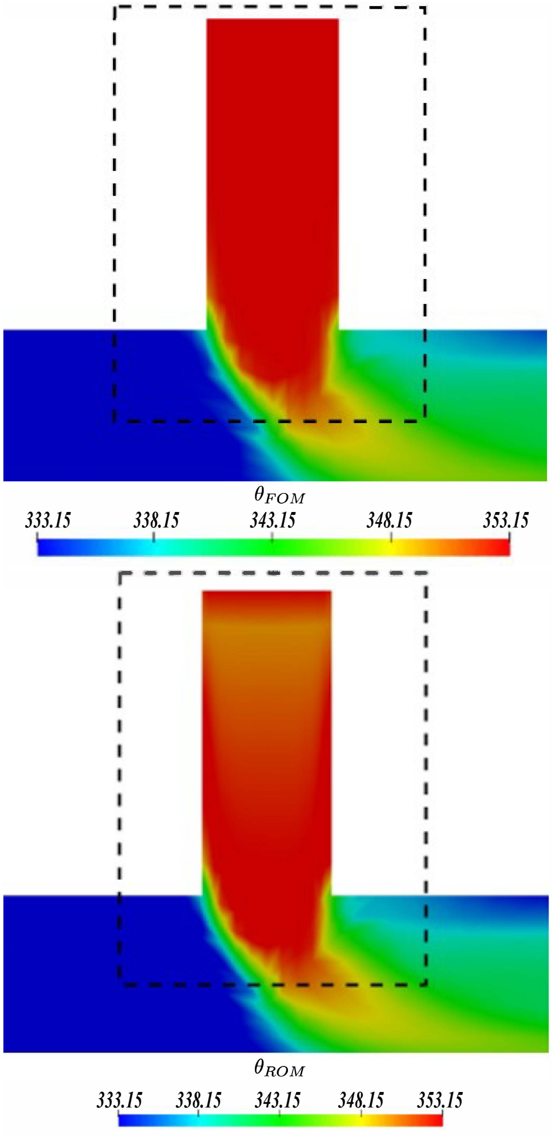

Figure 5.12: Zoom of the area with the biggest relative error between the FOM (first row) and the ROM (second row) for temperature field. The figure is a vertical slice through the pipe's centreline.

A comparison also for case D is illustrated in figure (5.13), where the ROM is tested for temperature inlets $\theta_m = 293.15K$ and $\theta_b = 313.15$K. The reduced model reproduces the main flow with a good accuracy, also for this case. The velocity and pressure fields are omitted in figure (5.13), as the change in temperature boundary conditions does not affect the velocity and the pressure fields. Thus, they remain as in figures (5.9) and (5.11). The simulations were performed on a computer with 4 cores, Intel Xeon with $3,07GHz$ processor. The CPU time of the FOM is 856.71s whereas, for the ROM, is 2.29s. This corresponds to a computational speed-up factor of ≈ 374.

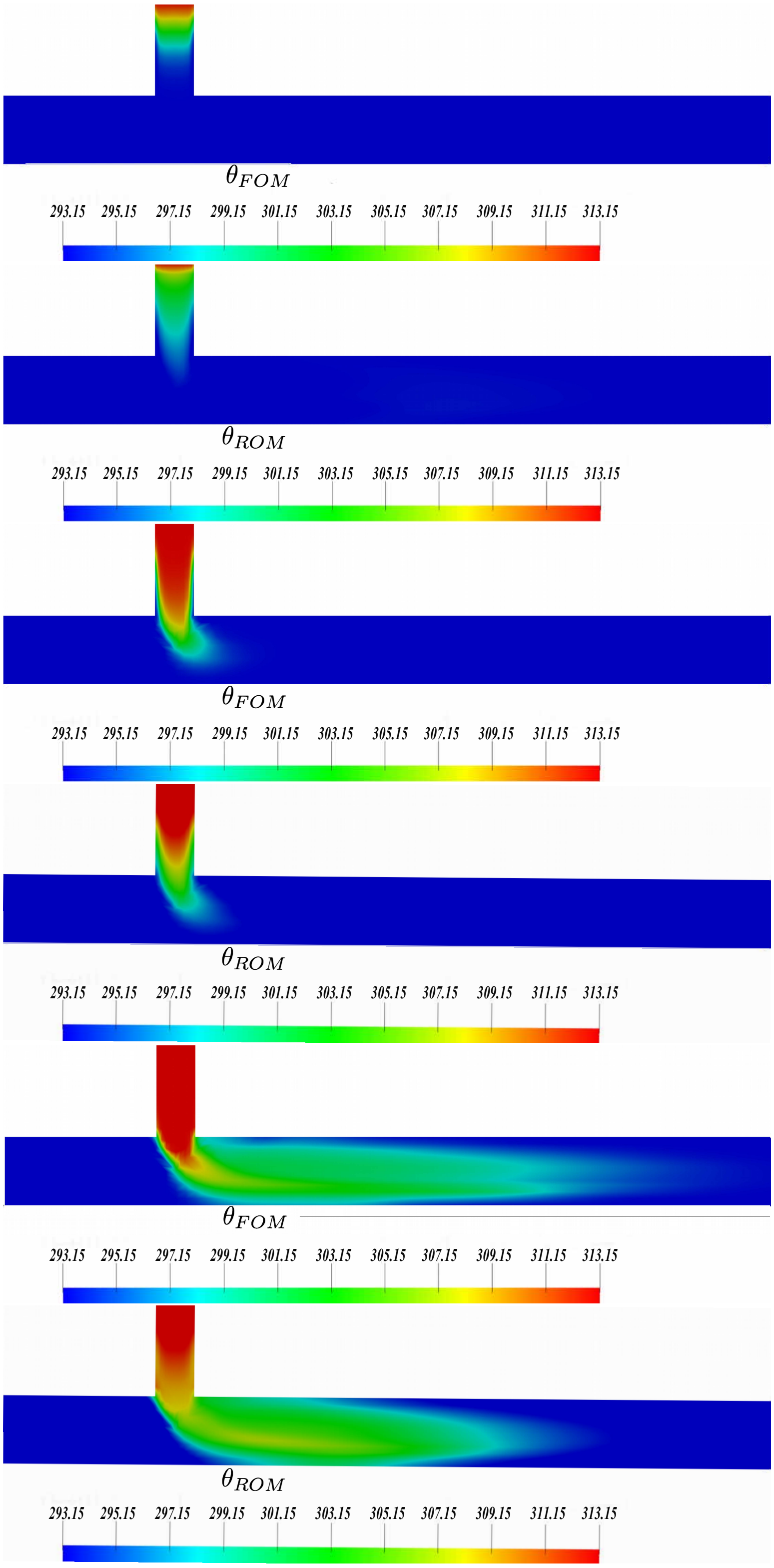

Figure 5.13: Comparison of the temperature field for the full order (odd rows) and reduced order model (even rows) for the testing case of temperature inlets $\theta_m = 293.15K$ and $\theta_b = 313.15$K. The fields are depicted for time instances equal to $t = 3$s, 10s and 45s. The figure is a vertical slice through the pipe's centreline.

5.4 Non-isothermal Mixing in T-junction - Parametrisation of the Kinematic Viscosity

The second case aims to parametrize the kinematic viscosity in the unsteady Navier-Stokes equations. Due to the non-linearity of the convective term, this case needs enrichment of the POD space with additional snapshots, which are solutions of a particular range of values of the parametrised quantity. For this purpose, the same model as described in section (5.3) is used and the POD space is enriched with additional sampling points for the parameter of interest.

Two sampling cases are considered. In the first case, 10 sampling points for the kinematic viscosity, corresponding to $\nu = [1 \times 10^{-6}, 2.55 \times 10^{-6}, 4.11 \times 10^{-6}, 5.66 \times 10^{-6}, 7.22 \times 10^{-6}, 8.77 \times 10^{-6}, 1.03 \times 10^{-5}, 1.18 \times 10^{-5}, 1.34 \times 10^{-5}, 1.5 \times 10^{-5}]$ and a second one with 5 sampling points corresponding to $\nu = [5 \times 10^{-6}, 7.5 \times 10^{-6}, 1 \times 10^{-5}, 1.25 \times 10^{-5}, 1.5 \times 10^{-5}]$. A convergence comparison between the two sampling spaces and the FOM is provided in figure (5.14) where one could observe that the differences between the two spaces are minimal. Therefore, for computational efficiency reasons, the test case will be performed on the space with the 5 sampling points. These sampling values correspond to Reynolds numbers $\mathrm{Re_m} = [280, 187, 140, 112, 93]$ for the main pipe and $\mathrm{Re_b} = [320, 213, 160, 128, 107]$ for the branch. Thus, the flow remains laminar in the total pipe length.

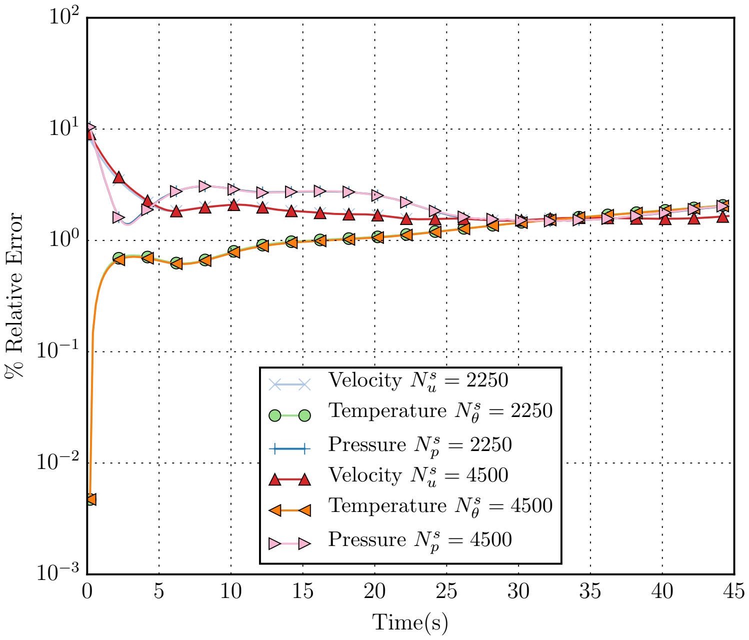

Figure 5.14: $\%\epsilon_{L^2}(t)$ error for two sampling spaces for the parameter (kinematic viscosity). These correspond to one with 5 sampling points for viscosity, where $N_u^s = N_\theta^s = N_p^s = 2250$ and one with 10 sampling points where, $N_u^s = N_\theta^s = N_p^s = 4500$s. The ROM is simulated for $\nu = 1.1 \times 10^{-5}$.

The FOM simulation is performed for each value of the kinematic viscosity in the above range, for 45s with time-step of $dt = 5 \times 10^{-3}$s. Snapshots are collected using the enhanced temporal sampling frequency according to the convergence study from the test case 1, figure (5.2). Therefore the snapshots are acquired every 0.1s, using an equispace grid method in time and parameter, which gives a total number of 2250 snapshots (450/case). A new value of the kinematic viscosity in which the ROM has not been trained but which belongs to the range of the training space, $\nu = 1.1 \times 10^{-5}$ ($\mathrm{Re_m}$=127, $\mathrm{Re_b} = 160$), is used to evaluate the capabilities of the parametrised ROM.

To retain around 99.9% of the system's energy, as shown in table (5.6) and figure (5.15), 10 modes for velocity, 5 for temperature, 2 for pressure and 3 for the supremizer are kept. The $\%\epsilon_{L^2}$ error between the FOM and ROM is plotted in figure (5.14), which indicates that the ROM is capable of reproducing the main characteristics of the flow. Error statistics are summarized in table (5.7). A comparison between the flow of the FOM and ROM models is illustrated in figures (5.16), (5.17) and (5.18), which indicates that the ROM is performing well in the reconstruction of the velocity, temperature and pressure fields.

Table 5.6: Cumulative Energy of the POD modes (1-5 and 10) for velocity, temperature, pressure and supremizer.

N Modes	$\boldsymbol{u}$	θ	p	$\boldsymbol{s}$
1	0.980889	0.908891	0.999999	0.997682
2	0.993338	0.976040	0.999999	0.999946
3	0.997342	0.991480	0.999999	0.999998
4	0.997521	0.996881	1.000000	0.999999
5	0.998132	0.998692	1.000000	0.999999
10	0.999964	0.999917	1.000000	0.999999

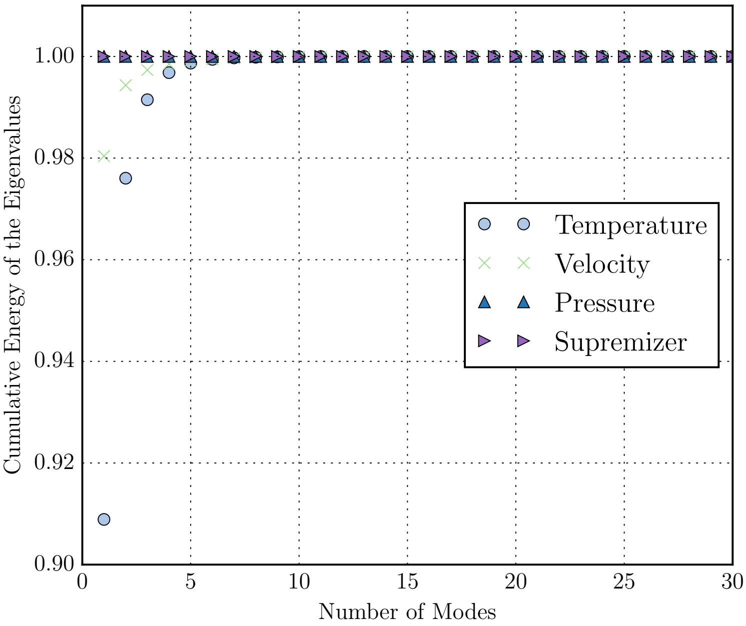

Figure 5.15: Cumulative energy of the eigenvalues for temperature, velocity, pressure and supremizer fields respectively.

Concerning the temperature field, the area of the branch pipe, where the biggest differences were found, has been improved, figure (5.19), compared to the first test case (5.12). The improved results could be a consequence of the enhanced sampling space, which used in this test case. The error on temperature is growing as the time progresses and the two different temperature fluids start to mix in the mixing region. Taking more snapshots during the mixing period could reduce the error. In addition, to enhance the accuracy of the results, one could perform a denser sampling of the parameter space, as discussed earlier, but this increases the overall time of the offline phase and, for laminar cases, like this one, the overall improvement would be minimal.

However, for more complicated cases, such as those in the turbulent range or in the transition range, enriching the POD space with additional sampling points of the kinematic viscosity would be essential. The CPU time of the FOM model is 969.23s and the one of the ROM is 4.23s. This corresponds to a speed-up of ≈ 211.

Table 5.7: Relative $\epsilon_{L^2}(t)\%$ error for velocity, temperature and pressure fields.

	$\boldsymbol{u}$ per 0.1s	θ per 0.1s	p per 0.1s
Minimum $\epsilon_{L^2}(t)\%$	1.502	0.005	1.399
Maximum $\epsilon_{L^2}(t)\%$	8.089	3.098	10.483
Average $\epsilon_{L^2}(t)\%$	1.916	2.120	2.2311

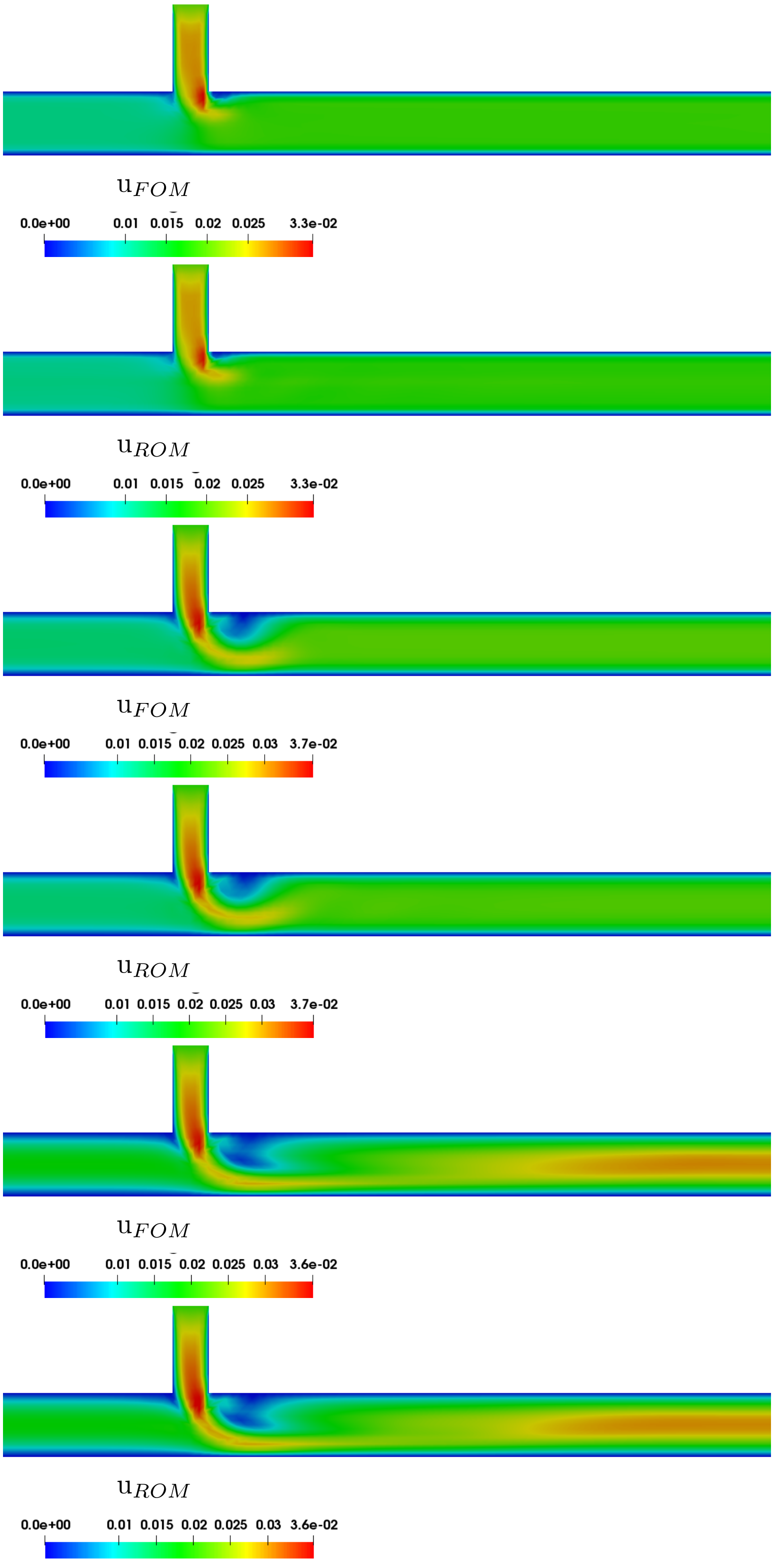

Figure 5.16: Comparison of the velocity field for the full order (odd rows) and reduced order model (even rows). The fields are depicted for time instances equal to $t = 3\text{s}, 10\text{s}$ and 45s. The viscosity is set to $\nu = 1.1 \times 10^{-5}$. The figure is a vertical slice through the pipe's centreline.

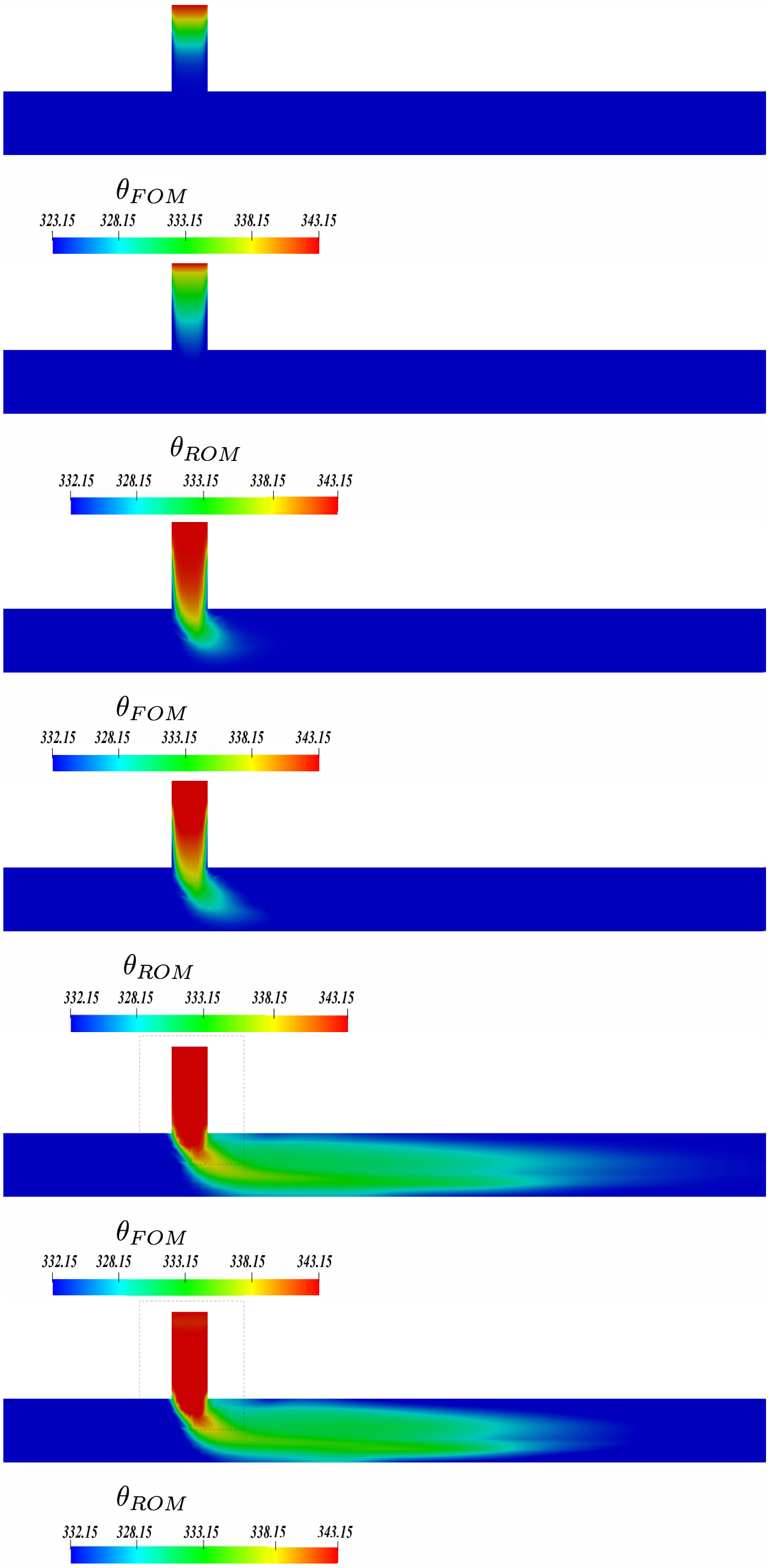

Figure 5.17: Comparison of the temperature field for the full order (odd rows) and reduced order model (even rows). The fields are depicted for time instances equal to $t = 3\text{s}, 10\text{s}$ and 45s. The viscosity is set to $\nu = 1.1 \times 10^{-5}$. The figure is a vertical slice through the pipe's centreline.

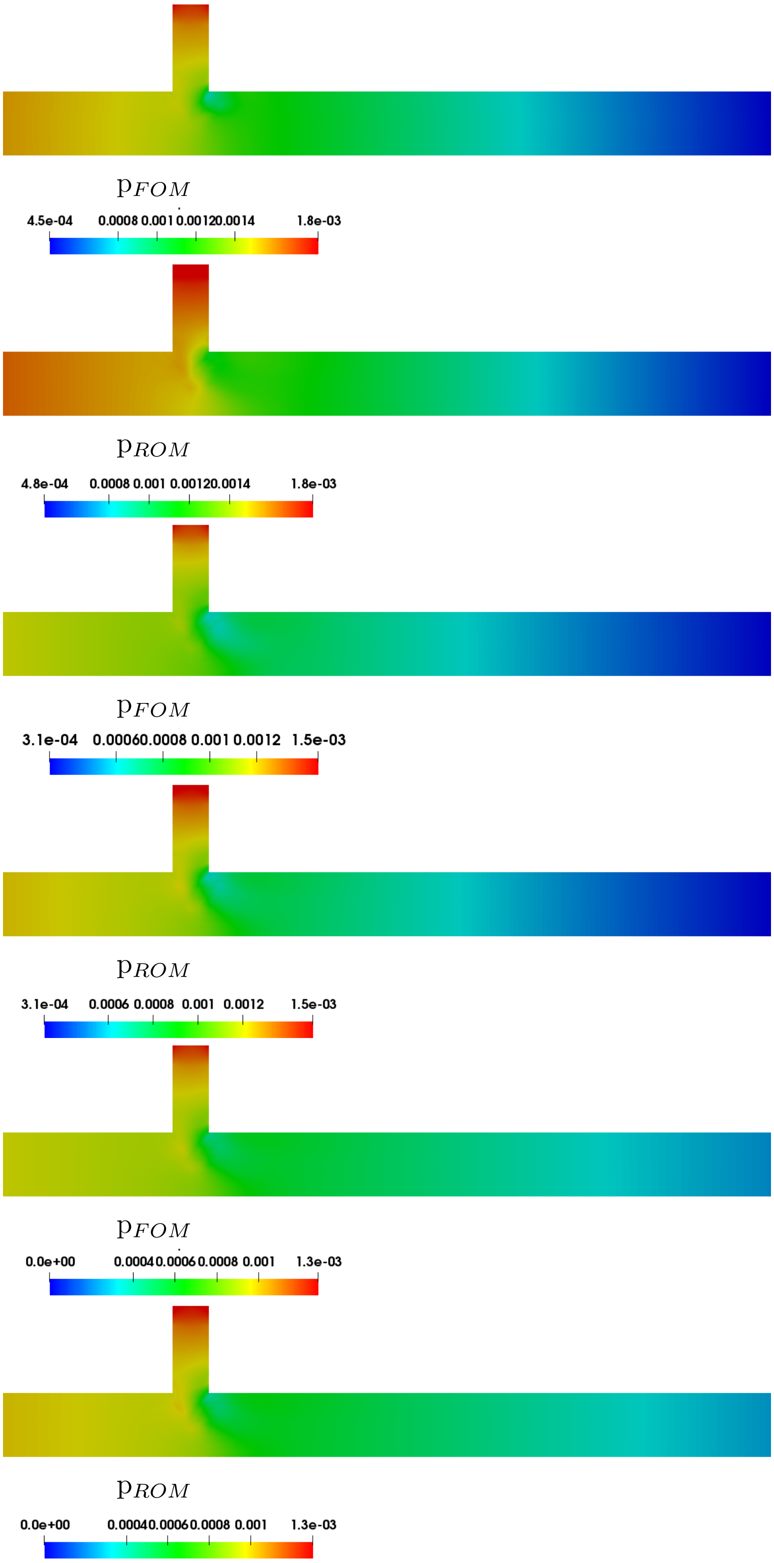

Figure 5.18: Comparison of the pressure field for the full order (odd rows) and reduced order model (even rows). The fields are depicted for time instances equal to $t = 3\text{s}, 10\text{s}$ and 45s. The viscosity is set to $\nu = 1.1 \times 10^{-5}$. The figure is a vertical slice through the pipe's centreline.

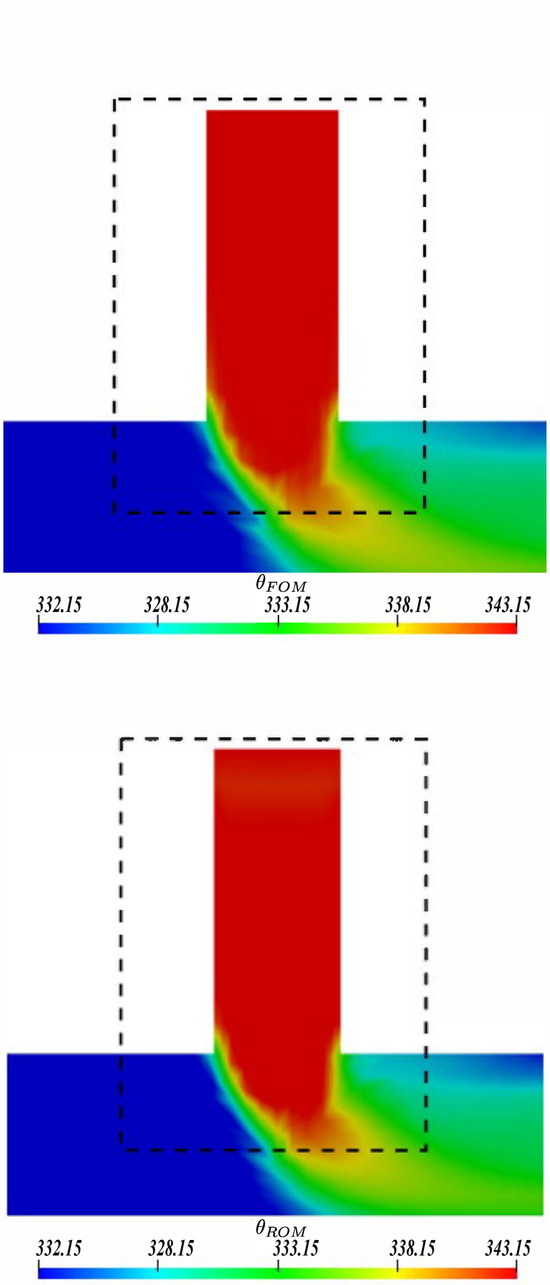

Figure 5.19: Zoom of the area with the biggest relative error between the FOM (left) and the ROM (right) for temperature field, $\nu = 1.1 \times 10^{-5}$. The figure is a vertical slice through the pipe's centreline.

5.5 Summary of the Chapter

In this chapter a parametrised ROM using POD-Galerkin method is presented for applications in the study of thermal mixing in pipes. Apart from the 3D incompressible Navier-Stokes equations, a third transport equation corresponding to energy has also been considered. The energy equation contains both convective and diffusive terms. The interest is on the reconstruction of velocity, pressure and temperature fields. The proposed ROM has been validated on a case of thermal mixing in a T-junction pipe, a common set-up found in nuclear power reactor cooling systems. Two different parametric cases have been considered, one where the parametrisation is on the temperature inlets and one where the parametrisation is on the kinematic viscosity. In both cases, the ROM is capable of reproducing the results when tested under the same boundary and initial conditions as in the FOM model, as well as, to predict the fields on different parameters, given a suitable training. In both cases a considerable computational speed up has been achieved, corresponding to a factor of approximately 374 and 211 respectively.

Chapter 6

Model Order Reduction for Turbulent Heat Transfer

In this chapter, the 3D parametric transient Navier-Stokes equations, coupled with the energy equation (one-way coupling) are considered. In particular, the method presented in this work is applied to the modelling of turbulent thermal mixing in a T-junction pipe. This configuration is commonly found in nuclear power reactor cooling systems and plays a crucial role in the safety of reactors. The mixing of two different temperature streams leads to high transient temperature fluctuations in the pipe wall regions, which can potentially lead to thermal fatigue and subsequent failure of the piping material (cracks formation, breakage etc). Turbulent thermal mixing has been studied both experimentally and computationally in (Ayhan and Sokmen 2012; Frank, Lifante, Prasser, and Menter 2010; Kuczaj, Komen, and Loginov 2010; Naik-Nimbalkar, Patwardhan, Banerjee, Padmakumar, and Vaidyanathan 2010; Tunstall, Laurence, Prosser, and Skillen 2016b; Walker, Simiano, Zboray, and Prasser 2009).

In the computational case, various turbulent modelling techniques have been studied, including Large Eddy Simulation (LES) and Unsteady Reynolds Averaged Navier-Stokes (URANS). These methods, given the high Reynolds numbers and the nature of the problem, require fine 3D meshes, which lead to very high CPU and memory costs. A ROM could therefore play a key role in such studies, giving the ability to obtain fast and realiable simulations. Model order reduction for nuclear applications has been previously applied in (Sartori, Cammi, Luzzi, and Rozza 2016c) for modelling the movement of the control rods in a nuclear reactor and in (Buchan, Pain, Fang, and Navon 2013b) for reactor critically problems.

This work extends the previous work of (Georgaka, Stabile, Rozza, and Bluck 2019) from laminar to turbulent heat transfer case. To the author's knowledge, a ROM for modelling the parametric 3D Navier-Stokes equations, coupled with the energy equation (one-way coupling), including turbulence modelling is presented here for the first time. The reduced basis is computed with two different approaches: a standard POD and a nested POD method. It is known that, in the turbulent case, the POD-Galerkin method suffers stability issues due to the trancation of the less energetic but highly dissipative modes. Several solutions have been proposed, including closure methods (Wang, Akhtar, Borggaard, and Iliescu 2012) or artificial viscosity methods (Borggaard, Iliescu, and Wang 2011).

In this work, the ROM is stabilised with the incorporation of the eddy viscosity term in the ROM momentum equation. For this, an approach similar to the one developed in (Hijazi, Ali, Stabile, Ballarin, and Rozza 2018; Hijazi, Stabile, Mola, and Rozza 2019) is followed. This approach is data-driven and based on the use of PODI with Radial Basis Function (RBF) interpolation for the calculation of the temporal coefficients of the eddy viscosity field. The POD-RBF method has been previously applied in the model order reduction context in (Dehghan and Abbaszadeh 2016) as a non-intrusive model order reduction method as well as in (Xiao, Fang, Pain, Navon, Salinas, and Muggeridge 2015) for multiphase flow in porous media. In (Ostrowski, Bialecki, and Kassab 2008), a POD-RBF network for inverse heat conduction problems is presented.

The content of this chapter has been submitted in:

GEORGAKA, S., STABILE, G., STAR, K., ROZZA, G., and BLUCK, M.J. A Hybrid Reduced Order Method for Modelling Turbulent Heat Transfer Problems. Computers and Fluids, 2019

6.1 Mathematical Framework for the Full Order Model

In this section, the mathematical formulation of the FOM is presented which is described by the 3D, incompressible, transient, parametric Navier-Stokes equations one-way coupled with the 3D transient, parametric energy equation. Considering a Eulerian framework and domain $\mathcal{Q} = \Omega \times [0, T_s] \subset \mathbb{R}^d \times \mathbb{R}^+$ with $d = 2, 3$, the FOM equations are formulated as follow:

$$\begin{cases} \frac{\partial \boldsymbol{u}(\boldsymbol{x},\boldsymbol{\mu},t)}{\partial t} + \boldsymbol{\nabla} \cdot (\boldsymbol{u}(\boldsymbol{x},\boldsymbol{\mu},t) \otimes \boldsymbol{u}(\boldsymbol{x},\boldsymbol{\mu},t)) = & \\ = \nabla \cdot \big[(\nu + \nu_t) \cdot \frac{1}{2}\big(\nabla \boldsymbol{u}(\boldsymbol{x},\boldsymbol{\mu},t) + & \\ +(\nabla \boldsymbol{u}^T(\boldsymbol{x},\boldsymbol{\mu},t))\big) - p(\boldsymbol{x},\boldsymbol{\mu},t)\boldsymbol{I}\big], & \\ \boldsymbol{\nabla} \cdot \boldsymbol{u}(\boldsymbol{x},\boldsymbol{\mu},t) = \boldsymbol{0} & \text{in } \mathcal{Q}, \\ \frac{\partial \theta(\boldsymbol{x},\boldsymbol{\mu},t)}{\partial t} + \nabla \cdot (\boldsymbol{u}(\boldsymbol{x},\boldsymbol{\mu},t)\theta(\boldsymbol{x},\boldsymbol{\mu},t)) - & \\ -\alpha_{dif} \Delta \theta(\boldsymbol{x},\boldsymbol{\mu},t) = 0 & \text{in } \mathcal{Q}, \\ \boldsymbol{u}(\boldsymbol{x},\boldsymbol{\mu},t) = \boldsymbol{f}(\boldsymbol{x},\boldsymbol{\mu}) & \text{on } B_{In}, \\ \theta(\boldsymbol{x},\boldsymbol{\mu},t) = g(\boldsymbol{x}) & \text{on } B_{In}, \\ \nabla \theta \cdot \boldsymbol{n} = 0 & \text{on } B_w, \\ \boldsymbol{u}(\boldsymbol{x},\boldsymbol{\mu},t) = \boldsymbol{0} & \text{on } B_w, \\ (\nu \nabla \boldsymbol{u} - p\boldsymbol{I})\boldsymbol{n} = \boldsymbol{0} & \text{on } B_o. \end{cases} \tag{6.1.1}$$

The vector of parameters is represented by the greek letter $\boldsymbol{\mu}$. $B_{In} = \Gamma_{In} \times [0, T_s]$, $B_w = \Gamma_w \times [0, T_s]$ and $B_o = \Gamma_o \times [0, T_s]$, T_s represents the time-period of the simulation, $\Gamma = \Gamma_{In} \cup \Gamma_w \cup \Gamma_o$ is the boundary of $\mathcal{Q}$ and consists of three different parts Γ_{In}, Γ_o and Γ_w that indicate, respectively, inlet(s), outlet and physical wall boundaries (6.1. The functions $\boldsymbol{f}(\boldsymbol{x},\boldsymbol{\mu})$ and $g(\boldsymbol{x})$ represent Dirichlet boundary conditions for the non-homogeneous boundaries. Time independence of the boundary conditions $\boldsymbol{f}$ and g is also assumed. Since we are dealing with the incompressible equations, the density ρ has been omitted and is assumed to have the value of 1. In this work, the parametric dependency is on the velocity inlet boundary conditions.

6.2 Reduced Order Model Formulation

For the calculation of the temporal coefficients, a Galerkin approach is followed for the velocity, pressure and temperature fields, where the original equations are projected onto the reduced basis. The momentum equation is projected onto the spatial POD basis, $\boldsymbol{\phi}(\boldsymbol{x})$, while the continuity equation is projected onto the pressure spatial basis, $\psi(\boldsymbol{x})$, using the supremizer method (4.5.3). The energy equation is projected onto the temperature spatial basis, $\chi(\boldsymbol{x})$. The projection results in a set of ordinary differential equations for the evolution of the temporal coefficients for velocity, pressure and temperature fields:

$$\boldsymbol{M}\dot{\boldsymbol{\alpha}} + (\boldsymbol{B} + \boldsymbol{B}_T)\boldsymbol{\alpha} - \boldsymbol{\alpha}^T\boldsymbol{Q}\boldsymbol{\alpha} + \boldsymbol{l}^T\big(\boldsymbol{Q}_{T1} + \boldsymbol{Q}_{T2}\big)\boldsymbol{\alpha} - \boldsymbol{P}\boldsymbol{b} = 0, \tag{6.2.1}$$

$$\boldsymbol{R}\boldsymbol{\alpha} = 0, \tag{6.2.2}$$

$$\boldsymbol{K}\dot{\boldsymbol{c}} - \boldsymbol{\alpha}^T\boldsymbol{G}\boldsymbol{c} - \alpha_{dif_t}\boldsymbol{N}\boldsymbol{c} = 0, \tag{6.2.3}$$

where the dotted terms $\dot{\boldsymbol{\alpha}}$ and $\dot{\boldsymbol{c}}$ represent time derivatives and the reduced matrices are:

$$(\boldsymbol{M})_{ij} = \langle \boldsymbol{\phi}_i, \boldsymbol{\phi}_j \rangle_{L_2(\Omega)}, \tag{6.2.4}$$

$$(\boldsymbol{B})_{ij} = \langle \Delta\boldsymbol{\phi}_i, \boldsymbol{\phi}_j \rangle_{L_2(\Omega)} \tag{6.2.5}$$

$$(\boldsymbol{B}_T)_{ij} = \langle \nabla \cdot (\nabla(\boldsymbol{\phi}_i^T), \boldsymbol{\phi}_j \rangle_{L_2(\Omega)} \tag{6.2.6}$$

$$(\boldsymbol{Q})_{ijk} = \langle \nabla \cdot (\boldsymbol{\phi}_i \otimes \boldsymbol{\phi}_j), \boldsymbol{\phi}_k \rangle_{L_2(\Omega)}, \tag{6.2.7}$$

$$(\boldsymbol{Q})_{T1_{ijk}} \langle \xi_i \Delta\boldsymbol{\phi}_j, \boldsymbol{\phi}_k \rangle_{L_2(\Omega)}, \tag{6.2.8}$$

$$(\boldsymbol{Q})_{T2_{ijk}} \langle \nabla \cdot \xi_i(\nabla\boldsymbol{\phi}_j^T), \boldsymbol{\phi}_k \rangle_{L_2(\Omega)}, \tag{6.2.9}$$

$$(\boldsymbol{P})_{ij} = \langle \nabla\psi_i, \boldsymbol{\phi}_j \rangle_{L_2(\Omega)}, \tag{6.2.10}$$

$$(\boldsymbol{R})_{ij} = \langle \nabla \cdot \boldsymbol{\phi}_i, \psi_j \rangle_{L_2(\Omega)}, \tag{6.2.11}$$

$$(\boldsymbol{K})_{ij} = \langle \chi_i, \chi_j \rangle_{L_2(\Omega)}, \tag{6.2.12}$$

$$(\boldsymbol{G})_{ijk} = \langle \nabla \cdot (\boldsymbol{\phi}_i \chi_j), \chi_k \rangle_{L_2(\Omega)}, \tag{6.2.13}$$

$$(\boldsymbol{N})_{ij} = \langle \Delta\chi_i, \chi_j \rangle_{L_2(\Omega)}. \tag{6.2.14}$$

Considering the eddy viscosity field, the vector of temporal coefficients, $\boldsymbol{l}(t)$, is computed using the non-intrusive method of Radial Basis Function (RBF) interpolation.

In this way, since there is no projection of the eddy viscosity modes onto the turbulence modelling equations, the ROM is independent of the turbulent method used in the FOM.

The temporal coefficients, $l(\boldsymbol{\mu}, t)$, for a new value of the parameter, are calculated during the online stage as a linear combination of $N^s_{\nu_t}$ $(j = 1, 2, \ldots, N^s_{\nu_t})$ chosen radial basis functions kernels $\boldsymbol{\Theta}$:

$$l_i(\boldsymbol{\mu}, t) = \sum_{j=1}^{N^s_{\nu_t}} w_{i,j} \Theta_{i,j}(||\boldsymbol{\mu} - \boldsymbol{\mu}_j||_{L2}), \text{ for } i = 1, 2, \ldots, N_t, \tag{6.2.15}$$

where, $\boldsymbol{w}$ represents the vector of the linear weights, $\boldsymbol{\mu}$ are the sampling points (centers) corresponding to eddy viscosity snapshots ν_t and $\boldsymbol{\mu}$ is the value of the new input parameter, which does not coincide with any of the training points. For the RBFs, various kernels, $\boldsymbol{\Theta}$, can be used. In this work, Gaussian kernels are considered, defined as follows:

$$\boldsymbol{\Theta}(||\boldsymbol{\mu} - \boldsymbol{\mu}_j||_{L2}) = exp(-\gamma ||\boldsymbol{\mu} - \boldsymbol{\mu}_j||^2_{L2}), \tag{6.2.16}$$

where γ is a parameter, which determines the spread of the kernel. The RBF monotonically decreases as we move away from the centre. Gaussian RBFs response is local, meaning that their response is the best in the area near to the centre, in contrast to multiquadratic RBFs, which are global. The unknowns are computed in the offline stage.

The vector of the weights is calculated by solving the following linear system:

$$\sum_{j=1}^{N^s_{\nu_t}} w_{i,j} \Theta_{i,j}(||\boldsymbol{\mu}_k - \boldsymbol{\mu}_j||_{L2}) = l(\boldsymbol{\mu}, t)_{i,k}, \text{ for } k = 1, 2, \ldots, N_t. \tag{6.2.17}$$

The above equation can be written in matrix form and solved for the unknown weights as:

$$\boldsymbol{\Theta} \boldsymbol{w} = \boldsymbol{l} \Leftrightarrow \boldsymbol{w} = \boldsymbol{\Theta}^{-1} \boldsymbol{l}, \tag{6.2.18}$$

provided that the matrix $\boldsymbol{\Theta}$ is non-singular, therefore invertible and the temporal coefficients, $l(\boldsymbol{\mu}, t)_{i,j}$, are calculated by projecting the eddy viscosity snapshots onto the spatial eddy viscosity modes, for each timestep, as:

$$l_{i,j}(\boldsymbol{\mu}, t) = \langle \xi_i, \nu_{t_j} \rangle_{L_2(\Omega)}, \text{ for } j = 1, 2, \ldots, N^s_{\nu_t}. \tag{6.2.19}$$

Once the unknown weights are calculated in the offline phase, the system of equations (6.2.1), is ready to be solved.

6.3 Applications

The mathematical framework described in the previous sections is tested on a 3D T-junction pipe, where different temperature water streams are mixing in the tee area at high Reynolds numbers. The boundary of the domain Ω, denoted with Γ, consists of four parts $\Gamma = \Gamma_m \cup \Gamma_b \cup \Gamma_w \cup \Gamma_o$ as shown in figure 6.1. The geometrical properties of the pipe are shown in table 6.1 while the total length of the pipe is $L = 3.0$m. In section 6.4 the ROM is trained on ten different sets of inlet velocity values (table 6.2) and then is tested on four sets of values within the range of the training space (table 6.3). Then, in section 6.5, the set D is selected and a comparative study between standard and nested POD methods is performed.

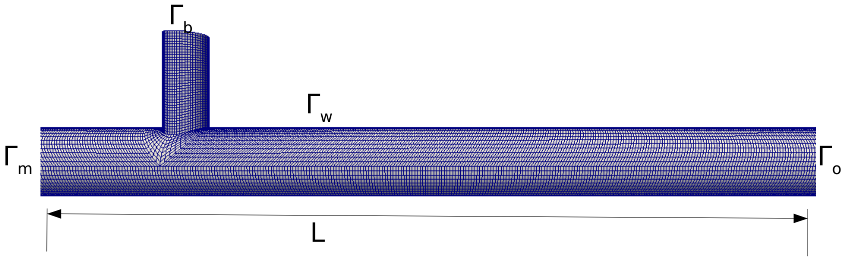

Figure 6.1: Computational mesh of the T-junction pipe.

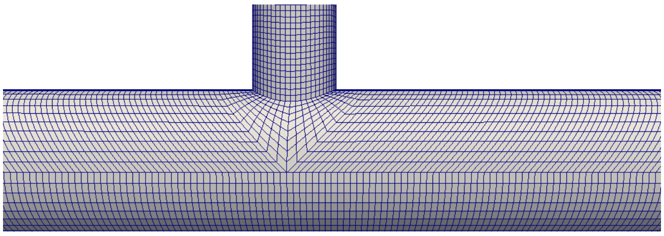

Figure 6.2: Mesh in T-junction region.

	Main Pipe	Branch Pipe
u (ms^{-1})	values in table (6.3)	values in table (6.3)
θ (K)	292.15	309.5
D (m)	0.14	0.08
Re	values in table (6.3)	values in table (6.3)

Table 6.1: Summary of the physical parameters for the reduced order model.

6.4 Numerical Study: Thermal mixing in T-junction pipe

A parametric turbulent case is studied, where the velocity inlet boundary conditions on both inlets are parametrised. This test case has been chosen as the parametric response is non-linear and a training is needed. The training space is constructed using ten sets of sampling points for the two velocity inlets, as shown in table (6.2). The reduced order model is evaluated on four sets of values (table (6.3)), which belong to the training range but they do not coincide with the samples used to train the ROM. It is known from the literature, (Feng, Frahi, and Baglietto 2018; Frank, Lifante, Prasser, and Menter 2010; Tunstall, Laurence, Prosser, and Skillen 2016a) that the modelling of turbulent non isothermal mixing in T-junctions appears to be a challenging test case and the LES method is usually required for the simulation of the transient velocity and temperature fields. However, since the intention of this work is to compare two different numerical approaches, the FOM simulation performed in OpenFOAM and the ROM simulation performed in ITHACA-FV C++ library, the URANS k-ω SST turbulence model has been considered for CPU and memory saving reasons. As the hybrid PODI-Galerkin method is non-intrusive with respect to the eddy viscosity field, any type of RANS turbulence modelling could be in principle used for the construction of the ROM.

$\boldsymbol{U_m}$ (ms^{-1})	$\boldsymbol{U_b}$ (ms^{-1})
(0.535,0,0)	(0,0,-0.715)
(0.545,0,0)	(0,0,-0.725)
(0.555,0,0)	(0,0,-0.735)
(0.565,0,0)	(0,0,-0.745)
(0.575,0,0)	(0,0,-0.755)
(0.585,0,0)	(0,0,-0.765)
(0.595,0,0)	(0,0,-0.775)
(0.605,0,0)	(0,0,-0.785)
(0.615,0,0)	(0,0,-0.795)
(0.625,0,0)	(0,0,-0.805)

Table 6.2: Sampling points for the parameters.

set	$\boldsymbol{U_m}$ (ms^{-1})	$\boldsymbol{U_b}$ (ms^{-1})	Re_m	Re_b
A	(0.550,0,0)	(0,0,-0.730)	77000	58400
B	(0.570,0,0)	(0,0,-0.750)	79800	60000
C	(0.580,0,0)	(0,0,-0.760)	81200	60800
D	(0.590,0,0)	(0,0,-0.770)	82600	61600

Table 6.3: Testing points for the parameters.

In the offline phase, the FOM is modelled using the transient *pisoFoam* solver. The simulation time is set to 3s with time-step $dt = 0.0025$s, to allow the flow to reach the outlet. The computational mesh, shown in figures (6.1) and (6.2), consists of 291816 cells (hexahedral). The y^+ value of the mesh is 126 and for this reason wall functions have been used (kqRWallFunction for k and omegaWallFunction for ω (Liu 2016)). The spatial and temporal discretisation schemes are summarised in table (6.4). The FOM is run 10 times (one for each sampling pair) with snapshots being collected every 0.1s. This makes a total of $30 \cdot 10 = 300$ snapshots (30 snapshots per sampling pair) for each field. Therefore, $N_u^s = N_p^s = N_{sup}^s = N_\theta^s = N_{\nu_t}^s = 300$. The reduced basis is computed with the POD method. The POD is applied directly to the global snapshots matrices, which contain both parameter and time information in an equi-spaced grid, according to (4.2) and the reduced spaces are then chosen according to the decay of the eigenvalues, as shown in figure (6.7). The retained modes are 6 for velocity, 10 for pressure and supremizer, 10 for the eddy viscosity and 11 modes for temperature.

The ROM is tested on four different sets of velocity inlet values that belong to the training space (table 6.3). Figures (6.3), (6.4), (6.5) and (6.6) show the relative $\%\epsilon_{L^2}(t)$ error of the velocity, pressure, eddy viscosity and temperature fields for the four test sets. According to these figures, for the velocity field, the ROM performs best on set D, while for pressure, temperature and eddy viscosity fields, the approximation results to almost similar relative errors. According to figure (6.3), the relative error on the non-linear velocity field grows for sets that lie closer to the lower limit of the training space. As the training space is enriched with new training points, the ROM appears to perform better, in terms of the velocity field, and therefore set D exhibits the lowest relative error, amongst the four sets.

	FOM	ROM
$\partial/\partial t$	Backward	Backward
$\nabla\cdot$	Upwind, Central	Upwind, Central
Δ	Central	Central

Table 6.4: Numerical Schemes for FOM and ROM.

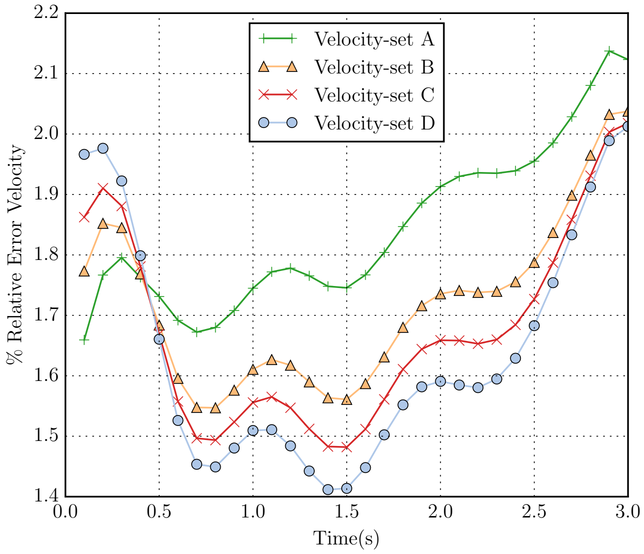

Figure 6.3: %$\epsilon_{L^2}(t)$ error of velocity field for the four test sets (6.3).

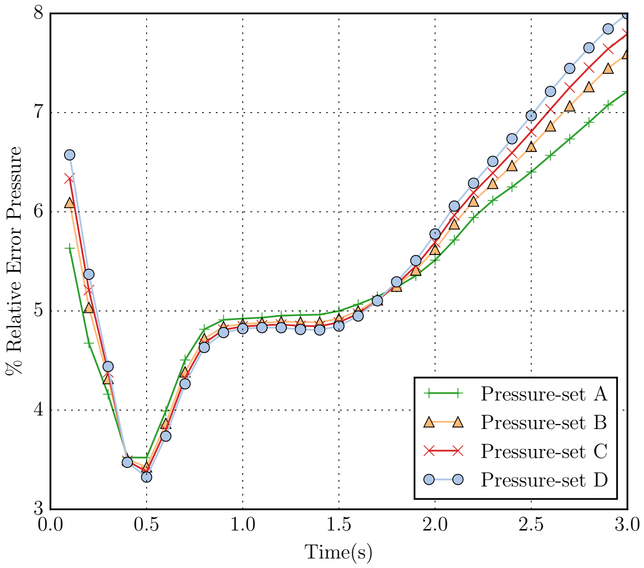

Figure 6.4: %$\epsilon_{L^2}(t)$ error of pressure field for the four test sets (6.3).

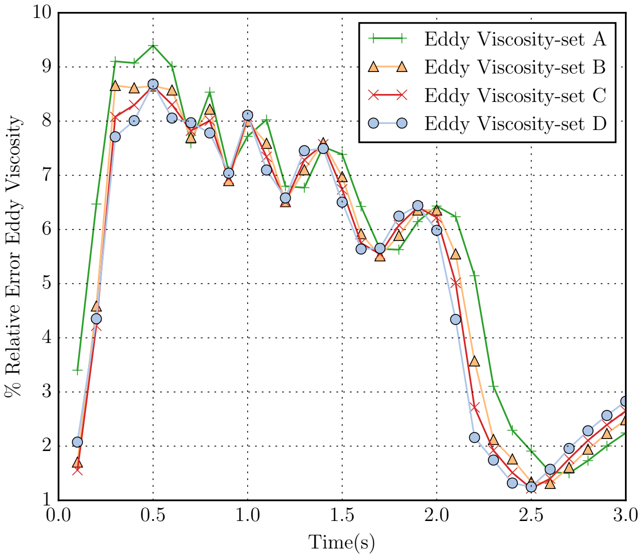

Figure 6.5: $\%\epsilon_{L^2}(t)$ error of eddy viscosity field for the four test sets (6.3).

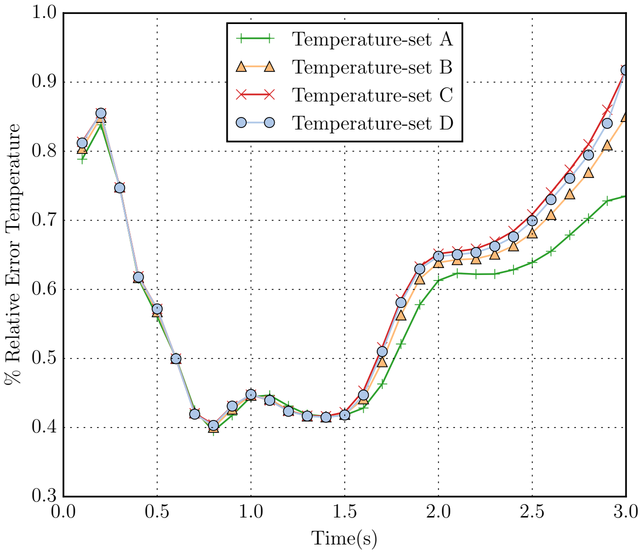

Figure 6.6: $\%\epsilon_{L^2}(t)$ error of teperature field for the four test sets (6.3).

6.5 Nested and Standard POD methods

In this section, a comparison between nested POD and standard POD methods for the test set D (table (6.3)) is presented. The boundary conditions for the FOM are shown in table (6.5). In the standard POD method, the POD is applied directly onto the global snapshots matrices, as explained in section 6.4. In the nested POD method, 10 local snapshot matrices are constructed, one for each sampling pair, and the POD is applied on each of them individually. The resulting basis functions are then truncated using the energy quantity (4.1.17), in order to retain approximately 99.9% of the total energy. The chosen POD basis are then weighted by their eigenvalues and a global weighted snapshot matrix is constructed for each field. For each sampling point, out of the 30 basis functions, only 10 are retained and weighted, giving a reduced dimension for the final global matrix of $N_u^{rn} = 10 \cdot 10 = 100$.

	Γ_m	Γ_b	Γ_w	Γ_o
$\boldsymbol{u}$	$(0.59, 0, 0)$	$(0, 0, -0.77)$	$(0, 0, 0)$	$\nabla \boldsymbol{u} \cdot \boldsymbol{n} = 0$
p	$\nabla p \cdot \boldsymbol{n} = 0$	$\nabla p \cdot \boldsymbol{n} = 0$	$\nabla p \cdot \boldsymbol{n} = 0$	0
θ	292.15	309.5	$\nabla \theta \cdot \boldsymbol{n} = 0$	$\nabla \theta \cdot \boldsymbol{n} = 0$

Table 6.5: Summary of boundary conditions where Γ_m is the main pipe inlet, Γ_b is the branch pipe and Γ_o is the outlet.

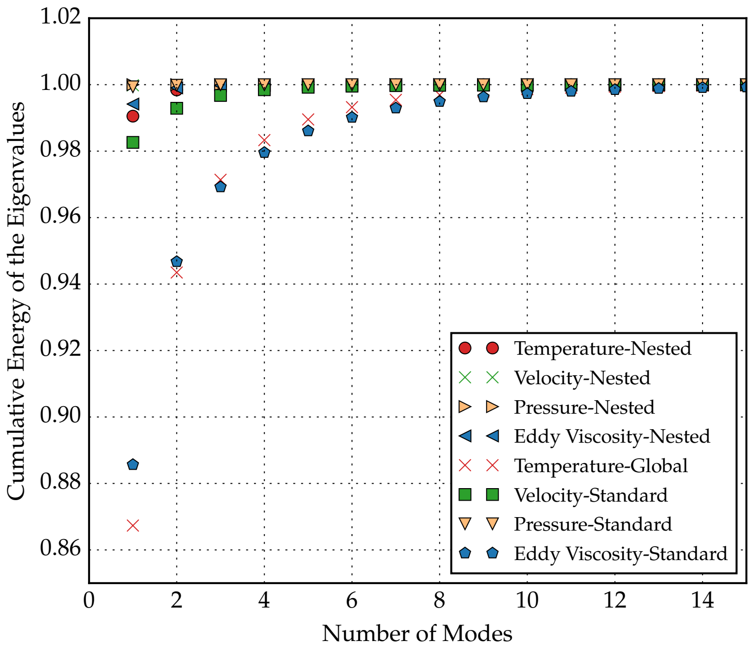

Figure 6.7: Cumulative energy of the eigenvalues for temperature, velocity, pressure and eddy viscosity fields for nested and standard POD methods, respectively.

The POD is applied on the weighted global matrix and the same procedure as in the standard POD is followed. The final decay of the eigenvalues is provided in figure (6.7). For the purposes of the comparison, the same number of modes for both the standard POD and the nested POD have been retained. This makes $N_u^r = 6$, $N_p^r = N_{sup}^r = 10$, $N_\theta^r = 11$ and $N_{\nu_t}^r = 10$. The numerical effort of the nested POD can be calculated as $\mathscr{O}([N_t^3 \cdot N_p + [N_u{}^{\text{nested}}]^3) = \mathscr{O}(30^3 \cdot 10 + [10 \cdot 10]^3) \approx 2 \cdot 10^6$, while for the standard POD $\mathscr{O}([N_t^3 \cdot N_p + [N_u{}^{\text{nested}}]^3) = \mathscr{O}([30 \cdot 10]^3) \approx 2 \cdot 10^7$. Therefore, the nested POD is one order of magnitude faster. For cases with a higher number of snapshots and sampling points, the smaller numerical effort of the nested POD is more apparent (Brands, Mergheim, and Steinmann 2016).

In the online phase, the ROM is evaluated on a new set of velocity inlet values, $\boldsymbol{U_m} = 0.59$ ms^{-1} and $\boldsymbol{U_b} = 0.77$ ms^{-1} (test set D). The ROM is tested for 3s with time-step $dt = 0.0025$s. The total execution time of the FOM, on a single Intel Xeon 3.07GHz processor, is 13782.1s, while of the ROM is 11.02s. This makes the ROM approximately 1259 times faster than the FOM (table 6.6).

	FOM	ROM
CPU Time(s)	13782.1	11.02

Table 6.6: Computational time for the full order (running on a single processor) and reduced order models.

A ROM simulation without the use of RBF for the eddy viscosity field is initially applied. In this case, the ROM from the laminar case has been used which does not contain the term associated with the eddy viscosity field (eq. 4.3.15). Figures (6.9) and (6.8) show the FOM and ROM velocity and temperature fields at time instance $t = 3s$, in the absence of RBF, as well as a comparison of the L^2 relative error for the velocity field, with and without RBF interpolation. It is clear from the aforementioned figures that the error between the FOM and ROM velocity fields is much higher in the latter case. The inconsistency between the FOM and ROM fields is also apparent in figure (6.9). The error also affects the temperature field, since there is an one-way coupling between those fields. Therefore, employing RBF interpolation during the ROM is essential. Similar behaviour is reported in (Hijazi, Ali, Stabile, Ballarin, and Rozza 2018) for a steady-state case and without taking the energy equation into account.

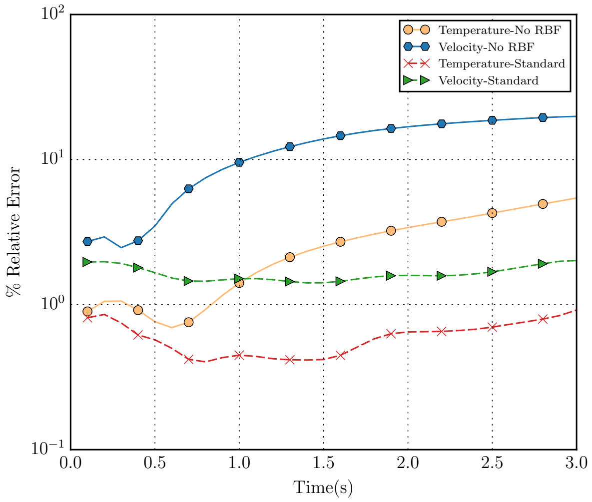

Figure 6.8: $\%\epsilon_{L^2}(t)$ error for velocity field with and without RBF eddy viscosity.

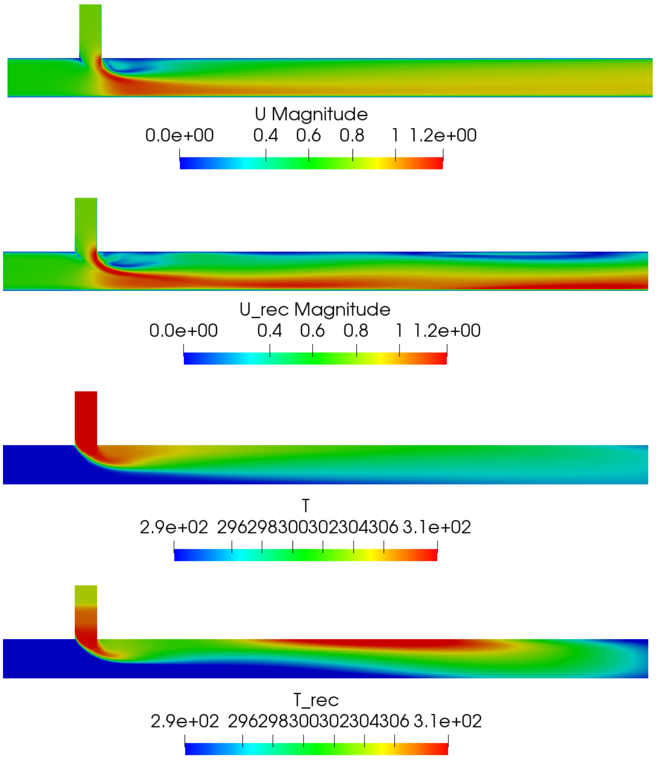

Figure 6.9: Comparison of the velocity and temperature fields of the full order (row 1 and 3, respectively) and reduced order model without use of RBF viscosity (row 2 and 4, respectively). The fields are depicted for time instances equal to $t = 3$s. The figure is a vertical slice through the pipe's centreline.

In the presence of RBF interpolation for the eddy viscosity field, figure (6.10) illustrates the relative $\%\epsilon_{L^2}$ error between the FOM and the ROM constructed using standard POD and nested POD methods.

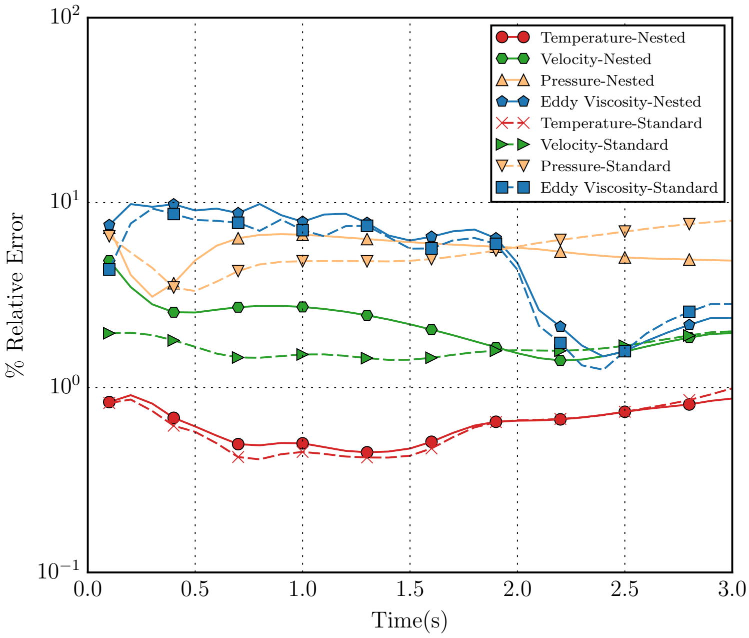

Figure 6.10: $\%\epsilon_{L^2}(t)$ error for temperature, velocity, pressure and eddy viscosity fields for the nested and standard POD methods, respectively.

According to this figure, the relative error for the standard POD method is slightly lower during the first 2 seconds of the simulation followed by similar or slightly better performance of the nested POD for the rest of the simulation. Tables (6.7) and (6.8) summarise a few statistics, showing minimum, maximum and average error for nested and standard POD methods, where, the average error appears to be very close for both cases. The pressure and eddy viscosity fields appear to have the largest relative error according to figure (6.10). For pressure, this can be attributed to the lack of an explicit equation, as in the ROM, the pressure basis functions are projected onto the continuity equation using the supremizer method (Ballarin, Manzoni, Quarteroni, and Rozza 2014; Rozza and Veroy 2007). An exploitation of a Poisson equation for pressure would probably improve the error (Caiazzo, Iliescu, John, and Schyschlowa 2014; Noack, Papas, and Monkewitz 2005b; Stabile, Hijazi, Mola, Lorenzi, and Rozza 2017). As for the eddy viscosity field, the use of a non-intrusive, pure data-driven method could cause the slighlty higher relative error, compared to the velocity and temperature fields, where the exact equations are projected onto the reduced basis. For the temperature field, the energy equation is still one-way coupled with the momentum equation, therefore the error appears to be smaller.

Nested	$\boldsymbol{u}$	θ	p	ν_t
Minimum	1.410	0.447	3.097	1.472
Maximum	4.856	0.909	7.299	9.826
Average	2.252	0.642	5.584	6.002

Table 6.7: % Relative $\epsilon_{L^2}(t)$ error for velocity, temperature and pressure and eddy viscosity fields for the nested POD method.

Standard	$\boldsymbol{u}$	θ	p	ν_t
Minimum	1.411	0.409	3.324	1.248
Maximum	2.012	0.990	7.996	9.293
Average	1.642	0.624	5.563	5.297

Table 6.8: % Relative $\epsilon_{L^2}(t)$ error for velocity, temperature and pressure and eddy viscosity fields for two the standard POD method.

A visualisation of the instantaneous fields is displayed in figures (6.11, 6.12, 6.13) and (6.14), for time instances $t = 0.5\text{s}, 1.5\text{s}$ and 3s, where both methods show similar qualitative performance. The relative difference between the FOM and ROM fields is visualised in figures (6.17) and (6.18). The largest difference is found in the mixing area of the pipe. This behaviour is expected, as in the mixing region, the flow is complex and highly transient. This behaviour is also apparent in figure (6.19) and (6.20), where the radial velocity is plotted against the arc length of the pipe, for $t = 0.5\text{s}$ and $t = 3\text{s}$, in three regions: before the mixing, in the mixing and after the mixing region, close to the outlet. The mixing region is where the radial velocity diverges the most.

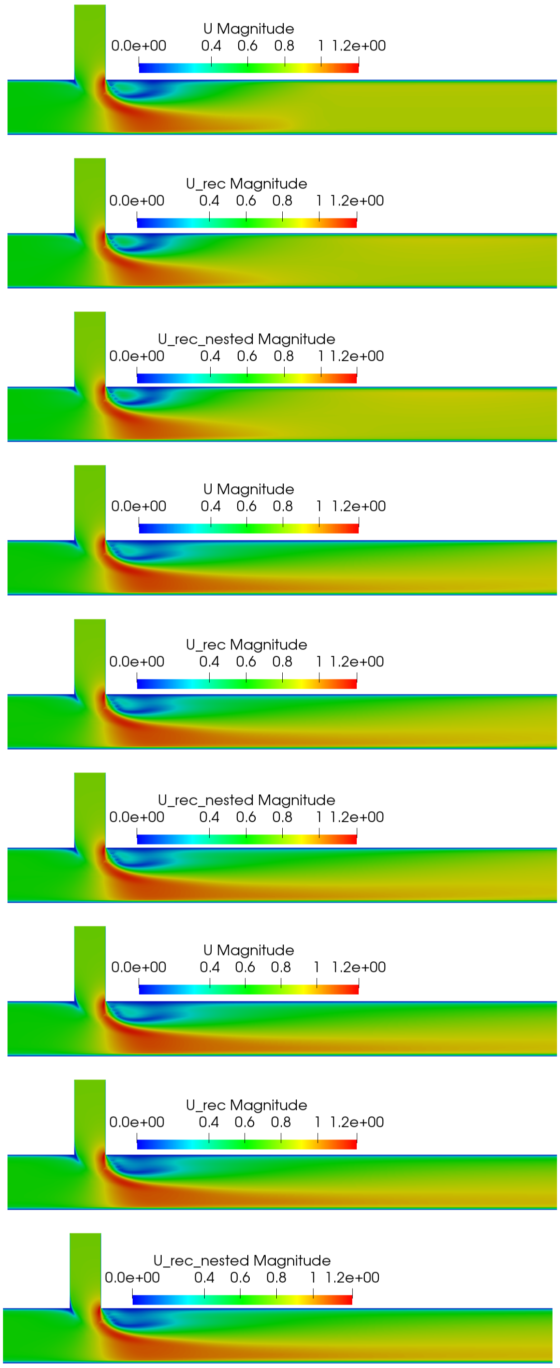

Figure 6.11: Comparison of the velocity field of the full order (row 1,4,7) and reduced order model using standard POD (row 2,5,8) and nested POD method (row 3,6,9) for test case D. The fields are depicted for time instances equal to $t = 0.5\text{s}, 1.5\text{s}$ and 3s. The figure is a vertical slice through the pipe's centreline.

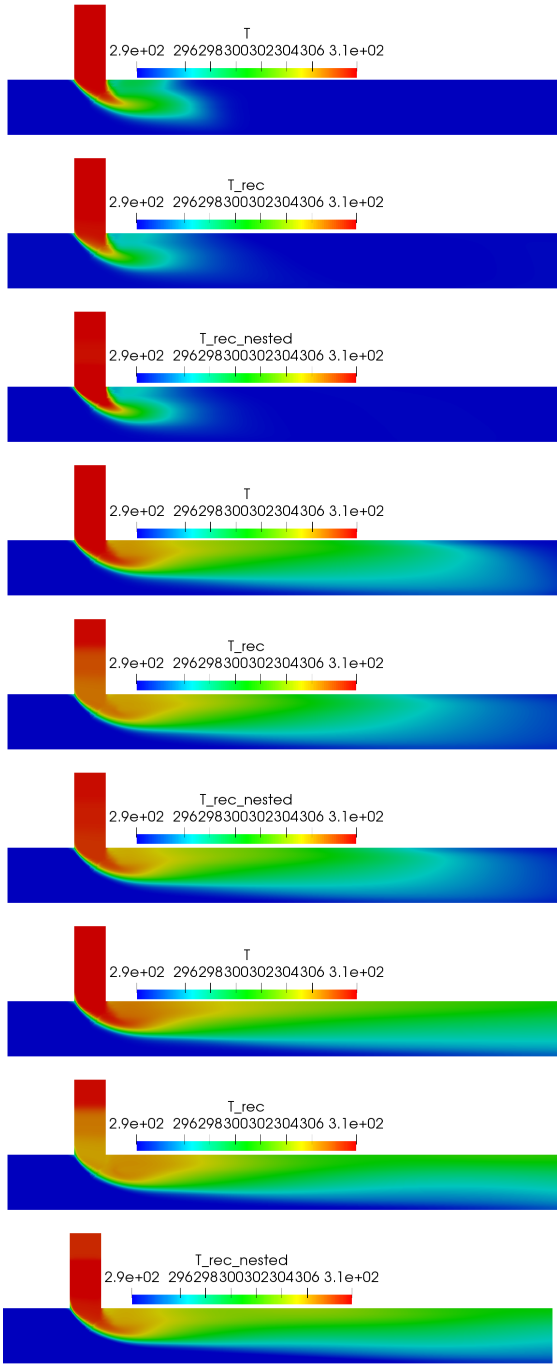

Figure 6.12: Comparison of the temperature field of the full order (row 1,4,7) and reduced order model using standard POD (row 2,5,8) and nested POD method (row 3,6,9) for test case D. The fields are depicted for time instances equal to $t = 0.5\text{s}, 1.5\text{s}$ and 3s. The figure is a vertical slice through the pipe's centreline.

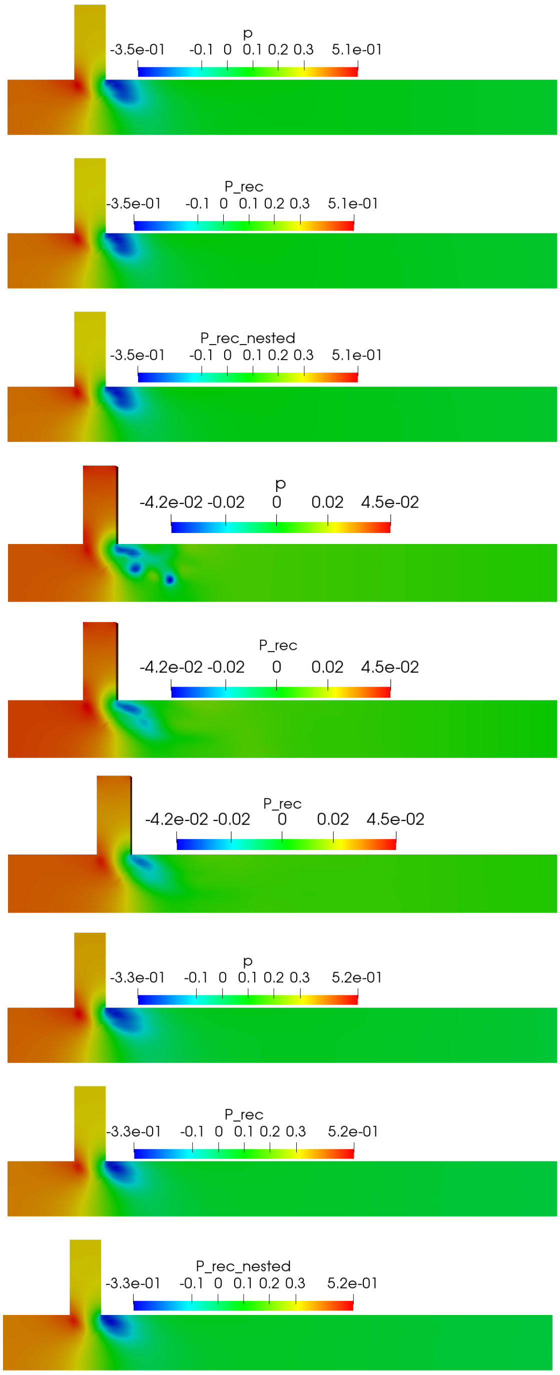

Figure 6.13: Comparison of the pressure field of the full order (row 1,4,7) and reduced order model using standard POD (row 2,5,8) and nested POD method (row 3,6,9) for test case D. The fields are depicted for time instances equal to $t = 0.5\text{s}, 1.5\text{s}$ and 3s. The figure is a vertical slice through the pipe's centreline.

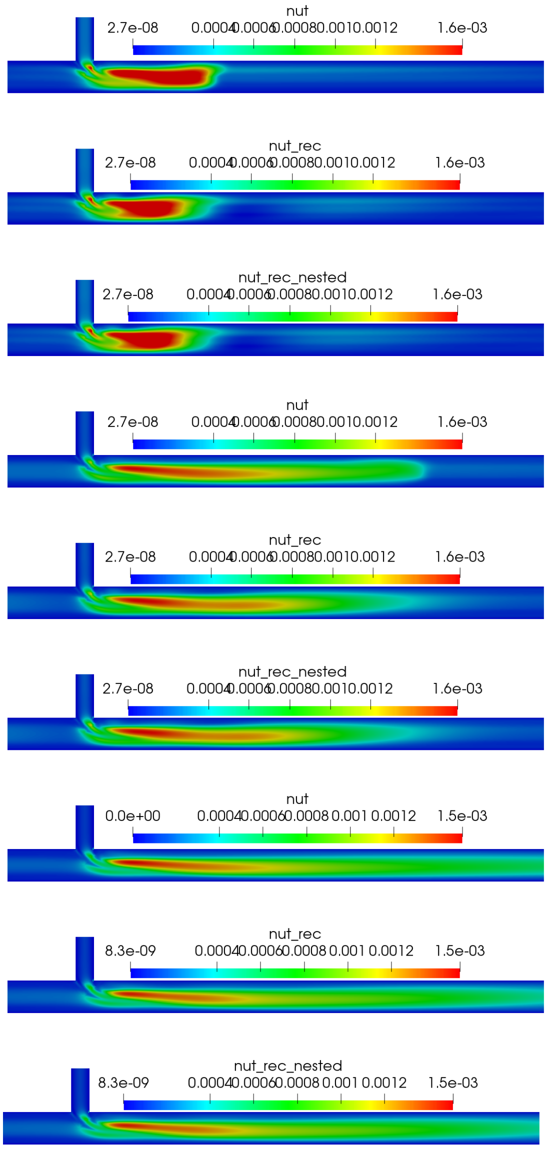

Figure 6.14: Comparison of the eddy viscosity field of the full order (row 1,4,7) and reduced order model using standard POD (row 2,5,8) and nested POD method (row 3,6,9) for test case D. The fields are depicted for time instances equal to $t = 0.5\text{s}, 1.5\text{s}$ and 3s. The figure is a vertical slice through the pipe's centreline.

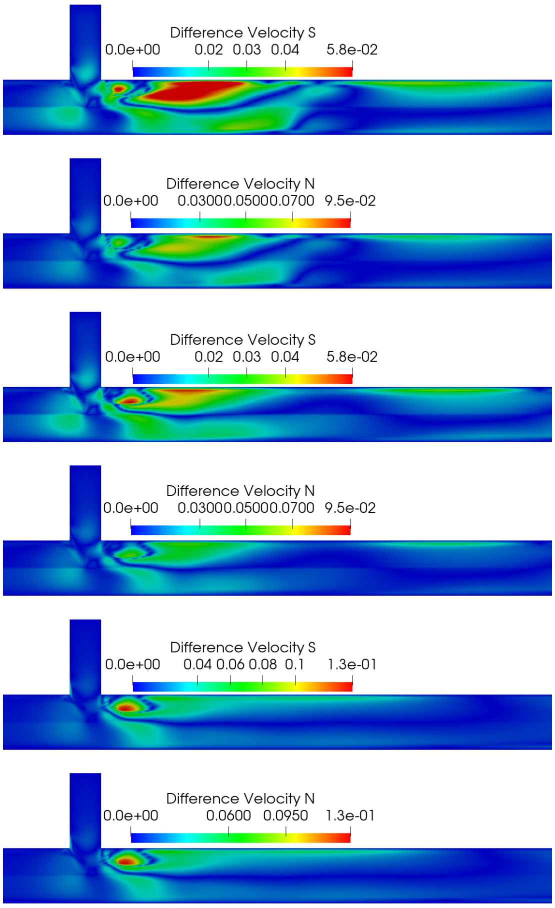

Figure 6.15: Difference between the velocity full order and reduced order standard POD (odd rows) and nested POD (even rows). The fields are depicted for time instances equal to $t = 0.5$s, 1.5s and 3s. The figure is a vertical slice through the pipe's centreline.

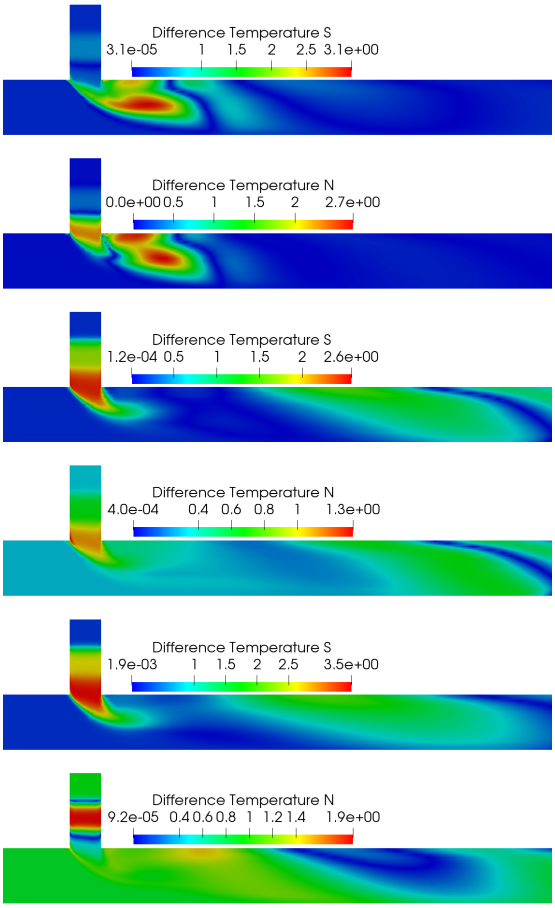

Figure 6.16: Difference between the temperature full order and reduced order standard POD (odd rows) and nested POD (even rows). The fields are depicted for time instances equal to $t = 0.5\text{s}, 1.5\text{s}$ and 3s and increasing from left to right. The figure is a vertical slice through the pipe's centreline.

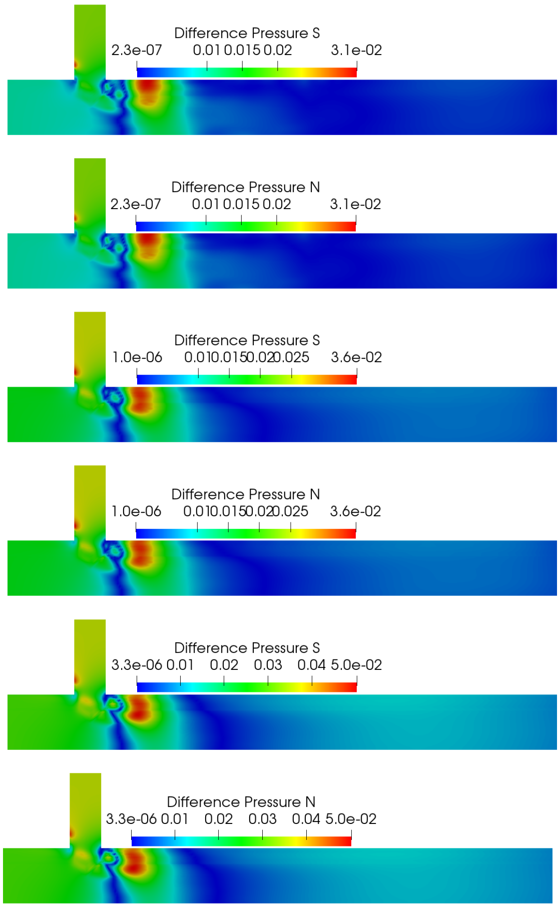

Figure 6.17: Difference between the pressure full order and reduced order standard POD (odd rows) and nested POD (even rows). The fields are depicted for time instances equal to $t = 0.5\text{s}, 1.5\text{s}$ and 3s and increasing from left to right. The figure is a vertical slice through the pipe's centreline.

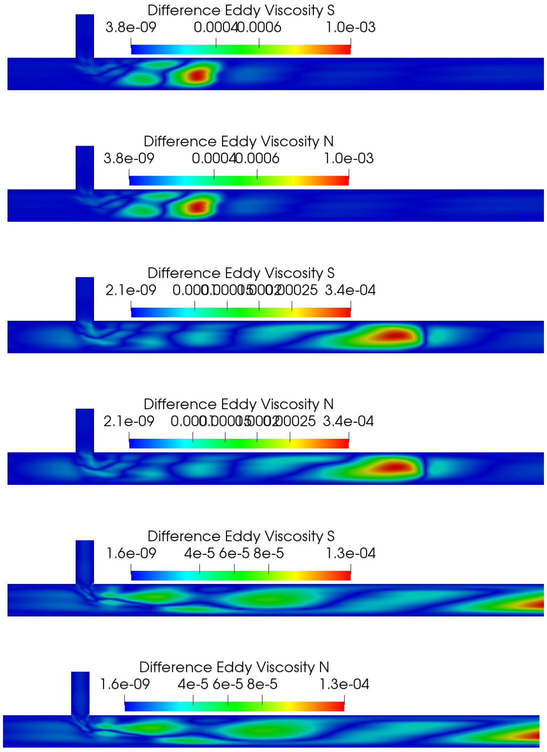

Figure 6.18: Difference between the full order and reduced order standard POD (first row) and nested POD (second row) for the eddy viscosity field. The fields are depicted for time instances equal to $t = 0.5\text{s}, 1.5\text{s}$ and 3s. The figure is a vertical slice through the pipe's centreline.

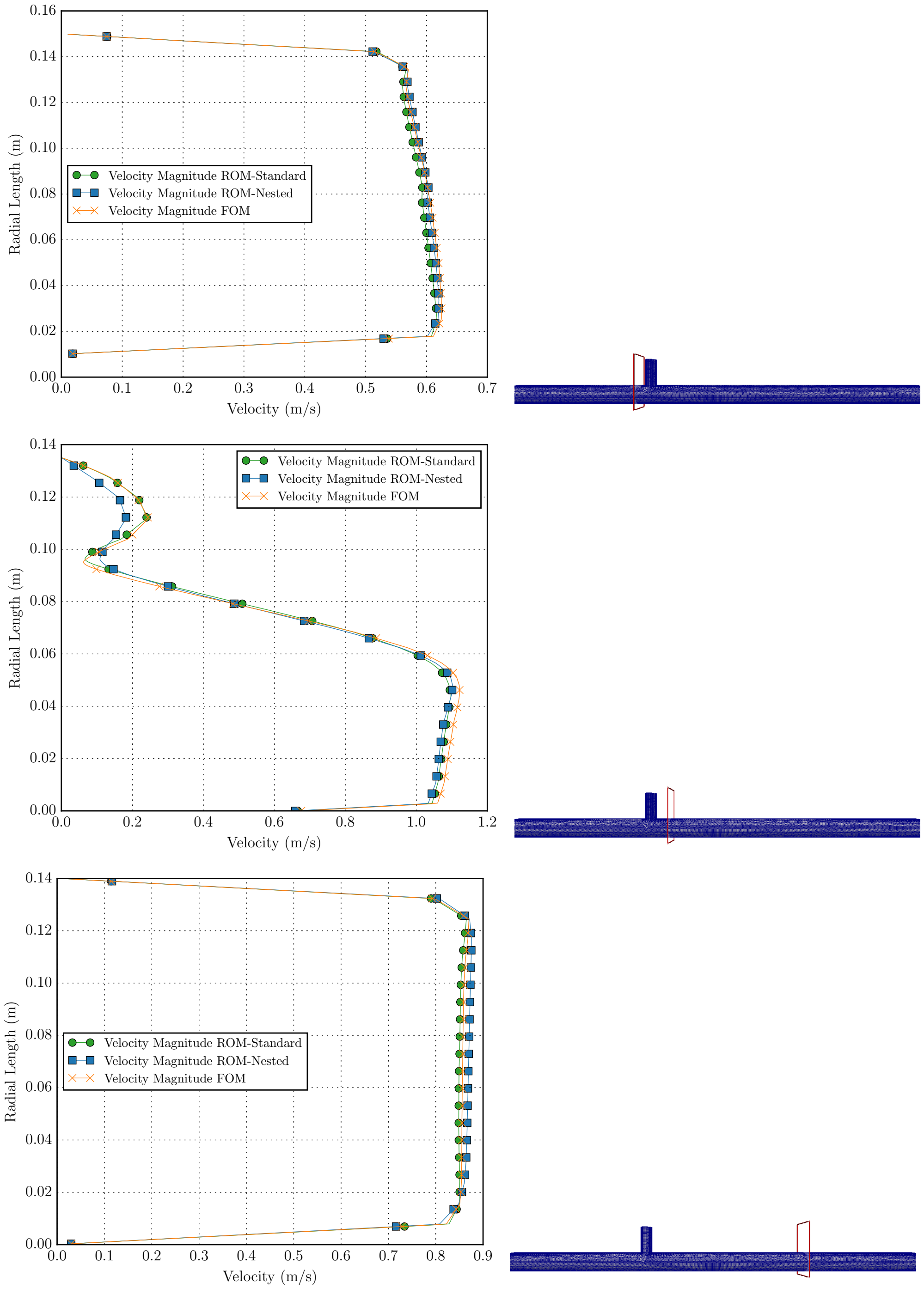

Figure 6.19: Comparison of the radial velocity between the FOM, ROM-Global and ROM-Nested for three different locations, before the mixing, in the mixing region and near the outlet for $t = 0.5$s.

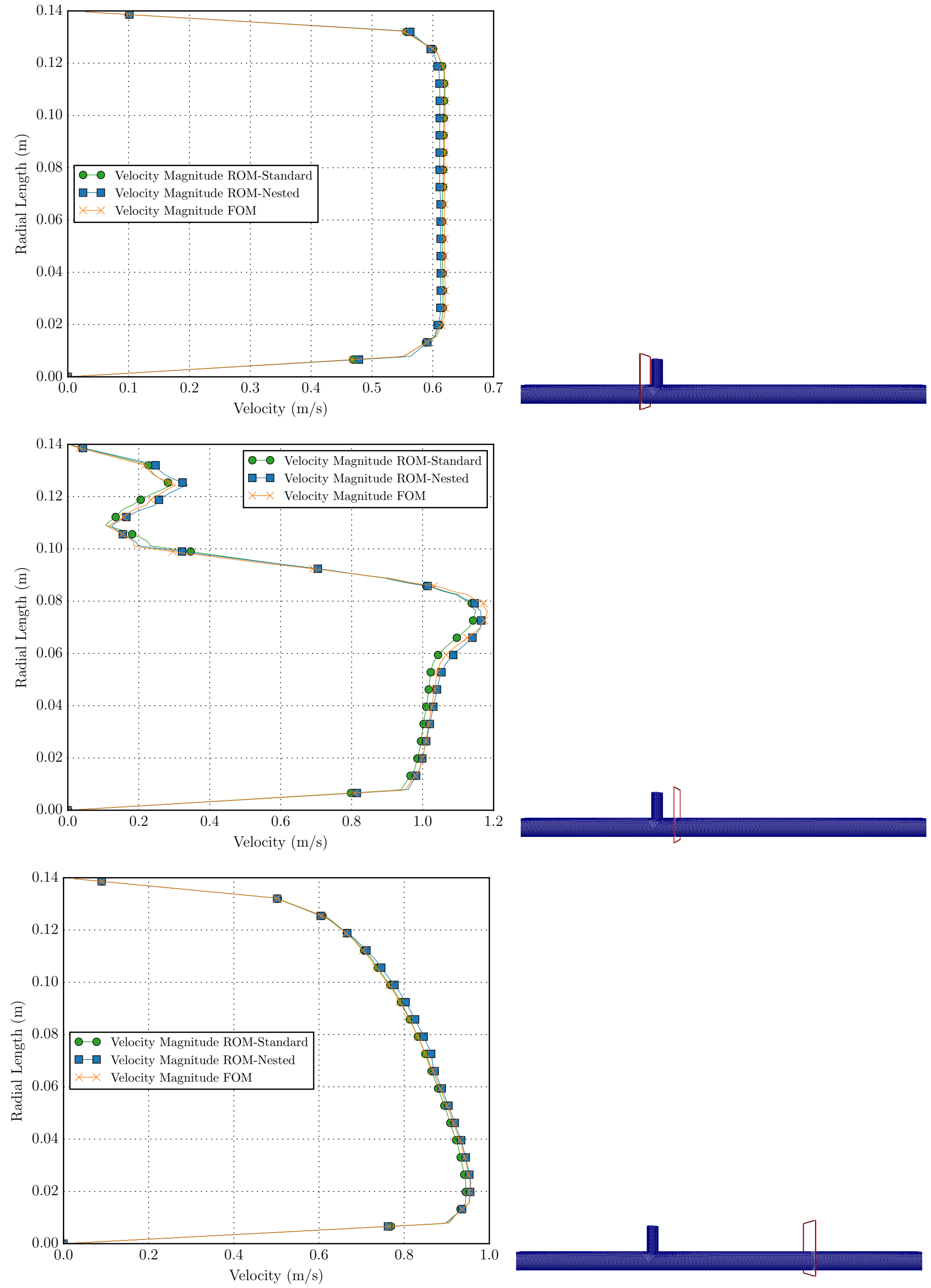

Figure 6.20: Comparison of the radial velocity between the FOM, ROM-Global and ROM-Nested for three different locations, before the mixing, in the mixing region and near the outlet for $t = 3$s.

To further assess the performance of the ROM against the FOM, the relative error of the total energy (kinetic and thermal) is plotted in figure (6.21), where it shows a small (less than 0.25%) relative error. Overall, both the ROM derived using standard and the ROM derived using nested POD methods are performing well throughout the simulation.

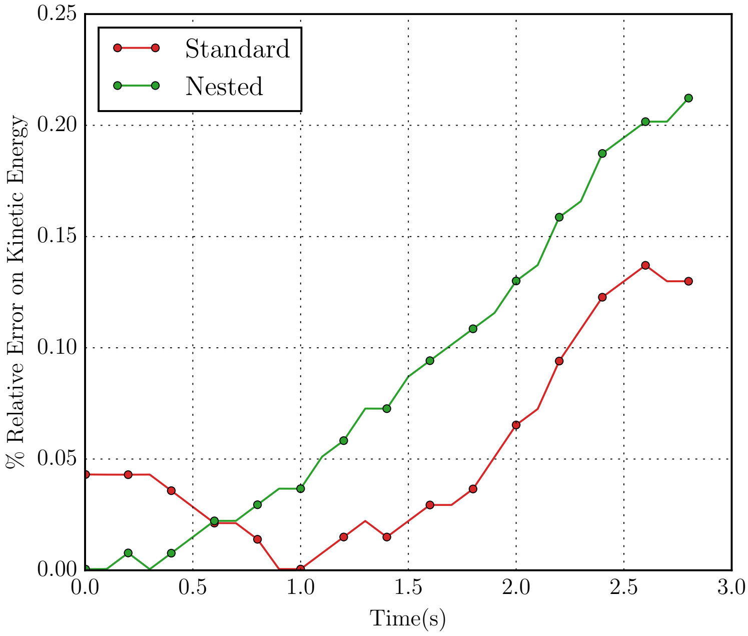

Figure 6.21: Relative error on total energy (kinetic and thermal) between the FOM and the ROM for standard and nested POD methods.

6.6 Summary of the Chapter

In this chapter a hybrid reduced order model for modelling turbulent heat transfer problems has been studied. The hybrid method consists of the POD-Galerkin approach for the velocity, temperature and pressure fields and PODI with RBF interpolation for the eddy viscosity field. From the discussion it is clear that the traditional POD-Galerkin approach alone is not sufficient for turbulent flows. Two variations of POD, standard and nested, have been studied and compared. The proposed method is tested on a T-junction pipe where turbulent thermal mixing takes place. According to the results, the ROM constructed using standard or nested POD is capable of reproducing the FOM results with good accuracy in both cases, while the nested POD method requires less numerical effort. A speed-up factor of approximately 1259 has been obtained, meaning that the ROM is three orders of magnitude faster than the FOM.

Chapter 7

Model Order Reduction for Buoyancy Driven Flows

In the present chapter model order reduction for buoyancy driven flows is discussed. Natural convection is a mechanism in which fluid motion is generated solely by density gradients induced by temperature gradients. The benefits of this mechanism have been recently recognised by the nuclear industry for the establishment of passive cooling systems in modern nuclear reactor designs, as no other artificial means of heat transfer, such as pumps, fans etc, are required for the removal of the decay heat. However, due to the complex physics of buoyancy driven flows arising from the strong coupling between the velocity and temperature fields, phenomena such as thermal stratification could affect the efficiency of the passive systems to remove heat.

This chapter deals with the modelling of the aforementioned flows from a model order reduction point of view. The effect of buoyancy is modelled using the Boussinesq approximation. In the first section, a parametric POD-Galerkin approach is followed for modelling enclosed buoyancy driven flows. Since enclosed flows are considered, the pressure field can be neglected. The method is tested on a differentially heated square cavity. This geometry, while simple, encompasses well the complex physics of natural convention and, therefore, is widely applied in many industrial applications.

In the second part of this chapter, open flows are studied and the pressure field is added in the ROM by implementing a PPE method. The ROM is tested on natural circulation in a U-bend pipe geometry, where a constant uniform cold heat flux is applied on a wall part. The introduction of the heat flux can cause the circulating flow to stall. The ability of the ROM to predict such behaviour is assessed and compared with the FOM, simulated in OpenFOAM.

The content of this chapter has been partially published in:

STAR, K., STABILE, G., GEORGAKA, S., BELLONI, F., ROZZA, G., and DEGROOTE, J. 2019. POD-Galerkin Reduced Order Model of the Boussinesq Approximation for Buoyancy - Driven Enclosed Flows. Building theory and applications : proceedings of M&C 2019. p.2452-2461.
My contribution to the above proceedings paper is on the development of the ROM mathematical framework for enclosed flows presented in the following chapter, as well as on the development of some parts of the ROM solver. All of the results presented in the subsequent chapter constitute my own work and are not part of the paper.

7.1 Mathematical Framework for the Full Order Model

In the presence of gravity body force, $\boldsymbol{g}$, the incompressible Navier-Stokes equations (3.1.5 3.1.6 3.1.7) are modified to accommodate for the extra term as follows:

$$\begin{cases} \rho\frac{\partial \boldsymbol{u}}{\partial t} + \boldsymbol{\nabla}\cdot(\rho\boldsymbol{u}\otimes\boldsymbol{u}) - \mu\Delta\boldsymbol{u} = -\nabla p + \boldsymbol{g}\rho & \text{in } Q, \\ \boldsymbol{\nabla}\cdot\boldsymbol{u} = \boldsymbol{0} & \text{in } Q, \\ \frac{\partial \theta}{\partial t} + (\nabla\cdot\boldsymbol{u})\theta - \alpha_{dif}\Delta\theta = 0 & \text{in } Q, \end{cases} \tag{7.1.1}$$

where ρ is the density.

In the case where the density and graviational acceleration are constant, the gravitational force can be written as:

$$\rho\boldsymbol{g} = \nabla(\rho\boldsymbol{g}\cdot\boldsymbol{r}), \tag{7.1.2}$$

where $\boldsymbol{r}$ is the position vector. Thus,

$$\nabla p - \rho\boldsymbol{g} = \nabla(p - \rho\boldsymbol{g}\cdot\boldsymbol{r}). \tag{7.1.3}$$

7.2 The Boussinesq Approximation

The Boussinesq approximation states that the density in intertia terms (unsteady convection terms) can be treated as constant (ρ_0), while the density in the gravitational term should be treated as variable (ρ). This approximation is valid only when $\Delta\rho << \rho_0$. Hence, the momentum and continuity equations are expressed as:

$$\begin{cases} \frac{\partial \boldsymbol{u}}{\partial t} + \boldsymbol{\nabla} \cdot (\boldsymbol{u} \otimes \boldsymbol{u}) - \nu \Delta \boldsymbol{u} = -\nabla \tilde{p} + \boldsymbol{g}\frac{\rho}{\rho_0} & \text{in } Q, \\ \boldsymbol{\nabla} \cdot \boldsymbol{u} = \boldsymbol{0} & \text{in } Q, \end{cases} \tag{7.2.1}$$

where $\tilde{p} = p/\rho_0$ is the normalised pressure and all the terms in the momentum equation have been devided by the constant density ρ_0. The non-constant density, ρ, is defined from the following Taylor expansion:

$$\rho = \rho_0 + \beta(\theta - \theta_0) + \mathcal{O}(((\theta - \theta_0)^2) \approx \rho_0[1 - \beta(\theta - \theta_0)], \tag{7.2.2}$$

where only the first order terms from the Taylor's expansion are retained. In the above expression, θ_0 is the reference temperature and β is the thermal expansion coefficient, defined as:

$$\beta = -\frac{1}{\rho_0}\frac{\partial \rho}{\partial \theta} \approx -\frac{1}{\rho_0}\frac{\rho - \rho_0}{\theta - \theta_0}. \tag{7.2.3}$$

In terms of implementation of the buoyant solvers in OpenFOAM, the pressure and buoyancy terms are treated as one term, p_{rgh}, for numerical convenience. The p_{rgh} pressure is defined as:

$$p_{rgh} = p - \rho \boldsymbol{g} \cdot \boldsymbol{r}, \tag{7.2.4}$$

where the term $\rho \boldsymbol{g} \cdot \boldsymbol{r}$ is the hydrostatic pressure and $\boldsymbol{r}$ is the position vector. The p_{rgh} pressure is sometimes called "pseudo-dynamic" pressure and has no physical meaning. It is just used for numerical convenience. In OpenFOAM, the family of *buoyantBoussinesq* solvers is only using the p_{rgh} pressure in the solution and therefore this is the pressure field of interest. However, for post-processing pressure calculations, the static pressure p has to be used. This can be achieved by substituting the p_{rgh}

and rearranging the equation 7.2.4, such that:

$$p = p_{rgh} + \rho \boldsymbol{g} \cdot \boldsymbol{r}. \tag{7.2.5}$$

In this chapter, all the pressure results report the p_{rgh} field. In the momentum equation, the pressure and gravity terms are rearranged with the help of the equations (7.1.3) and (7.2.4) as follows:

$$-\nabla p+\rho\boldsymbol{g} = -\nabla(p_{rgh}+\rho\boldsymbol{g}\cdot\boldsymbol{r})+\rho\boldsymbol{g} = -\nabla p_{rgh}-(\boldsymbol{g}\cdot\boldsymbol{r})\nabla\rho-\rho\boldsymbol{g}+\rho\boldsymbol{g} = -\nabla p_{rgh}-(\boldsymbol{g}\cdot\boldsymbol{r})\nabla\rho. \tag{7.2.6}$$

Regarding the energy equation, the heat capacity is assumed constant. The incompressible Navier-Stokes equations strongly coupled with energy equations are:

$$\begin{cases}
\frac{\partial \boldsymbol{u}(\boldsymbol{x},\boldsymbol{\mu},t)}{\partial t} + \boldsymbol{\nabla}\cdot(\boldsymbol{u}(\boldsymbol{x},\boldsymbol{\mu},t)\otimes\boldsymbol{u}(\boldsymbol{x},\boldsymbol{\mu},t)) & \\
-\nu(\boldsymbol{\mu})\Delta\boldsymbol{u}(\boldsymbol{x},\boldsymbol{\mu},t) = -\nabla p_{rgh}(\boldsymbol{x},\boldsymbol{\mu},t) - (\boldsymbol{g}\cdot\boldsymbol{r})\nabla\rho(\boldsymbol{x},\boldsymbol{\mu},t) & \text{in } Q,\\
\frac{\partial \theta(\boldsymbol{x},\boldsymbol{\mu},t)}{\partial t} + (\nabla\cdot\boldsymbol{u}(\boldsymbol{x},\boldsymbol{\mu},t))\theta(\boldsymbol{x},\boldsymbol{\mu},t) - \alpha_{dif}\Delta\theta(\boldsymbol{x},\boldsymbol{\mu},t) = 0 & \text{in } Q,\\
\boldsymbol{\nabla}\cdot\boldsymbol{u}(\boldsymbol{x},\boldsymbol{\mu},t) = \boldsymbol{0} & \text{in } Q,\\
\boldsymbol{u}(\boldsymbol{x},\boldsymbol{\mu},t) = 0 & \text{on } \Gamma,\\
\theta(\boldsymbol{x},\boldsymbol{\mu},t) = g(\boldsymbol{x}) & \text{on } \Gamma,\\
\boldsymbol{u}(\boldsymbol{x},\boldsymbol{\mu},t,0) = \boldsymbol{u}_0(\boldsymbol{x},\mu) & \text{on } \Gamma,\\
\theta(\boldsymbol{x},\boldsymbol{\mu},t,0) = \theta_0(\boldsymbol{x},\mu) & \text{on } \Gamma,
\end{cases} \tag{7.2.7}$$

where $\rho = 1 - \beta(\theta - \theta_0)$ is the effective kinematic density.

7.3 Reduced Order Model Formulation - Closed Flows

This section deals with enclosed flows where, according to section (4.4), the pressure term in the reduced order model vanishes. Therefore, an approximation and recovery of the pressure field will not be considered. The POD-Galerkin method is applied only on the velocity, $\boldsymbol{u}(\boldsymbol{x},\boldsymbol{\mu},t)$ and temperature $\theta(\boldsymbol{x},\boldsymbol{\mu},t)$ fields, which are approximated similarly to the previous sections as follows:

$$\boldsymbol{u}(\boldsymbol{x},\boldsymbol{\mu},t) \approx \boldsymbol{u}_r = \sum_{i=1}^{N_u^r} \alpha_i(\boldsymbol{\mu},t)\boldsymbol{\phi}_i(\boldsymbol{x}), \tag{7.3.1}$$

$$\theta(\boldsymbol{x},\boldsymbol{\mu},t) \approx \theta_r = \sum_{i=1}^{N_\theta^r} c_i(\boldsymbol{\mu},t)\chi_i(\boldsymbol{x}). \tag{7.3.2}$$

The new term in the Navier-Stokes equations, $(\boldsymbol{g}\cdot\boldsymbol{r})\nabla\rho$, depends only on temperature field and, therefore, there is no need for additional basis functions. It can be approximated using the already calculated temperature basis functions, $\chi(\boldsymbol{x})$. The Galerkin projection of equations (7.2.7) onto the basis functions $\phi(\boldsymbol{x})$ and $\chi(\boldsymbol{x})$ leads to the following reduced set of ODEs:

$$\begin{cases} \boldsymbol{M}\dot{\boldsymbol{\alpha}} = -\boldsymbol{\alpha}^T\boldsymbol{Q}\boldsymbol{\alpha} + \nu\boldsymbol{L}\boldsymbol{\alpha} - \boldsymbol{B}\boldsymbol{b}, \\ \boldsymbol{K}\dot{\boldsymbol{c}} = -\boldsymbol{\alpha}^T\boldsymbol{G}\boldsymbol{c} + \alpha_{dif}\boldsymbol{N}\boldsymbol{c}, \end{cases} \tag{7.3.3}$$

where the new matrix, B_{ij}, corresponds to the buoyant term and is defined as:

$$B_{ij} = \langle(\boldsymbol{g}\cdot\boldsymbol{r})\nabla(1-\beta(\chi_i-\theta_0)),\phi_j\rangle_{L_2(\Omega)}. \tag{7.3.4}$$

7.4 Numerical Study: Natural Convection in a Square Cavity

In this section, a benchmark case of natural convection in the well-studied 2D differentially heated square cavity filled with air is presented. A sketch of the cavity is demonstrated in figure (7.1), where the two vertical walls are maintainted under constant temperatures of $\theta_h = 302.5$K and $\theta_c = 297.5$K, respectively, while the horizontal walls are kept insulated. The initial temperature of the internal field is set at $\theta_{IF} = 300K$ corresponding to the reference temperature, θ_{ref}. The length of the square domain is $D = 0.1m$, where a uniform mesh of $100x100$ is constructed as shown in figure (7.1). A summary of the boundary conditions is shown in table (7.1) and the physical properties in table (7.2). For the P_{rgh}, the boundary condition "*fixedFluxPressure*" sets the pressure gradient to a value provided, such that the flux on the boundary is specified by the velocity boundary condition.

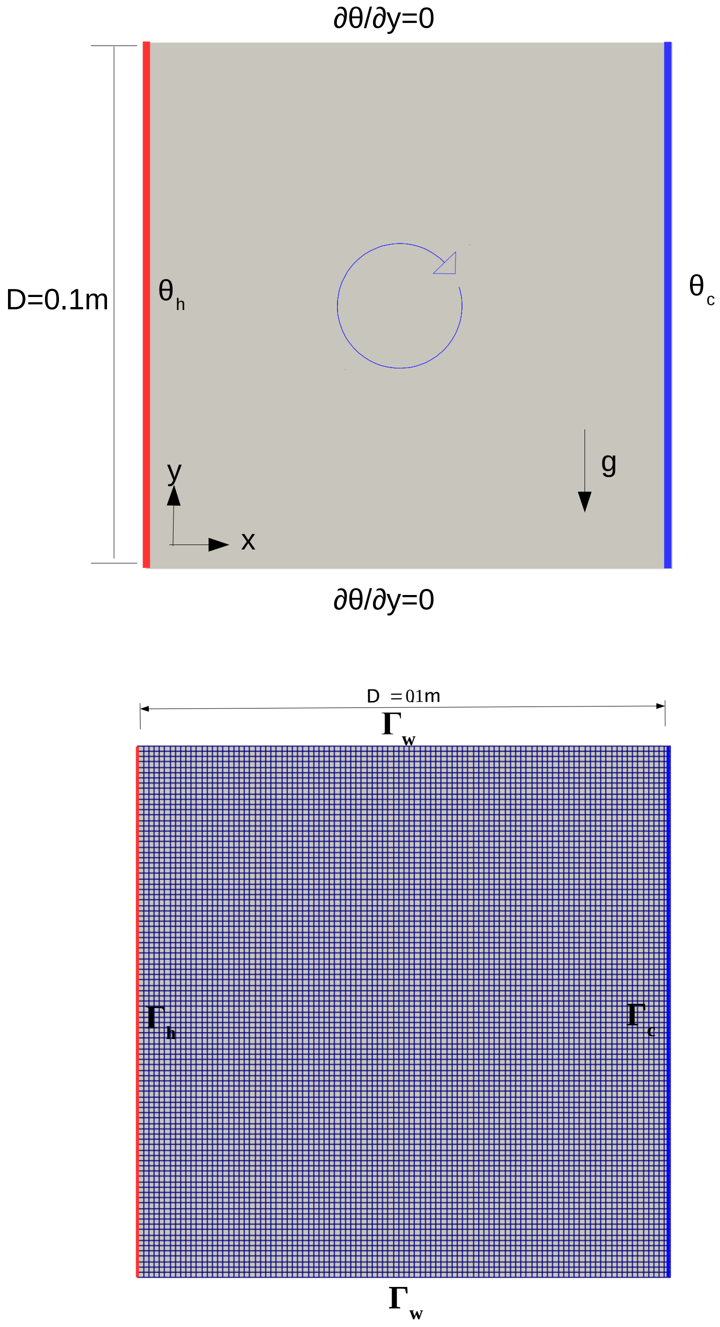

Figure 7.1: Square cavity geometry and computational mesh

	Γ_h	Γ_c	Γ_w	Γ_{IF}
$\boldsymbol{u}$	$(0,0,0)$	$(0,0,0)$	$(0,0,0)$	$(1\times10^{-4},0,0)$
p_{rgh}	$fixedFluxPressure$	$fixedFluxPressure$	$fixedFluxPressure$	0
θ	302.5	297.5	$\nabla\theta\cdot\boldsymbol{n}=0$	300

Table 7.1: Summary of the boundary conditions for the square cavity.

The FOM is solved in OpenFOAM using the *buoyantBoussinesqPimpleFoam* solver, which implements the PIMPLE alogorithm and the Boussinesq approximation for the buoyancy term, while the ROM is solved in ITHACA-FV. For the discretisation of the convective terms in both the FOM and the ROM, upwind schemes have been selected, while the diffusive terms have been discretised by central differencing schemes. The temporal discretisation is handled by the Euler backward scheme, in both models. The simulation time is set to 10s with time-step of $dt = 0.005$s.

Quantity	Value
Pr	0.71
β (K^{-1})	0.003
D (m)	0.1
$\boldsymbol{g}$ (ms^{-2})	9.81
ν ($\mathrm{m}^2\mathrm{s}^{-2}$)	*see table 7.3
Ra ($\mathrm{m}^2\mathrm{s}^{-2}$)	*see table 7.3

Table 7.2: Summary of the FOM physical parameters for the square cavity.

The kinematic viscosity, ν, has been chosen as the varied parameter. This variation affect also the Rayleigh number, Ra, which is defined as the product of the dimensionless Grashof and Prandtl numbers, according to the following relation:

$$\mathrm{Ra} = \mathrm{Gr} \times \mathrm{Pr} = \frac{g\beta\Delta\theta L^3}{\nu\alpha_{dif}}, \tag{7.4.1}$$

where $\Delta\theta$ is the temperature difference and the thermal diffusivity is taken as $\alpha_{dif} = \nu/Pr$. The Prandtl number, Pr$= \nu/\alpha_{dif}$, measures the momentum to heat diffusivity ratio, while the Grashof number, $Gr = g\beta\Delta\theta L^3/\nu^2$, represents the buoyancy to viscous forces ratio. In natural convection, the Grashof number can be seen as the equivalent to Reynolds number, in forced convection. The sampling of the parameter space for the kinematic viscosity is handled by an equispaced grid method. The sampling points are shown in table (7.3), corresponding to Rayleigh numbers in the order of 10^5. Velocity and temperature snapshots are collected every 0.05s resulting to a total of 200 snapshots for each field per parameter value. This makes a total of 2200 snapshots for each field and, therefore, the dimension of the POD space is $N_u^s = N_\theta^s = 2200$. Since we are dealing with enclosed flow, the pressure term has been neglected.

ν ($\mathrm{m^2s^{-1}}$)
1.0×10^{-5}
1.1×10^{-5}
1.2×10^{-5}
1.3×10^{-5}
1.4×10^{-5}
1.5×10^{-5}
1.6×10^{-5}
1.7×10^{-5}
1.8×10^{-5}
1.9×10^{-5}
2.0×10^{-5}

Table 7.3: Sampling points for the kinematic viscosity.

The ROM simulations are performed in ITHACA-FV library, where the ROM equations (7.3.3) are handled in a coupled manner. The ROM is tested on a non-trained value of the kinematic viscosity, $\nu = 1.65 \times 10^{-5}$, within the range of the training space, while all the other physical parameters, as well as the boundary conditions, are kept the same (table 7.4). The POD method is applied on the correlation matrices for velocity and temperature and the cumulative energy of the corresponding eigenvalues is illustrated in figure (7.2), where a decaying trend is observed. According to the energy quantity (4.1.17), 18 modes for velocity and 10 for temperature are retained. This reduces the original POD space from $N_u^s = N_\theta^s = 2200$ to $N_u^r = 18$. and $N_\theta^r = 10$.

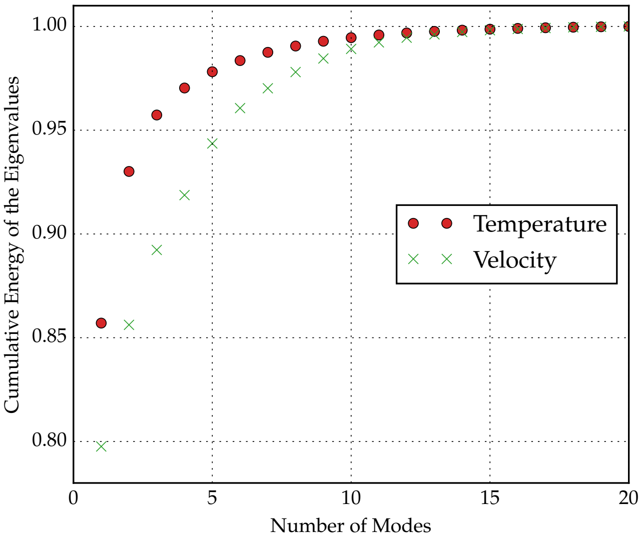

Figure 7.2: Cumulative energy of the eigenvalues for temperature, velocity, pressure and nut fields for nested and global pod methods, respectively.

Quantity	Value
Pr	0.71
β (K^{-1})	0.003
D (m)	0.1
$\boldsymbol{g}$ (ms^{-2})	9.81
ν (m^{2}s^{-2})	1.65×10^{-5}
Ra (m^{2}s^{-2})	272463

Table 7.4: Summary of the ROM physical parameters for the square cavity.

The first 6 POD basis for velocity and temperature are shown in figure (7.3), where, for velocity, a symmetry pattern is observed and the first POD mode resembling the steady-state. For temperature, the modes have been homogenised using lifting functions according to algorithm (3), where the control function has been obtained by solving the steady-state Laplace problem. Therefore, the first POD mode for temperature appears to be a fluctuation around the mean field.

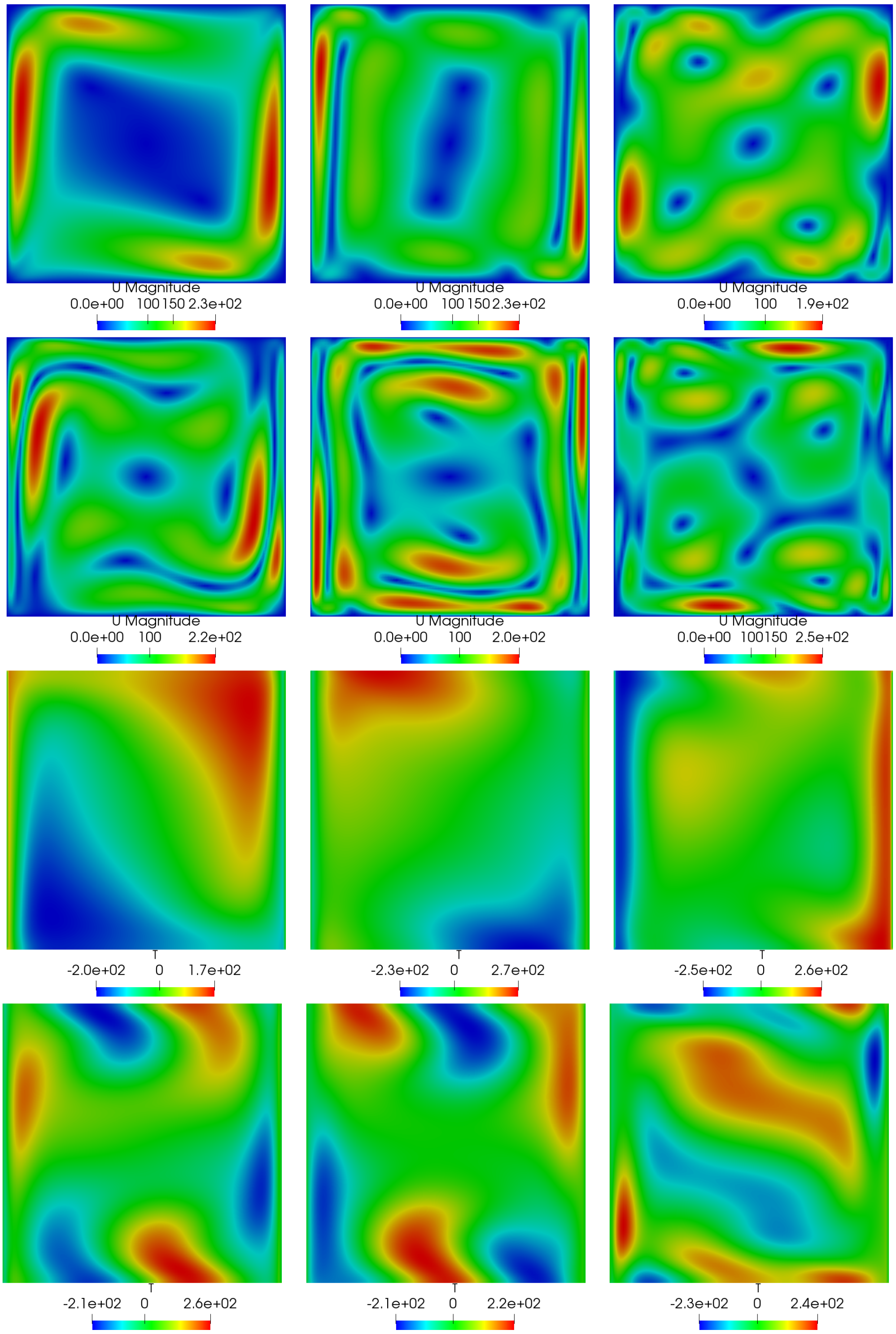

Figure 7.3: First six basis functions for velocity (first two rows) and temperature (last two rows).

The relative L^2 error between the FOM and ROM solutions, for the testing value of the kinematic viscosity ($\nu = 1.65 \times 10^{-5}$), is plotted in figure (7.4). As the flow starts at rest, the error on both velocity and temperature fields is higher during the first iterations of the simulation. After a few seconds, it drops to approximately 4% for velocity, while, for temperature, it remains low (less than 0.009%) throughout the simulation. Statistics of the relative L^2 error are shown in table (7.5). In the work of (Star, Stabile, Georgaka, Belloni, Rozza, and Degroot 2019), the same numerical experiment is discussed, while the parametrisation is applied on the temperature inlet boundary conditions. A non-trained ROM was studied and, for temperature difference of $\Delta\theta = 4K$, the ROM exhibits some instabilities and the L^2 error grows to rather large values. In contrast, the trained ROM presented in this chapter appears to be more stable, even for a larger temperature difference ($\Delta\theta = 5K$).

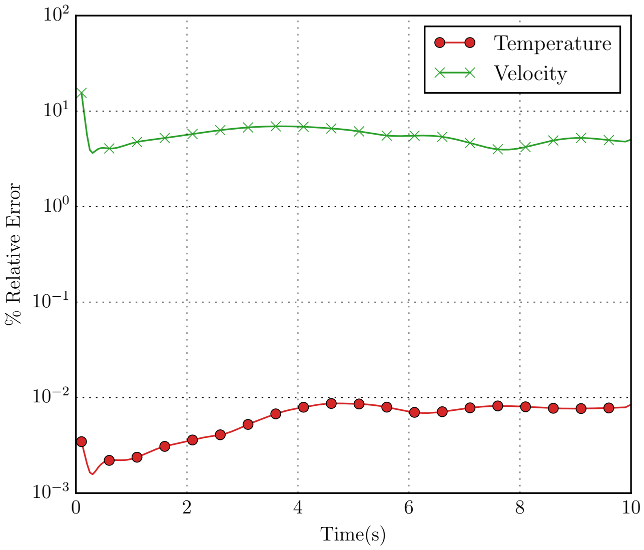

Figure 7.4: $\%\epsilon_{L^2}(t)$ error for velocity and temperature fields for $\nu = 1.65 \times 10^{-5}$.

Table 7.5: Relative $\epsilon_{L^2}(t)\%$ error for velocity and temperature fields.

	$\boldsymbol{u}$	θ
Minimum $\epsilon_{L^2}(t)\%$	3.64	0.0015
Maximum $\epsilon_{L^2}(t)\%$	15.53	0.009
Average $\epsilon_{L^2}(t)\%$	5.50	0.006

The FOM and ROM velocity and temperature fields, as well as their absolute difference, are visualised for time instances $t = 5s$ and $t = 10s$ in figures (7.5), (7.6) and (7.7) where the reconstructed fields appear to be in good agreement.

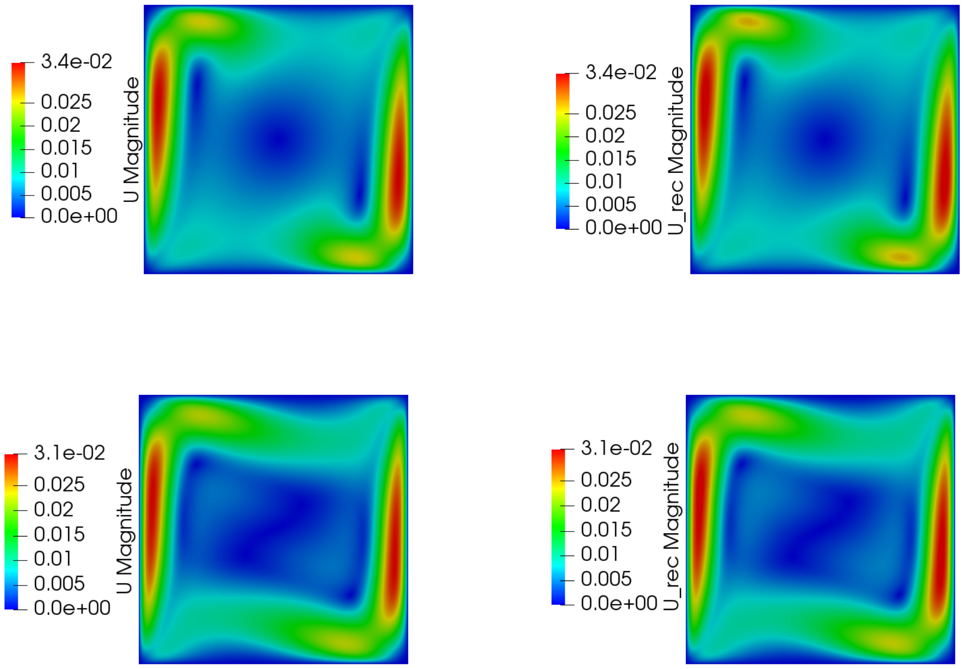

Figure 7.5: Comparison of the velocity field for the full order (first column) and reduced order model (second column). The fields are depicted for time instances equal to $t = 5$s (first row) and 10s (second row).

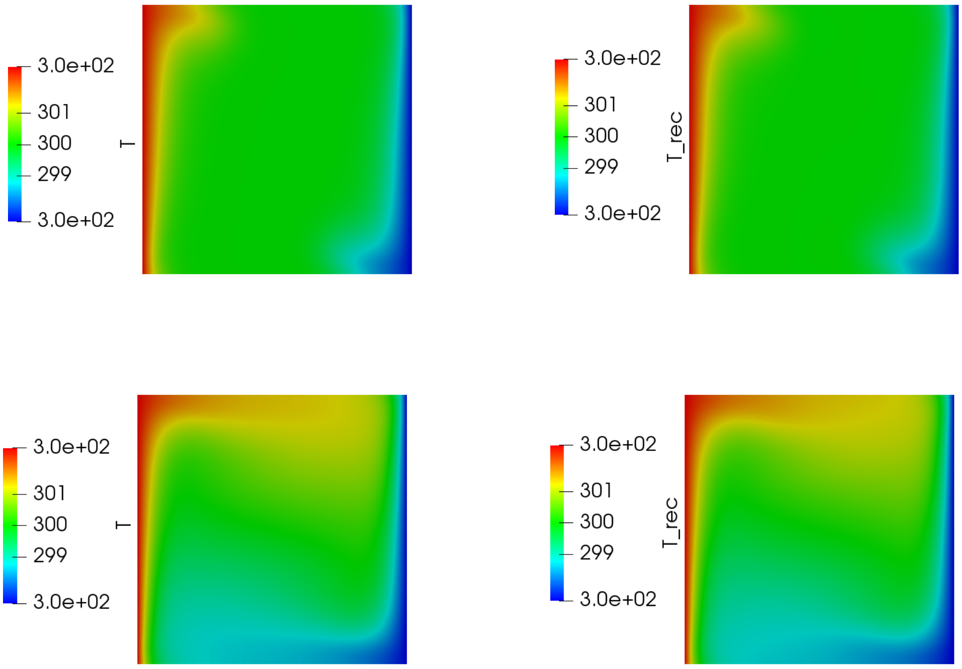

Figure 7.6: Comparison of the temperature field for the full order (first column) and reduced order model (second column). The fields are depicted for time instances equal to $t = 5$s (first row) and 10s (second row).

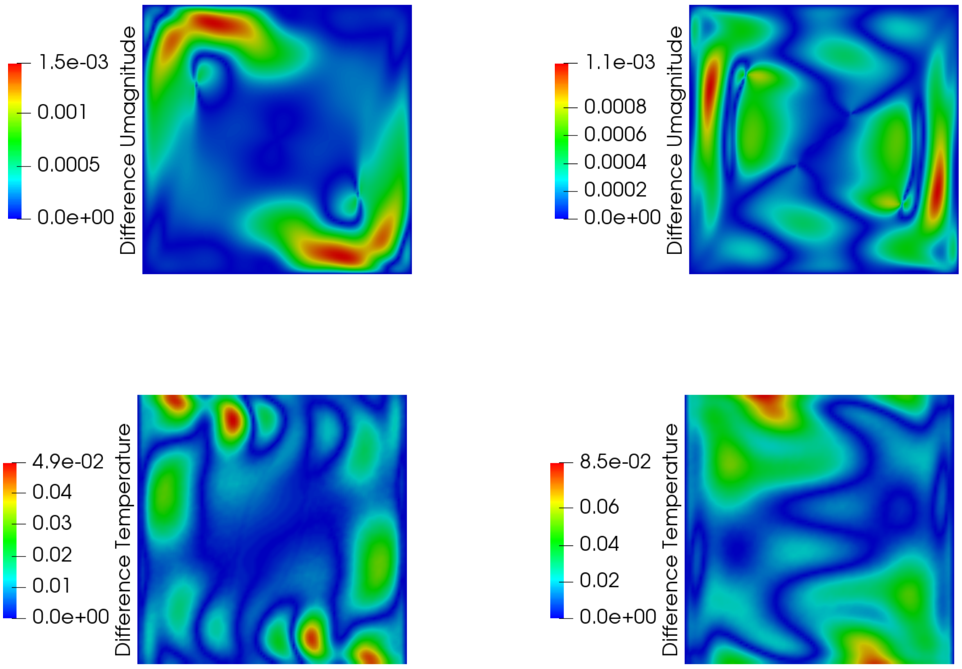

Figure 7.7: Difference between the FOM and ROM for velocity (first row) and temperature (second row) fields. The fields are depicted for time instances equal to $t = 5$s (first row) and 10s (second row).

A comparison between the velocity streamlines and temperature isotherms is illustrated in figures (7.8) and (7.9). For the streamlines, which are in good agreement, two clockwise rotating vortices approaching the corners can be observed. This pattern is characteristic of Rayleigh numbers in the order of 10^5 (Garoosi, Garoosi, and Hooman 2014). The FOM and ROM isotherms are also in good agreement, showing almost horizontal lines in the central region, indicating that the heat is mainly transfered by convection.

Figure 7.8: Comparison of the velocity streamlines for the full order (left) and reduced order model (right) corresponding to Rayleigh number in the order of 10^5.

Figure 7.9: Comparison of the temperature isotherms for the full order (left) and reduced order model (right) corresponding to Rayleigh number in the order of 10^5.

The vertical velocity and temperature profiles in the horizontal mid-plane at $t = 2.5s$ and $t = 10s$ are plotted in figure (7.10). From the plot, it can be oberved that the ROM approximates the FOM profile very well. Table (7.6) shows the CPU time for the FOM, POD, projection and ROM solution, where a computational speed-up of ≈ 75 has been achieved.

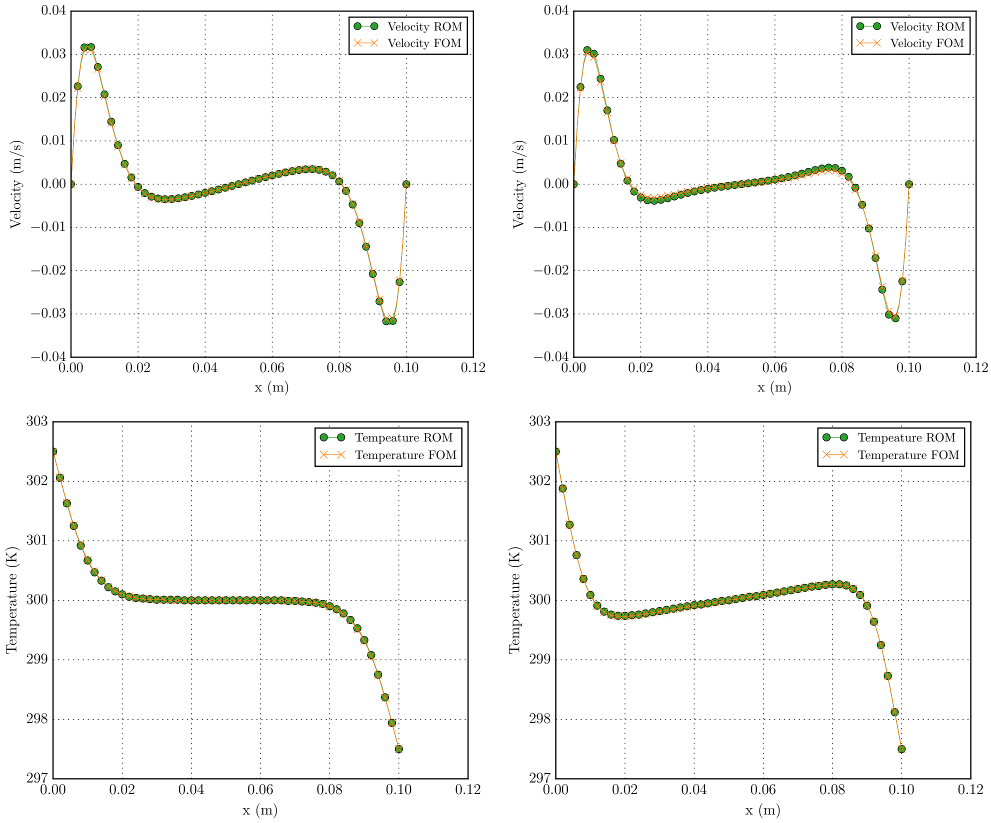

Figure 7.10: Comparison of the FOM and ROM vertical velocity and temperature profiles in the horizontal mid plane $y = D/2$, for $t = 2.5$s and $t = 10$s.

	ROM	FOM
POD (s)	89.83	N/A
Projection (s)	11.02	N/A
Solution (s)	7.52	563

Table 7.6: Computational time for the full order (running on a single processor) and reduced order models.

7.5 Reduced Order Framework - Open Flows

In the previous section, an enclosed flow configuration had been considered and the gradient of pressure term, as well as the recovery of it, had been neglected. However, this is not always the case. For instance, when open flows are studied, this assumption is invalid and can lead to erroneous ROM results, as discussed in chapter 4. In this section, the PPE method has been chosen as a way of including the pressure in the ROM level. Since the *buoyantBoussinesqPimpleFoam* solver exploits a PPE for tackling the velocity-pressure coupling, a similar method employed in the reduced level, could result to a more consistent approximation.

The implementation of the PPE method presented in section (4.6) is adapted to account for the buoyancy force. The momentum and PPE equations are modified to accomodate for the extra body force term, as follows:

$$\begin{cases} \frac{\partial \boldsymbol{u}}{\partial t} + \boldsymbol{\nabla} \cdot (\boldsymbol{u} \otimes \boldsymbol{u}) - \nabla \cdot \nu \nabla \boldsymbol{u} = -\nabla p_{rgh} - (\boldsymbol{g} \cdot \boldsymbol{r}) \nabla \rho & \text{in } Q, \\ \Delta p_{rgh} = -\nabla \cdot (\boldsymbol{u} \cdot \nabla \boldsymbol{u}) - (\boldsymbol{g} \cdot \boldsymbol{r}) \Delta \rho, & \text{in } Q, \\ \frac{\partial \theta}{\partial t} + (\nabla \cdot \boldsymbol{u}) \theta - \alpha_{dif} \Delta \theta = 0 & \text{in } Q, \end{cases} \tag{7.5.1}$$

where, instead of the static pressure p, the shifted p_{rgh} pressure is now considered, so that there is a consistency between the OpenFOAM and the ROM solvers. The Galerkin projection of the above equations is according to the equations derived in 4.3:

$$\begin{cases} \langle (\frac{\partial \boldsymbol{u}}{\partial t} + \boldsymbol{\nabla} \cdot (\boldsymbol{u} \otimes \boldsymbol{u}) - \nabla \cdot \nu \nabla \boldsymbol{u} + \nabla p_{rgh} + (\boldsymbol{g} \cdot \boldsymbol{r}) \nabla \rho), \boldsymbol{\phi}) \rangle_{L_2(\Omega)} = 0, \\ \langle \nabla p_{rgh}, \nabla \psi \rangle_{L_2(\Omega)} + \langle \nabla \cdot (\boldsymbol{u} \cdot \nabla \boldsymbol{u}), \psi \rangle_{L_2(\Omega)} + \langle (\boldsymbol{g} \cdot \boldsymbol{r}) \Delta \rho, \psi \rangle_{L_2(\Omega)} = 0, \\ \langle (\frac{\partial \theta}{\partial t} + \nabla \cdot (\boldsymbol{u} \theta) - \alpha_{dif} \Delta \theta), \chi \rangle_{L_2(\Omega)} = 0. \end{cases} \tag{7.5.2}$$

The modified ROM equations are:

$$\begin{cases} \boldsymbol{M} \dot{\boldsymbol{\alpha}} = -\boldsymbol{P} \boldsymbol{b} - \boldsymbol{\alpha}^T \boldsymbol{Q} \boldsymbol{\alpha} + \nu \boldsymbol{L} \boldsymbol{\alpha} - \boldsymbol{B} \boldsymbol{b}, \\ \boldsymbol{K} \dot{\boldsymbol{c}} = -\boldsymbol{\alpha}^T \boldsymbol{G} \boldsymbol{c} + \alpha_{dif} \boldsymbol{N} \boldsymbol{c}, \\ \boldsymbol{D} \boldsymbol{b} = -\boldsymbol{\alpha}^T \boldsymbol{U} \boldsymbol{\alpha} - \boldsymbol{X} \boldsymbol{c}, \end{cases} \tag{7.5.3}$$

where the new matrix, $\boldsymbol{X}$ is defined as:

$$(\boldsymbol{X}_{ij}) = \langle (\boldsymbol{g} \cdot \boldsymbol{r}) \Delta \rho_{k_i}, \psi_j \rangle_{L_2(\Omega)}. \tag{7.5.4}$$

7.6 Numerical Study: "Cold-trap" formation in a U-bend Pipe

To test the proposed ROM, presented in 7.5, a more applied and challenging geometrical configuration is considered. Passive safety systems, such as the natural circulation loop in the primary circuit, are found in modern nuclear power plants. In PWRs the design of the natural circulation loop is such that the steam generator is in a higher elevation with respect to the core. Under normal opearational conditions, the removal of the decay heat, produced in the core, is removed by forced circulation, using centrifugal pumps. In an accident case, should the pumps fail, the decay heat is removed by the natural circulation loop. In a gravity environment, the sufficient temperature difference between the steam generators and the core can generate a flow rate, which removes the decay heat without the need of "artificial" external energy sources.

There are some reactor designs, which use natural circulation during normal operation, for example the VK-50 Russian reactor, or in the emergency heat removal systems, as in the BN-type reactors (sodium cooled fast breader type). For power levels lower than 40% of the full power, BWRs can also operate under natural circulation. The simplified design of the natural circulation loop, resulted by the reduction in components needed, can reduce costs and, most importantly, enhance the safety of nuclear power plants. It is therefore of highly importance to understand the underlying physics and mechanics of natural circulation as well as to predict occasions where the natural circulation could fail to drive the necessary flow rate for cooling.

One of the drawbacks of natural circulation is the lower driving force with respect to the forced circulation systems (eg. pumps). Phenomena such as heat losses due to un-insulated components or pressure drop due to vertical bends could significantly affect the potential of the natural circulation to drive the flow. One particular scenario of such behaviour is called the "cold-trap". Formed in the loop seal, cold-traps can result from flow reversal which is caused by heat losses at the surface of upward flowing pipes. In addition, the lower driving forces that characterise the natural circulation could give rise to 3D phenomena. Therefore, the thermal-hydraulic behaviour of such systems should be carefully examined.

The study of the “cold-trap” in a U-bend pipe has been selected in order to assess the ability of ROMs to model such complex behavior and potentially predict the formation of such phenomena. This study does not aim to replace current established computational methods, such as the coupled systems codes and CFD but to suggest an alternative, modern computational approach, which could lead to much faster high fidelity simulations.

7.6.1 Steady-State

The configuration, which is representative of reactor primary loop seal (figure 7.11), consists of a 3D U-bend pipe as shown in figure 7.12. A detailed study of “cold-trap” formation in such geometry has been studied in (Sebilleau 2016). The geometrical parameters of the pipe domain are also summarized on table 7.7. To achieve an established natural circulation prior to appling the cooling, a steady-state simulation is performed, using the *simpleFoam* solver. At this stage, the energy equation as well as buoyancy effects are not taken into account and only the hydrodynamic profiles are of interest. Therefore, the blue area in figure 7.12 is neglected. The initial Reynolds number is Re= 1900 and, therefore, the flow is considered laminar. Atmospheric pressure is taken as reference for all the computations and the initial temperature of the inlet water is at $363.15K$ (this temperature applies for the unsteady simulation only). Under these conditions, the properties of the water are summarized in table 7.8.

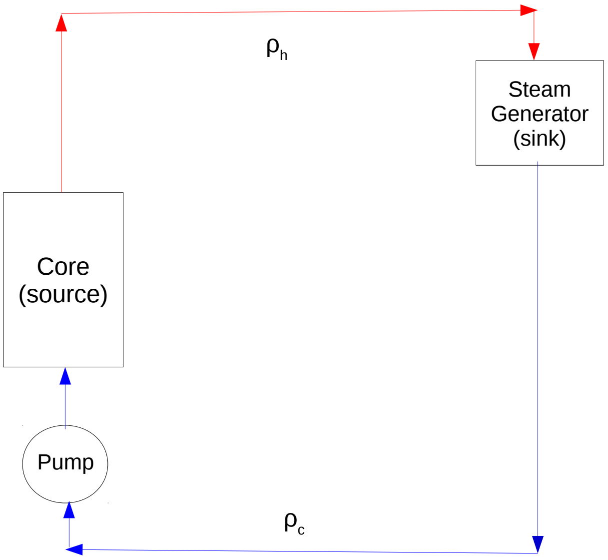

Figure 7.11: Nuclear reactor primary loop schematic.

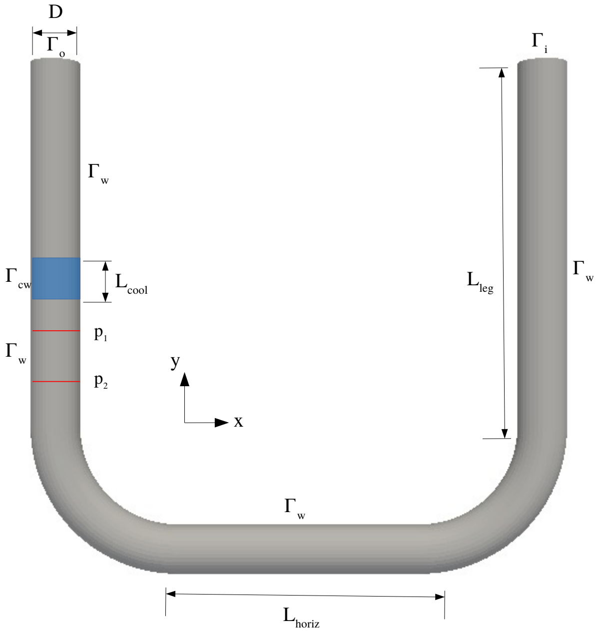

Figure 7.12: U-bend pipe configuration and region of sampling positions for the plots.

Quantity	Value
D (m)	0.2
L_{leg} (m)	1.5
L_{cool} (m)	0.16
L_{horiz} (m)	1.0

Table 7.7: Summary of the geometrical parameters of the U-bend pipe configuration.

Quantity	Value
Kinematic Viscosity ν (m^2s^{-1})	3.14×10^{-7}
Density ρ_0 (kgm^{-3})	961.65
Thermal expansion coefficient β (K^{-1})	6.95×10^{-7}
Thermal conductivity k ($Wm^{-1}k^{-1}$)	0.677
Gravity magnitude (ms^{-2})	9.81

Table 7.8: Summary of water properties at $368.15K$ and atmospheric pressure.

The computational mesh, consisting of 85050 hexahedral cells, is illustrated in figure (7.13). In order to achieve a pressure driven flow, a *pressureInletOutletVelocity* (PIOV) is prescribed on the velocity inlet and outlet. This boundary condition assigns a *zeroGradient* condition for outflow, while for the inflow, the velocity is calculated from the flux in the normal direction. A *noSlip* condition is applied on the pipe walls. For pressure, a *totalPressure* is assigned on the inlet and outlet of the pipe with a kinematic pressure (p/ρ) difference $\Delta p = 0.000007m^2s^{-2}$. This corresponds to about $\Delta p = 0.007Pa$. This condition assigns a user-specified reference pressure, p_0, for outflow and for inflow, the pressure is calculated as $p_0 - 1/2|\boldsymbol{u}|^2$. The boundary conditions are summarized in table (7.9).

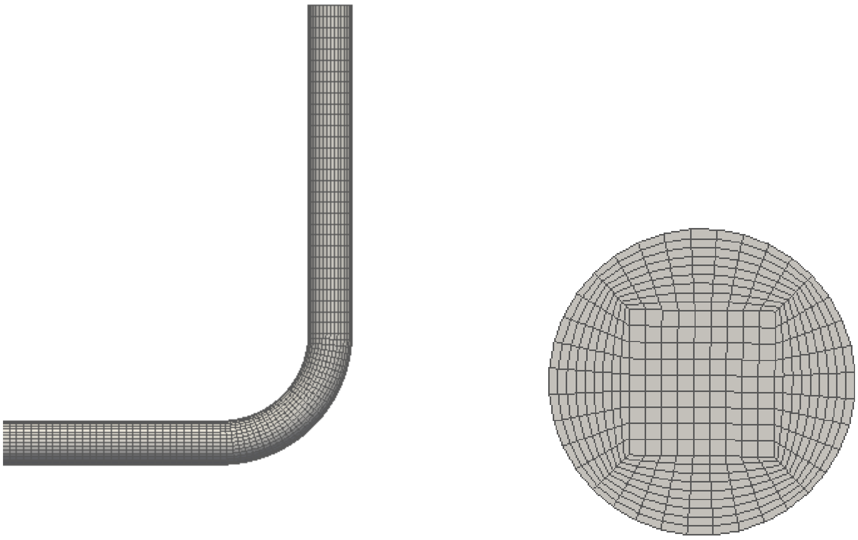

Figure 7.13: Mesh layout of the U pipe.

	Γ_i	Γ_o	Γ_w	Γ_{cw}	Γ_{IF}
$\boldsymbol{u}$	$PIOV$	$PIOV$	$(0,0,0)$	$(0,0,0)$	$(0,0,0)$
p	1	0.999993	$\nabla p \cdot \boldsymbol{n}$	$\nabla p \cdot \boldsymbol{n}$	0.999993

Table 7.9: Summary of the boundary conditions for the U pipe - steady-state case.

The convergence criteria (tolerance) for the SIMPLE algorithm set to 1×10^{-10} for both velocity and pressure. Figure (7.14) depicts the behaviour of the velocity components and pressure residuals with respect to the number of iterations. To ensure that the solution converges, the flow rate at the inlet patch is monitored, as shown in figure (7.15). According to this figure, the flow rate reaches a steady value after about 1400 iterations, and therefore, the simulation was manually stopped, before the residuals reach the prescribed convergence criteria. At this point, the velocity and pressure profiles are shown in figure (7.16).

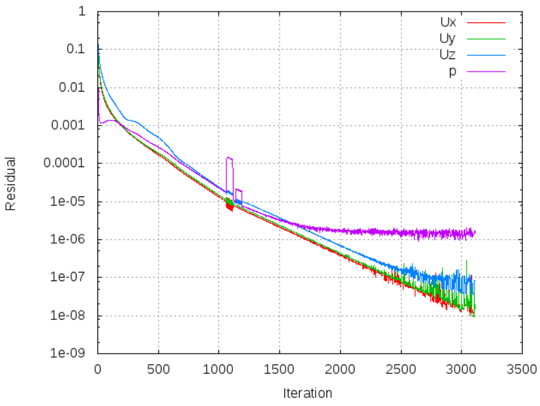

Figure 7.14: Convergence of the residuals in the steady-state case.

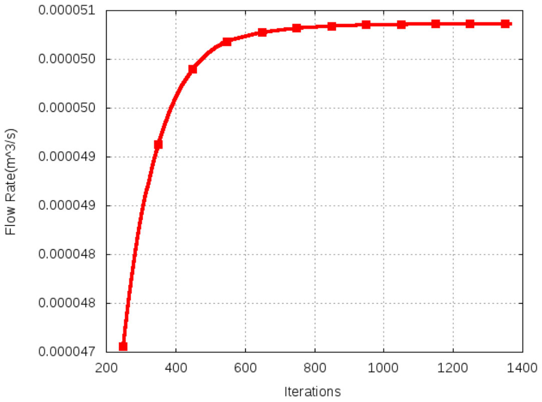

Figure 7.15: Convergence of the flow-rate in the steady-state case.

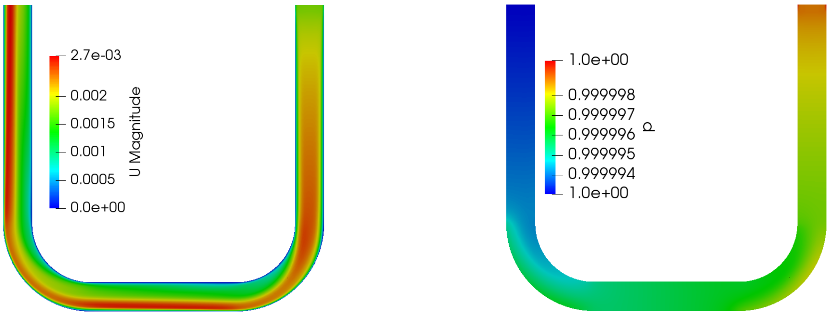

Figure 7.16: Steady-state velocity and pressure profiles.

7.6.2 Unsteady-State Case

For the unsteady-state simulation, local heat losses on the left leg of the U-bend geometry are represented by a uniform constant heat flux applied on the blue patch, as shown in figure (7.12). The heat losses are, for example, a consequence of the uninsulated pump shown in figure (7.11), which is colder than the coolant temperature. Three arbitrary cooling heat flux cases are studied, where the heat flux values are shown in table (7.10). B and C cases have been selected *a posteriori*, after assessing the behaviour of the ROM for the case A. The transient *buoyantBoussinesqPimpleFoam* solver is selected for the FOM, with a time-step of $dt = 1s$ and total time of simulation equal to $710s$. The total duration of the simulation has been selected so that to allow the flow rate to drop very close to zero, as shown in figure (7.17), for the case A.

Case	Cooling heat flux (Wm^{-2})
A	10
B	5
C	2

Table 7.10: Cooling cases.

The boundary conditions used for the FOM are shown in table (7.11). In the Γ_i, the fully developed velocity profile obtained from the steady-state simulation of the previous subsection is used as inlet condition for velocity. For the hydrostatic pressure, p_{rgh}, the pressure profile from the steady-state case is prescribed as initial boundary condition. The value of the internal field, Γ_{IF}, is set to a constant temperature of $363.15K$, while the boundary Γ_{cw}, which represents the cooling patch, is assigned a uniform cooling heat flux. The rest of the pipe walls are under the adiabatic condition. The boundaries are shown in figure (7.12) and Γ_{IF} represents the initial internal field value. Regarding the discretisation schemes, the second-order implicit backward scheme is used for the transient term, upwind (first-order accurate) for the divergence and central differencing (second-order accurate) for the diffusion term (table 7.12).

	Γ_i	Γ_o	Γ_w	Γ_{cw}	Γ_{IF}
$\boldsymbol{u}$	profile from steady-state case				
p_{rgh}	profile from steady-state case				
θ	363.15	$\nabla\theta \cdot \boldsymbol{n} = 0$	$\nabla\theta \cdot \boldsymbol{n} = 0$	*heatFlux* -10	363.15

Table 7.11: Summary of the boundary conditions for the U pipe - unsteady case.

With the above settings, and considering scenario A (-10Wm^{-2}), a reduction in the flow rate and a resulting downflow are observed, as shown in figure (7.17). According to this figure, the flow rate drops to zero after about 700s. This phenomenon is termed as "cold-trap", and is formed due to the ability of the buoyant force to oppose the flow. Of course, the formation of the "cold-trap" is geometry and condition dependent. In this geometry, due to the large pipe diameter, tiny cooling is sufficient to suppress the flow. The interest in this work is to assess the ability of the ROM to predict this phenomenon.

	FOM	ROM
$\partial/\partial t$	Backward	Backward
$\nabla\cdot$	Upwind	Upwind
Δ	Central	Central

Table 7.12: Numerical Schemes for FOM and ROM.

The ROM (ITHACA-FV) is tested on the same boundary and physical conditions as those defined for the FOM. Therefore, this is a non-parametric case. For the pressure, the PPE method is used. During the training, a sampling frequency of 1Hz was initially selected. For the total duration of the simulation this makes 700 snapshots for each field, hence the initial dimension of the POD spaces is $N_u^s = N_\theta^s = N_{p_{rgh}}^s = 700$. Applying truncation based on the cumulative energy (retain approximately 99.9% of the energy) of the eigenvalues, figure (7.18), the dimension of the resulting POD spaces is reduced to $N_u^r = 8$, $N_\theta^r = 2$ and $N_{p_{rgh}}^r = 1$. The comparison between the ROM and FOM flow rates in terms of their $\%L^2$ relative error is shown in figure

(7.19). For the case A, both models follow a decreasing trend. However, there are some discrepancies in the rate of reduction. At $t = 700s$, the ROM flow rate reaches the very small value 2.15×10^{-6} while the FOM flow rate is 2.40×10^{-6}. This leads to a relative error of 10.7%.

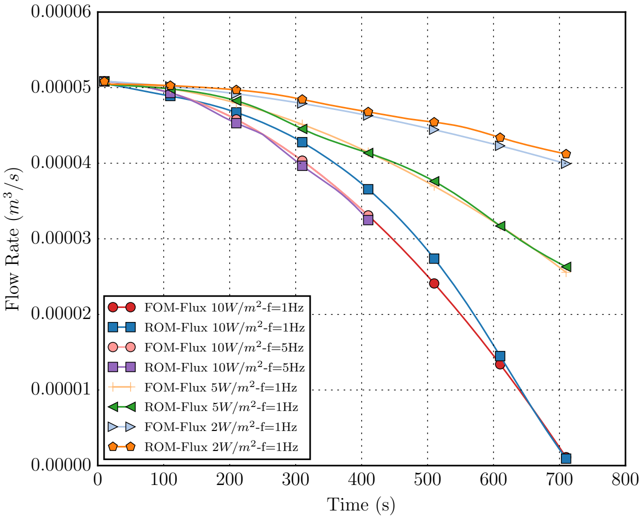

Figure 7.17: Comparison between the FOM and ROM flow rate for the various cooling scenarios and sampling frequencies. The data is acquired in the outlet patch.

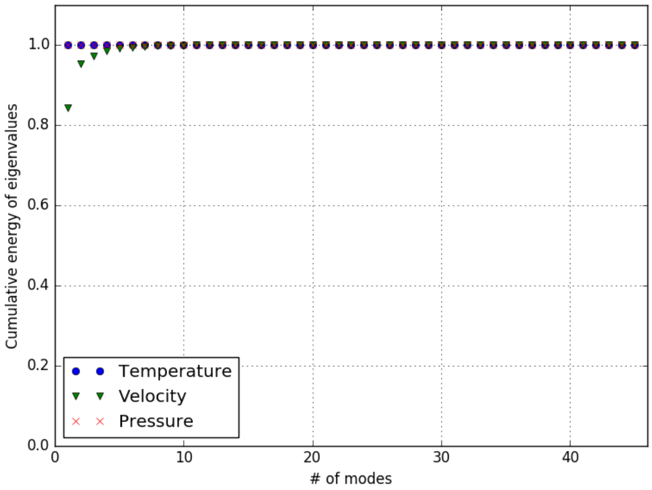

Figure 7.18: Cumulative energy of the velocity, temperature and pressure eigenvalues.

The relative $\epsilon_{L^2}(t)\%$ for velocity, temperature and p_{rgh} pressure fields is depicted in figures (7.20), where the average error for velocity is 14.37%, for temperature is 6.52% and for pressure is 3.75%. Figures (7.21) show the average truncation $\epsilon_{L^2}(t)$ error for velocity, temperature and pressure fields, with respect to the number of modes retained in the projection phase. In this case, the fields are obtained from

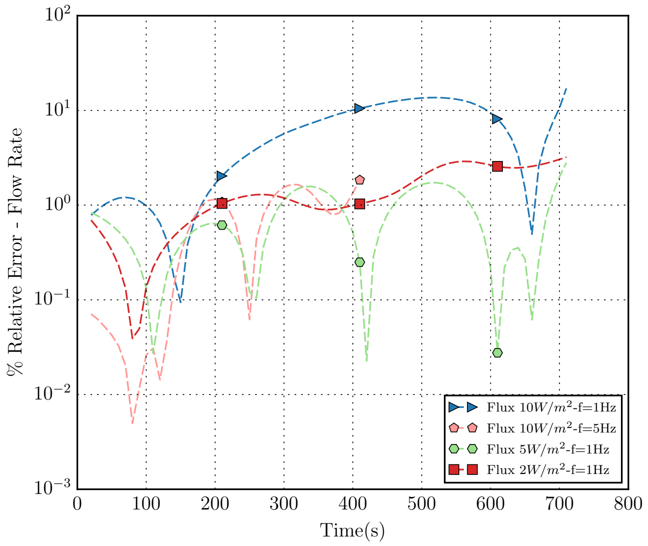

Figure 7.19: % Relative error between the FOM and ROM flow rates for various cooling scenarios and sampling frequencies.

their approximations (following equations 4.1.10) with the temporal coefficients calculated from the basis projection (4.1.21).

The figures suggest that, the higher the number of retained modes are, the smaller the truncation error is. Furthermore, according to these figures, for the number of modes that have been selected prior to the Galerkin projection, 8 for velocity, 2 for temperature and 1 for pressure, the average $\epsilon_{L^2}(t)\%$ for velocity is close to 8%, for temperature 0.5% and for pressure around $5 \times 10^{-4}\%$. Although this is almost true for the velocity relative error resulted from the ROM, for temperature field the average relative error is one order of magnitude larger and for pressure the average error is much higher (3.75%).

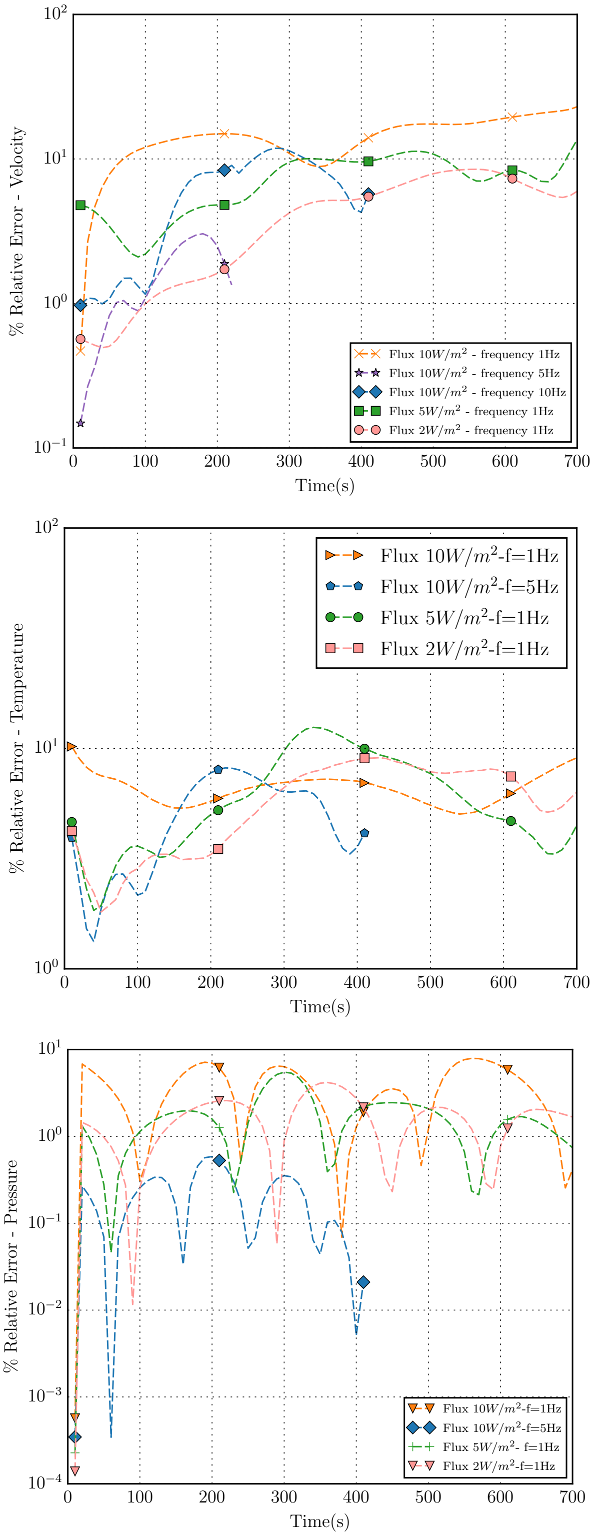

Figure 7.20: Relative $\epsilon_{L^2}(t)\%$ errors for velocity, temperature and pressure fields for various cooling fluxes and sampling frequencies.

To investigate possible sources of the error in the velocity field, two strategies have been followed. The first one is to check the response of the ROM to lower cooling heat fluxes and the second one is to follow a denser sampling strategy. Regarding the first one, two more cooling heat fluxes have been studied, shown in table (7.10). The ROM is trained on these values with sampling frequency of $1Hz$, resulting in 700 snapshots. All the other conditions remain the same, including same number of retained modes with the previous case. Figures (7.17) and (7.19) plot the flow rate and the relative percentage errors for these two new cases. The ROM and FOM flow rates for cases B and C look to deviate much less than in case A. Of course, the flow rate in cases B and C have not dropped to or near zero but, for the duration of the $700s$, the error between the FOM and the ROM appears to be lower than in the case A (figure 7.19). Comparing for the same flow rate values (horizontally in figure (7.17), again, cases B and C deviate less. The relative $\epsilon_{L^2}(t)\%$ errors for velocity, temperature and pressure fields are shown in figure (7.20) where the lowest cooling heat flux (case C) exhibits the lowest error.

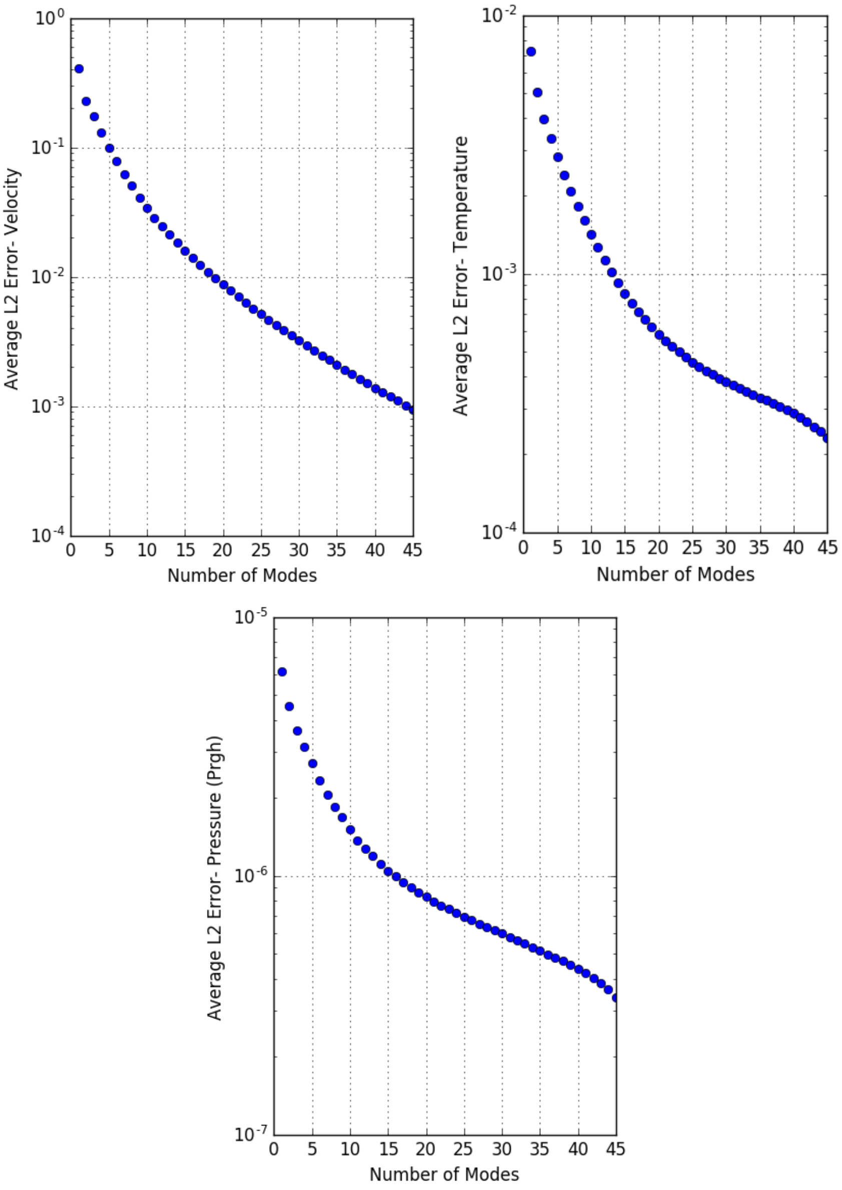

Figure 7.21: Time averaged $\epsilon_{L^2}(t)$ projection error per number of modes for velocity, temperature and pressure (p_{rgh}) fields, respectively.

Regarding the second strategy, fixing the cooling heat flux to the most challenging case A, two sampling frequencies have been tested: $5Hz$ and $10Hz$. The time-step of the FOM and ROM was decreased to $dt = 0.01s$. However, due to memory limitations, this study is limited to $400s$ and $220s$, respectively. The first sampling frequency ($5Hz$ for $400s$) corresponds to a total of 2000 snapshots, while the second to 2200 snapshots. Retaining the same number of modes as in case A and monitoring only the velocity field (which is the one that deviates the most), figure (7.17) shows a much better aggreement between the FOM and the ROM for the two denser sampling rates. According to this figure, for a given simulation duration ($220s$), sampling frequency $10Hz$ results to the most accurate ROM, compared to other two sampling frequencies, while the least accurate is the one derived from $1Hz$ sampling frequency. The complexity of the studied case and the sudden change of the velocity sign, could justify such behaviour. Therefore, adding more snapshots for a given training duration, will result to a more accurate ROM. This fact was not apparent in the laminar T-junction case of chapter 5 (figure 5.14), where, the enhanced training space did not make much difference, since the flow was not as complex as the one that this chapter deals with.

For the rest of the chapter, the discussion focuses on the most challeging case A, for two sampling frequencies: $5Hz$ and $1Hz$. A comparison between the velociy, temperature and pressure (p_{rgh}) ROM derived with sampling frequency $5Hz$ and the FOM is depicted in figures (7.22), (7.23) and (7.24), respectively. The first row of these figures corresponds to time instance $t = 120s$ where the FOM, ROM and their absolute difference is illustrated. Row two corresponds to time instance $t = 400s$. The PPE method has been selected for the pressure field. In all cases, the area with the largest error is around the cooling patch. The maximum error is located mostly on the left wall near the cooling patch.

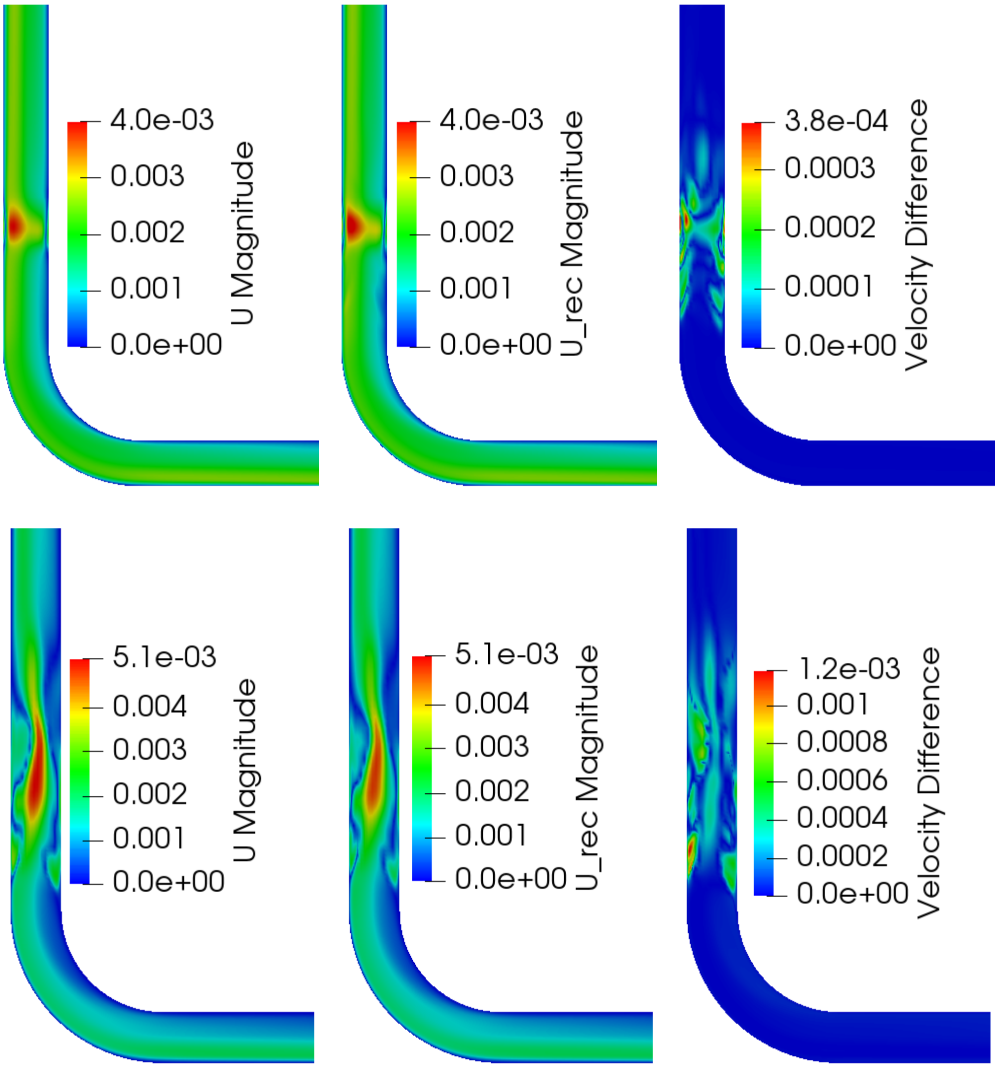

Figure 7.22: Comparison between the FOM and ROM for velocity field for sampling frequency $f = 5Hz$ (first two columns). The fields are depicted for time instances equal to $t = 120$s (first row) and 400s (second row). The third column depicts the absolute difference between the FOM and ROM velocity fields.

The maximum error for the velocity field is lower at $t = 120s$, while for temperature, the opposite behaviour is observed. The energy equation is linear and, in regards to the temperature field, the changes are relatively small. However, as cold water accumulates in the vertical position, the buoyant force term in the momentum equation becomes stonger with time and therefore opposes the flow in an increasing way. This fact could partially explain the relative percentage and absolute errors of velocity in figures (7.20) and (7.22). The error of the p_{rgh} pressure field exhibits an oscillatory behaviour but, overall remains less than 8%. Same oscillatory behaviour for pressure is observed in (Hijazi, Stabile, Mola, and Rozza 2019).

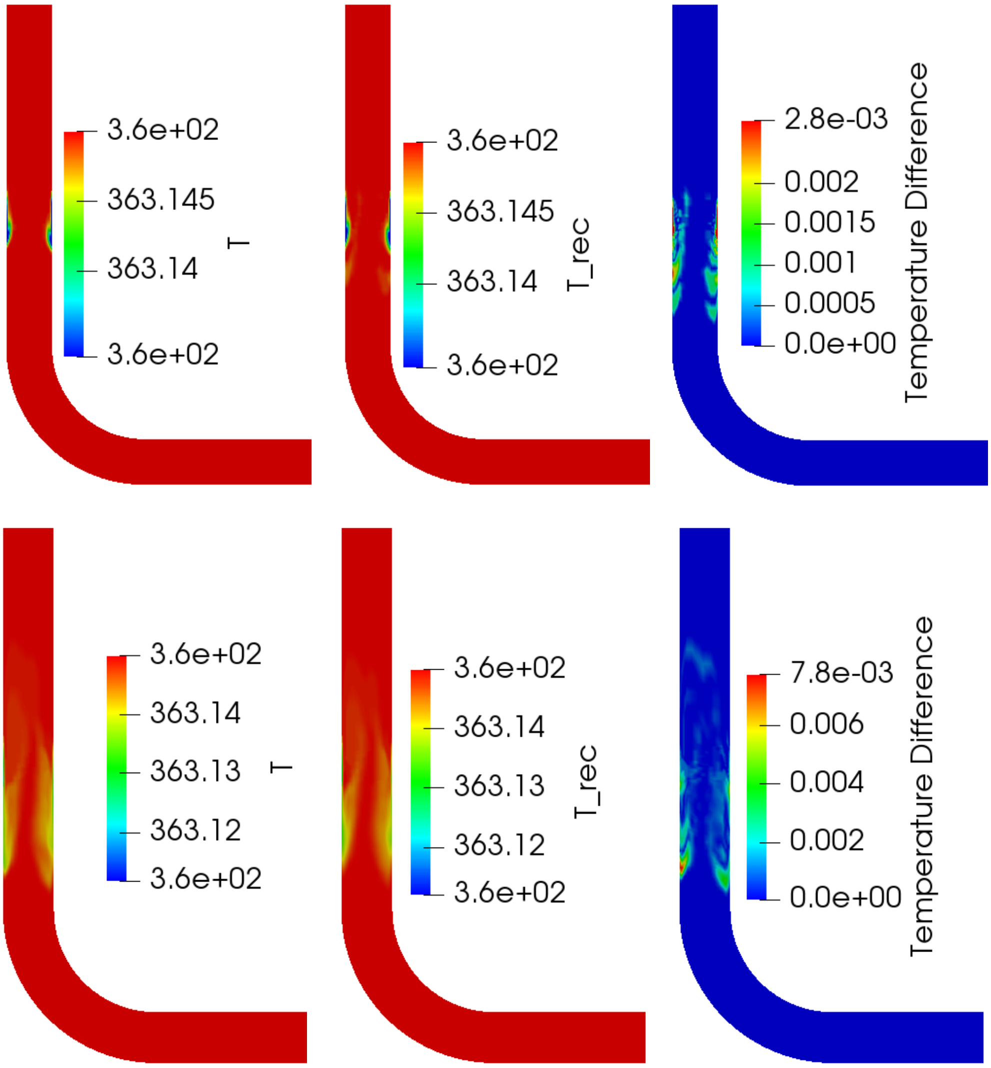

Figure 7.23: Comparison between the FOM and ROM for temperature field for sampling frequency $f = 5Hz$ (first two columns). The fields are depicted for time instances equal to $t = 120$s (first row) and 400s (second row). The third column depicts the absolute difference between the FOM and ROM velocity fields.

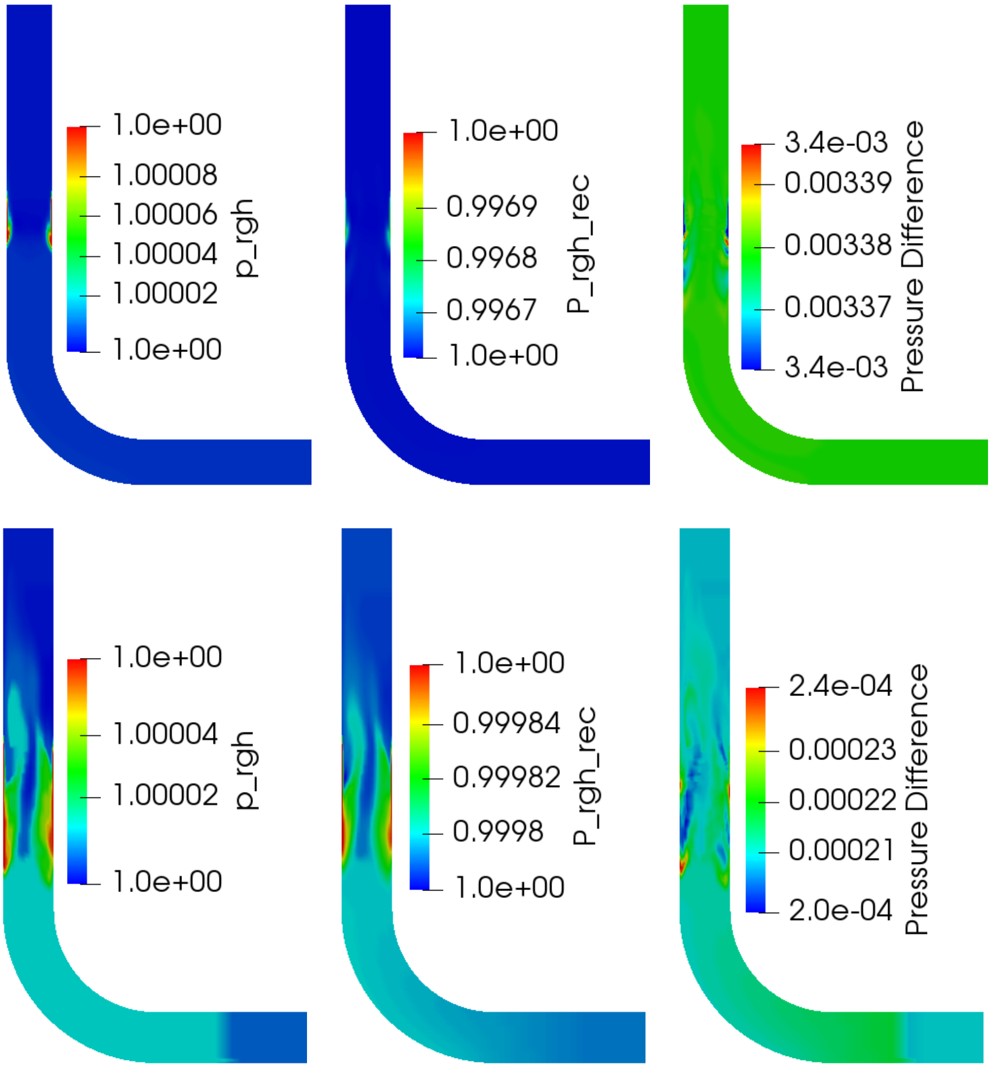

Figure 7.24: Comparison between the FOM and ROM for pressure field (p_{rgh}) for sampling frequency $f = 5Hz$ (first two columns). The fields are depicted for time instances equal to $t = 120$s (first row) and 400s (second row). The third column depicts the absolute difference between the FOM and ROM velocity fields.

Figure (7.25) plots the $y-$component velocity radial profiles at the two sampling locations shown in figure (7.12). The profiles follow the same trend, while the largest difference is observed in pos 2 in the region close to the left wall, where the $y-$velocity takes negative values. The same area is also confirmed in figure (7.22) to exhibit the highest error.

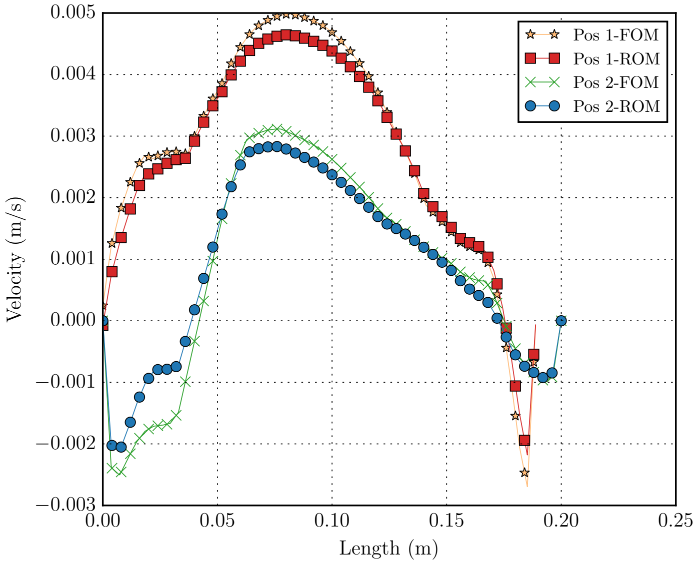

Figure 7.25: Comparison between the FOM and ROM radial velocity profiles at $t = 400$s. Pos 1 and Pos 2 correspond to the p1 and p2 locations shown in figure (7.12)

The final case considered in this work is a comparison between the PPE and the SUP methods. For the comparison, the ROM of the case A, with sampling frequency $1Hz$ has been selected. A case where the pressure gradient and the reconstruction of pressure field are neglected has also been also studied ("No Pressure"). Unlike the previous cases, two pressure modes are retained, therefore $N^r_{p_{rgh}} = 2$. The rest of the conditions remain the same. Figure (7.26) plots the relative $\epsilon_{L^2}(t)\%$ errors for velocity, temperature and pressure fields, for PPE, SUP and no-pressure cases. A velocity field with high relative error is resulted, when the pressure gradient is neglected. The average error in this case is 102%, indicating than the pressure gradient can not be neglected. The temperature field follows the same behaviour, much higher error for the no-pressure case (maximum relative error is 25.5%) which is mainly triggered by the coupling between the momentum and energy equations.

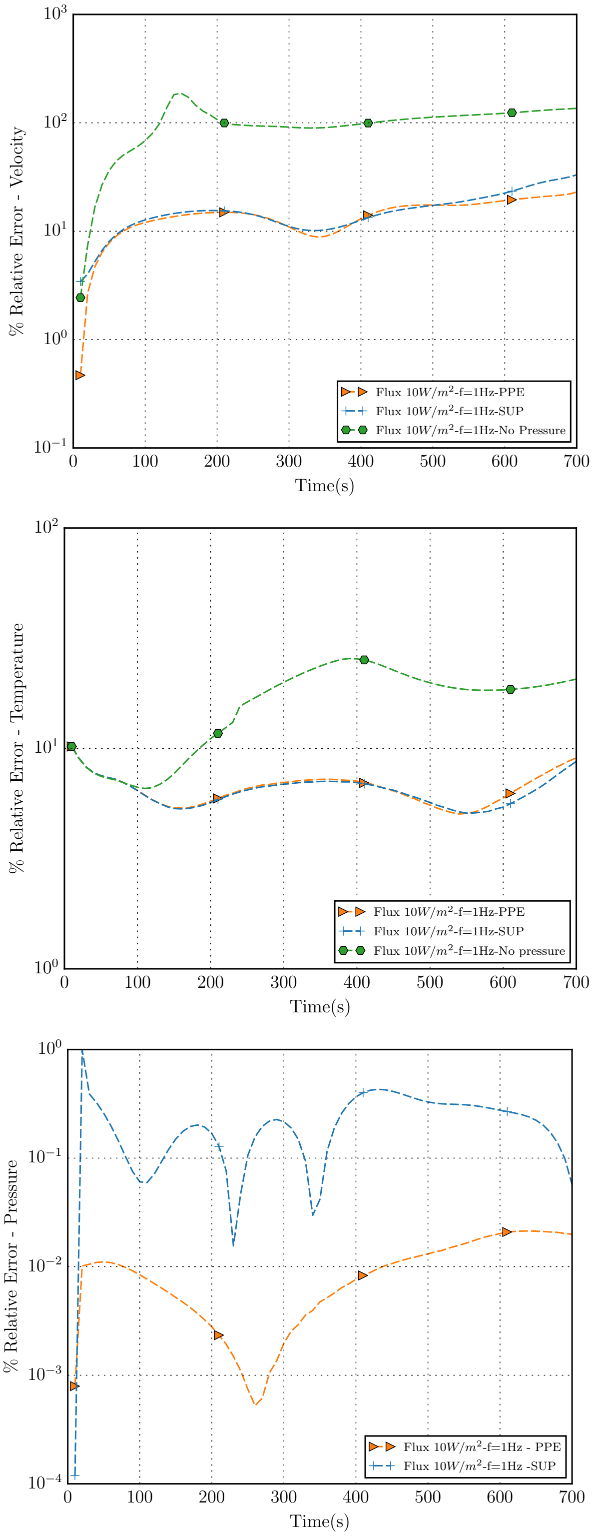

Figure 7.26: Relative $\epsilon_{L^2}(t)\%$ errors for velocity, temperature and pressure fields for cooling flux $10Wm^{-2}$ and sampling frequency $1Hz$. The errors are shown for the PPE, SUP and no pressure gradient cases.

Further to this, both PPE and SUP methods result to similar results. The PPE method exhibits better perfomance for the velocity during the final time-steps, while the SUP method is performing slighlty better for the temperature field. Regarding pressure, clearly, the PPE method results to a better approximation for the given number of modes. Adding one more pressure mode to the approximation, the average error for pressure dropped to 0.016% compared to 3.75% of the single mode approximation. The error also looks smoother than the cases where only one p_{rgh} mode were retained. A comparison for the ROM-PPE, ROM-SUP and FOM flow rates and their corresponding relative percentage error is plotted in figures (7.27) and (7.28), where similar accuracy of both methods is achieved.

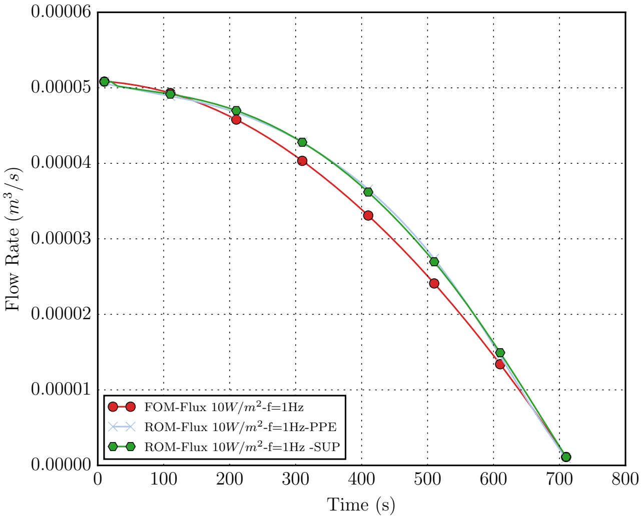

Figure 7.27: Comparison between the FOM, PPE-ROM and SUP-ROM flow rate for cooling flux $10Wm^{-2}$ and sampling frequency $1Hz$. The data is acquired in the outlet patch.

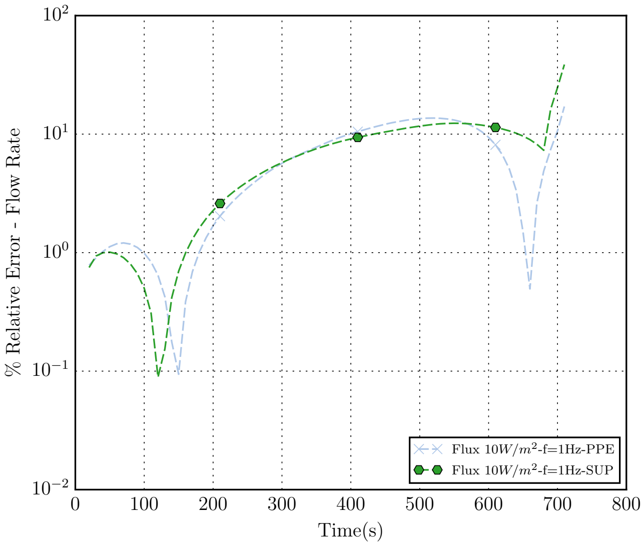

Figure 7.28: Relative $\epsilon_{L^2}(t)\%$ errors of the flow rate for between the FOM and PPE-ROM and SUP-ROM, for cooling flux $10Wm^{-2}$ and sampling frequency $1Hz$.

Figures (7.29), (7.30) and (7.31) show snapshots of velocity, temperature and pressure of the FOM, PPE-ROM, SUP-ROM and no-pressure-ROM, respectively. The first row corresponds to the FOM, PPE-ROM, SUP-ROM and no-pressure-ROM at $t = 700s$ while the second row depicts the absolute difference between the FOM and the PPE-ROM, SUP-ROM and no-pressure-ROM, respectively. The maximum error is in agreement with the error plots (7.26) and is located close to the left wall region.

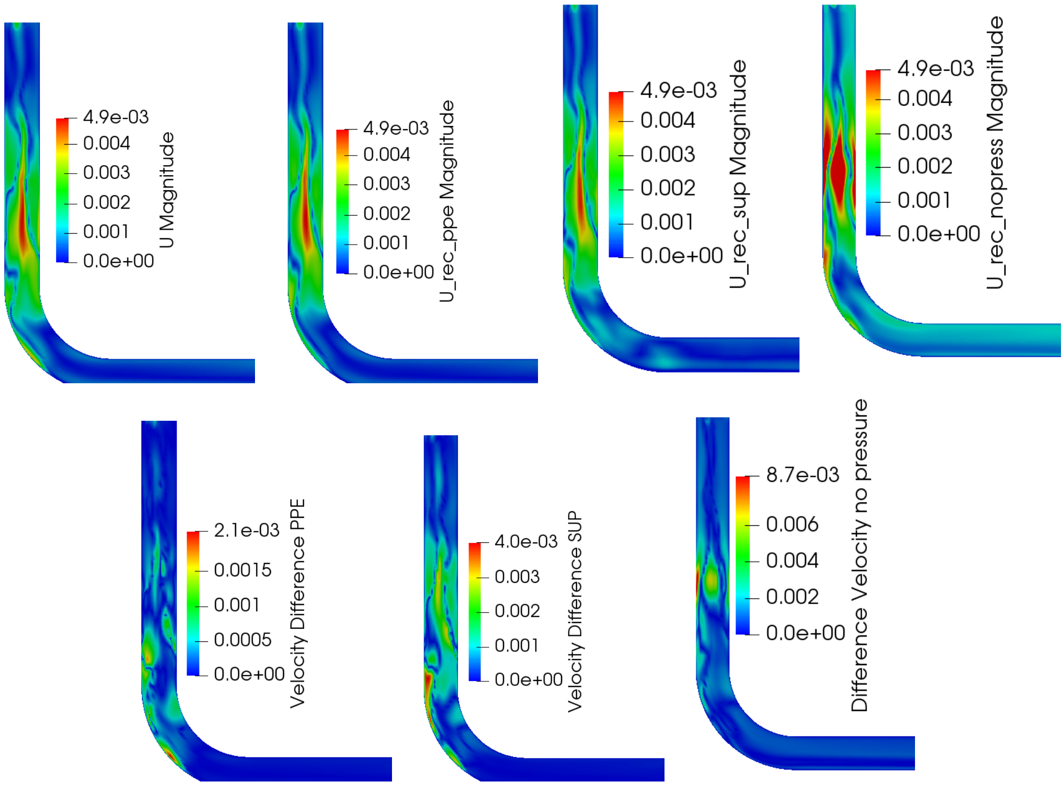

Figure 7.29: Comparison between the FOM, PPE-ROM, SUP-ROM and no-pressure gradient ROM for velocity fields for sampling frequency $f = 1Hz$. The fields are depicted for time instances equal to $t = 700$s. The second row depicts the absolute difference between the FOM and each-ROM velocity fields.

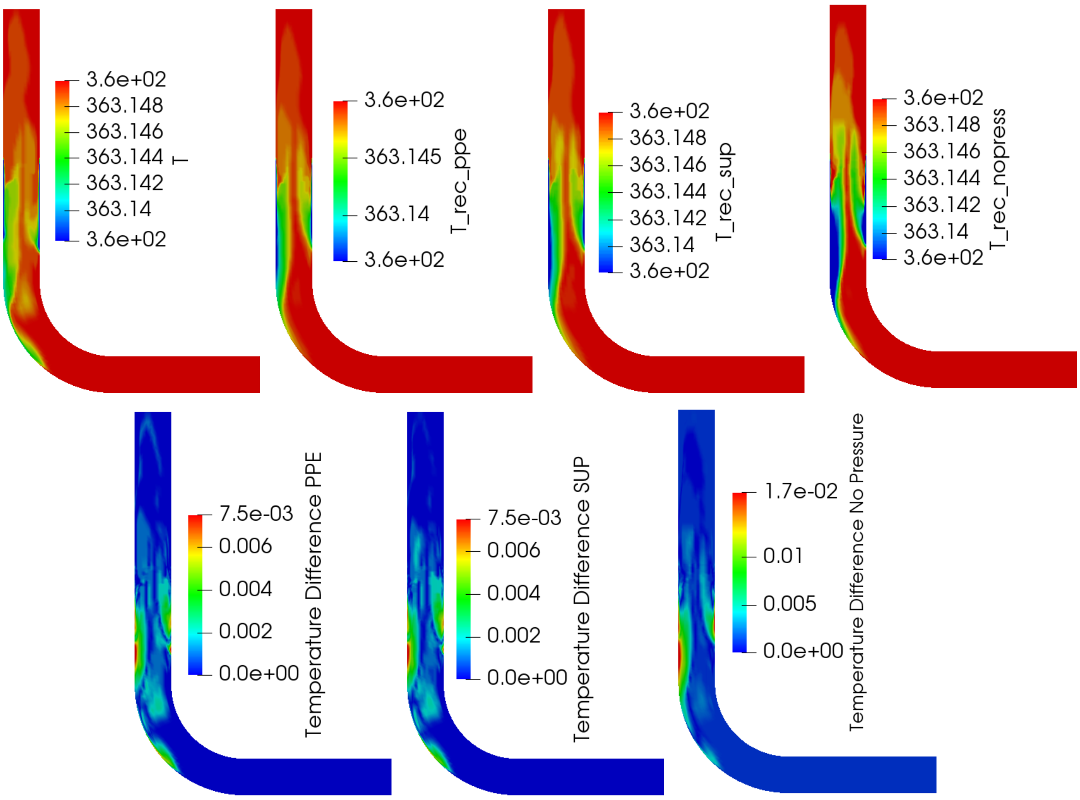

Figure 7.30: Comparison between the FOM, PPE-ROM, SUP-ROM and no-pressure gradient ROM for temperature fields for sampling frequency $f = 1Hz$. The fields are depicted for time instances equal to $t = 700$s. The second row depicts the absolute difference between the FOM and each-ROM temperature fields.

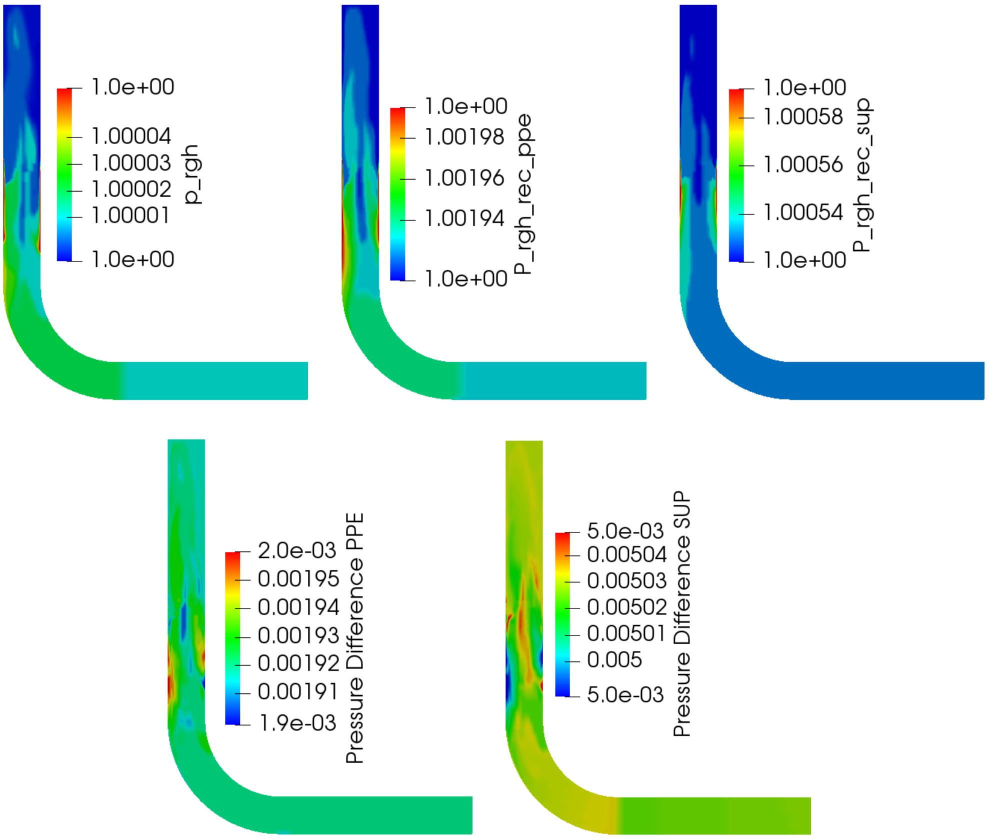

Figure 7.31: Comparison between the FOM, PPE-ROM and SUP-ROM for pressure fields for sampling frequency $f = 1Hz$. The fields are depicted for time instances equal to $t = 700$s. The second row depicts the absolute difference between the FOM and each-ROM pressure fields.

Plots of radial $y-$component velocity profiles at sampling locations p1 and p2 (7.12) of the u pipe are plotted in figures (7.32) and (7.33), respectively. In both positions, the PPE-ROM and SUP-ROM deviate the most in the region where the velocity field is negative, close to the walls - right wall of the cold leg in p1 and left wall in p2.

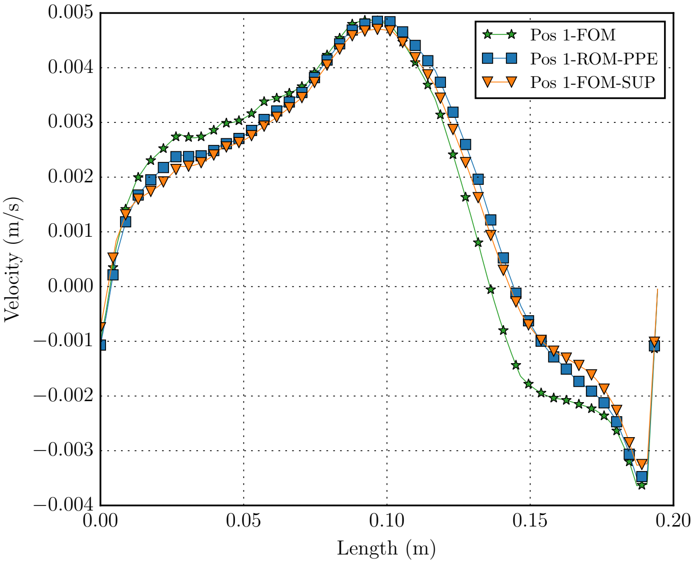

Figure 7.32: Comparison between the FOM and ROM radial velocity profiles at $t = 700$s. Pos 1 corresponds to p1 location shown in figure (7.12)

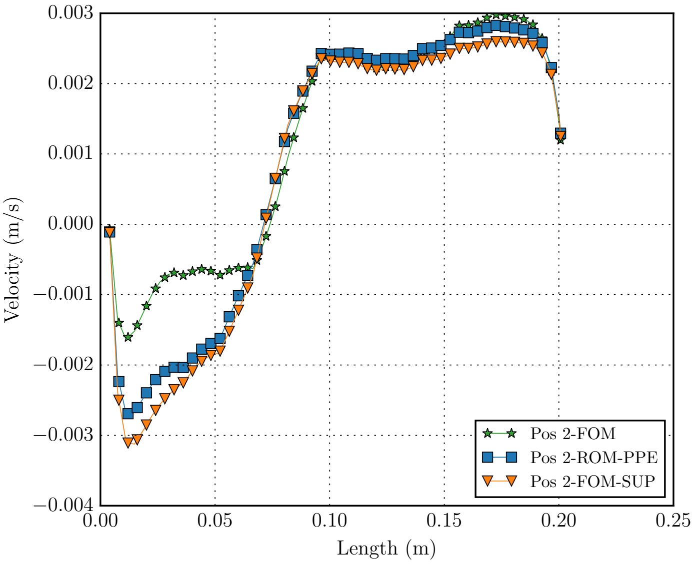

Figure 7.33: Comparison between the FOM and ROM radial velocity profiles at $t = 700$s. Pos 2 corresponds to p2 locations shown in figure (7.12)

	PPE-ROM	SUP-ROM	FOM
POD(s)	83.20	214.91	N/A
Projection(s)	51.07	33.45	N/A
Solution(s)	4.77	4.82	717

Table 7.13: Computational time for the full order (running on a single processor) and reduced order models (700 snapshots.

Table (7.13) shows the computational time for the FOM, POD, Projection and ROM solution. Comparing the solution times between the FOM and the ROM, a speed-up factor of ≈ 150 in the PPE case and of ≈ 149 in the SUP case is obtained. The SUP method is slightly slower because the supremizer modes need to be taken into account. The POD phase in the latter case is also slower. However, in both cases, a considerable speed-up factor has been obtained.

Overall, even in the most 'coarse' sampling case, the PPE-ROM and SUP-ROM can predict the reversal of the flow and the subsequent formation of the "cold-trap", while the former method gives a better approximation of the FOM. As demonstrated, to enhance the accuracy of the ROM, a denser sampling is essential. However, this increases the computational resources required for the offline phase. Hence, there is always a trade-off between accuracy and computational cost.

7.7 Summary of the Chapter

In the above chapter, model order reduction techniques for buoyancy driven flows with the Boussinesq approximation were presented. The parametric POD-Galerkin method fistly applied to enclosed flows, where the pressure term was neglected. A second non-parametric case of the POD-Galerkin was applied to open flows, where, as demonstrated, the pressure gradient should be taken into account. In the former case, the suggested method was applied to a parametric differentially heated square cavity, with parametrized kinematic viscosity. The ROM was tested on a new value of the parameter within the training range and a good approximation of the FOM was achieved. In the latter case, a PPE method was suggested for the coupling between the pressure and velocity fields. To the best of the author's knowledge, a reduced level PPE method accounting also for the gravity term, is, for the first time, applied in this work. This method tested on a U-bend pipe, where, after application of local wall cooling, complex phenomena occur. As demonstrated, given the complexity of the flow, both PPE-ROM and SUP-ROM methods lead to good approximations. In both cases, considerable amount of computational savings have been achieved.

Chapter 8

Synopsis

In this chapter conclusions about this thesis are drawn. A synopsis of the methods and findings of this thesis as well as suggestions for further research are discussed.

8.1 Conclusions

The central scope of this thesis revolved around the research of state-of-the-art model order reduction techniques for applications in the modelling of nuclear reactor thermal hydraulics. As mentioned in the introduction, complex phenomena, such as heat transfer, thermal mixing, natural convection and multiphase flow occur in such systems. Therefore, a high fidelity CFD simulation of these phenomena in complex geometries (e.g. entire power plant) would be computationally intractable. To address this issue, one dimensional system codes, which rely on simplifications, have been extensively used in the nuclear industry for many years. The aim of this work is not to replace these established system codes but to suggest and assess an alternative modelling method, which couples the benefits of the abovementioned methods. Having said this, ROMs would be ideal candidates as they inherit the fidelity of the FOM (CFD), while keeping the computational time low (system codes).

Taking into consideration the nature of the aforementioned systems and some key phenomena that occur, the study focused on the ROM approximation of the incompressible 3D Navier-Stokes coupled with the energy equation. To that extend, amongst various methods for the development of the ROM, the POD-Galerkin method had been selected as the most appropriate method to model such incompressible flows.

The well-known success of the POD method in the calculation of the reduced basis of incompressible flows lies in the property of the POD to optimally describe the kinematic information included in the FOM snapshot realisations. To integrate the dynamics of the FOM into the reduced basis, the POD modes are projected onto the original set of the FOM equations, resulting to a dynamical ROM, which accurately describes the dynamics of the FOM system. The choice of the Galerkin L^2-norm projection method is supported by the definition of the L^2 norm of the velocity solution vector, $\langle \boldsymbol{u} \rangle_{L_2(\Omega)}$, to represent a measure of the global kinetic energy of the system in Ω. Therefore, this norm is physically rational for model order reduction of incompressible flows. Considering this method, the following cases along with their key findings are summarised below:

- In **chapter 5**, a parametric model order reduction method for laminar flows governed by the parametric, transient, 3D Navier-Stokes equations one-way coupled with the energy equation was developed. To the author's knowledge, such setting is presented for the first time in (Georgaka, Stabile, Rozza, and Bluck 2019) and hence in this thesis. The parametric POD-Galerkin method used for the construction of the ROM and tested on thermal-mixing in a 3D T-junction pipe. In particular, two parametric cases were considered: parametrisation of the temperature inlet boundary conditions and parametrisation of the kinematic viscosity. The drive for the parametrisation cases was to demonstrate that, the ROM is able to approximate well a full order solution with different temperature inlet boundary conditions, even without prior training. This fact lies on the one hand in the linearity of the energy equation and on the other hand in the one-way coupling between the momentum and energy equations (no buoyancy is taken into account in this case). However, in the second case, the parametrisation of the kinematic viscosity found in the non-linear convective term, entails a-priori enrichment of the POD space with snapshots from different values of the parameter. Regarding the treatment of the parametrised boundary conditions for temperature, a lifting function method for the energy equation was presented in this work for the first time. For both cases, accurate reduced order approximations of the FOM were achieved with a considerable computational speed-up of 374 and 211, respectively.

- In **chapter 6**, a turbulent version of the previous laminar case was considered. The parametric, transient, 3D Navier-Stokes equations are still one-way coupled with the energy equation, while the URANS $k-\omega$ SST is used for modelling the turbulence. The hybrid PODI-Galerkin with Radial Basis Function interpolation method was developed, where the classical POD-Galerkin method was implemented for the velocity, temperature and pressure fields, while, the eddy viscosity field coefficients were computed with the non-intrusive POD-RBF method. The reason behind choosing an interpolation method and not a projection was to circumvent the projection of the k and ω equations onto the POD basis. This method sets the ROM transparent to each turbulence modelling method used in the FOM (i.e $k-\omega$, $k-\epsilon$, LES etc). A variation of the POD method, the Nested POD was developed and compared against the standard POD, in an attempt to reduce the computational time of the standard POD method for problems with large parametric spaces. The aforementioned methods were applied to the modelling of thermal mixing in T-junction. Parametrisation introduced on the velocity inlet boundary conditions and ten sets of training points were considered. The ROM was tested on four sets of new parameter values within the training range achieving good accuracy with errors of less than 3% for the velocity field in all cases. The comparison between the nested and standard POD methods implemented on the best approximated set of boundary conditions, showed almost similar accuracy in the approximation of the fields, while the nested POD results to a faster computation of the POD phase.

- In **chapter 7**, strong coupling between the momentum and energy equations was studied, where, for the FOM, the Boussinesq approximation was applied. Two POD-Galerkin ROM cases were considered: an enclosed flow, where the pressure term is neglected and, an open flow case, where the pressure is incorporated in the ROM with the PPE method. In both cases, the Rayleigh numbers correspond to laminar flow and hence no turbulence modelling is considered. The enclosed ROM was tested on natural convection in a parametric differentially heated square cavity, where the kinematic viscosity, was chosen as the varied parameter. The pressure-free POD-Galerkin ROM, tested on a non-trained value of the kinematic viscosity was in a good agreement with the

FOM. However, the average relative L^2 error for the velocity field appears to be a bit larger (6%) than in the one-way coupled cases of the previous chapters. This is expected since buoyancy driven flows, and hence the strong coupling between the equations, leads to more complex phenomena. The open flow case, with the implentation of a PPE in the reduced level, was tested on a more applied and realistic flow configuration. Influenced by passive safety systems in modern nuclear reactors, the application of interest consisted of a U bend pipe, where a uniform cooling heat flux was suddenly introduced on a part of the wall, during an enstablished natural circulation. Depending on the geometry and conditions of the pipe and hence on the value of the heat flux, a phenomenon of flow reversal and stalling of the flow could occur. The ROM, derived from such configuration, was assessed on the same boundary and physical conditions as those in the FOM. The ROM was able to predict the formation of the so-called "cold-trap" and the subsequent reduction of the flow rate to zero. However, the average relative L^2velocity error was found to be around 14%, higher than all the previous test cases. From the radial velocity plots, it seems that the ROM is struggling with the sudden change of the velocity sign, due to the reversal of the flow. Due to the high complexity of the flow, this error, as demonstrated, could be reduced with a denser training strategy. However, such an approach could be computationally expensive for realistic, industrial cases. A comparison between the PPE and SUP methods showed that the PPE method is able to approximate the velocity and pressure fields better. Indeed, an implementation of the PPE method in the reduced level leads to a ROM, which is more consistent with the solution approach (PISO/PIMPLE algorithm) of the FOM.

General Observations: All the test cases used in this thesis led to high computational speed-ups, while keeping the L^2 error between the FOM and the ROM within reasonable levels. Of course, the threshold of the accuracy between the two models is usually case/application dependend and each user should define the levels of accepted error accordingly. The same is happening in CFD, where, depending on the application, the level of accuracy of a particular simulation is a multiparametric function: depends on the resolution of the mesh, the boundary conditions, the tolerance of the residuals, the turbulence modelling, etc.

The accuracy of the ROM is also a multiparametric function. A first inshight in the accuracy of the POD-Galerkin ROM starts during the training phase - the quality and the number of the snapshots can have a strong influence on the accuracy of the ROM, as observed in chapter 7, as well as in the work of (Sirisup and Karniadakis 2004) and (Akhtar, Nayfeh, and Ribbens 2009a). If a specific information (such as bifurcation) is missing from the snapshots, it will be missing from the ROM too. This is crucial especially for flows that undergo strong changes. The laminar case of chapter 5 did not show much improvement when a denser POD basis was constructed. However, in chapter 7, the coarser training space led to a less accurate ROM. The number of retained POD modes also affects the accuracy of the ROM. In theory, as the munber of modes in the approximation expansion of the fields increases, the approximation should be closer to the real value of the field.

For turbulent flows, it is known that the POD-Galerkin method exhibits some instabillities, which are more apparent for long-time intergrations. Despite the success of the POD method to rank the modes according to their kinetic energy, instabillities occur, for turbulent flows, due to the truncation of the low-energetic POD modes. The reason is that the turbulent small scales are the most dessipative ones. Excluding these modes from the POD basis leads to a less dissipative ROM. As addressed in chapter 6, several methods have been proposed to tackle this issue. The need of incorporation of these dissipative modes into the ROM is apparent in figure (6.8), where the L^2 error grows in time. The approach followed in this thesis, influenced by the approach used in one or two equation turbulence models, was to stabilise the ROM momentum equation by incorporating the eddy viscosity field into the ROM equations. Snapshots for eddy viscosity field were taken and a POD method was applied to extract the most energetic modes. However, unlike the Galerkin projection used for the velocity, temperature and pressure fields, the eddy viscosity coefficients were calculated with a data-driven RBF interpolation method.

Limitations and difficulties of the POD-Galerkin method became apparent in two occasions during this thesis. Firstly, during the computation of the reduced matrix associated with the non-linear convective term, Q_{ijk}, which proved to be computationally expensive both CPU and memory wise. This is due to the dimension of this matrix, which increases with the cube of the number of retained POD basis functions. The second limitation arose in chapter 7, where denser sampling of the POD space was essential. Although the first difficulty did not cause any mojor issues since the retained modes were relatively low, the storage and manipulation of dense data files resulting from more realistic industrial cases was a major obstacle in obtaining an accurate ROM. Nevertheless, the second issue can be easily solved with the use of a computer cluster or computers with a better RAM memory. For problems where a large number of POD modes needs to be retained, efficient computation of the non-linear convective term can be achieved by employing, for instance, a GNAT method based on the gappy-POD as suggested in (Carlberg, Farhat, Cortial, and Amsallem 2013) or the Discrete Empirical Interpolation Method (DEIM) (Chaturantabut and Sorensen 2010).

Overall, although this study could not by any mean be exhaustive in terms of the various exhisting model order reduction techniques, the proposed POD-Galerkin and the hybrid PODI-Galerkin ROMs studied in this thesis proved to be a promising alternative to tackle current difficulties associated with the modelling of nuclear reactor thermal hydraulics. A few future suggestions on improving the proposed method are discussed in the following section.

8.2 Outlook

Based on the findings of this thesis, further investigation is suggested below:

- The proposed ROM in chapter 6 was based on URANS modelling of the FOM. It is known that, for the studied T-junction application, predictions made by URANS models are not very accurate. It would be interesting to test and compare the behaviour of a ROM constructed from LES or DNS data. A comparison with experimental results would add even more value to the accuracy of the POD-Galerkin method. In addition, the assumption that the T-junction velocity inlets are under a fixed value could be replaced with a fully developed profile in order to be compliant with current studies in litterature.
- In the solution of the ROM, a monolithic approach for the coupling between the momentum and pressure equations was followed. However, the family of *PISO*

and *PIMPLE* solvers are based on a segregated approach. This causes some incosistencies between the ROM and the FOM. A segregated approach could improve even more the ROM accuracy.

- In chapter 7, the study of the U-bend pipe was not parametric. A parametrisation of such problem entails some difficulties: expensive training as well as incorporation of a parametrised heat flux boundary condition (Neumann boundary condition) in the ROM. For the latter, a penalty approach, which explicitly imposes the heat flux in the ROM, suggested in (Vergari, Cammi, and Lorenzi 2020) could be followed. A turbulent version of this problem would also be of interest.
- This study accounted only one-phase flows. However, two-phase flow heat transfer is also encounter in nuclear reactor thermal hydraulics and therefore it would be an interesting extension to the current research.

Bibliography

Akhtar, I., A. H. Nayfeh, and C. J. Ribbens (July 2009a). "On the stability and extension of reduced-order Galerkin models in incompressible flows. A numerical study of vortex shedding". In: *Theoretical and Computational Fluid Dynamics* 23.3, pages 213–237. DOI: `10.1007/s00162-009-0112-y` (cited on page 160).

— (2009b). "On the stability and extension of reduced-order Galerkin models in incompressible flows". In: *Theoretical and Computational Fluid Dynamics* 23.3, pages 213–237. DOI: `10.1007/s00162-009-0112-y` (cited on page 56).

Aling, H., S. Banerjee, A. K. Bangia, V. Cole, J. Ebert, A. Emami-Naeini, K. F. Jensen, I. G. Kevrekidis, and S. Shvartsman (1997). "Nonlinear model reduction for simulation and control of rapid thermal processing". In: *American Control Conference, 1997. Proceedings of the 1997*. Volume 4. IEEE, pages 2233–2238. DOI: `10.1109/ACC.1997.608956` (cited on page 26).

Alonso, D., A. Velazquez, and J. Vega (2009). "Robust reduced order modeling of heat transfer in a back step flow". In: *International Journal of Heat and Mass Transfer* 52.5-6, pages 1149–1157. DOI: `10.1016/j.ijheatmasstransfer.2008.09.011` (cited on page 26).

Amsallem, D. and C. Farhat (2008). "Interpolation method for adapting reduced-order models and application to aeroelasticity". In: *AIAA journal* 46.7, page 1803 (cited on page 30).

Ayhan, H. and C. N. Sokmen (2012). "CFD modeling of thermal mixing in a T-junction geometry using LES model". In: *Nuclear Engineering and Design* 253. SI : CFD4NRS-3, pages 183–191. ISSN: 0029-5493. DOI: `https://doi.org/10.1016/j.nucengdes.2012.08.010` (cited on pages 13, 88).

Bakewell, H. P. (1967). "Viscous Sublayer and Adjacent Wall Region in Turbulent Pipe Flow". In: *Physics of Fluids* 10.9, page 1880. DOI: `10.1063/1.1762382` (cited on page 24).

Ballarin, F., E. Faggiano, S. Ippolito, A. Manzoni, A. Quarteroni, G. Rozza, and R. Scrofani (2016). "Fast simulations of patient-specific haemodynamics of coronary artery bypass grafts based on a POD Galerkin method and a vascular shape parametrization". In: *Journal of Computational Physics* 315, pages 609–628. ISSN: 0021-9991. DOI: `https://doi.org/10.1016/j.jcp.2016.03.065` (cited on page 29).

Ballarin, F., A. Manzoni, A. Quarteroni, and G. Rozza (2014). "Supremizer stabilization of POD-Galerkin approximation of parametrized steady incompressible Navier-Stokes equations". In: *International Journal for Numerical Methods in Engineering* 102.5, pages 1136–1161. DOI: `10.1002/nme.4772` (cited on pages 29, 56, 57, 101).

Ballarin, F. and G. Rozza (2016). "POD-Galerkin monolithic reduced order models for parametrized fluid-structure interaction problems". In: *International Journal for Numerical Methods in Fluids* 82.12, pages 1010–1034. DOI: `10.1002/fld.4252` (cited on page 29).

Baltzer, J., R. Adrian, and X. Wu (2010). "Turbulent boundary layer structure identification via POD". In: *Proceedings of the summer program*, page 55 (cited on page 25).

Banyay, G. A., M. Ahmadpoor, and J. C. Brigham (2014). "Proper Orthogonal Decomposition Based Reduced Order Modeling of the Very High Temperature Reactor Lower Plenum Hydrodynamics". In: *ASME 2014 4th Joint US-European Fluids Engineering Division Summer Meeting collocated with the ASME 2014 12th International Conference on Nanochannels, Microchannels, and Minichannels*. American Society of Mechanical Engineers, V01DT27A013–V01DT27A013 (cited on page 11).

Barton, I. E. (1998). "Comparison of SIMPLE- and PISO-type algorithms for transient flows". In: *International Journal for Numerical Methods in Fluids* 26.4, pages 459–483. DOI: `10.1002/(SICI)1097-0363(19980228)26:4<459::AID-FLD645>3.0.CO;2-U` (cited on page 38).

Bendotti, P. and C. L. Beck (1999). "On the role of LFT model reduction methods in robust controller synthesis for a pressurized water reactor". In: *IEEE Transactions on Control Systems Technology* 7.2, pages 248–257 (cited on page 11).

Bendotti, P., B. Codrons, C.-M. Falinower, and M. Gevers (1998). "Control oriented low order modelling of a complex PWR plant: a comparison between open loop and closed loop methods". In: *Decision and Control, 1998. Proceedings of the 37th IEEE Conference on*. Volume 3. IEEE, pages 3390–3395 (cited on page 10).

Bergmann, M., C.-H. Bruneau, and A. Iollo (2009). “Enablers for robust POD models”. In: *Journal of Computational Physics* 228.2, pages 516–538. DOI: `10.1016/j.jcp.2008.09.024` (cited on page 56).

Berkooz, G., P. Holmes, and J. L. Lumley (1993). “The proper orthogonal decomposition in the analysis of turbulent flows”. In: *Annual review of fluid mechanics* 25.1, pages 539–575 (cited on pages 24, 45, 47, 48).

Bernero, S. and H. Fiedler (2000). “Application of particle image velocimetry and proper orthogonal decomposition to the study of a jet in a counterflow”. In: *Experiments in Fluids* 29, S274–S281 (cited on page 25).

Boffi, D., F. Brezzi, and M. Fortin (2013). *Mixed Finite Element Methods and Applications.* 1st edition. Springer-Verlag Berlin Heidelberg. ISBN: 978-3-642-36518-8. DOI: `10.1007/978-3-642-36519-5` (cited on page 56).

Borggaard, J., T. Iliescu, and Z. Wang (2011). “Artificial viscosity proper orthogonal decomposition”. In: *Mathematical and Computer Modelling* 53.1, pages 269–279. ISSN: 0895-7177. DOI: `https://doi.org/10.1016/j.mcm.2010.08.015`. URL: `http://www.sciencedirect.com/science/article/pii/S0895717710003894` (cited on page 89).

Bourguet, R., M. Braza, and A. Dervieux (2007). “Reduced-order modeling for unsteady transonic flows around an airfoil”. In: *Physics of Fluids* 19.11, page 111701. DOI: `10.1063/1.2800042` (cited on page 25).

Brands, B., J. Mergheim, and P. Steinmann (2016). “Reduced-order modelling for linear heat conduction with parametrised moving heat sources”. In: *GAMM-Mitteilungen* 39.2, pages 170–188. DOI: `10.1002/gamm.201610011` (cited on page 99).

Brezzi, F. and K.-J. Bathe (1990). “A discourse on the stability conditions for mixed finite element formulations”. In: *Computer Methods in Applied Mechanics and Engineering* 82.1. Proceedings of the Workshop on Reliability in Computational Mechanics, pages 27–57. ISSN: 0045-7825. DOI: `https://doi.org/10.1016/0045-7825(90)90157-H` (cited on page 56).

Buchan, A., C. Pain, F. Fang, and I. Navon (2013a). “A POD reduced-order model for eigenvalue problems with application to reactor physics”. In: *International Journal for Numerical Methods in Engineering* 95.12, pages 1011–1032 (cited on page 11).

— (2013b). “A POD reduced-order model for eigenvalue problems with application to reactor physics”. In: *International Journal for Numerical Methods in Engineering* 95.12, pages 1011–1032 (cited on page 88).

Bui-Thanh, T., M. Damodaran, and K. E. Willcox (2004). “Aerodynamic data reconstruction and inverse design using proper orthogonal decomposition”. In: *AIAA journal* 42.8, pages 1505–1516 (cited on page 25).

Busto, S., G. Stabile, G. Rozza, and M. Vazquez-Cendon (2019). “POD Galerkin reduced order methods for combined Navier Stokes transport equations based on a hybrid FV-FE solver”. In: *Computers Mathematics with Applications*. ISSN: 0898-1221. DOI: `https://doi.org/10.1016/j.camwa.2019.06.026` (cited on page 26).

Caiazzo, A., T. Iliescu, V. John, and S. Schyschlowa (2014). “A numerical investigation of velocity-pressure reduced order models for incompressible flows”. In: *Journal of Computational Physics* 259, pages 598–616. ISSN: 0021-9991. DOI: `http://dx.doi.org/10.1016/j.jcp.2013.12.004` (cited on page 101).

Carlberg, K., C. Farhat, J. Cortial, and D. Amsallem (2013). “The GNAT method for nonlinear model reduction: Effective implementation and application to computational fluid dynamics and turbulent flows”. In: *Journal of Computational Physics* 242, pages 623–647. ISSN: 0021-9991. DOI: `http://dx.doi.org/10.1016/j.jcp.2013.02.028` (cited on page 161).

Chaturantabut, S. and D. C. Sorensen (2010). “Nonlinear model reduction via discrete empirical interpolation”. In: *SIAM Journal on Scientific Computing* 32.5, pages 2737–2764 (cited on page 161).

Chen, X., I. M. Navon, and F. Fang (2011). “A dual-weighted trust-region adaptive POD 4D-VAR applied to a finite-element shallow-water equations model”. In: *International Journal for Numerical Methods in Fluids* 65.5, pages 520–541. DOI: `10.1002/fld.2198`. eprint: `https://onlinelibrary.wiley.com/doi/pdf/10.1002/fld.2198` (cited on page 71).

Clausse, A. and R. T. Lahey (1991). “The analysis of periodic and strange attractors during density-wave oscillations in boiling flows”. In: *Chaos, Solitons & Fractals* 1.2, pages 167–178 (cited on page 9).

Condon, M. and R. Ivanov (2004). “Empirical balanced truncation of nonlinear systems”. In: *Journal of Nonlinear Science* 14.5, pages 405–414 (cited on page 23).

Deane, A. E., I. G. Kevrekidis, G. E. Karniadakis, and S. A. Orszag (1991). “Low-dimensional models for complex geometry flows: Application to grooved channels and circular cylinders”. In: *Physics of Fluids A: Fluid Dynamics* 3.10, pages 2337–2354. DOI: `10.1063/1.857881` (cited on page 56).

Degroote, J., J. Vierendeels, and K. Willcox (2010). “Interpolation among reduced-order matrices to obtain parameterized models for design, optimization and probabilistic analysis”. In: *International Journal for Numerical Methods in Fluids* 63.2, pages 207–230 (cited on page 30).

Dehghan, M. and M. Abbaszadeh (2016). “Proper orthogonal decomposition variational multiscale element free Galerkin (POD-VMEFG) meshless method for solving incompressible Navier–Stokes equation”. In: *Computer Methods in Applied Mechanics and Engineering* 311, pages 856–888 (cited on page 89).

Deparis, S. and G. Rozza (2009). “Reduced basis method for multi-parameter-dependent steady Navier–Stokes equations: applications to natural convection in a cavity”. In: *Journal of Computational Physics* 228.12, pages 4359–4378 (cited on page 30).

Dergham, G., D. Sipp, J.-C. Robinet, and A. Barbagallo (2011). “Model reduction for fluids using frequential snapshots”. In: *Physics of Fluids* 23.6, page 064101 (cited on page 27).

Dokhane, A. (2004). “BWR stability and bifurcation analysis using a novel reduced order model and the system code RAMONA”. In: (cited on page 10).

Dokhane, A., D. Hennig, Rizwan-uddin, and R. Chawla (2007). “Interpretation of in-phase and out-of-phase BWR oscillations using an extended reduced order model and semi-analytical bifurcation analysis”. In: *Annals of Nuclear Energy* 34.4, pages 271–287. ISSN: 0306-4549. DOI: `https://doi.org/10.1016/j.anucene.2006.12.005`. URL: `http://www.sciencedirect.com/science/article/pii/S0306454906002398` (cited on page 10).

Dones, I., S. Skogestad, and H. A. Preisig (2011). “Application of balanced truncation to nonlinear systems”. In: *Industrial & Engineering Chemistry Research* 50.17, pages 10093–10101 (cited on page 23).

Feng, J., T. Frahi, and E. Baglietto (2018). “STRUCTure-based URANS simulations of thermal mixing in T-junctions”. In: *Nuclear Engineering and Design* 340, pages 275–299. ISSN: 0029-5493. DOI: `https://doi.org/10.1016/j.nucengdes.2018.10.002`. URL: `http://www.sciencedirect.com/science/article/pii/S0029549318303765` (cited on page 94).

Flinois, T. L., A. S. Morgans, and P. J. Schmid (2015). “Projection-free approximate balanced truncation of large unstable systems”. In: *Physical Review E* 92.2, page 023012 (cited on page 27).

Frank, T., C. Lifante, H.-M. Prasser, and F. Menter (2010). “Simulation of turbulent and thermal mixing in T-junctions using URANS and scale-resolving turbulence models in

ANSYS CFX". In: *Nuclear Engineering and Design* 240.9. Experiments and CFD Code Applications to Nuclear Reactor Safety (XCFD4NRS), pages 2313–2328. ISSN: 0029-5493. DOI: `https://doi.org/10.1016/j.nucengdes.2009.11.008` (cited on pages 13, 88, 94).

Garoosi, F., S. Garoosi, and K. Hooman (2014). "Numerical simulation of natural convection and mixed convection of the nanofluid in a square cavity using Buongiorno model". In: *Powder Technology* 68, pages 279–292. ISSN: 0032-5910. DOI: `https://doi.org/10.1016/j.powtec.2014.08.006` (cited on page 127).

Georgaka, S., G. Stabile, G. Rozza, and J. M. Bluck (2019). "Parametric POD-Galerkin Model Order Reduction for Unsteady-State Heat Transfer Problems". In: *Communications in Computational Physics* 27.1, pages 1–32. ISSN: 1991-7120. DOI: `https://doi.org/10.4208/cicp.OA-2018-0207` (cited on pages 89, 157).

Ginestar, D., R. Miro, G. Verdu, and D. Hennig (2002). "A transient modal analysis of a BWR instability event". In: *Journal of Nuclear Science and Technology* 39.5, pages 554–563 (cited on page 10).

Glover, K. (1984). "All optimal Hankel-norm approximations of linear multivariable systems and their L,âˆž-error bounds". In: *International journal of control* 39.6, pages 1115–1193 (cited on page 22).

Graham, W. R., J. Peraire, and K. Y. Tang (1999). "Optimal control of vortex shedding using low-order models. Part I:open-loop model development". In: *International Journal for Numerical Methods in Engineering* 44.7, pages 945–972. ISSN: 1097-0207. DOI: `10.1002/(SICI)1097-0207(19990310)44:7<945::AID-NME537>3.0.CO;2-F` (cited on page 61).

Guennebaud, G., B. Jacob, et al. (2010). *Eigen v3*. http://eigen.tuxfamily.org (cited on page 54).

Guerrero, J. (July 2015). *Introduction to Computational Fluid Dynamics: Governing Equations, Turbulence Modeling Introduction and Finite Volume Discretization Basics.* DOI: `10.13140/RG.2.1.1396.4644` (cited on page 40).

Gunzburger, M. D., J. S. Peterson, and J. N. Shadid (2007). "Reduced-order modeling of time-dependent PDEs with multiple parameters in the boundary data". In: *Computer Methods in Applied Mechanics and Engineering* 196.4-6, pages 1030–1047. DOI: `10.1016/j.cma.2006.08.004` (cited on page 61).

Haasdonk, B. and M. Ohlberger (2008). “Reduced basis method for finite volume approximations of parametrized linear evolution equations”. In: *Mathematical Modelling and Numerical Analysis* 42.2, pages 277–302. DOI: `10.1051/m2an:2008001` (cited on page 25).

Hall, K. C., J. P. Thomas, and E. H. Dowell (2000). “Proper orthogonal decomposition technique for transonic unsteady aerodynamic flows”. In: *AIAA journal* 38.10, pages 1853–1862 (cited on page 25).

Han, D., B. Yu, and X. Zhang (2014). “Study on a BFC-Based POD-Galerkin Reduced-Order Model for the Unsteady-State Variable-Property Heat Transfer Problem”. In: *Numerical Heat Transfer, Part B: Fundamentals* 65.3, pages 256–281. DOI: `10.1080/10407790.2013.849989` (cited on page 26).

Hijazi, S., S. Ali, G. Stabile, F. Ballarin, and G. Rozza (2018). “The Effort of Increasing Reynolds Number in Projection-Based Reduced Order Methods: from Laminar to Turbulent Flows” (cited on pages 89, 99).

Hijazi, S., G. Stabile, A. Mola, and G. Rozza (2019). “Data-Driven POD-Galerkin reduced order model for turbulent flows”. In: *submitted* (cited on pages 89, 145).

Hollnagel, E. and Y. Fujita (2013). “The Fukishima disaster - Systemic failures as the lack of resilience”. In: *Nuclear Engineering and Technology* 45.1, pages 13–20. ISSN: 1738-5733. DOI: `https://doi.org/10.5516/NET.03.2011.078`. URL: `http://www.sciencedirect.com/science/article/pii/S1738573315300024` (cited on page 13).

Ilak, M. and C. W. Rowley (2008). “Modeling of transitional channel flow using balanced proper orthogonal decomposition”. In: *Physics of Fluids* 20.3, page 034103 (cited on page 27).

Issa, R. (1986). “Solution of the implicitly discretised fluid flow equations by operator-splitting”. In: *Journal of Computational Physics* 62.1, pages 40–65. ISSN: 0021-9991. DOI: `https://doi.org/10.1016/0021-9991(86)90099-9` (cited on page 38).

Jasak, H. (1996). “Error analysis and estimation for the finite volume method with applications to fluid flows”. PhD thesis. Imperial College, University of London (cited on pages 44, 46, 64).

Kuczaj, A., E. Komen, and M. Loginov (2010). “Large-Eddy Simulation study of turbulent mixing in a T-junction”. English. In: *Nuclear Engineering and Design* 240.9, pages 2116–2122. DOI: `10.1016/j.nucengdes.2009.11.027` (cited on pages 13, 88).

Lall, S., J. E. Marsden, and S. Glavaški (2002). “A subspace approach to balanced truncation for model reduction of nonlinear control systems”. In: *International journal of robust and nonlinear control* 12.6, pages 519–535 (cited on page 23).

Lee, M. W. and E. H. Dowell (2020). “On the Importance of Numerical Error in Constructing POD-based Reduced-Order Models of Nonlinear Fluid Flows”. In: *AIAA Scitech 2020 Forum*. DOI: `10.2514/6.2020-1067` (cited on page 55).

Li, H., Z. Luo, and J. Chen (2011). “Numerical simulation based on POD for two-dimensional solute transport problems”. In: *Applied Mathematical Modelling* 35.5, pages 2489–2498. DOI: `10.1016/j.apm.2010.11.064` (cited on page 26).

Li, K., H. Su, J. Chu, and C. Xu (2013). “A fast-POD model for simulation and control of indoor thermal environment of buildings”. In: *Building and Environment* 60, pages 150–157. DOI: `10.1016/j.buildenv.2012.11.020` (cited on page 26).

Lieu, T., C. Farhat, and M. Lesoinne (2005). “POD-based aeroelastic analysis of a complete F-16 configuration: ROM adaptation and demonstration”. In: *AIAA Paper* 2295.2005, page 910 (cited on page 29).

Lieu, T. and M. Lesoinne (2004). “Parameter adaptation of reduced order models for three-dimensional flutter analysis”. In: *AIAA Paper* 888, page 2004 (cited on page 29).

Liu, F. (2016). “A Thorough Description Of How Wall Functions Are Implemented in Open-FOAM”. In: *Proceedings of CFD with OpenSource Software, 2016, Edited by Nilsson H.* (Cited on page 95).

Lorenzi, S., A. Cammi, L. Luzzi, and G. Rozza (2016). “POD-Galerkin method for finite volume approximation of Navier-Stokes and RANS equations”. In: *Computer Methods in Applied Mechanics and Engineering* 311, pages 151–179. DOI: `10.1016/j.cma.2016.08.006` (cited on page 25).

Lumley, J. L. (1967). “The structure of inhomogeneous turbulent flows”. In: *Atmospheric turbulence and radio wave propagation* (cited on page 24).

Ma, X. and G. Karniadakis (2002). “A low-dimensional model for simulating three-dimensional cylinder flow”. In: *Journal of Fluid Mechanics* 458, pages 181–190. DOI: `10.1017/S0022112002007991` (cited on page 56).

Menter, F. R. (1994). “Two-equation eddy-viscosity turbulence models for engineering applications”. In: *AIAA Journal* 32.8, pages 1598–1605. ISSN: 0001-1452. DOI: `10.2514/3.12149` (cited on page 37).

Merzari, E. and H. Ninokata (2011). “Proper orthogonal decomposition of the flow in a tight lattice rod-bundle”. In: *Nuclear Engineering and Design* 241.11, pages 4621–4632 (cited on page 11).

Miró, R., D. Ginestar, G. Verdú, and D. Hennig (2002). “A nodal modal method for the neutron diffusion equation. Application to BWR instabilities analysis”. In: *Annals of Nuclear Energy* 29.10, pages 1171–1194 (cited on page 10).

Moore, B. (1981). “Principal component analysis in linear systems: Controllability, observability, and model reduction”. In: *IEEE transactions on automatic control* 26.1, pages 17–32 (cited on page 21).

Moukalled, F., L. Mangani, and M. Darwish (2015). *The Finite Volume Method in Computational Fluid Dynamics: An Advanced Introduction with OpenFOAM and Matlab*. 1st. Springer Publishing Company, Incorporated. DOI: `10.1007/978-3-319-16874-6` (cited on pages 41, 42, 44).

Müller, F., P. Jenny, and D. W. Meyer (2011). “Probabilistic collocation and lagrangian sampling for advective tracer transport in randomly heterogeneous porous media”. In: *Advances in Water Resources* 34.12, pages 1527–1538. DOI: `10.1016/j.advwatres.2011.09.005` (cited on page 26).

Munoz-Cobo, J., S. Chiva, and A. Sekhri (2004). “A reduced order model of BWR dynamics with subcooled boiling and modal kinetics: application to out of phase oscillations”. In: *Annals of Nuclear Energy* 31.10, pages 1135–1162 (cited on page 10).

Munoz-Cobo, J. and G. Verdú (1991). “Aplication of Hopf bifurcation theory and variational methods to the study of limit cycles in boiling water reactors”. In: *Annals of Nuclear Energy* 18.5, pages 269–302 (cited on page 9).

Naik-Nimbalkar, V., A. Patwardhan, I. Banerjee, G. Padmakumar, and G. Vaidyanathan (2010). “Thermal mixing in T-junctions”. In: *Chemical Engineering Science* 65.22, pages 5901–5911. ISSN: 0009-2509. DOI: `https://doi.org/10.1016/j.ces.2010.08.017` (cited on pages 13, 88).

Nguyen, C., G. Rozza, D. Huynh, and A. T. Patera (2010). *Reduced basis approximation and a posteriori error estimation for parametrized parabolic PDEs; application to real-time Bayesian parameter estimation*. Technical report. John Wiley & Sons (cited on page 30).

Noack, B. R., P. Papas, and P. A. Monkewitz (2005a). “The need for a pressure-term representation in empirical Galerkin models of incompressible shear flows”. In: *Journal of Fluid Mechanics* 523, pages 339–365. DOI: `10.1017/S0022112004002149` (cited on page 56).

— (2005b). “The need for a pressure-term representation in empirical Galerkin models of incompressible shear flows”. In: *Journal of Fluid Mechanics* 523, pages 339–365. DOI: `10.1017/S0022112004002149` (cited on page 101).

Noor, A. K. and J. M. Peters (1980). "Reduced basis technique for nonlinear analysis of structures". In: *Aiaa journal* 18.4, pages 455–462 (cited on page 30).

OpenFOAM user guide (2016-2017). Accessed: 2020-03-25. URL: `https://www.openfoam.com/documentation/guides/latest/doc/guide-turbulence-ras-k-omega-sst.html` (cited on page 37).

OpenFOAM website (2011-2012). Accessed: 13-10-2017. URL: `https://openfoam.org/` (cited on pages 39, 176).

Ostrowski, Z., R. A. Bialecki, and A. J. Kassab (2008). "Solving inverse heat conduction problems using trained POD-RBF network inverse method". In: *Inverse Problems in Science and Engineering* 16.1, pages 39–54. DOI: `10.1080/17415970701198290` (cited on page 89).

Pasetto, D., A. Guadagnini, and M. Putti (2011). "POD-based Monte Carlo approach for the solution of regional scale groundwater flow driven by randomly distributed recharge". In: *Advances in Water Resources* 34.11, pages 1450–1463. DOI: `10.1016/j.advwatres.2011.07.003` (cited on page 26).

Patankar, S. and D. Spalding (1972). "A calculation procedure for heat, mass and momentum transfer in three-dimensional parabolic flows". In: *International Journal of Heat and Mass Transfer* 15.10, pages 1787–1806. ISSN: 0017-9310. DOI: `https://doi.org/10.1016/0017-9310(72)90054-3`. URL: `http://www.sciencedirect.com/science/article/pii/0017931072900543` (cited on page 37).

Payne, F. and J. L. Lumley (1967). "Large eddy structure of the turbulent wake behind a circular cylinder". In: *The Physics of Fluids* 10.9, S194–S196 (cited on page 24).

Pernebo, L. and L. Silverman (1982). "Model reduction via balanced state space representations". In: *IEEE Transactions on Automatic Control* 27.2, pages 382–387 (cited on page 22).

Quarteroni, A., A. Manzoni, and F. Negri (2016). *Reduced Basis Methods for Partial Differential Equations*. Springer International Publishing. ISBN: 9783319154305. DOI: `10.1007/978-3-319-15431-2` (cited on page 50).

Raghupathy, A. P., U. Ghia, K. Ghia, and W. Maltz (2009). "Boundary-condition-independent reduced-order modeling of complex 2D objects by POD-Galerkin methodology". In: *2009 25th Annual IEEE Semiconductor Thermal Measurement and Management Symposium*. IEEE. DOI: `10.1109/stherm.2009.4810765` (cited on page 26).

Ravindran, S. S. (2000). “A reduced-order approach for optimal control of fluids using proper orthogonal decomposition”. In: *International journal for numerical methods in fluids* 34.5, pages 425–448 (cited on page 25).

Reis, T. and T. Stykel (2008). “Balanced truncation model reduction of second-order systems”. In: *Mathematical and Computer Modelling of Dynamical Systems* 14.5, pages 391–406 (cited on page 22).

Rempfer, D. and H. F. Fasel (1994). “Evolution of three-dimensional coherent structures in a flat-plate boundary layer”. In: *Journal of Fluid Mechanics* 260, pages 351–375 (cited on page 25).

Rozza, G. and K. Veroy (2007). “On the stability of the reduced basis method for Stokes equations in parametrized domains”. In: *Computer Methods in Applied Mechanics and Engineering* 196.7, pages 1244–1260. ISSN: 0045-7825. DOI: `http://dx.doi.org/10.1016/j.cma.2006.09.005` (cited on pages 56, 101).

Sartori, A., D. Baroli, A. Cammi, L. Luzzi, and G. Rozza (2014). “A reduced order model for multi-group time-dependent parametrized reactor spatial kinetics”. In: *2014 22nd International Conference on Nuclear Engineering*. American Society of Mechanical Engineers, V005T17A048–V005T17A048 (cited on page 12).

Sartori, A., A. Cammi, L. Luzzi, and G. Rozza (2016a). “A multi-physics reduced order model for the analysis of Lead Fast Reactor single channel”. In: *Annals of Nuclear Energy* 87, pages 198–208 (cited on page 12).

— (2016b). “A Reduced Basis Approach for Modeling the Movement of Nuclear Reactor Control Rods”. In: *Journal of Nuclear Engineering and Radiation Science* 2.2, page 021019 (cited on page 12).

— (2016c). “A reduced basis approach for modeling the movement of nuclear reactor control rods”. In: *Journal of Nuclear Engineering and Radiation Science* 2.2, page 021019 (cited on page 88).

Sebilleau, F. C. M. (Dec. 2016). “Computational analysis of buoyancy driven flows across scales”. PhD thesis. Department of Mechanical Engineering, Imperial College London (cited on page 132).

Sirisup, S. and G. E. Karniadakis (2004). “A Spectral Viscosity Method for Correcting the Long-Term Behavior of POD Models”. In: *J. Comput. Phys.* 194.1. ISSN: 0021-9991. DOI: `10.1016/j.jcp.2003.08.021`. URL: `https://doi.org/10.1016/j.jcp.2003.08.021` (cited on page 160).

Sirovich, L. (1987a). “Turbulence and the Dynamics of Coherent Structures Part II: Symmetries and Transformations”. In: *Quarterly of Applied Mathematics* XLV, pages 573–82. DOI: `10.1090/qam/910463` (cited on page 24).

— (1987b). “Turbulence and the Dynamics of Coherent Structures; Part I: Coherent Structures, Q”. In: *Appl. Math* 45, pages 561–571 (cited on page 23).

Stabile, G. and G. Rozza (no date). *ITHACA-FV - In real Time Highly Advanced Computational Applications for Finite Volumes*. Accessed: 2018-01-30. URL: `http://www.mathlab.sissa.it/ithaca-fv` (cited on page 53).

Stabile, G., S. Hijazi, A. Mola, S. Lorenzi, and G. Rozza (2017). “POD-Galerkin reduced order methods for CFD using Finite Volume Discretisation: vortex shedding around a circular cylinder”. In: *Communications in Applied and Industrial Mathematics* 8.1, pages 210–236. DOI: `10.1515/caim-2017-0011` (cited on page 101).

Stabile, G. and G. Rozza (2018). “Finite volume POD-Galerkin stabilised reduced order methods for the parametrised incompressible Navier–Stokes equations”. In: *Computers & Fluids* 173, pages 273–284. DOI: `10.1016/j.compfluid.2018.01.035` (cited on pages 25, 56, 57, 61).

Star, K., G. Stabile, S. Georgaka, F. Belloni, G. Rozza, and J. Degroot (2019). “POD-Galerkin Reduced Order Model of the Boussinesq Approximation for Buoyancy-Driven Enclosed Flows”. In: *Proceedings of International Conference on Mathematics and Computational Methods applied to Nuclear Science and Engineering, Portland, Oregon USA, 2019* (cited on pages 54, 124).

Tunstall, R., D. Laurence, R. Prosser, and A. Skillen (2016a). “Benchmarking LES with wall-functions and RANS for fatigue problems in thermal hydraulics systems”. In: *Nuclear Engineering and Design* 308, pages 170–181. ISSN: 0029-5493. DOI: `https://doi.org/10.1016/j.nucengdes.2016.08.022`. URL: `http://www.sciencedirect.com/science/article/pii/S0029549316302825` (cited on page 94).

— (2016b). “Large eddy simulation of a T-Junction with upstream elbow: The role of Dean vortices in thermal fatigue”. In: *Applied Thermal Engineering* 107, pages 672–680. ISSN: 1359-4311. DOI: `https://doi.org/10.1016/j.applthermaleng.2016.07.011` (cited on pages 13, 88).

Vergari, L., A. Cammi, and S. Lorenzi (2020). “Reduced order modeling approach for parametrized thermal-hydraulics problems: inclusion of the energy equation in the POD-FV-ROM method”. In: *Progress in Nuclear Energy* 118, page 103071. ISSN: 0149-1970. DOI: `https://doi.org/10.1016/j.pnucene.2019.103071` (cited on page 162).

Veroy, K. and A. Patera (2005). "Certified real-time solution of the parametrized steady incompressible Navier–Stokes equations: rigorous reduced-basis a posteriori error bounds". In: *International Journal for Numerical Methods in Fluids* 47.8-9, pages 773–788 (cited on page 30).

Veroy, K., C. Prud'Homme, D. Rovas, and A. Patera (2003). "A posteriori error bounds for reduced-basis approximation of parametrized noncoercive and nonlinear elliptic partial differential equations". In: *16th AIAA Computational Fluid Dynamics Conference*, page 3847 (cited on page 30).

Walker, C., M. Simiano, R. Zboray, and H.-M. Prasser (2009). "Investigations on mixing phenomena in single-phase flow in a T-junction geometry". In: *Nuclear Engineering and Design* 239.1, pages 116–126. ISSN: 0029-5493. DOI: `https://doi.org/10.1016/j.nucengdes.2008.09.003` (cited on pages 13, 88).

Wang, Y., B. Yu, Z. Cao, W. Zou, and G. Yu (2012). "A comparative study of POD interpolation and POD projection methods for fast and accurate prediction of heat transfer problems". In: *International Journal of Heat and Mass Transfer* 55.17-18, pages 4827–4836. DOI: `10.1016/j.ijheatmasstransfer.2012.04.053` (cited on page 26).

Wang, Z., I. Akhtar, J. Borggaard, and T. Iliescu (2012). "Proper orthogonal decomposition closure models for turbulent flows: A numerical comparison". In: *Computer Methods in Applied Mechanics and Engineering* 237-240, pages 10–26. ISSN: 0045-7825. DOI: `https://doi.org/10.1016/j.cma.2012.04.015`. URL: `http://www.sciencedirect.com/science/article/pii/S0045782512001429` (cited on page 89).

Wilcox, D. C. (1998). *Turbulence modeling for CFD*. Volume 2. DCW industries La Canada, CA (cited on page 35).

Xiao, D., F. Fang, C. Pain, I. Navon, P. Salinas, and A. Muggeridge (2015). "Non-intrusive reduced order modeling of multi-phase flow in porous media using the POD-RBF method". In: *J. Comput. Phys.* (Cited on page 89).

Appendix A

Glossary

BuoyantBoussinesqPimpleFoam: OpenFOAM transient solver for incompressible buoyant turbulent flow, based on the PIMPLE algorithm.

fixedFluxPressure: Boundary condition in OpenFOAM where the pressure gradient is adjusted so that the flux on the boundary is specified by the velocity boundary condition.

fixedValue: Boundary condition in OpenFOAM where a constant value at the boundary is applied.

icoFoam: OpenFOAM transient solver for incompressible laminar flow, based on the PISO algorithm.

noSlip Boundary condition in OpenFOAM where the velocity is set to zero.

pisoFoam: OpenFOAM transient solver for incompressible turbulent flow, based on the PISO algorithm.

pressureInletOutletVelocity: Boundary condition in OpenFOAM where, for outflow, a zero-gradient condition is applied while, for inflow, the velocity is calculated from the patch-face normal component of the internal-cell value (*OpenFOAM website* 2011-2012).

totalPressure: Boundary condition in OpenFOAM where, for incompressible fluids, the value of the patch pressure, p_p, is calculated as $p_p = p_0 - 0.5U^2$. The total pressure, p_0, is specified by the user.

zeroGradient: Boundary condition in OpenFOAM where a zero-gradient is applied from the internal field patch onto the face patch.

Appendix B

Copyright Authorisations

This appendix provides authorisations for the reproduction of materials from my own publications:

GEORGAKA, S., STABILE, G., ROZZA, G., and BLUCK, M.J. 2020. Parametric POD-Galerkin Model Order Reduction for Unsteady-State Heat Transfer Problems. Communications in Computational Physics, Vol 27, No. 1, pp. 1-32.

GEORGAKA, S., STABILE, G., STAR, K., ROZZA, G., and BLUCK, M.J. A Hybrid Reduced Order Method for Modelling Turbulent Heat Transfer Problems. Computers and Fluids, 2019

STAR, K., STABILE, G., GEORGAKA, S., BELLONI, F., ROZZA, G., and DEGROOTE, J. 2019. POD-Galerkin Reduced Order Model of the Boussinesq Approximation for Buoyancy - Driven Enclosed Flows. Building theory and applications : proceedings of M&C 2019. p.2452-2461.

GLOBAL SCIENCE PRESS
CONSENT TO PUBLISH AND COPYRIGHT AGREEMENT
Communications in Computational Physics

CICP-OA-2018-0207.R2
Manuscript Number

The Publisher hereby requests that the Author(s) complete and return this form promptly so that the Work may be finalized for publication. The copyright form should be sent or faxed to Prof. T. Tang, Managing Editor, Department of Mathematics, The Hong Kong Baptist University, Kowloon Tong, Hong Kong; Email: cicp@global-sci.com; Fax: (852) 3411-5185.

Article Title (the "Work"): Parametric POD-Galerkin Model Order Reduction for Unsteady-State Heat Transfer Problems

Names of Authors: Sokratia Georgaka, Giovanni Stabile, Gianluigi Rozza, Michael J Bluck

1. The Author(s) hereby consents that the Publisher publishes the Work.
2. The Author(s) must confirm the following: a) the Work has not been published before in any form except as a preprint; b) the work is not concurrently submitted to another publication; c) all Authors are properly credited; d) the Author(s) has the right to make the grants made to the Publisher complete and unencumbered. The Author(s) must also confirm that the Work does not libel anyone, infringe on anyone's copyright, or otherwise violate anyone's statutory or common law rights.
3. The Author(s) hereby transfers to the Publisher the copyright of the Work named above, whereby the Publisher shall have the exclusive and unlimited right to publish the given Work and to have it translated wholly or in part throughout the world during the full term of copyright. This includes renewals, extensions, and all subsidiary rights as stipulated above, subject only to item 4.
4. The Work may be reproduced by any means for educational and scientific purposes by the Author(s) or by others without fee or permission with the exception of reproduction by services that collect fees for delivery of documents. The Author(s) may use part or all of this Work or its image in any further work of his/her (their) own. In any reproduction, the original publication by the Publisher must be credited in the following manner: "First published in [Publication] in [volume and number, or year], published by Global Science Press," and the copyright notice in proper form must be placed on all copies. Any publication or other form of reproduction not meeting these requirements will be deemed unauthorized.
5. If the Author(s) wishes to retain copyright of the content and image of this Work in the Author(s) name(s) or in the name of a third party (e.g. an employer), the Author may strike out items 3, and 4 above. In this case, the Author(s) nevertheless gives the Publisher unlimited rights to publish and distribute the Work in any form, and to have it translated wholly or in part throughout the world, and to accept payment for this. The copyright holder retains the right to duplicate the Work by any means, and to permit others to do the same, with the exception of reproduction by services which collect fees for delivery of documents.
6. If the Article was prepared under a U.S. Government contract, the government shall have the rights under the copyright to the extent required by the contract.

This form is to be signed by the Author(s). In the case of more than one Author, either all of them must sign the Consent to Publish and Copyright Agreement, or one Author may sign for everyone.

Giovanni Stabile 21/01/2019
Author Signature(s) Date

Sokratia Georgaka Giovanni Stabile Gianluigi Rozza Michael J Bluck
Name(s) (print)

If the Article has been prepared as a Work Made For Hire, the transfer should be signed by **both** the employee (above) **and** the employer (below):

Employer

Authorized Signature(s) Name(s) (print) Title Date

U.S. GOVERNMENT EMPLOYEES

A work prepared by a U.S. Government officer or employee* as part of his or her official duties is not eligible for U.S. copyright. If at least one of the authors is *not* in this category, that author should sign the transfer Agreement above. If all the authors are in this category, one of the authors should sign below, and indicate his or her affiliation.

Authorized Signature(s) Name(s) (print) Institution (e.g., Naval Research Laboratory, NIST) Date

* Employees of national laboratories, e.g., Argonne National Laboratory, are not U.S. Government employees.

American Nuclear Society
555 N. Kensington Ave. · La Grange Park, IL 60526 · USA
Tel: 708-352-6611 · Fax: 708-352-8313 · Email: NUCLEUS@ans.org

Date June 17th 2019

AGREEMENT ON COPYRIGHT

Certain rights under copyright to the article (MS. 27473) submitted with the title POD-Galerkin reduced order model of the Boussinesq approximation for buoyancy-driven enclosed flows by Star K, Stabile G, Georgaka S, Belloni F, Rozza G, Degroote J (the "Assignor") are assigned to the American Nuclear Society (ANS), effective when the article ("work") is accepted for presentation or publication by ANS, and secured by ANS registration of publication collective works of which this article will be a part.

The Assignor (author or authors) warrants that they have full right to make this Agreement, that their work does not violate the rights of other persons nor infringe upon any existing copyrighted work. If copyrighted material of a third party is included, the Assignor agrees that they will obtain required permission for its reuse.

The Assignor retains the right to reproduce this article for their own use. Also, the Assignor keeps the right to use all or part of the work in future works they prepare—but not within six months after ANS publishes this article, unless agreed to by ANS.

The Assignor also retains the right to grant to third parties permission to republish all or part of the work, provided written permission also is given by ANS. Proprietary rights other than copyrights, such as patent rights, also are retained by the Assignor.

If the Assignor is acting for other authors, their rights are retained or transferred in the same manner under this Agreement.

If the author(s) created this work while employed by the U.S. Government or one of its contractors, and within the scope of such employment, the U.S. Government is granted a nonexclusive royalty-free license to publish, republish, or reproduce the work or to allow others to reproduce this work for U.S. Government purposes.

Signature SKStar	Signature
Print Name Star Sabrina Kelbij	Print Name
Address Boeretang 203	Address
City/State Mol, Belgium	City/State

The above-identified work is accepted for publication in the M&C 2019